UNIVERSITY OF CALIFORNIA
SANTA CRUZ

WHEN THERMAL MEETS NON-THERMAL: INVESTIGATING GAMMA-RAY EMISSION FROM VERY-HIGH-ENERGY BLAZARS

A dissertation submitted in partial satisfaction of the
requirements for the degree of

DOCTOR OF PHILOSOPHY

in

PHYSICS

by

Caitlin Anne Johnson

December 2018

The Dissertation of Caitlin Anne Johnson
is approved:

Professor Tesla Jeltema, Chair

Professor David A. Williams

Professor Jason X. Prochaska

Lori Kletzer
Vice Provost and Dean of Graduate Studies

Table of Contents

List of Figures

List of Tables

Abstract

When Thermal Meets Non-thermal:
Investigating Gamma-ray Emission from Very-High-Energy Blazars

by

Caitlin Anne Johnson

Blazars, active galactic nuclei with their jets aligned along our line of sight, emit radiation in all bands of the electromagnetic spectrum. Many questions remain about the emission mechanisms, and this dissertation investigates how thermal emission originating outside of the jet plays a role in producing the non-thermal radiation created in the jet. We present multi-wavelength observations of the very-high-energy-emitting blazar 3C 66A taken from 2007 to 2016 by VERITAS, the *Fermi*-Large Area Telescope, the Neil Gehrels *Swift* Observatory, and ground-based optical observatories including the Tuorla Observatory and Fred Lawrence Whipple Observatory. 3C 66A is a TeV-emitting intermediate-synchrotron-peaked blazar, a relatively small class of TeV-detected AGN. We construct the multi-wavelength spectral energy distribution during multiple epochs of observation and present the first spectral energy distributions of 3C 66A in quiescent flux states. To explain the emission, we develop and implement a Markov Chain Monte Carlo method to fit single-zone gamma-ray emission models. Additionally, we study the gamma-ray flux and optical spectral features of five TeV-detected blazars: Mrk 501, Mrk 421, 3C 279, PKS 1441+25 and PKS 1222+216. Correlations between optical spectral features and gamma-ray flux can give insight to the interplay between region producing non-thermal emission in the jet and thermal components such as the broad line region in the blazar environment.

To my village.

Chapter 1

Introduction to Very High Energy Blazars

For millennia, humans have looked to the skies above for answers about the laws of nature. In the mid-1900s, astronomers began to grasp the immense physical scale of the Universe in which we live and the variety of environments that exist in it. One type of astrophysical object that was initially discovered in the 1960's, active galactic nuclei (AGN), has turned out to host multiple environments useful for studying fundamental physics and the nature of galaxies in the Universe. This thesis investigates a subset of AGN, blazars, and aims to understand the physics of how gamma rays are produced in this extreme environment and the role of thermal emission and geometry. This chapter introduces some of the context and fundamental physics relevant to the study of gamma-ray emission from blazars.

1.1 Active Galactic Nuclei

AGN are compact regions near the center of galaxies with a super massive black hole (SMBH), 10^6 - 10^8 Solar masses. The AGN is typically accreting

matter onto a disk, and a small fraction host two relativistic jets emanating from either side of the accretion disk. AGN have a variety of observed properties, and significant work over the past several decades has been in an effort to unify these properties. Our current picture is that the variety of observables can be explained primarily based on the viewing geometry of the AGN, but they are also impacted by the mass of the black hole, rate of accretion and obscuration by dust (Urry and Padovani, 1995).

When the jet of an AGN is aligned close to our line of sight, it is called a blazar. Details of the implications for this orientation are in Section 1.4. There are two types of blazars, classified based on their observed optical spectral features. BL Lacertae type objects, or simply BL Lacs, have spectral features with equivalent widths (EW) < 5 Angstroms. Flat spectrum radio quasars (FSRQs) have spectral features with EW > 5 Angstroms. Understanding the underlying physics describing these two classes of blazars and how they are related is part of the effort towards blazar unification.

A defining characteristic of blazars is their observed flux variability. They have been observed to undergo changes in brightness in almost all wavebands and with a range of time scales and amplitudes. For example, in the gamma-ray band, BL Lac has exhibited variability on the timescale of minutes while PKS 1424+240 has exhibited longer term variability on the timescale of years (Archambault et al., 2014), (Abeysekara et al., 2018). Currently, aperiodic variability is the norm in observed blazar phenomena, though there has been possible periodic variability observed in a few blazars (e.g. PG 1553+113 (Ackermann et al., 2015)).

1.2 Observations of Gamma-ray Blazars

Blazars are detected in every wave band, from radio up to gamma rays. Advances in gamma ray astrophysics over the past few decades have shown that blazars in fact dominate the extragalactic gamma-ray sources observed (Acero et al., 2015). High-energy (HE; ∼100 MeV - 100 GeV) gamma rays are currently observed by the Large Area Telescope (LAT) on board the *Fermi* Gamma Ray Space Telescope. *Fermi* was launched in June, 2008 and continues to take observations. The LAT operates in sky-survey mode, observing the entire sky every three hours. Except for a few pointed observations during its lifetime, the observing is unbiased in its sky coverage. The data collected by the LAT are made public a few hours after they have been taken, and they can be analyzed with publicly released software called the Fermi Science Tools. Very-high-energy (VHE; >100 GeV) gamma rays are best observed by ground-based telescopes such as VERITAS. See Chapter 2 for further details on VERITAS and the imaging atmospheric Cherenkov telescope technique of observation. There are two additional major observatories which utilize this technique to observe gamma rays from the ground: HESS in Namibia and MAGIC on La Palma. VHE data are generally not public, and observations are pointed due to the smaller field of view compared to the LAT. The overlap in energy coverage and different observing scenarios make LAT and ground-based instruments complimentary for detecting sources and answering questions about the fundamental physics occurring in blazars and AGN of all types.

As of May 1st, 2018, there are 210 VHE sources, 54 of which have been detected by VERITAS[1]. The full VERITAS catalog is shown in galactic coordinates in Fig. 1.1. Of the full catalog of VHE sources, 70 are blazars and 33 of these blazars

[1] `http://tevcat2.uchicago.edu/`

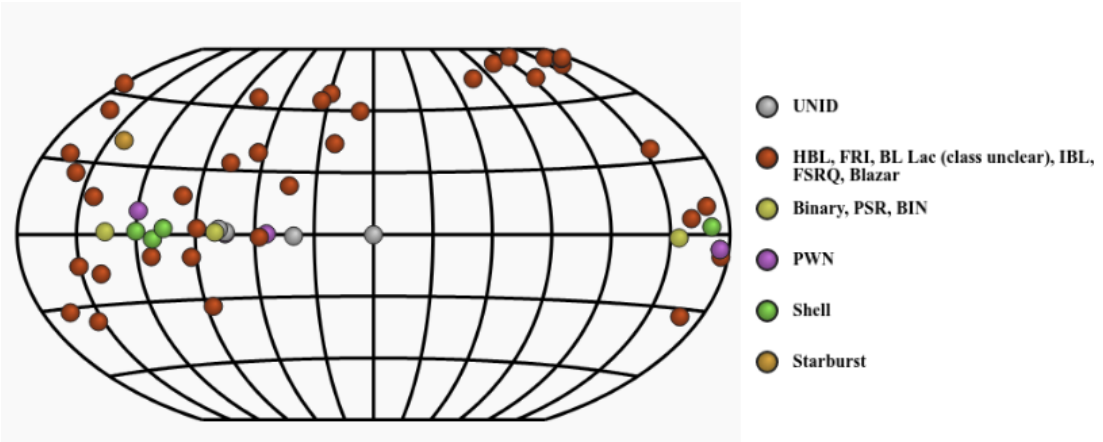

Figure 1.1: The VERITAS catalog as of May 1st, 2018 shown in galactic coordinates. Image is generated via TeVCat (http://tevcat2.uchicago.edu/). All types of source classes are shown and indicated by the color of each marker.

have been detected by VERITAS.

1.3 The Blazar Spectral Energy Distribution

A spectral energy distribution (SED) shows energy flux as a function of energy, and it illustrates which part of the spectrum carries most of the observed energy. The blazar SED is characteristically double peaked. The lower energy peak is known to be the result of synchrotron radiation from relativistic electrons; however, the origin of the higher-energy peak is one of the major open questions in blazar physics. The higher energy peak can extend up to TeV energies, and it is unknown exactly how jets accelerate particles to these extreme energies. By studying blazars where the rising edge of the gamma-ray peak occurs in the *Fermi*-LAT energy regime and the falling edge occurs in the VERITAS energy regime, we can model the entire high-energy emission. A few models that fully describe the entire blazar SED have crystallized over the past several years. In leptonic models, photons are upscattered via inverse-Compton scattering off the relativis-

tic electrons which created the synchrotron radiation. However, the spatial origin of the upscattered photons is still not well understood. In a synchrotron-self-Compton (SSC) scenario, the photon field is the synchrotron radiation created by the same relativistic electrons. In an external-Compton (EC) scenario, the photon field originates outside the jet and could be from a variety of sources (e.g. the broad line region, accretion disk, dusty torus, etc.). While processes in the jet are generally accepted to be leptonic, hadronic models have not been completely ruled out. In both scenarios, protons can be present in the jet. If the protons are ultrarelativistic and exceed the threshold for photo-pion production, they will initiate electromagnetic cascades which may dominate the high-energy emission. In addition to understanding jet mechanisms, SEDs are also used as a blazar classification system. Specifically, blazars are classified based on the location of the synchrotron (lower energy) peak. A low-synchrotron-peaked (LSP) blazar is one where the synchrotron peak occurs at $\nu_{peak} < 10^{14}$ Hz. Intermediate-synchrotron-peaked (ISP) blazars have $10^{14} < \nu_{peak} < 10^{15}$, and high-synchrotron-peaked (HSP) blazars have $\nu_{peak} > 10^{15}$. Of all VHE-detected blazars, 48 are classified as HSPs, 8 are ISPs and 2 are LSPs. ISPs and LSPs are the least numerous class of detected VHE blazars, and this is currently believed to be a selection effect. The lower energy peaks of these classes mean that the bulk of the high energy emission falls lower in energy than the sensitivity of current ground-based gamma-ray observatories. The five ISPs that VERITAS has detected are 3C 66A, W Comae, S3 1227+25, BL Lacertae, and VER J0521+211. Emission from HSPs has often been successfully explained with pure SSC models, while LSPs often require a substantial EC component. However, not all SEDs fit these trends and there is much to be learned about how the classifications relate to the physics of the environment.

1.4 Blazar Physics

The generation and observation of electromagnetic radiation in the jets of blazars utilize physics processes that we've come to understand over the past century or so. The open questions about jet physics are more related to how different pieces interplay than the discovery of new physics. However, the observation of AGN can be used to search for violations of known physics such as Lorentz invariance violation. Thermal processes for generating radiation are those associated with a temperature of a system, and follow Planck's law. Non-thermal processes are all other types and are the most dominant type of radiation in the blazar jet. The following few paragraphs introduce and outline some of the common physics processes found in this dissertation and the study of blazars.

The emitting region moving down the jet is thought to contain a relativistic population of particles and a tangled magnetic field. In a model when the particles are electrons and positrons, it is considered a *leptonic model*. In models where there are protons and other heavier particles, it is considered a *hadronic model*.

When a charged particle is accelerated, it radiates. In the case of a non-relativistic particle being accelerated by a magnetic field, as is seen in every introductory physics course, cyclotron radiation is produced. When the particle is moving relativistically, synchrotron radiation is produced; the frequency spectrum for synchrotron radiation is more complex than that of cyclotron (Rybicki and Lightman, 1979).

Compton scattering is the transfer of energy from photons to electrons. After the scattering process, the photons have less energy than they did initially. Inverse Compton scattering is easily inferred from its name: the electrons impart their energy to the photons so that the photons have more energy than before the scattering. In these systems, the electrons are moving relativistically and are

therefore able to scatter photons in the optical range up to gamma-ray energies.

1.4.1 Synchrotron Self-Compton Scenario

One of the simplest models describing emission in the jet of the blazar is a single-zone SSC model. In this model, the photon population resulting from the synchrotron radiation is that which is upscattered in the inverse Compton process. The single-zone refers to the single emitting region within the jet giving rise to all observed radiation. This model is typically the initial scenario used to describe a blazar SED due to its simplicity.

1.4.2 External Compton Scenario

In the external Compton (EC) scenario, the seed photons for the inverse-Compton scattering process originate outside of the jet. These can come from a dusty torus or the accretion disk outside the jet. Radiation is emitted from these and travels directly into the jet, or is reflected off the broad line region (BLR) and into the jet. For this scenario to work, the gamma-ray emitting region must be close to the base of the jet or within the BLR.

1.5 The Extragalactic Background Light

The Universe is filled with cosmic radiation fields, one of which is the extragalactic background light (EBL). The EBL is the entirety of light emitted since the Big Bang from AGN, stars and galaxies and its emission spans the ultraviolet, optical and infrared bands. Today, the observed EBL consists of the light integrated from every epoch in the Universe as it has been redshifted and diluted by cosmic expansion (Gilmore et al., 2012). Since the EBL reflects the formation of

galaxies and stars, understanding its evolution with time is a way to understand how galaxies and stars themselves evolved throughout the history of the Universe. Direct measurements of the EBL are difficult due to its faintness, and they only capture its current state as opposed to its evolution over time. Lower limits on the EBL flux density can be provided via galaxy catalogs.

While propagating through the Universe, VHE gamma rays encounter EBL photons. Production of an electron-positron pair via scattering of two photons, known as pair production, occurs when there is enough energy in the center-of-mass frame of the photons. This can be written in Equation 1.1 as

$$\sqrt{2E_1E_2(1-\cos\theta)} \geq 2m_ec^2, \tag{1.1}$$

where E_1 and E_2 are the energies of the two photons, θ is the angle of incidence and m_e is the mass of the electron. If E_1 and E_2 are the energies of an EBL photon and a gamma ray, we can define the minimum energy of the EBL photon, E_{th}, that would interact via pair production with a gamma ray of E_γ in Equation 1.2 as

$$E_{th} = \frac{2m_e^2c^4}{E_\gamma(1-\cos\theta)}\,. \tag{1.2}$$

The cross-section for this process is (Gilmore et al., 2012)

$$\sigma(E_1, E_2, \theta) = \frac{3\sigma_T}{16}(1-\beta^2) \times \left[2\beta(\beta^2-2) + (3-\beta^4)\ln\left(\frac{1+\beta}{1-\beta}\right)\right], \tag{1.3}$$

where σ_T is the Thomson cross-section and β is defined as

$$\beta = \sqrt{1 - \frac{2m_e^2c^4}{E_1E_2(1-\cos\theta)}} \ . \tag{1.4}$$

The cross section for three values of the angle of incidence, θ, is shown in Fig. 1.2. For an angle of incidence of $\theta = \pi/2$, the maximal cross section occurs when $E_1 = 1.044\,(\mathrm{TeV}/E_2)$ eV. This means that photons from ∼50 GeV to above 10 TeV, HE and VHE gamma rays, pair produce with the EBL photons and are effectively absorbed. Accounting for this absorption, the observed flux is simply related to the emitted flux by

$$F_{observed} = e^{-\tau(z,E_\gamma)} F_{emitted} \ . \tag{1.5}$$

The optical depth, τ, is calculated as:

$$\tau(z_0, E_\gamma) = \frac{1}{2}\int_0^{z_0} dz \frac{dl}{dz} \int_{-1}^{-1} du(1-u) \int_{E_{min}}^{\infty} dE_{EBL} n(E_{EBL}, z)\sigma(E_\gamma(1+z), E_{EBL}, \theta)) \tag{1.6}$$

where the integral is performed along the line of sight, z_0 indicates the redshift of the gamma-ray emitter, $u = \cos(\theta)$, $n(E_{EBL}, z)$ is the density of EBL photons, $\frac{dl}{dz}$ is the cosmological line element, and $E_{min} = E_{th}(1+z)^{-1}$. The EBL density, n, can be semi-analytically modeled by combining observational inputs with theoretical insights, and multiple efforts have been undertaken in previous years (e.g. Gilmore et al. (2012)). In all models, the opacity increases with redshift and energy of the emitted gamma ray. An example of this behavior can be seen in the opacity edges plotted in Figure 1.2.

Absorption of gamma rays by the EBL has implications for observations of VHE emitters such as blazars and gamma-ray bursts (GRBs). Due to the increased absorption with redshift, it is difficult to detect VHE gamma rays from dis-

tant sources. To date, the most distant source detected at VHE is the gravitationally-lensed blazar S3 0218+357 at a redshift of only z= 0.944 ± 0.002 (Mirzoyan, 2014). It was detected by the ground-based gamma-ray observatory MAGIC in 2014. Though challenging to observe, high redshift emitters of VHE gamma rays are interesting and exciting because they allow for the EBL models to be tested. Observations that are impacted by high opacities of the EBL are the most useful, and that requires observations at increased energies and high redshifts. In recent years, observations of a few key blazars have pushed these limits and provided insight into cosmic processes. Future VHE telescopes such as the Cherenkov Telescope Array will build on these successes and attempt to better constrain the EBL and understand cosmic evolution.

1.6 Detection of VHE Emission from PKS 1441+25

An excellent example of the importance of observing high redshift VHE blazars despite the impact of EBL absorption is the detection of the FSRQ PKS 1441+25. This blazar, located at z=0.939, is the second highest redshift VHE emitter detected to date. It was detected by both VERITAS and MAGIC in April of 2015 (Abeysekara et al., 2015; Ahnen et al., 2015). The VHE detection and full gamma-ray spectrum allowed for the calculation of upper limits on the amount of EBL absorption present and its impact on VHE gamma rays originating from the source. In April of 2015, the source went into an elevated flux state and both MAGIC and VERITAS detected VHE emission from it (Mukherjee, 2015).

VHE gamma rays from this FSRQ were detected while it was exhibiting an increase in flux and a hardening in its high-energy spectrum as seen by *Fermi*-LAT. Observing high redshift sources during outbursts is one of the powerful ways we can gather the statistics required to investigate science questions about

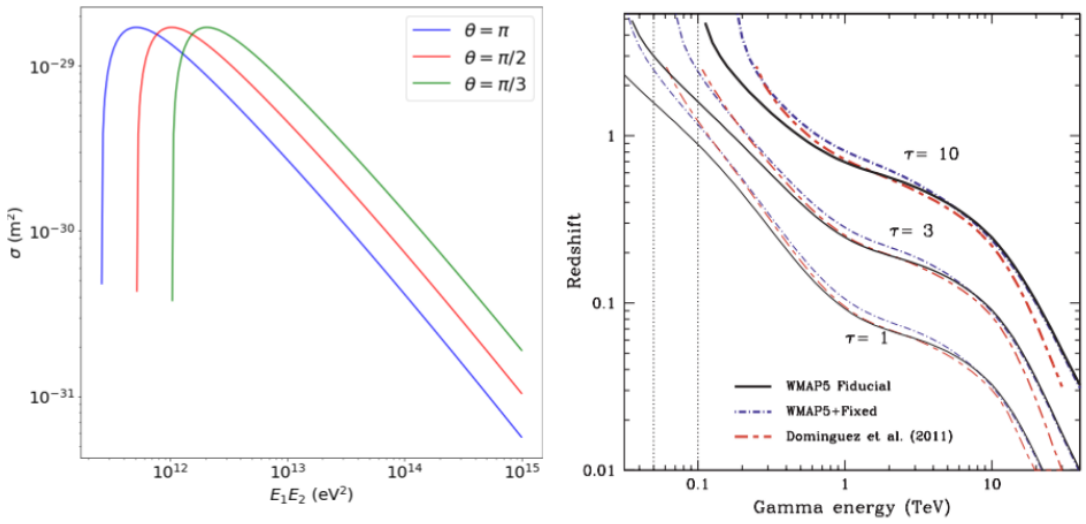

Figure 1.2: Left: The cross-section for interactions between two photons creating an electron-positron pair as a function of the product of their energies. Three values of θ, the angle of incidence, are shown. Right: Figure from Gilmore et al. (2012) showing the gamma-ray attenuation edges for various models of the EBL. The curves show the redshift at which the pair production optical depth τ reaches the indicated value for a particular observed gamma-ray energy. The groups of curves from lower left to upper right are the contours for $\tau = 1$, 3 and 10. There are vertical lines to guide the eye at 50 and 100 GeV.

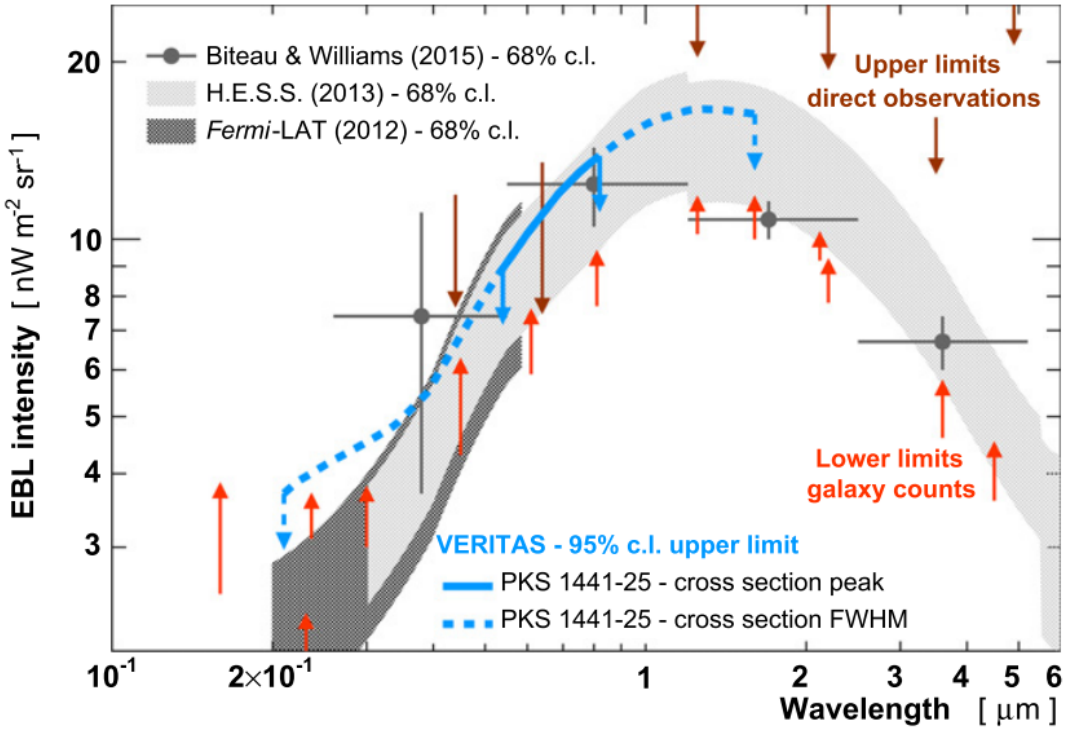

Figure 1.3: From Abeysekara et al. (2015): "Near-ultraviolet to near-infrared spectrum of the EBL. The upper limit from this work is shown in blue, in regions corresponding to the peak and full-width-half-max of the cross section ($1 < \tau < 2$)."

the EBL, and the *Fermi*-LAT is particularly useful for triggering ground-based VHE observations. The LAT's unbiased sky coverage combined with the public availability of the data within hours of being taken allow for fast follow-up of transient events. For sources of interest to studies of the EBL, the energy coverage of the LAT is ideal. The range overlaps with that covered by VHE observatories, but it extends lower in energy so the detectable flux is less likely to be impacted by EBL absorption.

The construction of a VHE spectrum from such a high redshift source allowed for a constraint on the amount of EBL absorption. The spectral index on the deabsorbed VHE spectrum was limited based on extrapolating the lower-energy *Fermi*-LAT data which are unaffected by the EBL. The 95% confidence upper

limits from such an analysis are shown in Figure 1.3. They are consistent with the lower limits provided by direct galaxy counts, and the normalization on the EBL is consistent with the model of Gilmore et al. (2012).

Chapter 2

Ground-based Gamma-ray Astrophysics with VERITAS

When gamma rays or charged particles hit Earth's atmosphere, they collide with molecules and instigate a shower of particles. These showers consist of charged particles moving faster than the speed of light in the atmosphere; they therefore create Cherenkov radiation. The imaging atmospheric Cherenkov telescope (IACT) technique relies on imaging this flash of radiation and allows gamma rays above $\sim$50 GeV to be studied by ground-based instruments. Details of the IACT implementation by the Very Energetic Radiation Imaging Telescope Array System (VERITAS) follow.

2.1 Extensive Air Showers & Cherenkov Radiation

An extensive air shower (EAS) is a cascade of radiation and charged particles that propagates through the atmosphere. An EAS can be instigated by a variety of

particles including photons, protons and nuclei. Cherenkov radiation is produced when a charged particle travels faster than the phase velocity in a medium, and particles in EAS can certainly meet this criterion. This creates a flash of light lasting $\sim$ 5 ns and peaking in the ultraviolet at $\sim$350 nm (Bouvier et al., 2013). For primary energies less than $\sim$20 TeV, the particle cascade dies out in the upper atmosphere, but the Cherenkov light continues and creates a "light pool" on the ground below. This light carries with it information about the energy and the location in the sky of the shower-instigating particle which we can reconstruct in our data analysis (Fegan, 1997).

2.2 The VERITAS Instrument

VERITAS is an array of four telescopes located at the base of Mount Hopkins at the Fred Lawrence Whipple Observatory in southern Arizona. It uses the IACT technique to stereoscopically observe VHE gamma rays and is one of three current-generation major IACTs in operation. VERITAS has been fully operational since 2007, and has undergone two major upgrades. The array configuration for the first two fully operational seasons of VERITAS (September 2007 - July 2009) is called V4. In the summer of 2009, one of the telescopes (T1) was relocated to increase the effective area of the telescopes. This new array configuration is called V5. In the summer of 2012, the cameras were upgraded with higher-efficiency photomultiplier tubes (PMTs), and this upgraded array configuration is called V6.

2.2.1 Telescope Structure & Mirrors

Each individual telescope consists of a metal positioner that accommodates altitude-azimuth motion. Mounted on each positioner is the optical support structure (OSS). A telescope is shown in Figure 2.1. The OSS supports a 12m dish of 345 hexagonal mirrors arranged in a segmented Davies-Cotton design (Roache et al., 2008). Quadrapod arms mount the camera to the rest of the telescope structure and house the cables bringing information down from the camera and into electronics trailers on the ground below. Each telescope is also equipped with a raised platform allowing for access to the camera by personnel.

2.2.2 Camera

Mounted at the focal plane of each telescope is a camera with a field of view 3.5° in diameter consisting of 499 PMTs. A PMT uses a photocathode that can absorb photons then release electrons (photoelectrons). Applying a high voltage ($\sim$1000 V) directs these photoelectrons towards multiple stages of dynodes, each of which multiplies the photoelectrons, and feeds them onto an anode. PMTs work well as pixels in Cherenkov telescopes due to their fast time response and their amplification of faint light signals. The quantum efficiency (QE) of a PMT is defined as the probability of a photoelectron being released when the photocathode is struck by a photon, and this property is dependent on both the material of the photocathode and the wavelength of the original photon. The VERITAS cameras were originally populated with Photonis XP 2970/2 PMTs which had a QE of $\sim$25% at 400 nm and a gain of 2×10^5 (Cogan, 2006). In 2012, the pixels in all four VERITAS cameras were replaced with Hamamatsu high quantum efficiency PMTs with peak QE >32%. These new PMTs increased the photon detection efficiency of each camera by 50%. One major upgrade in performance is the lowered energy

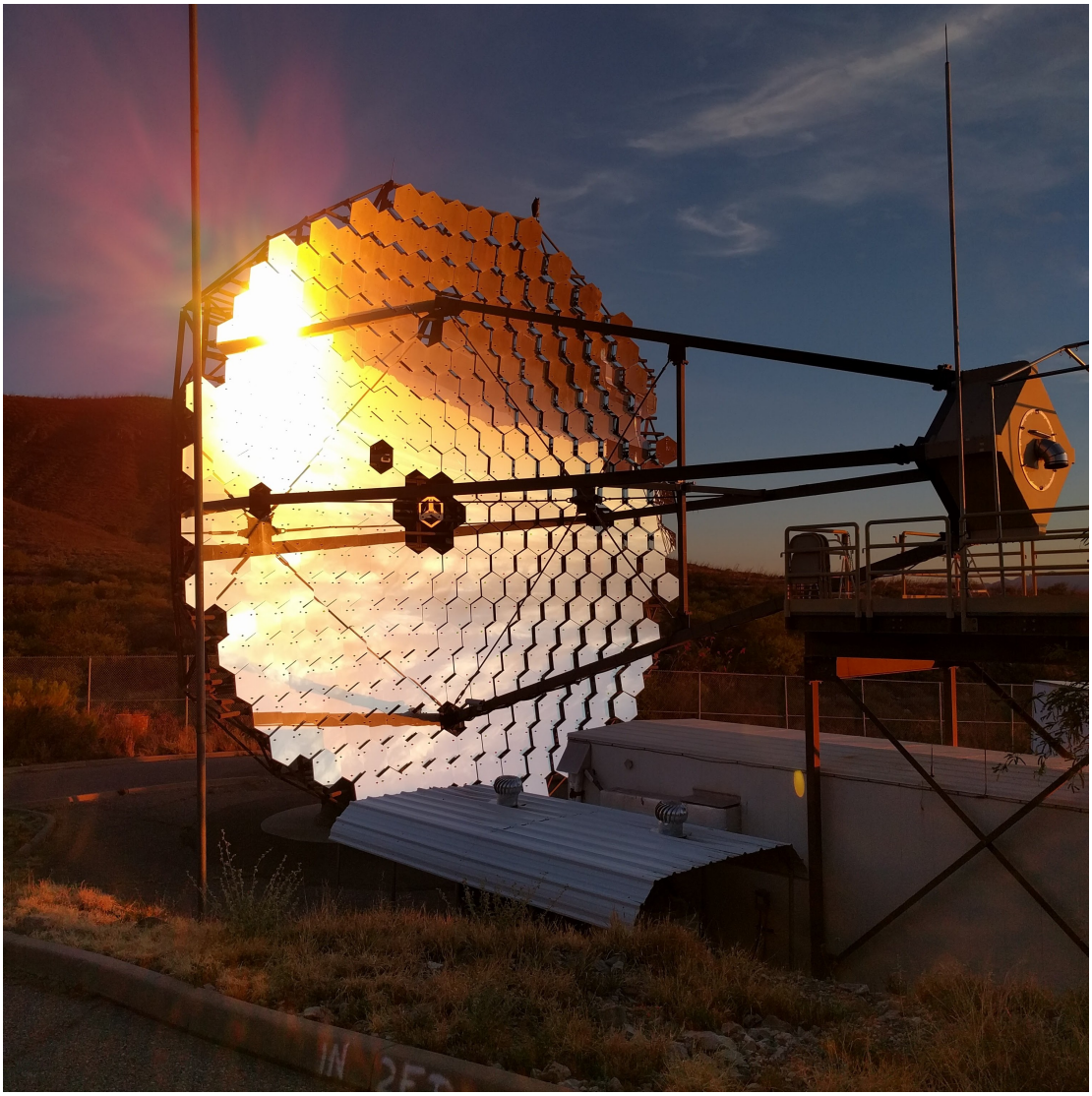

Figure 2.1: VERITAS Telescope 2 with a view of the mirrors, quadropod arms and camera mounted at the focal plane.

threshold of the entire array allowed by the higher QE PMTs. Further details of the performance of the new PMTs can be found in (D. B. Kieda for the VERITAS Collaboration, 2013). While PMTs are very sensitive to faint light, large amounts of background illumination degrades their efficiency over time. They are therefore operated only at night and under low light conditions (Archambault et al., 2017). See Section 2.2.5 for further details on the operation of VERITAS. Mounted in front of the PMTs is a plate of Winston cones, as seen in Fig. 2.2. The Winston cones reduce light losses by directing light falling between the circular PMTs onto the PMTs themselves. A preamplifier is used for each PMT to amplify its signal at the camera before being sent $\sim$50 m down to the electronics trailers.

2.2.3 FADCs

Signals from each PMT are sent into two subsystems: the constant fraction discriminator (CFD) and the flash analog-to-digital converter (FADC). Signal cables from the PMTs going into the FADC crates are shown in Fig. 2.3. The CFDs decide whether or not the signal from an individual PMT is significantly bright; this is discussed further in Section 2.2.4. The FADCs sample the output voltage from the PMT at 2 ns intervals and convert it to digital counts (Rebillot et al., 2003). There is a gain switch that allows the conversion to happen in the default high-gain state or to switch over to a low-gain state. In either state, the range of counts is from 0 to 255. In the case of a large signal, the FADCs switch to low-gain which allows counts up to the equivalent of 1500 high-gain counts. This allows for a wide dynamic range; bright showers do not saturate while maintaining good resolution for the dimmer showers. A buffer of 64 μs stores the digitized signal; this allows the array to continue operating while it is decided if the signal is to be read out.

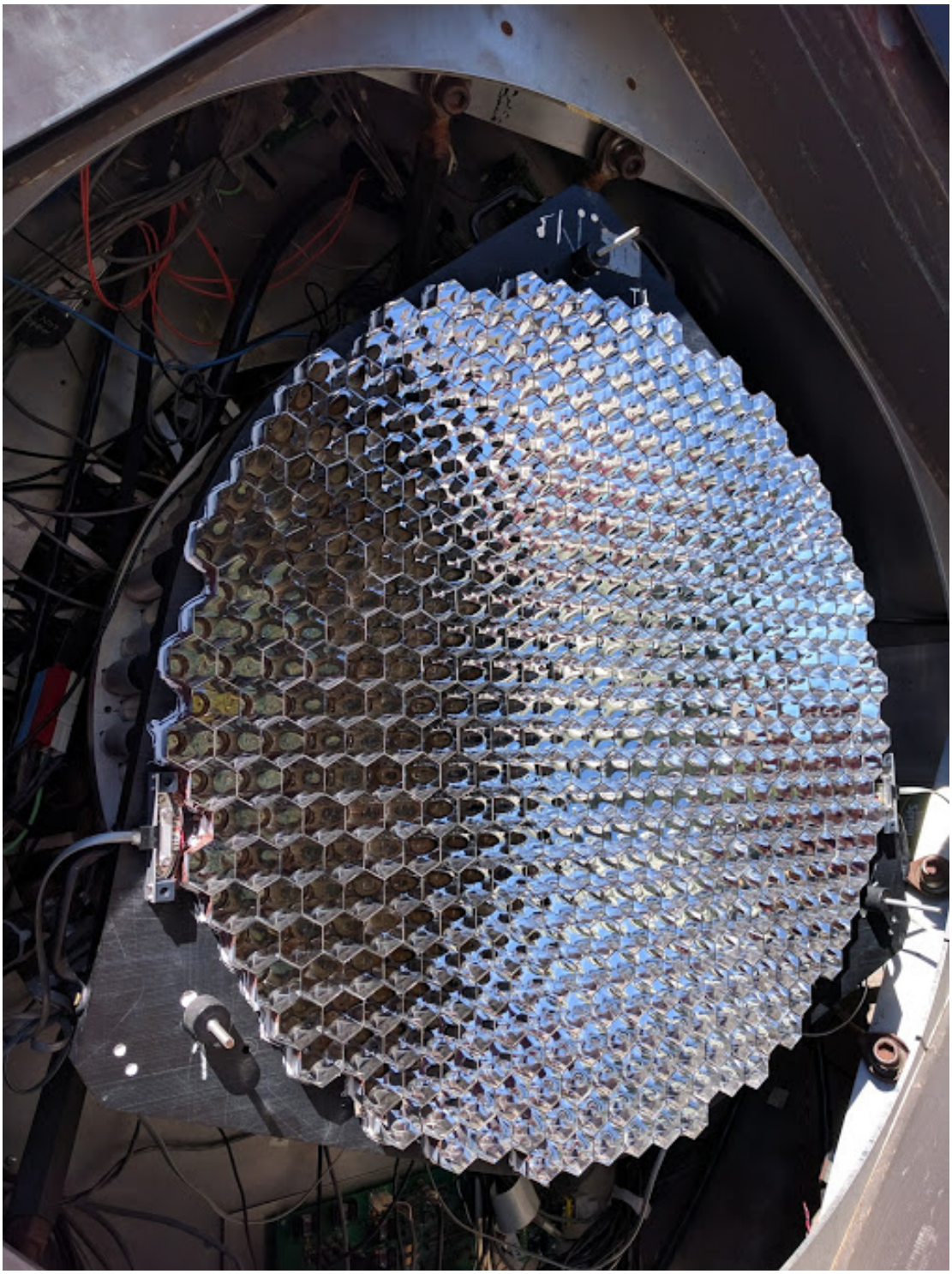

Figure 2.2: The front of one VERITAS camera with mounted Winston cones.

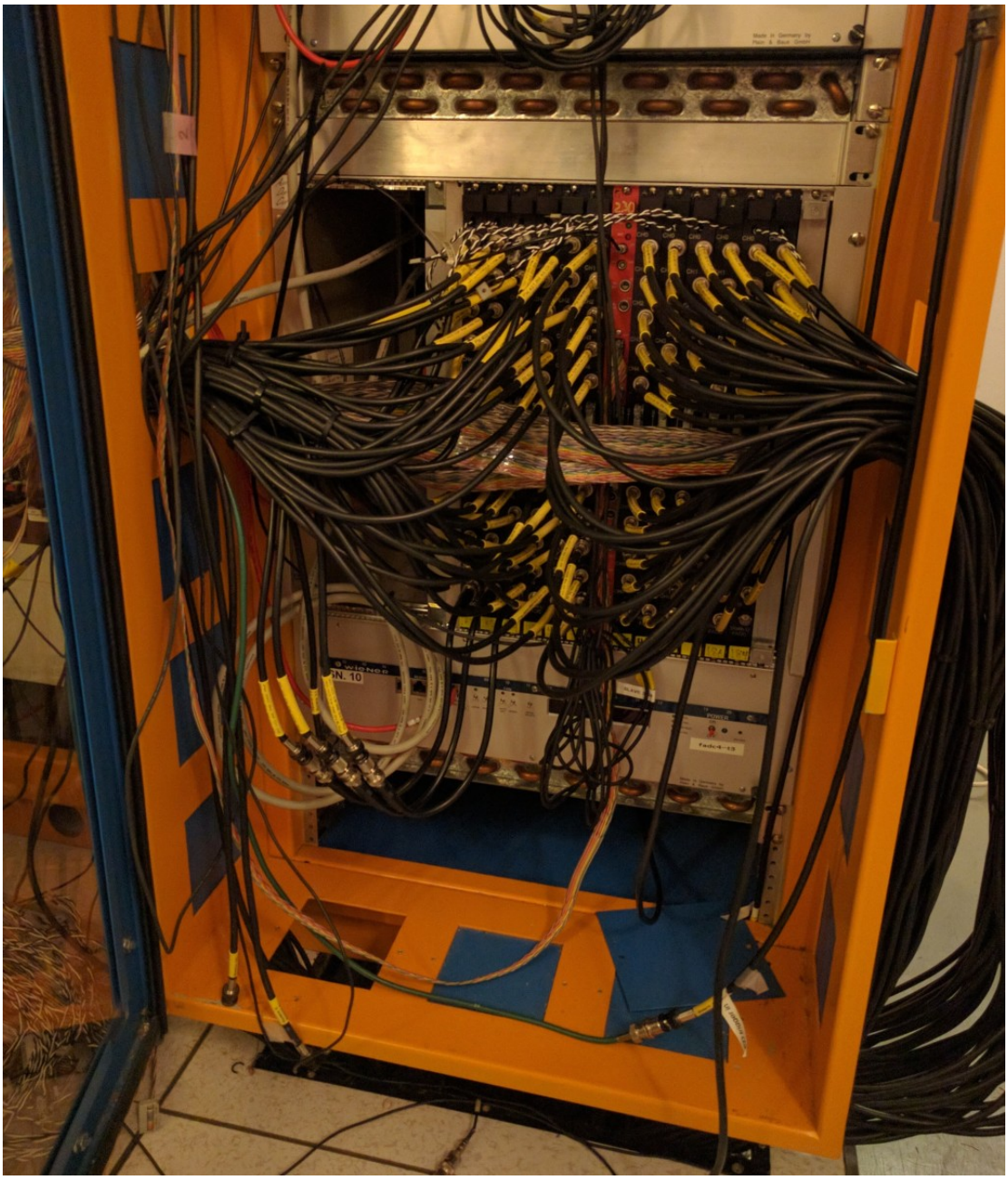

Figure 2.3: Signal cables (black) from the PMTs plugged into the FADCs in one of the VERITAS electronics trailers.

2.2.4 Trigger System

Reading out data takes observing time away from the operation of the telescope. This lost time is called *deadtime*, and the VERITAS array relies on a 3-level trigger system to decide whether or not a signal is worth reading out. This greatly reduces the dead time of the array. The first trigger level, L1, is related to the strength of the signal in an individual PMT. The CFDs determine whether the signal from an individual pixel crosses a programmable threshold that indicates it is sufficiently bright. In standard operation, this threshold is 45 mV. The L1 trigger is still susceptible to variations in the night sky brightness (NSB) or a bright star in a pixel.

The second trigger level, L2, decides whether or not an entire individual telescope is triggered. Triggering of the L2 requires that three neighboring pixels all pass the L1 trigger within a short time frame. In fact, the signals from the FADCs first go into the L1.5 board. The L1.5 trigger divides the camera into three overlapping regions and requires that the triggered PMTs all reside in the same subsection of the camera before the nearest neighbor pattern is applied. Requiring bright neighboring pixels cuts down on triggering due to small fluctuations in the NSB or an individual pixel anomaly such as after pulsing. The L2 trigger was upgraded in 2011 and currently uses fast FPGAs for the pattern recognition logic and a narrow time coincidence of $\sim$5 ns (B. Zitzer for the VERITAS Collaboration, 2013).

The third and final trigger, L3, is an array-level trigger that requires multiple telescopes see an event. The signals from each telescope are sent to the VERITAS control building, and the L3 determines if more than one telescope was triggered within a window of 50 ns. Time delays due to the different telescope distances to the control building as well as an estimate of the propagation time of

the Cherenkov shower front are both taken into account during this coincidence trigger. Muons, a large source of background, are often only seen in one telescope, so the L3 trigger is useful in reducing that background. Once the L3 trigger has been passed, the information is read out from all telescopes for offline analysis (Weinstein, 2008). The L3 trigger rates in the most recent seasons of VERITAS operation are ∼300-400 Hz and the entire trigger system allows for a deadtime less than ∼15% during nominal operation. While the triggers are applied to the data stream in series, the overall improvements from each are not independent. For example, the presence of the L3 trigger allows the L1 trigger level to be lower to pass dimmer signals and lower the energy threshold of the array. Implementation of all three levels together is a powerful way to reduce the VERITAS backgrounds and the deadtime of the instrument while improving other aspects of performance and observing capabilities.

2.2.5 Calibrations & Observing

The VERITAS telescopes have been in operation each year since 2007 from September through June. During July and August, the telescopes are shut down as monsoons come through the area. Each night the telescopes are operated by an on-site observing team. VERITAS has three common observing modes, and they depend on the impact moonlight has on the PMT currents in the camera. The first, dark time observing, occurs when the Moon is not above the horizon or when it is not bright enough for the PMT currents to be above 10 μA. The second mode is called "moonlight" observations, which occur when the current in the PMTs is between 10 and 15 μA. During moonlight operation, the CFD threshold is increased to 60 mV. This raises the threshold at which the L1 is triggered, so there is less frequent triggering on the brighter NSB. This sacrifices sensitivity to

the dimmest showers, so targets are selected for observing during this time which are appropriate for the raised energy threshold of the telescopes. Since extended exposure to light degrades PMTs, times when the Moon is even brighter require different operation of the PMTs. This third observing mode is called reduced high voltage (RHV) where the high voltage supplied to the PMTs is set to 81% of the nominal HV values. During RHV observations the CFD thresholds are lowered to 25 mV. Dark time typically occurs when the Moon illumination is <35%, moonlight is used when a bright Moon is rising or setting and RHV is used otherwise. There are no observations taken when the Moon is bright enough to incur PMT currents above 10 μA while in RHV mode. Additionally, when the Moon is above the horizon, targets are chosen such that they are approximately 90° from the Moon in the sky in order to minimize the amount of light seen by the camera. The decision to switch between each mode is made by the observing team based on that night's sky conditions.

To monitor and calibrate the PMTs in the camera, VERITAS uses a flasher system. The entire field of the camera is flashed with light to measure and monitor the relative gains and timing offsets between pixels. For the first few years of operation, the light was provided by a nitrogen laser producing pulses of ultra violet light at a frequency of 10 Hz. This system was both time and financially expensive, and it was upgraded to an LED-based system (Hanna et al., 2010). The upgraded system consists of six blue LEDs that can be illuminated in different numbers to control the amount of light on the camera, though newer iterations have more than six LEDs. The maximum rate of flashing is controlled by the data acquisition of the VERITAS electronics instead of the flasher itself, and so a flasher run with very high statistics can be taken in only a few minutes. Flasher runs are taken nightly, and separate flasher runs are taken during dark

time and RHV observations. Each telescope in a science observation is assigned a corresponding flasher run to be used for calibration in the off-line analysis. Several other calibrations are taken at a lower cadence than the flasher runs to track the performance of the VERITAS hardware. The timing of these calibrations is chosen such that they occur as much as possible during poor weather, bright moonlight, or other conditions that reduce impact on dark observing time.

2.3 VERITAS Data Analysis

There are currently two packages used for the analysis of VERITAS data: EventDisplay and the VERITAS Gamma-ray Analysis Suite (VEGAS). The following sections detail the general analysis of IACT data and its implementation in VEGAS. VEGAS analysis consists of 5 stages: 1, 2, 4, 5 and 6. Stage 3 no longer exists for historical reasons. Each stage has a myriad of configuration options, and development is always under way which allows for a fully customizable and evolving software package. Unless explicitly stated, the standard VEGAS analysis is what is described here; there are also multiple advanced analysis techniques being developed and implemented by VERITAS collaboration members (see for example S. Vincent for the VERITAS Collaboration (2015), J. Cardenzana for the VERITAS Collaboration (2015), R. Wells for the VERITAS Collaboration (2017), J. Christiansen for the VERITAS Collaboration (2017)). These techniques are not discussed as they have not yet been fully tested nor are they ready to be applied to the data presented here.

2.3.1 Calibration

In the first stage of VEGAS, the raw data from the telescope is read into the software in the form of VERITAS bank format (VBF) files. This step calculates hardware specific calibration values for the run as well as collecting the pixel, telescope and array information necessary for analysis. Connection to the database is required, but all information is saved in the output files so that later stages of analysis do not need access to the database.

2.3.2 Image Parameterization

The calibration information generated in stage 1 is applied to the data on an event-by-event basis and the cleaned image from each telescope is individually parameterized as a 2-dimensional ellipse using the Hillas parameters in stage 2 of VEGAS (Hillas, 1985). Figure 2.4 gives a representation of these parameters; fortunately, Hillas parameterization has a low computational cost since it is a moment analysis. The major axis of the ellipse is found, and the RMS spread of the light parallel and perpendicular to this axis are defined as the *length* and *width*, respectively, of the image. The image *size* is the total charge in all pixels in the image, and the *fracN* is the fraction of image charge in the brightest N pixels. FracN is useful for characterizing light concentration, and, interestingly, the original Hillas parameters only use frac2. The *distance*, d, is the distance between the ellipse centroid and the center of the camera. The *azimuthal-width* is the image width along an axis that connects the image centroid to the center of the camera. The *miss* is the perpendicular distance between the image axis and the center of the camera. Though the original Hillas parameters include the azimuthal-width and the miss, they are not currently used in VERITAS image parameterization.

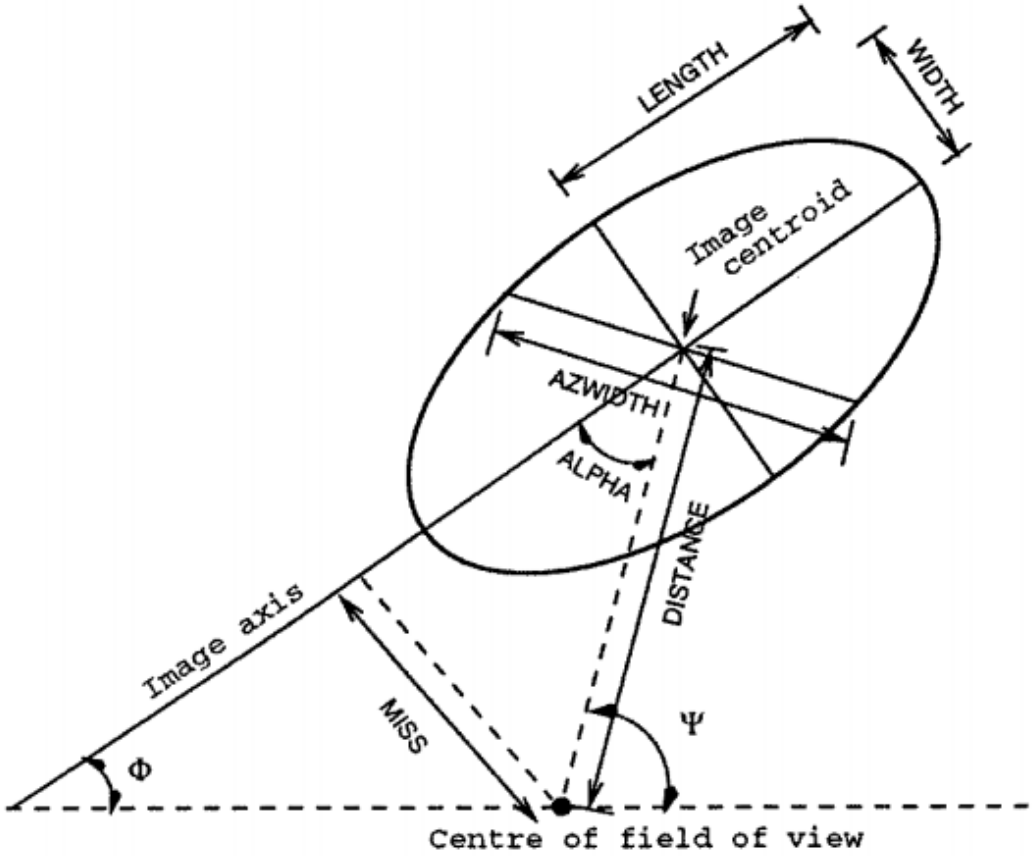

Figure 2.4: Shower image parameters based on a moment analysis from Fegan (1997). The image is approximated by an ellipse where the semi-major and semi-minor axes reflect the length and width parameters and represent the "shape" of the captured image. The alpha, miss and azimuthal-width (azwidth) parameters relate to the "orientation" or "pointing" of the image. The distance parameter is a measure of the image centroid from the center of the camera field of view.

2.3.3 Shower Parameterization

A significant source of strength in the current generation of IACTs comes from the ability to observe Cherenkov showers stereoscopically. This requires that individual images from multiple telescopes be combined in order to parameterize the observed shower. In stage 4 of VEGAS, the shower direction, core location, height of shower maximum and energy of the individual events are reconstructed at the array level. Quality cuts are applied on each image prior to this reconstruction based on the size, number of pixels and the distance of an image. Images that are faint, small or close to the edge of the camera are not used in shower reconstruction. Sets of cuts have been optimized a priori, and are based on the expected spectral shape of an observed source: soft, medium or hard. In version 2.5 of VEGAS, the standard analysis cuts require images to have at least 5 pixels and a distance $<1.43°$. The minimum size is dependent on the array configuration and cut type, as shown in Table 2.1. In VEGAS, a shower with an image from only one telescope is not used for shower reconstruction.

Table 2.1: Quality cuts used in stage 4. Each value is the minimum required size for an image in digital counts (dc).

	V4	V5	V6
Soft	200	200	400
Medium	400	400	700
Hard	1000	1000	1200

The *shower direction*, or the arrival direction of the primary particle, is determined by overlaying each image in the camera plane and calculating where the axes overlap. The *shower core* location is defined as the position on the ground where the shower axis hits. This is equivalent to the location where the shower-instigating particle would have hit the ground. Determination of the shower core location is done similarly to the shower direction by determining the intersection

of the major axes of each image in the ground plane. Generally, for more than two telescopes, the intersection of any two axes does not occur in exactly the same location. Each image axis is weighted by its size, then the location is determined by minimizing the perpendicular distance from each weighted image axis. After the shower core location is determined, it is useful to calculate and define the *impact parameter* as the distance between any given telescope and the core location. The *shower maximum* is the height in the atmosphere where the most particles and Cherenkov light in the cascade are produced and can be determined from the impact parameters and a simple geometry calculation. Shower maximum is a useful value for determining the type of instigating particle because cosmic rays tend to penetrate further into the atmosphere before interacting and have a different rate of shower development than gamma rays. See Section 2.3.4 for more details on determining the type of primary particle. For vertically incident gamma rays, this height is near an altitude of $\sim$10 km. The *shower energy* is the energy of the primary particle and is determined using Monte-Carlo simulations of many EAS. Simulations of showers are combined with simulations of the VERITAS optics and electronics to determine the size of a gamma ray given its direction and known energy. Using these simulations, "look up tables" are constructed which give the energy of a gamma ray as a function of the impact distance, size, pointing coordinates of the telescopes and NSB noise level. The standard deviation of the energy is also determined using these tables and is used as a weight when determining the energy of the shower as seen by multiple telescopes.

2.3.4 Gamma-Hadron Separation

As mentioned in Section 2.1, gamma rays are not the only particle that can instigate EAS and produce Cherenkov radiation. In fact, hadronic cascades ini-

tiated by non-gamma rays are the largest source of background for IACTs. The feasibility and sensitivity of VERITAS and other IACTs depends on the efficient rejection of the hadronic background and the retention of genuine gamma-ray events (Fegan, 1997). Fortunately, showers instigated by different types of particles propagate differently through the atmosphere, and we can use their geometry for separation. Fig. 2.5 shows stereotypical cosmic ray and gamma ray events as seen by VERITAS. Stage 5 of VEGAS takes the reconstructed showers and separates those instigated by gamma rays from those instigated by cosmic rays. Two more shower-level parameters are calculated in stage 4 then used in separation: mean scaled length (MSL) and mean scaled width (MSW) as defined in Equations 2.1 and 2.2:

$$MSW = \frac{1}{N_{images}} \sum_{i=1}^{N_{images}} \frac{width_i}{width_{sim}(\theta_i, r_i, size_i)}\,, \tag{2.1}$$

$$MSL = \frac{1}{N_{images}} \sum_{i=1}^{N_{images}} \frac{length_i}{length_{sim}(\theta_i, r_i, size_i)}\,. \tag{2.2}$$

The $length_{sim}$ and $width_{sim}$ correspond to the average lengths and widths for the simulated set of gamma-ray images with zenith angle (θ), $size$ and impact distance (r). Therefore, MSL and MSW values close to 1.0 are most gamma-like.

"Gamma-hadron" separation is done using "box cuts," where each parameter used in classification has an upper and lower limit. A shower falling within the limits for each parameter is considered to be a gamma-ray shower. These cuts are optimized *a priori* using data taken on a known VHE source. Data are processed up to the point of applying the size cut. The parameter space of shower max height, MSL, MSW is then scanned, and the values which optimize the signal are chosen. For the 2.5 version of VEGAS, the optimized cut values are shown in Table 2.2.

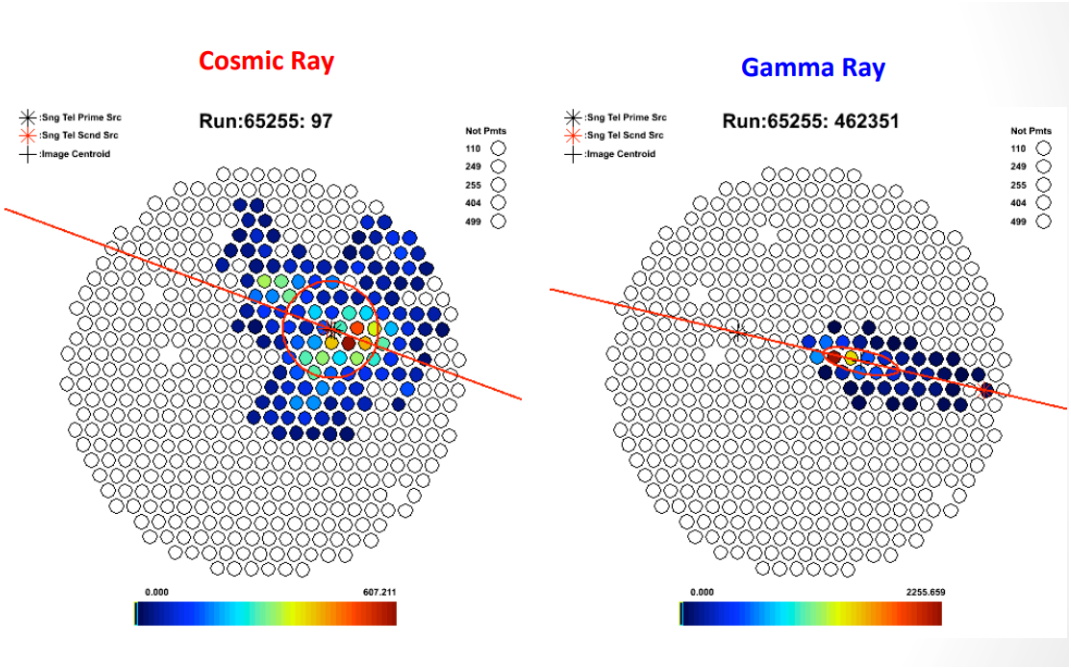

Figure 2.5: Two cleaned images as seen by VERITAS; the red lines show the image parameterization produced by VEGAS. The left shows a stereotypical cosmic ray event and the right shows a stereotypical gamma ray event. Image credit: Jon Dumm

Table 2.2: Gamma-hadron separation cuts used in stage 5. Ranges indicate retained (or "gamma-like") parameter values.

Cut Type	MSL	MSW	Shower Max
Soft	$0.05 < \text{MSL} < 1.3$	$0.05 < \text{MSW} < 1.1$	>7 km
Medium	$0.05 < \text{MSL} < 1.3$	$0.05 < \text{MSW} < 1.1$	>7 km
Hard	$0.05 < \text{MSL} < 1.4$	$0.05 < \text{MSW} < 1.1$	none

2.3.5 Background Estimation and Source Detection

After the gamma-ray events are isolated in stage 5 of VEGAS, stage 6 calculates the statistics and other results necessary for science interpretation. The first calculation is the background. Very generally, we define the ON region to be the region of interest for science, and the OFF region to be a background region used to calculate the background rate of events. For a point source, the ON region encompasses the point of interest in the sky. VERITAS observes the ON and OFF regions at the same time, in the same field of view. We define N_{excess} in Equation 2.3 where N_{ON} and N_{OFF} are the number of events falling in the ON and OFF regions, respectively (Li and Ma, 1983):

$$N_{excess} = N_{ON} - \alpha N_{OFF} \,. \tag{2.3}$$

The parameter α is the ratio of exposure in the ON region to that in the OFF region. Calculation of α is not trivial, and is discussed further in Section 2.3.8. One factor in the calculation of α is the *acceptance*, or the relative sensitivity at which the camera detects showers. The acceptance is primarily radially dependent in the VERITAS cameras and decreases farther from the center. The statistical significance of a source in the ON region is found using Equation 17 in Li and Ma (1983). It is reproduced here in Equation 2.4:

$$S = \sqrt{2}\left(N_{ON}\ln\left[\frac{1+\alpha}{\alpha}\frac{N_{ON}}{N_{ON}+N_{OFF}}\right] + N_{OFF}\ln\left[(1+\alpha)\frac{N_{OFF}}{N_{ON}+N_{OFF}}\right]\right)^{1/2}. \quad (2.4)$$

In the analysis of point sources, there are two typical techniques for the selection of the ON and OFF regions: reflected region and ring background method (RBM). All blazars detected to date are point sources at VHE, so only these techniques are described and used in this thesis. Figure 2.6 shows a schematic with the geometry of each method. In the reflected regions method, both the source and background regions are located at the same radial distance (or *offset*) from the center of the camera (generally 0.5°) in order to have the same acceptance for gamma rays in each region (Fomin et al., 1994). In the RBM, the background region is in the shape of an annulus around the source. RBM is useful for making sky maps since the background region can be an annulus around any position in the field of view.

2.3.6 Spectral Reconstruction

Spectral reconstruction and determination of an observed flux measurement are done in stage 6 of VEGAS using a binned approach. Flux calculations require N_{excess}, the live time and the effective area of the instrument all binned in energy. The effective area is essentially a measure of the collecting area of the telescope array. Anything that impacts the sensitivity to the detection of gamma rays by VERITAS impacts the effective area: zenith angle, NSB noise level, season and analysis cuts. Monte-Carlo simulations of air showers are used to calculate the effective area as a function of these parameters by running the simulations through the detector response and analysis software. The differential energy spectrum is

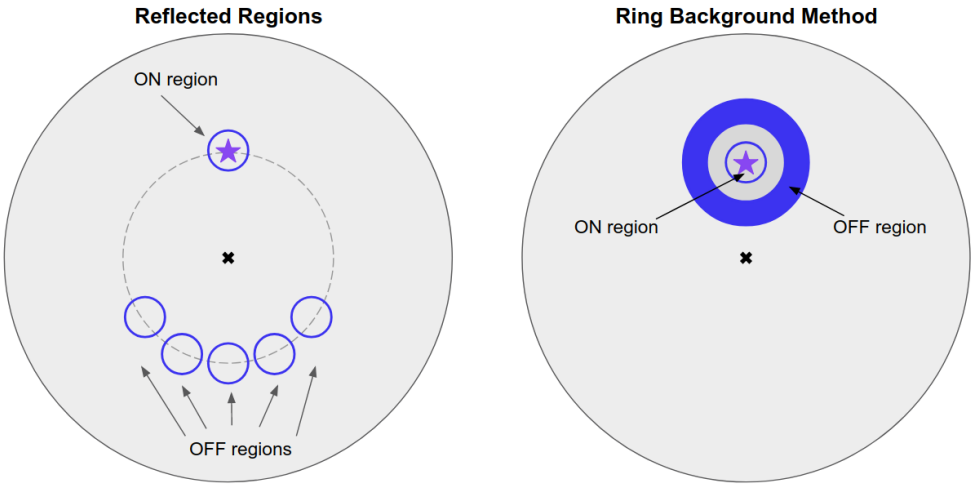

Figure 2.6: Schematic of the reflected regions and ring background methods of selecting the background region. Each large grey circle represents the field of view of the VERITAS camera. The cross represents the center of the camera and the purple star indicates the expected location of the source. The reflected regions method (left) consists of ON and OFF regions at the same radial distance away from the center of the VERITAS camera. The ring background method (right) has the background region in the shape of an annulus around the source region.

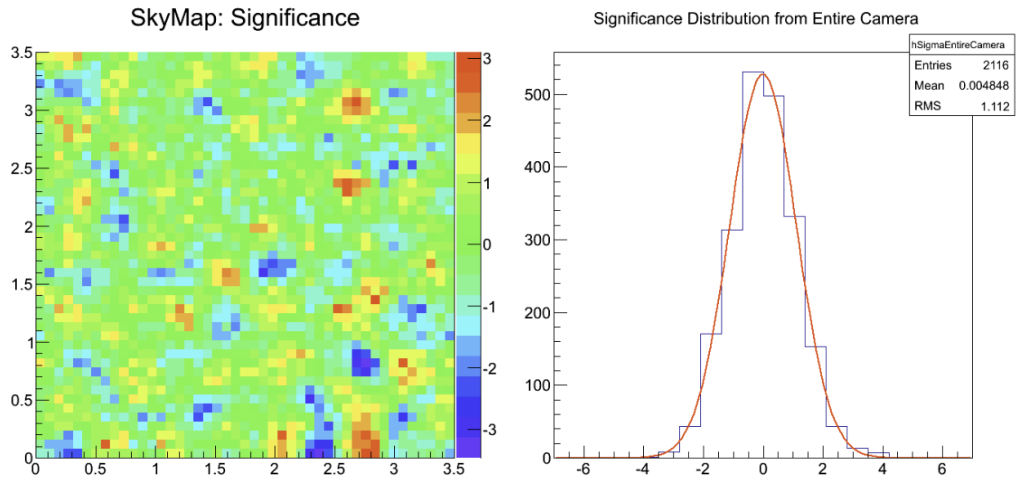

Figure 2.7: A simulated sky map assuming a count rate Poisson distributed with a mean count per pixel of 1000. The bin size is chosen such that four bins make up the area of approximately one PMT in the VERITAS camera. The left shows the sky map with significance calculated using Equation 2.4. The distribution on the right is the distribution of significances from the entire simulated field of view; a Gaussian of width 1.0 and mean 0.0 is overlaid in red.

given by

$$\frac{dN}{dE} = \frac{d}{dE}\frac{N_{excess}(E)}{A(E)T} \tag{2.5}$$

where A(E) is the effective area at a given energy, N_{excess}(E) is the excess counts at a given energy, and T is the live time of the observation. In VEGAS, this is done on an event-by-event basis since each event can have different observing conditions which require a different value for the effective area. The spectrum is constructed up to the energy bin where the statistical significance is at least 2σ and there are at least 5 excess counts.

2.3.7 Energy Threshold Determination

Determination of the energy threshold in IACT data can be done in a few different ways. There are three methods built into VEGAS to calculate the safe energy range which is used as the energy threshold of a spectral reconstruction:

- E_EnergyStandard: Energy threshold is the energy at the peak of the sensitivity distribution.
- E_EnergyEAPrecision: Requires the uncertainty in effective area to be less than some value.
- E_EnergyBias: Requires the energy bias to be less than some value. Typically this is values is 0.1.

The default method used in VEGAS is E_EnergyEAPrecision with a maximum allowed uncertainty of 0.2. For the analysis of 3C 66A data presented in Chapter 4, we use a more conservative upper limit on the effective area uncertainty of 0.1. While the effective areas are a function of the true energy because they

originate from simulations, an analysis produces results dependent on the reconstructed energy. The effective areas are modified, and take into consideration the the energy bias and resolution of the instrument. These modified effective areas are also dependent on the spectral shape of the source, and are created iteratively in stage 6 of VEGAS.

2.3.8 Background Systematic Errors

In the absence of any signal and sufficiently large statistics, analysis of uncorrelated gamma-ray observations should produce a Gaussian distribution of significances with width unity and mean zero when using Equation 17 in Li & Ma and in accordance with Wilks's theorem. A simulated significance sky map assuming a Poisson-distributed count rate with an expected mean counts per pixel of 1000 is shown in Figure 2.7. Each bin is approximately 25% of the area of a VERITAS pixel. There is no signal in the simulation, and the significance distribution accompanying the sky map has a mean of 0.0 and an RMS of 1.1. However, with deep VERITAS exposures, it has become important to understand the systematic effects contributing to the calculation of the background. We see two such effects which become prominent with longer and deeper exposures. One effect is that of zenith-dependent acceptance (not only radially dependent acceptance). We have utilized a correction to this acceptance that accounts for the change in zenith angle across the camera. For a full description of this correction, see Zitzer (2015). The second effect is discussed in Spengler (2015), which derives a modified significance equation that incorporates the systematic uncertainty on the acceptance. See B. Zitzer for the VERITAS Collaboration (2017) for more details and how these corrections impact VERITAS data analysis.

Chapter 3

An MCMC Technique for Fitting Blazar SEDs with the Synchrotron Self-Compton Model

Fitting a blazar SED to even a simple emission model in a statistically robust way is difficult and computationally expensive. The resulting SED is not an independent or analytic function of the input parameters, and often there are more input parameters than observables. However, in order to rigorously distinguish between models, we need a way to statistically evaluate a fit and explore the parameter space. Here, we implement a Markov Chain Monte Carlo (MCMC) technique for fitting a blazar SED with a single-zone, purely leptonic, synchrotron self-Compton (SSC) emission model. The following sections describe the SSC model, the MCMC technique and its implementation in fitting blazar SEDs. It is validated on the VHE blazar 1RXS J101015.9-311909 then applied to 3C 66A in Chapter 4.

3.1 Synchrotron Self-Compton Model

In modeling this scenario, we assume a single emitting region moving relativistically down the jet of the blazar (Katarzyński et al., 2001). The region is assumed to be spherical with a size given by R and uniformly filled with a tangled magnetic field of strength B. The region is moving down the jet with a bulk Lorentz factor of Γ. The emission we observe at Earth from this region has been relativistically boosted, and the factor determining this Lorentz boost is called the Doppler factor, δ. It is defined as

$$\delta \equiv \frac{1}{\Gamma(1 - \beta_\Gamma \mu_{obs})} \tag{3.1}$$

where $\mu_{obs} \equiv \cos\theta_{obs}$ and β_Γ is the normalized speed (v/c) of the region. The angle of the jet with respect to our line of sight is θ_{obs}, and for blazars it is small. It is important to note that there is degeneracy here between the speed of the emitting region, our angle of observation of the jet and the resulting Doppler factor.

In the emitting region, we inject a population of relativistic electrons with an energy spectrum described by a broken power law as shown in Figure 3.1. The electron energies have Lorentz factors from γ_{min} to γ_{max} with the spectral break occurring at γ_{break}. The lower energy portion of the distribution is characterized by an index of α_1 and the higher energy portion by α_2. The normalization of the broken power law spectrum is given by K and is defined as the particle density (number per volume) at $\gamma = 1.0$. Though the normalization is given at a non-relativistic Lorentz factor, the spectrum generally begins at $\gamma > 1.0$ due to the relativistic nature of the electron population. The presence of relativistic electrons begs the question of how they came to exist with the specified distribution in the first place. An overview of acceleration mechanisms is outside the scope of this discussion, though a generally accepted theory is through diffusive shock

acceleration. This produces a single power-law energy spectrum. However, the energy losses from synchrotron and inverse-Compton processes imply a break in the stationary-state distribution (Inoue and Takahara, 1996). Another motivation for the break is the fact that the size of the accelerating zone is finite; the process decreases in efficiency as the energy increases and results as a steepening in the spectrum. A broken power law reflects this steepening. All input parameters are summarized in Table 3.1.

This population of electrons inhabiting a region filled with a tangled magnetic field naturally creates synchrotron radiation which gives rise to the lower energy peak in the typical blazar SED. The "self" in the SSC model name comes from the creation of the higher energy peak in the blazar SED. The population of photons created by the synchrotron radiation process are the same ones that are upscattered to higher energies via inverse-Compton scattering; hence the "self" upscattering. In other models, the photons that are upscattered originate outside the jet. These models are called external Compton (EC) models, and often are modeled as a SSC scenario with contribution from an EC component.

A few of the SSC parameters can be constrained in ways other than modeling the full, multiwavelength SED. The most straightforward constraint relies on the observation of variability and causality arguments (Boettcher et al., 2012). If the emitting region is transparent to the radiation that we see, variation of this emitted radiation is diluted by the finite travel time through the region. The travel time is given by $\Delta t_{emitted} \sim R/c$ where R is the size of the region. Since the region is moving relativistically, we observe a time contraction such that $\Delta t_{observed} = \Delta t_{emitted}/\delta$. Therefore, the smallest variability that we may observe from a relativistically moving source with size R is $\Delta t_{observed,min} \geq \delta^{-1} R/c$. Given the smallest observed timescale of variability, some knowledge of the Doppler

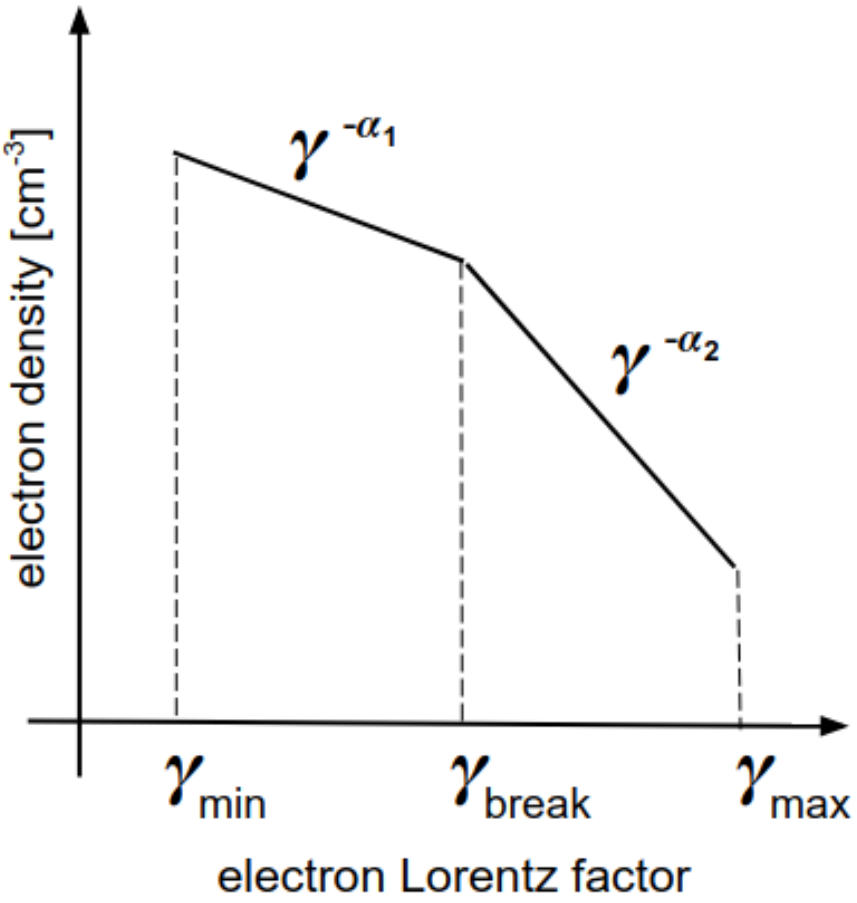

Figure 3.1: The injected electron energy distribution is described using a broken power law. The electron density is given as a function of the Lorentz factor of the electrons. Each portion is described by a power law with the higher energy portion softer than that of the lower energy ($\alpha_2 > \alpha_1$).

factor and the source redshift to account for expansion of the Universe, we can constrain the size of the emitting region to be

$$R \leq \frac{c\Delta t_{observed,min}\delta}{1+z} \,. \tag{3.2}$$

It is also possible to constrain the index of the electron energy distribution if the X-ray observations lie on the falling edge of the synchrotron peak in the SED (Rybicki and Lightman, 1979). The spectral index of the power spectrum resulting from synchrotron radiation, s, given an electron population with a power-law energy distribution with index p is given as

$$s = \frac{p-1}{2} \,. \tag{3.3}$$

The photon index from X-ray observations, Γ_X, is given by $\Gamma_X = s+1$. The index of the injected population of electrons is given by α_2 in our notation which means that α_2 is related to Γ_X as

$$\alpha_2 = 2\Gamma_X - 1 \,. \tag{3.4}$$

In the spirit of applying as few assumptions as possible to fitting the SED, we do not fix either α_2 based on the X-ray data nor constrain the size of the emitting region based on variability arguments in the MCMC. However, it is useful to use these constrains as a comparison to the results obtained from the MCMC.

The redshift of the blazar is the final parameter required to generate the SED, but it is independent of the emission model itself. This is necessary in order to account for cosmological redshifting and absorption of VHE photons by the EBL. In the latter process, the model of (Franceschini et al., 2008) is used to obtain the EBL opacities and deabsorb the SED appropriately. For this work, we choose a

redshift to use based on any known information about the distance of the blazar.

3.2 MCMC & emcee Overview

Generation of a single SED using the SSC simulation takes roughly 1.5 seconds. If we chose only 10 values for 9 free parameters in order to create a grid of models to evaluate, generation of the models alone would take ∼50 years. Likelihood maximization techniques similarly take a long time, with the amount of time increasing as the number of parameters squared, and they can easily get stuck in local extrema. These time intensive processes to fit an SED are not computationally realistic. Additionally, we would like a way to evaluate the uncertainty on each parameter which requires understanding the distribution from which it arises. Bayesian inference has been used with increasing frequency in astrophysics, and it allows for understanding of such posterior distributions. MCMCs are a random-walk method which, over time, draws samples in such a way that it is representative of the distribution. When they are used to sample from the posterior probability distribution function (PDF), they can efficiently provide a sampled approximation of this posterior. The technique creates a series of positions as it steps through the parameter space called a "chain"; any step in the chain is only dependent on the step before it.

The simplest and most common MCMC algorithm is that of Metropolis-Hastings (M-H). In this iterative process, you have a position in the parameter space, X, at a given step, t: $X(t)$. A new position is proposed, Y, from the transition distribution $Q(Y; X(t))$. The new position is accepted with the probability

$$\min\left(1, \frac{p(Y|D)}{p(X(t)|D)} \frac{Q(X(t); Y)}{Q(Y; X(t))}\right) \tag{3.5}$$

where D is the observations or data. $Q(Y; X(t))$ is symmetric in Y and X and is commonly a multivariate Gaussian centered at $X(t)$. If the position is accepted, the next step in the chain becomes the proposed position: $X(t+1) = Y$. If it is not accepted, the new position is set to the old position, $X(t+1) = X(t)$, so it is repeated in the chain. An important and useful metric to define is the *acceptance fraction* which is the fraction of steps accepted out of the total proposed. A small acceptance fraction means that the parameter space is neither being sampled efficiently nor obtaining many independent samples. A large acceptance fraction means that the chain is a pure random walk with no information about the target density being sampled; the sample will not be representative of the posterior distribution. The rule of thumb is that the acceptance fraction should be between 0.2 and 0.5. To reduce the sample's dependence on the initial condition of a chain, a "burn-in" period consisting of the first portion of the chain is identified and removed when constructing PDFs.

For this work, we use a Python-implementation of an MCMC called `emcee`.[1] In this method, an affine-invariant sampling technique is used (informally called a "stretch-move" algorithm). The full details of the technique can be found in Goodman and Weare (2010). Essentially, the method employs an ensemble of walkers instead of a single walker and uses information from all walkers to step through the parameter space. Specifically, we have an ensemble of K walkers, $S = \{X_k\}$, where the proposal distribution of one walker, k, is calculated from the positions of the other K-1 walkers in the ensemble. To update the position of a walker, k, at position $X_k(t)$, a random walker, X_j, is drawn from the remaining walkers. The proposed position for X_k is

$$Y = X_j + Z[X_k(t) - X_j] \tag{3.6}$$

[1] http://dfm.io/emcee/

where Z is a random variable drawn from a distribution g(z). Details on properties of g(z) can be found in Goodman and Weare (2010) and Foreman-Mackey et al. (2013a), and it behaves as

$$g(z) \propto \begin{cases} \frac{1}{\sqrt{z}} \text{ if } \frac{1}{a} \leq z \leq a \\ 0 \text{ otherwise} \end{cases} \tag{3.7}$$

where a is an adjustable scale parameter set to 2 by default. The ensemble of walkers can be initialized in a variety of ways, though two are common. A very general approach is to initialize the walkers uniformly over the range of each parameter's bounds. Alternatively, if any information is known about the most likely set of parameters, the walkers can be initialize as a Gaussian ball around that point in the parameter space. The former approach is more general, though the latter is more efficient and less likely to get stuck in a local maximum.

3.3 Implementation in SED Modeling

In the MCMC, we fit nine parameters: R, B, δ, γ_{min}, γ_{break}, γ_{break}, K, α_1, and α_2. Both the redshift of the source and the value of θ are fixed. Due to the degeneracy between the bulk Lorentz factor, Doppler factor and the angle with the line of sight, only the Doppler factor is a free parameter in this fit. Since we have that $\sin\theta_{emitted}/\delta = \sin\theta_{observed}$, and $\sin\theta_{emitted}$ must be less than 1.0, we have the constraint that

$$\delta \sin\theta_{observed} < 1\,. \tag{3.8}$$

Therefore we choose a theta value such that the Doppler factor can be as large as 100; $\theta_{observed}$ is fixed to 0.57 degrees.

The bounds of each parameter are shown in Table 3.1; several parameters are sampled logarithmically allowing for a range of values to span several orders of magnitude. For γ_{break}, the bounds are given by γ_{min} and γ_{max}, and a check is done verifying that $\gamma_{min} < \gamma_{max}$. Additionally, there is the constraint that the second index on the electron energy distribution must be softer than the first ($\alpha_2 > \alpha_1$). The initial walker values are uniformly distributed over each parameter's range given in Table 3.1 except for γ_{break} which is initially uniformly distributed over (2.0, 7.0).

Table 3.1: Synchrotron self-Compton parameter definitions and bounds implemented in the MCMC code.

Model Parameter	**Variable**	**Range**
Size of emitting region [cm]	log R	(14.0, 19.0)
Magnetic field strength [G]	log B	(-4.0, 0.0)
Doppler factor	δ	(0, 100)
Low-energy cutoff	log γ_{min}	(0.0, 5.0)
Break energy	log γ_{break}	(γ_{min}, γ_{max})
High-energy cutoff	log γ_{max}	(3.0, 8.0)
Particle density [cm^{-3}]	log K	(0.0, 8.0)
First index	α_1	(1.0, 5.0)
Second index	α_2	(2.0, 5.0)

To quantify the quality of the fit, we use the χ^2 statistic

$$\chi^2 = \sum_{i=1}^{N} \frac{(\nu F_\nu(\nu_i) - \text{model}(\nu_i))^2}{\sigma(\nu_i)^2} \tag{3.9}$$

where N is the number of data points, νF_ν is the measured energy flux at frequency ν_i, $\sigma(\nu_i)$ is the uncertainty on the measured energy flux and model(ν_i) refers to the modeled energy flux at ν_i. `emcee` requires the log probability of a model rather than the χ^2, so in the probability function we have implemented, we are using

$$\ln p = -\chi^2/2 \ . \tag{3.10}$$

This means that the MCMC will work to maximize this probability which is naturally equivalent to minimizing the χ^2 value.

The SED model is generated numerically and creates a set of 99 data points evenly spaced logarithmically from 5×10^7 to 1×10^{29} Hz. In order to generate model(ν_i), the data points are interpolated in νF_ν using a 1-D interpolation from SciPy.[2] The best fit model is the one with the smallest χ^2 value, χ^2_{min}. The power in the MCMC technique of fitting blazar SEDs is the ability to determine not only the best fit model, but also a statistically defined confidence limit on the value of each fit parameter. We consider all models which have $\chi^2 < \chi^2_{min} + \Delta\chi^2$ as within 1-sigma of the best value, where $\Delta\chi^2$ is dependent on the number of parameters being fit (Lampton et al., 1976). The value of $\Delta\chi^2$ is calculated as

$$\Delta\chi^2 = \chi^2_p(\alpha) \tag{3.11}$$

where χ^2_p is the formal chi-squared distribution with degrees of freedom p, evaluated at a confidence, α (e.g. $\alpha = 0.32$ for a "1σ" contour) (Lampton et al., 1976). Several values of $\Delta\chi^2$ are tabulated in Table 3.2.

Table 3.2: Values of $\Delta\chi^2 = \chi^2_p(\alpha)$

	p = 1	2	3	...	7	8	9
1σ ($\alpha = 0.32$)	1.00	2.28	3.51	...	8.14	9.27	10.39
2σ ($\alpha = 0.05$)	4.00	5.99	7.81	...	14.07	15.51	16.92

3.4 Validation on 1RXS J101015.9-311909

To test the MCMC blazar SED fitting technique, we apply it to a blazar that has already been successfully modeled with a single-zone leptonic SSC model

[2]https://www.scipy.org/

by Cerruti et al. (2013): 1RXS J101015.9-311909, detected at VHE by H.E.S.S. (H.E.S.S. Collaboration et al., 2012). In the modeling of this source, the authors present a numerical algorithm using a sparse grid of simulated SEDs in an attempt to study the entire parameter space. Instead of using the SED data points themselves, the authors define seven observables from the SED: the spectral slopes and normalizations of the Fermi and the VHE data, the frequency and flux of the synchrotron peak, and the X-ray spectral index. From each SED is extracted the value of the observables, then each observable is parameterized as a function of the SSC parameters. Finally, they are able to solve the system for a given set of measured observables. They use this technique to find a good solution to 1RXS J101015.9-311909 using an SSC model and quantify the parameter space to determine uncertainties on the fitted values. We therefore consider their resulting best fit model a good way to compare and evaluate how this MCMC method performs. In order to reduce the parameter space for the SED grid generation, Cerruti et al. (2013) fix a few of the parameters. The distribution of electron energies is fixed by setting $\gamma_{min} = 100$ and $\gamma_{max} = 5 \times 10^6$. Using the X-ray photon index, α_2 is fixed to 4.0; this reduces the number of observables to six. They consider solutions that have only three values of α_1 in order to reduce computational time: 1.6, 1.8 and 2.0. These constraints reduce the system to six observables and six free parameters. There is no flaring behavior observed, so they are not able to use the timescale of variability as a constraint. The best fit parameters are summarized in Table 3.3 and the best fit SED is reproduced in Figure 3.2. The normalization on the electron density spectrum is defined differently than what we have defined as K in section 3.1. They define and use a normalization of

$$K' = K\gamma_{break}^{-\alpha_1} \ . \tag{3.12}$$

We run our MCMC on the SED published in Cerruti et al. for 3000 steps using 300 walkers. This blazar has a known redshift of z=0.143 which we fix in our SSC model, but we do not fix α_2, γ_{min}, γ_{max} or α_1. The status of all walkers at each step in the chain is shown in Figs. 3.4, 3.5 and 3.6. A burn in of 200 steps is used to ensure that the sampling is independent of the initialized parameter values. The χ^2 values sampled in the MCMC accepted steps range between 237.22 and 5.2×10^9, and truncated distributions are shown in Figure 3.3. The peak of the distribution is at a χ^2 value outside the 1σ interval, ~ 260, resulting in 86 out of the 91,452 accepted steps to fall within that interval. This behavior is presumably due to the walkers spending many steps in a local maximum. When looking at all *attempted* steps, the behavior is similar: 166 models fall within the 1σ range and the peak of the χ^2 distribution occurs at $\chi^2 \sim 260$. The best fit parameters resulting from the MCMC are listed in Table 3.3. Both K and K' are listed for these MCMC results, though an accurate computation of the 1σ bounds on K from Cerruti et al. (2013) is not available. Plots of χ^2 for each parameter value and the distributions of each parameter are shown in Figs. A.1 - A.9.

Table 3.3: Best Fit SSC Parameters for 1RXS J101015.9-311909.

	Cerruti et al. (2013)		This work	
Parameter	Best Value	1σ Range	Best Value	1σ Range
R [cm]	1.3×10^{16}	(0.49-11.57) $\times10^{16}$	8.03×10^{18}	$(5.96\text{-}8.73)\times10^{18}$
B [G]	0.015	(0.51-4.09) $\times10^{-2}$	1.05×10^{-4}	$(1.00\text{-}1.45)\times10^{-4}$
δ	96.83	32.07-99.53	44.05	(41.12-51.79)
α_1	2.0	fixed	2.75	(2.65-2.81)
α_2	4.0	fixed	4.03	(3.59-4.21)
K' [cm^{-3}]	8.94×10^{-8}	(0.01-7.30) $\times10^{-7}$	2.28×10^{-15}	$(1.24\text{-}6.72)\times10^{-15}$
K [cm^{-3}]	252.07	unavailable	406.21	(70.30-910.83)
γ_{min}	100	fixed	7.42×10^3	$(5.98\text{-}7.72)\times10^3$
γ_{break}	5.31 $\times10^4$	(3.48-13.15) $\times10^4$	1.86×10^6	$(1.29\text{-}2.14)\times10^6$
γ_{max}	5 $\times10^6$	fixed	3.74×10^7	$(0.75\text{-}7.63)\times10^7$
Reduced χ^2		1.06	237.220/31 = 7.65	

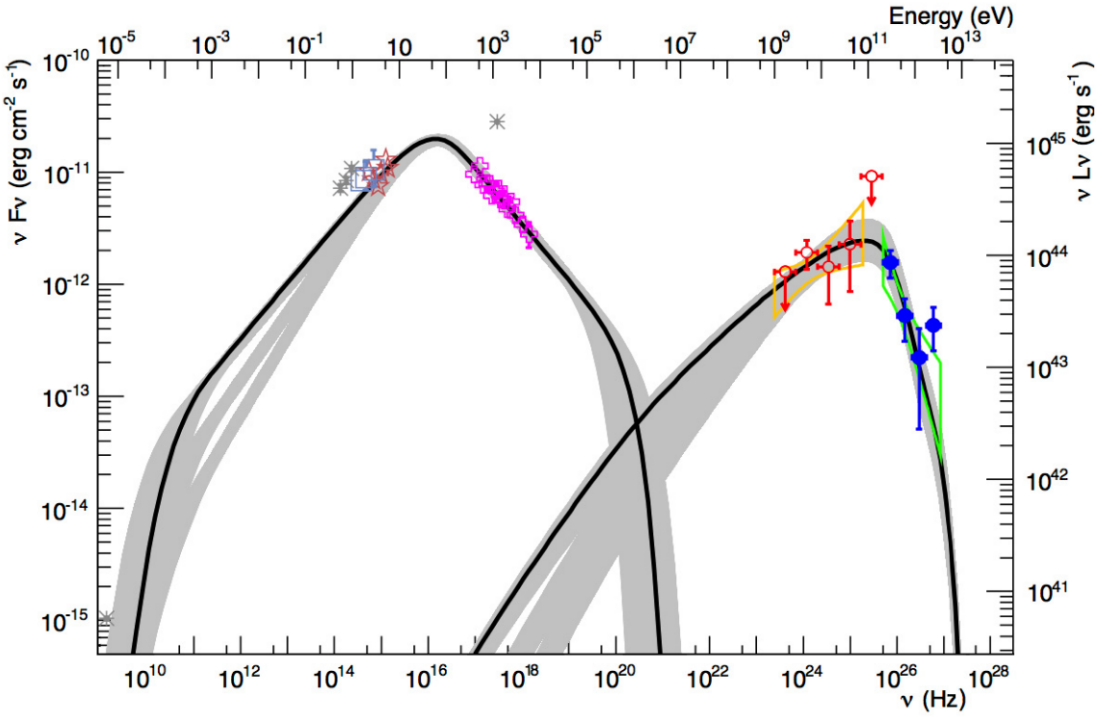

Figure 3.2: From Cerruti et al. (2013): "SED of 1RXS J101015.9-311900 (H.E.S.S. Collaboration et al. (2012); the H.E.S.S. spectrum is represented by the green bow-tie and the blue points, the *Fermi*-LAT spectrum by the orange bow-tie and the red empty circles; *Swift*-XRT data are shown by the pink crosses, *Swift*-UVOT data by the red stars, ATOM data by the blue open boxes, and archival data from the NED in grey). All the SSC models which describe the SED, as found with our [Cerruti et al.] algorithm, are plotted in grey, while the solid black curve represents the best-fit solution with reduced χ^2=1.06. It is characterized by an extreme value of δ=96.83, B=0.015 G, R=1.3×10^{16}cm, α_1=2.0,K=8.94×10^{-8} cm^{-3},and $\gamma_{break} = 5.31 \times 10^4$.The three different families of solutions, which can be distinguished in the range between 10^{11} and 10^{14} Hz, correspond to α_1 =1.6, 1.8, and 2.0. The infrared and visible data can be reproduced by taking into account the host-galaxy contribution."

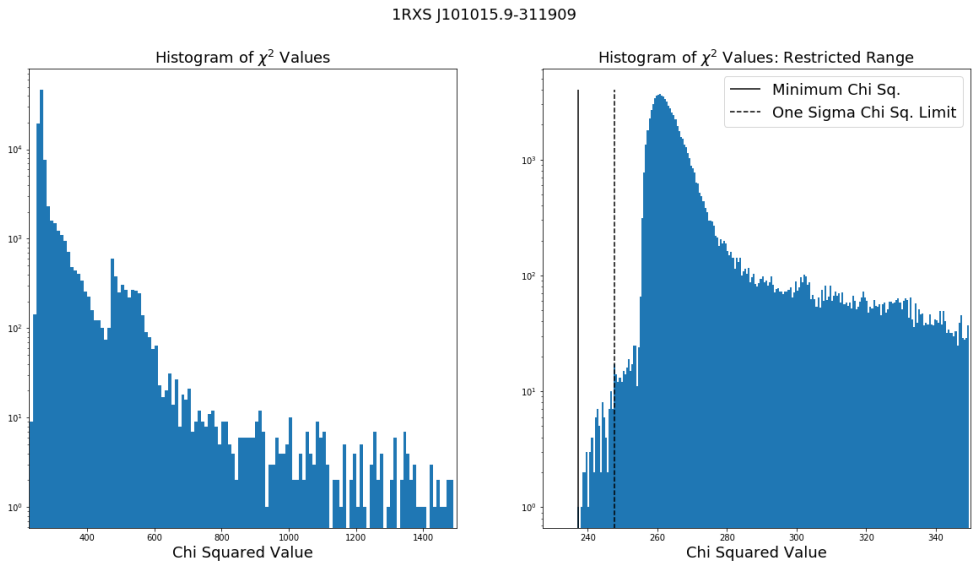

Figure 3.3: Histograms of the χ^2 values in the accepted MCMC steps for 1RXS J101015.9-311909. Left: Histogram truncated at χ^2=1500. Right: Histogram restricted to show the distribution near its peak and the minimum χ^2 value.

The best fit SED for the MCMC SSC modeling of 1RXS J101015.9-311909 is shown in Figure 3.8. We use all SED points presented in H.E.S.S. Collaboration et al. (2012) including the archival data. Also shown is the SED using the best-fit values from Cerruti et al. (2013) which result in a χ^2 value of 1856.29 from the same observables–the SED data points–as those used in the MCMC method. There is a significantly better fitted result using the MCMC technique which allows more free parameters and fewer assumptions. Though the goal of this validation was simply to prove that it can model a blazar SED using an SSC scenario and not to reproduce the exact input parameters, it is interesting to compare our results to those of Cerruti et al. (2013). There are several significant differences between the two models including the value of α_1, δ and K'. We did not assume any value of α_1 and found that the best value of $\alpha_1 = 2.75$ is larger than any of the values tested by Cerruti et al. (2013). In fact, the entire 1σ range determined from

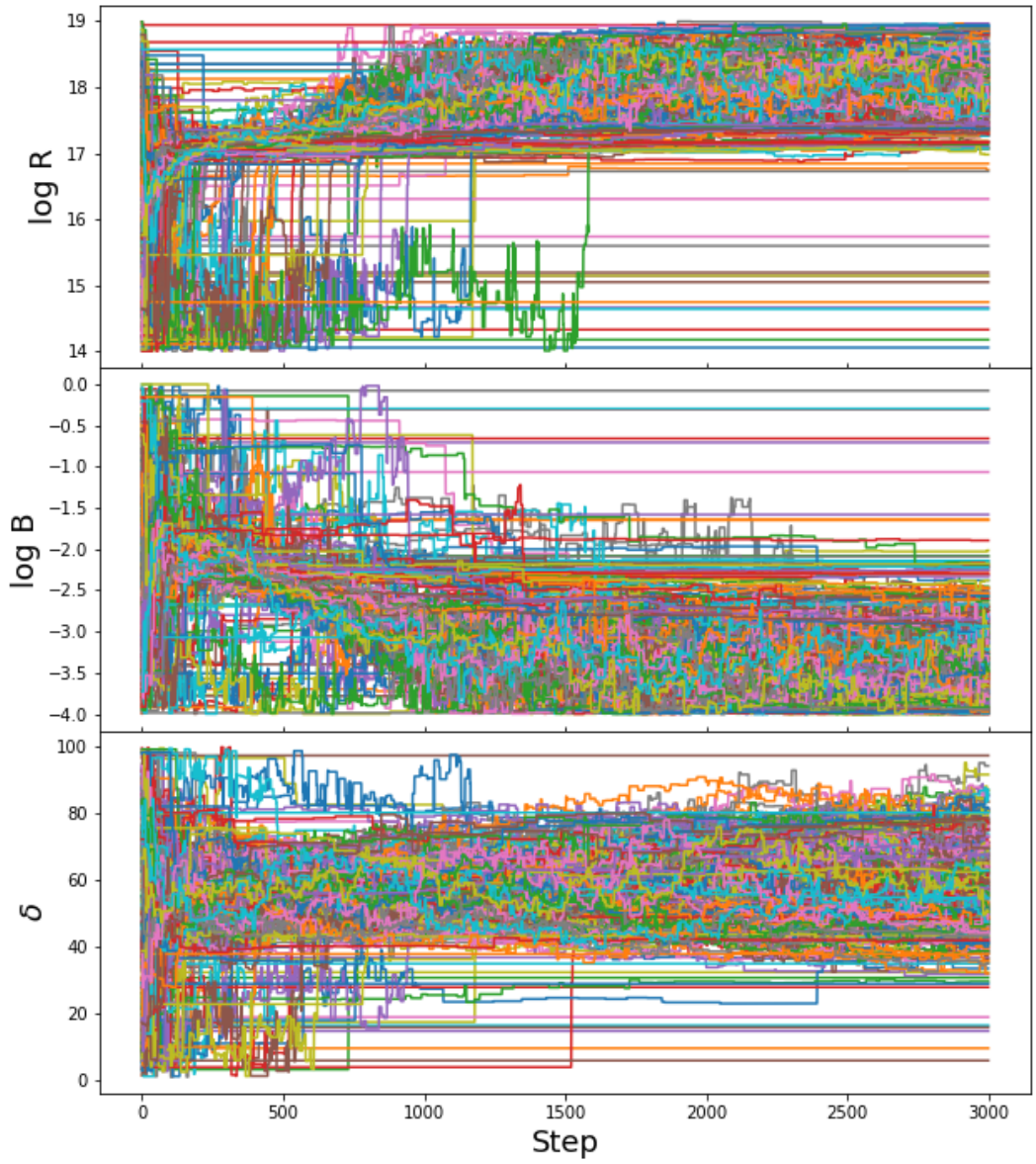

Figure 3.4: Values of R, B and δ at each step of the MCMC chain for 1RXS J101015.9-311909. Each line tracks the position of a different walker; 300 walkers are shown.

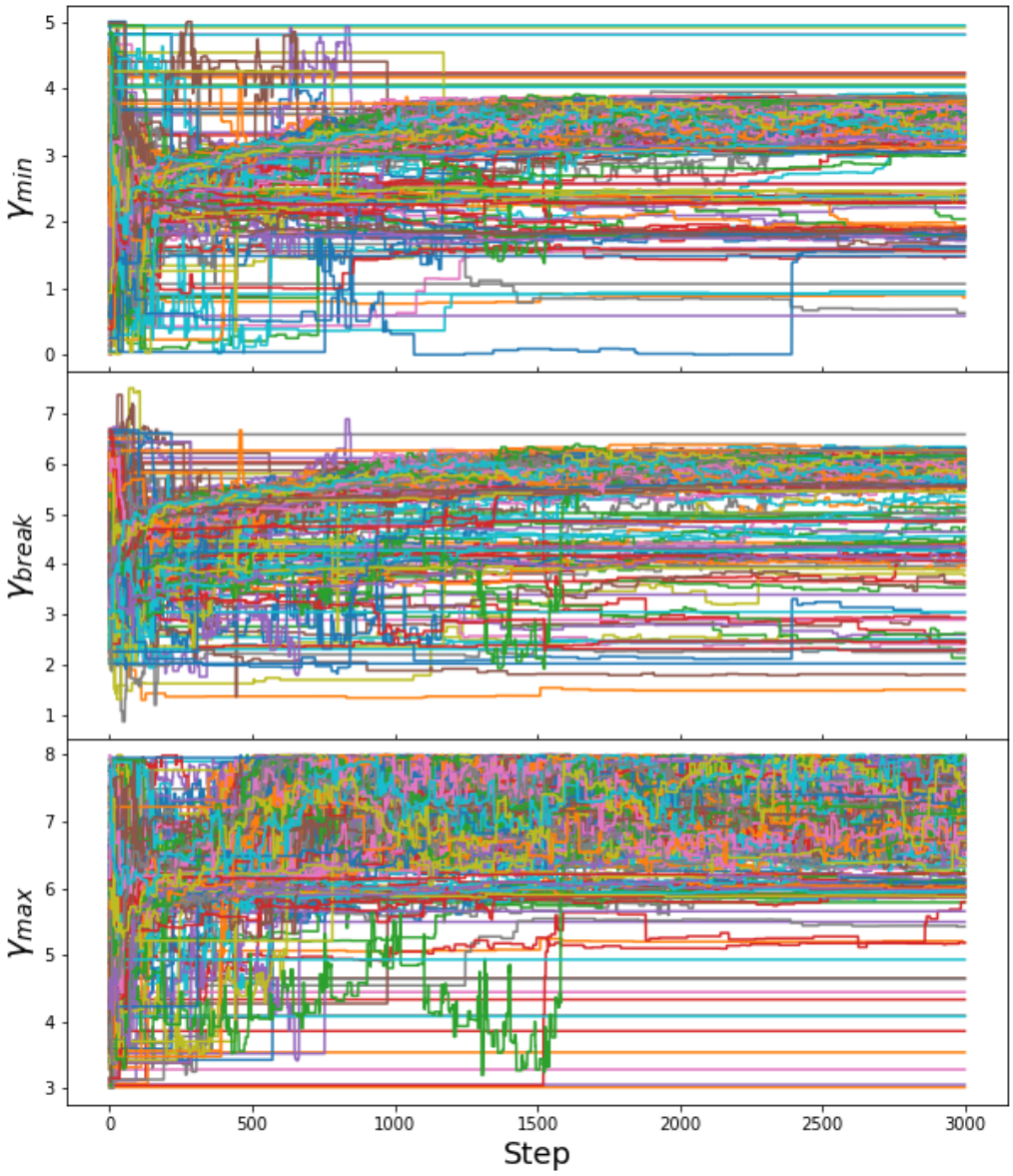

Figure 3.5: Chain status for gammas. Values of γ_{min}, γ_{break} and γ_{max} at each step of the MCMC chain for 1RXS J101015.9-311909. Each line tracks the position of a different walker; 300 walkers are shown.

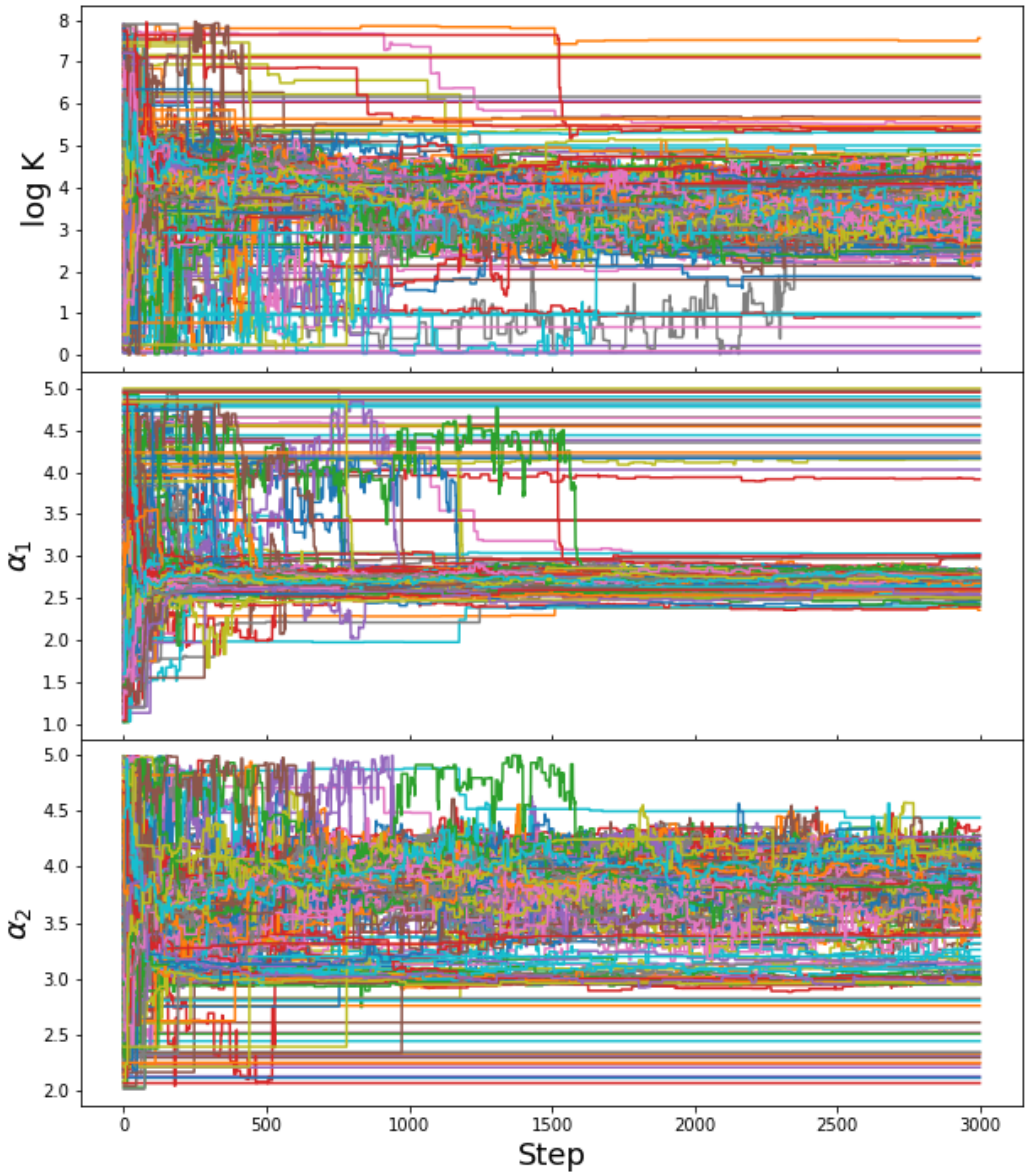

Figure 3.6: Values of α_1, α_2 and K at each step of the MCMC chain for 1RXS J101015.9-311909. Each line tracks the position of a different walker; 300 walkers are shown.

the MCMC method is larger than the largest value of 2.0 used in the previous modeling. We do not see the stratification of models near $\nu \sim 10^{11}$ - 10^{14} Hz as is seen in the previous results reproduced in Figure 3.2; this behavior is due to the different assumed α_1 values. For comparison, if we remove all attempted MCMC steps that have $\alpha_1 > 2.0$, the smallest χ^2 in the set is 1500.18 and has $\alpha_1 = 1.97$; these are closer in value to the best fit SED from Cerruti et al. (2013). The second parameter, the Doppler factor, we found to be 44.05, which is much lower than the extreme value of 96.83. The 1σ range determined by Cerruti et al. (2013) includes this value determined by the MCMC, but the converse is not true. The MCMC technique tightly constrains the Doppler factor 1σ range to $41.12 < \delta < 51.79$. This is a narrower range than that in Cerruti et al. (2013) as well as the results presented in Chapter 4 for the blazar 3C 66A. Perhaps this is due to the inclusion of the radio observations in this SED fit, which are not included as an observable in the fit from Cerruti et al. (2013) nor the 3C 66A work. The normalization of the electron spectrum, K', is also found to be significantly different between the two modeling results. Cerruti et al. (2013) restrict K' from 2×10^{-9} to 2×10^{-6} cm^{-3} while the MCMC results in K' constrained to $\sim 10^{-15}$ cm^{-3}. As seen in Figure 3.7, these normalizations and α_1 values result in very different injected electron spectra. However, the α_2 values are in agreement and the different electron spectra still produce SEDs that are very similar in several frequency bands.

Overall, this MCMC method for fitting a blazar SED to a single-zone, pure-leptonic emission model is a promising technique. It does not require many assumptions about the values of input parameters, and it provides the ability to put statistical uncertainties on best fit values. In the application to 1RXS J101015.9-311909, we require fewer assumptions than the previous modeling results in Cerruti et al. (2013) and are able to incorporate all data points in the SED, including

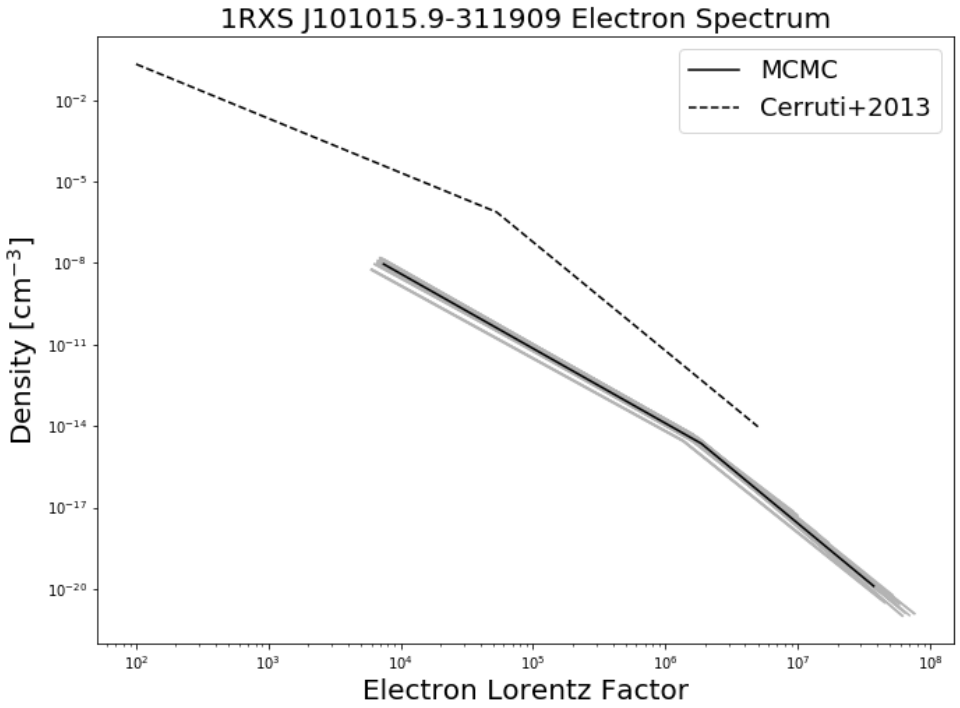

Figure 3.7: The injected electron spectra used in modeling the SED of 1RXS J101015.9-311909. For the MCMC results, the spectrum used in the best fit is shown in black and all electron spectra used for SEDs falling within 1σ of the best fit are shown in grey. The electron spectrum used in the best fit from Cerruti et al. (2013) is shown as a dashed line.

the data points in the radio band which were previously not included. The use of emcee, a freely available python package, makes this technique simple to implement given an SED generating code.

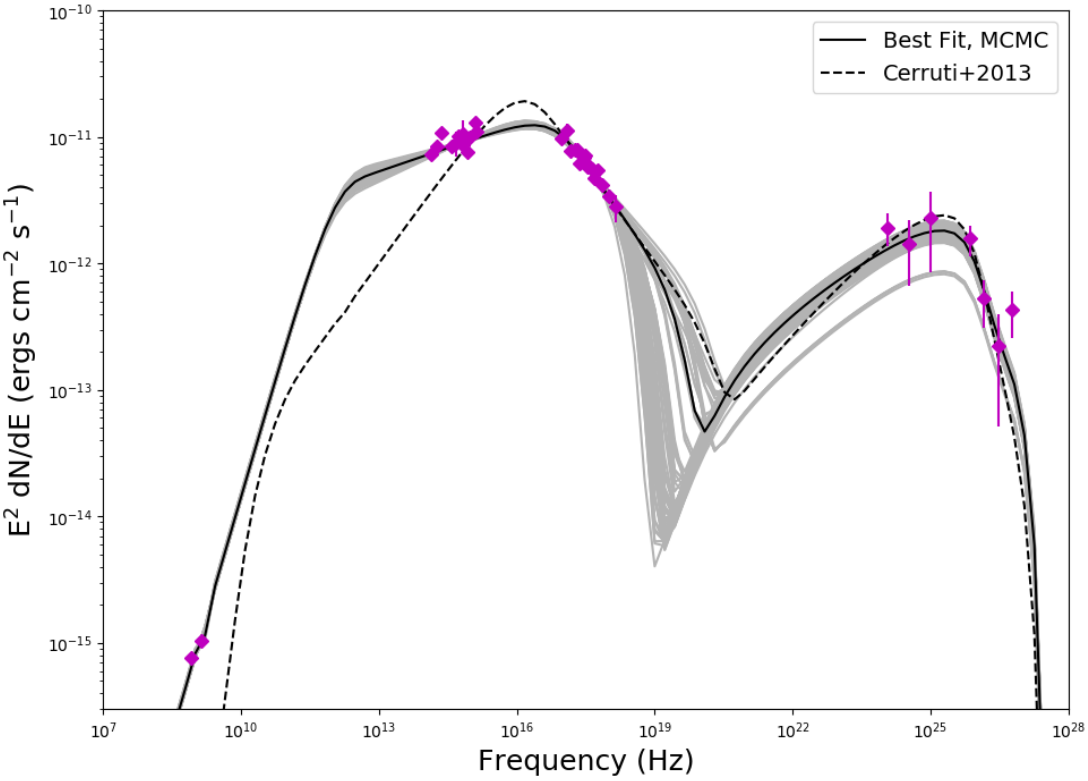

Figure 3.8: The fitted SED for 1RXS J101015.9-311909 along with the data points from H.E.S.S. Collaboration et al. (2012) shown in purple. The best fit from the MCMC method is shown in black and all SED falling within 1σ of the best fit are shown in grey. The best fit SED from Cerruti et al. (2013) is shown in a dashed line.

Chapter 4

Long-term Observations of 3C 66A

4.1 Introduction

Thirty years ago, our view of the universe significantly changed with the discovery of VHE gamma rays from the Crab Nebula (Weekes et al., 1989). We are now in an era where multiple instruments are not only sensitive to many types of VHE emitting objects, but they have also amassed large datasets over extended timescales. The current generation of ground-based VHE telescopes has been online for several years now, allowing us to make deep gamma-ray observations of blazars, the most populous category of extragalactic VHE sources. One of these blazars is 3C 66A, a blazar that is of BL Lac type. BL Lacs exhibit no or weak spectral lines that would lead to a redshift measurement, and 3C 66A is no exception. The redshift is constrained to $0.3347 \leq z < 0.41$, where the lower limit is based on absorption by intervening Lyα and the upper limit is set statistically based on the non-detection of more distant absorbing systems (Furniss et al.,

2013). Recent results propose that 3C 66A is hosted by a galaxy belonging to a cluster at $z = 0.340$ (Torres-Zafra et al., 2018). This distance is consistent with the spectroscopically determined limits.

3C 66A was first detected above 100 GeV in 1998 at the Crimean Astrophysical Observatory (Neshpor et al., 1998), and has since been detected with VERITAS (Swordy, 2008) and MAGIC (Aleksić et al., 2011). The VHE spectra are well described by a power law with a soft photon index, Γ. The VERITAS collaboration reports an observed index of $\Gamma = 4.1 \pm 0.6_{stat} \pm 0.6_{sys}$ during September and October of 2008 (MJD 54734-54749) (Abdo et al., 2011). This time interval encompasses significant night-to-night flux variability. The MAGIC collaboration reports an observed spectral index of $\Gamma = 3.64 \pm 0.38_{stat} \pm 0.25_{sys}$ during December, 2009 and January, 2010 (Aleksić et al., 2011). This is consistent, within errors, with the VERITAS measurement. The MAGIC collaboration also detected VHE emission associated with 3C66B, a radio galaxy 6′ from 3C 66A at $z = 0.0215$ (Aliu et al., 2009).

3C 66A is an intermediate synchrotron peaked (ISP) BL Lac object (Abdo et al., 2010). These have the high energy bump of the spectral energy distribution (SED) peaking below the sensitivity of ground-based gamma-ray instruments; this makes it difficult to detect ISPs in the VHE band. ISPs are often only detected during infrequent and unpredictable increases of flux associated with flaring behavior. However, observing these sources in a lower, constant flux state is critical to understanding the physical processes creating VHE emission. One way to obtain a detection of this flux state is through deep, long-term observations allowing the accumulation of statistics.

VHE photons traveling through the universe are absorbed by the EBL via pair production. The VHE flux observed at Earth is smaller than the emitted flux by

a factor of $e^{-\tau}$, where $\tau(E, z)$ is the gamma-ray opacity (Nikishov, 1962). The opacity increases with redshift, so the VHE flux from relatively distant sources, such as 3C 66A, is significantly attenuated. The benefit of significant absorption is that we can probe high opacities of the EBL and examine the deabsorbed spectrum for unexpected signatures, such as spectral hardening or anomalous features.

One major open question in astrophysics is the source of ultra-high-energy cosmic rays (UHECRs), and active galactic nuclei (AGN) are excellent candidates. If AGN are indeed a source, cosmic rays could interact with cosmic microwave background (CMB) and EBL photons to create secondary gamma rays observable by Cherenkov telescopes (e.g. Essey and Kusenko (2010)). These secondary gamma rays would contribute to the VHE spectrum of blazars as a hard, slowly varying component. The relative contribution would be greater for more distant sources and could be ruled out by rapid variability at high opacities of the EBL. This chapter reports on the results and discussion of deep, long-term observations of 3C 66A going back to September of 2007.

4.2 VERITAS Observations

Between 18 September 2007 and 5 December 2016 (MJD 54361-57727), VERITAS collected 131 hours of observations on 3C 66A. After accounting for deadtime, bad weather and data quality cuts, the total live time is 87 hours. These data span three different array configurations, separated by two major instrument upgrades. In the summer of 2009 one of the telescopes was relocated to provide better sensitivity, and during the summer of 2012 the photomultiplier tubes (PMTs) in the cameras were replaced by PMTs with higher quantum efficiency. Each upgrade independently improved the sensitivity of VERITAS, and the observations of 3C 66A benefit from these improvements. We analyzed the data on 3C 66A using the stan-

dard VERITAS analysis package as described in Cogan (2008) and Daniel (2008). We used two separate sets of cuts: soft and medium. The main difference between the cuts is the minimum size (corresponding to how much charge is contained in the image) and the θ^2 cut (corresponding to the angular separation, θ). In this VERITAS analysis, soft cuts are used for E<200 GeV and medium cuts are used for E>200 GeV in spectral reconstruction.

Li and Ma (1983) defines and derives a few key statistics based on gamma-ray observations which we utilize here. N_{excess} is the excess number of counts in a given region of the sky, defined as $N_{excess} = N_{on} - \alpha N_{off}$. N_{on} is the number of counts in the "on" or source region of the sky, N_{off} is the number of counts in the "off" or background region, and α indicates the ratio of exposure between the on and off regions. The statistical significance of the gamma-ray excess in the on region is given by Equation 17 of Li and Ma (1983). Utilizing a reflected region (Fomin et al., 1994) analysis of the 87 hours of data, we detect a source with a statistical significance of 24.4σ using soft cuts and 15.7σ using medium cuts.

4.2.1 Background Systematics

Analysis of gamma-ray observations without any signal should produce a Gaussian distribution of significances in a sky map with width unity and mean zero when using Equation 17 in Li and Ma (1983) and in accordance with Wilks's theorem. Analysis of the 87 hour VERITAS exposure on 3C 66A produced a background significance distribution with an RMS of 1.51 using soft cuts. With deeper exposures, it has become more pertinent to understand the systematic effects within the VERITAS analysis which contribute to the calculation of the background.

We see two such effects in this dataset which become prominent with longer

and deeper exposures. One effect is that of zenith-dependent acceptance of the camera. Standard VERITAS analysis uses only a radially dependent acceptance, so we have utilized a correction to this acceptance that accounts for the change in zenith angle across the camera. For a full description of this correction, see Zitzer (2015). Applying this correction brings the RMS of the background significance distribution to 1.37. The second effect is discussed in Spengler (2015), which derives a modified significance equation that incorporates the systematic uncertainty on the acceptance. Applying this modified Li & Ma equation brings the RMS to 1.34. Applying both corrections brings the RMS to 1.22. Using medium cuts, the uncorrected background significance distribution has an RMS of 1.08. Applying the Modified Li & Ma algorithm brings this to 1.02, applying the zenith correction brings it to 1.06 and applying both brings it to 1.00. Any VERITAS results based on the sky map in this chapter have both corrections applied. See B. Zitzer for the VERITAS Collaboration (2017) for more details and how these corrections impact VERITAS data analysis.

4.2.2 VERITAS Light Curve & Treatment of Flux Variability

The full VERITAS light curve binned by season is shown in Fig. 4.5. The benefit of using long-term time-averaged data is the large number of statistics available with which to construct an SED. However, since blazars exhibit variable flux, time averaged spectra can produce unphysical features in the SED. To separate different flux states, we first construct the daily VERITAS light curve and a distribution of these fluxes, seen in Fig. 4.4. Based on the flux distribution, we define a high flux state as days with flux $> 0.3 \times 10^{-6}$ m^{-2} s^{-1} and with a statistical significance $> 3.0\sigma$. This produces a set of three consecutive days from

8 October 2008 to 10 October 2008 (MJD 54747-54749) which we define as the *VHE high flux state*. The high statistical significance of the VHE emission combined with the consecutive nature of the days makes this a more physical choice rather than a purely statistical one. These dates are consistent with the VHE flare previously published by Abdo et al. (2011).

A simple histogram of flux is ideal for picking out outlying time bins of flux, but with low photon statistics in many bins, it is difficult to determine if there is variability in the quiescent bins of flux. Additionally, a single histogram ignores the time ordering of the bins and uncertainties on the flux measurements. We adopt the treatment of variability and definitions of flux states based on a Bayesian Block analysis of the *Fermi*-LAT data as detailed in Section 4.3. The data are sub-divided into six blocks which we use in the rest of this analysis. The time periods of each block are contained in Table 4.2; the VHE flare is contained within block 2. While there are observations in blocks 1, 2, 3, 5 and 6, there are enough statistics in only blocks 1, 2, 5 and 6 to conduct the relevant science analyses. In block 3, we obtain a 4.4σ detection of 3C 66A using soft cuts, and there are not enough consecutive energy bins to construct a spectrum. Block 4 consists of a week-long outburst in May of 2009. At this time, 3C 66A was not visible at night from the northern hemisphere, so there are no VERITAS observations during this time.

4.2.3 Location of the Gamma-Ray Excess

In recent years, VHE emission from both 3C 66A and 3C 66B have been reported. 3C 66B is a radio galaxy, a known type of VHE-emitter (e.g. M 87, Aharonian et al. (2003) and 3C 264, Mukherjee (2018)). In order to determine the location of the VHE emission in this data set, we fit the map of background-

subtracted events to a single 2D Gaussian. The results are shown in Table 4.1, and all locations are consistent with the radio coordinates (J2000: 35.665, 43.036) of 3C 66A within statistical uncertainties. Figure 4.3 shows the VERITAS sky maps from these observations with the fitted excess locations marked. For this work, we assume that the emission comes from only 3C 66A.

Table 4.1: Locations of VHE emission determined by fitting a 2D Gaussian function to the excess maps seen by VERITAS. The statistical uncertainties for each fit are shown; there is an additional 0.01° systematic uncertainty on each value.

Cuts	data set	RA (J2000)	Dec (J2000)
Soft	Block 1	$35.65° \pm 0.01°$	$43.03° \pm 0.01°$
Soft	Block 2	$35.67° \pm 0.01°$	$43.03° \pm 0.01°$
Soft	VHE flare state	$35.67° \pm 0.01°$	$43.03° \pm 0.01°$
Soft	Block 5	$35.65° \pm 0.06°$	$43.06° \pm 0.03°$
Soft	Block 6	$35.67° \pm 0.01°$	$43.03° \pm 0.01°$
Medium	Block 1	$35.65° \pm 0.01°$	$43.05° \pm 0.01°$
Medium	Block 2	$35.66° \pm 0.01°$	$43.03° \pm 0.01°$
Medium	VHE flare state	$35.65° \pm 0.01°$	$43.02° \pm 0.01°$
Medium	Block 5	$35.62° \pm 0.03°$	$43.05° \pm 0.03°$
Medium	Block 6	$35.68° \pm 0.02°$	$43.03° \pm 0.02°$

4.2.4 Spectral Reconstruction

Each observed VHE spectrum is fit with both a power law (PWL)

$$dN/dE = N(E/E_o)^{-\Gamma} \tag{4.1}$$

and a log parabola (LGP)

$$dN/dE = N(E/E_o)^{-\Gamma+\beta log(E/E_o)}. \tag{4.2}$$

We find that each observed spectrum is well fit by a power law; there is no statistically significant curvature in any of the spectra. The spectral fit parameters are

provided in Table 4.2 and the observed spectral energy distributions are shown in Figure 4.2. These fit results are, at first glance, in contrast with the VERITAS spectrum shown at the 2015 International Cosmic Ray Conference (ICRC) where the presented VHE low state 3C 66A spectrum was best fit by a log parabola (J. Vievering for the VERITAS Collaboration, 2015). The results shown at the ICRC were analyzed as a part of this project, and are a subset of what is shown here. The SED is shown in Figure 4.1, and this analysis result underscores the effect of time averaging on constructing blazar spectra. That low flux dataset consists of 61 hours of livetime spanning September 2007 to January 2015 except for the three-day VHE flare on MJD 54747-54749. The spectrum is modeled as both a PWL and a LGP with a 4.1σ preference for the LGP shape. The time frame is roughly consistent with the analyses done here in blocks 1, 5 and 6. As seen in Table 4.2 and Figure 4.2, the SED constructed in block 1 has a higher energy threshold and normalization than blocks 5 and 6. With no spectral information lower than 150 GeV in the higher flux state of block 1 and the lower energy threshold for the lower flux states (135 GeV and 119 GeV for blocks 5 and 6, respectively), an averaged spectrum produces a turn over at low energies leading to the observed spectral curvature shown in J. Vievering for the VERITAS Collaboration (2015).

To account for absorption of VHE photons by the EBL, we correct (or, "de-absorb") the observed spectra using the model of Gilmore et al. (2012). Since there are only lower and upper spectroscopic limits on the redshift of 3C 66A, we use the EBL opacity values at these two limits. Note that the redshift of z=0.34 from Torres-Zafra et al. (2018) is very close to the spectroscopic lower limit. The deabsorbed VHE spectra are shown in Figure 4.2. Each deabsorbed spectrum is well fit with a power law.

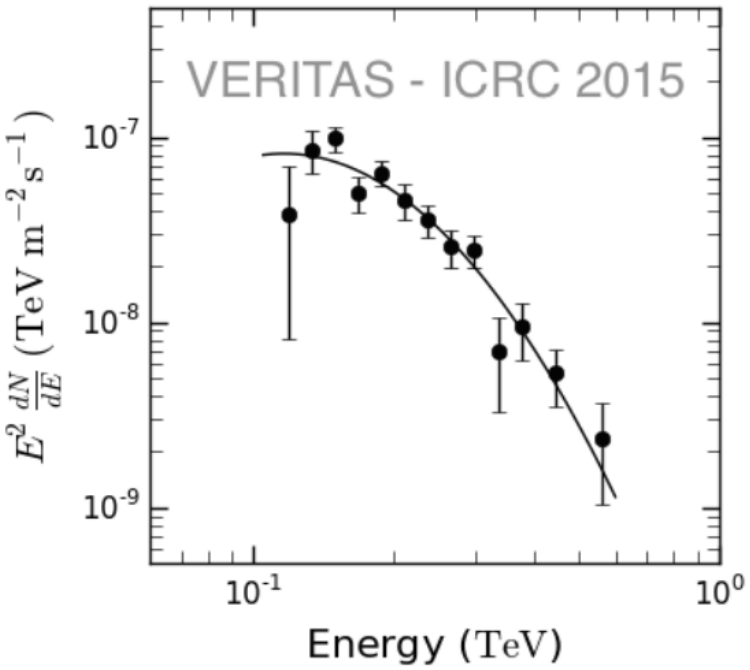

Figure 4.1: Low-flux-state VHE spectrum of 3C 66A from J. Vievering for the VERITAS Collaboration (2015) shown in the E^2dN/dE representation (TeV $m^{-2}s^{-1}$). 3C 66A is detected in a low-flux state at 12σ with 61 hours of observations. A log-parabolic function is used to model the data.

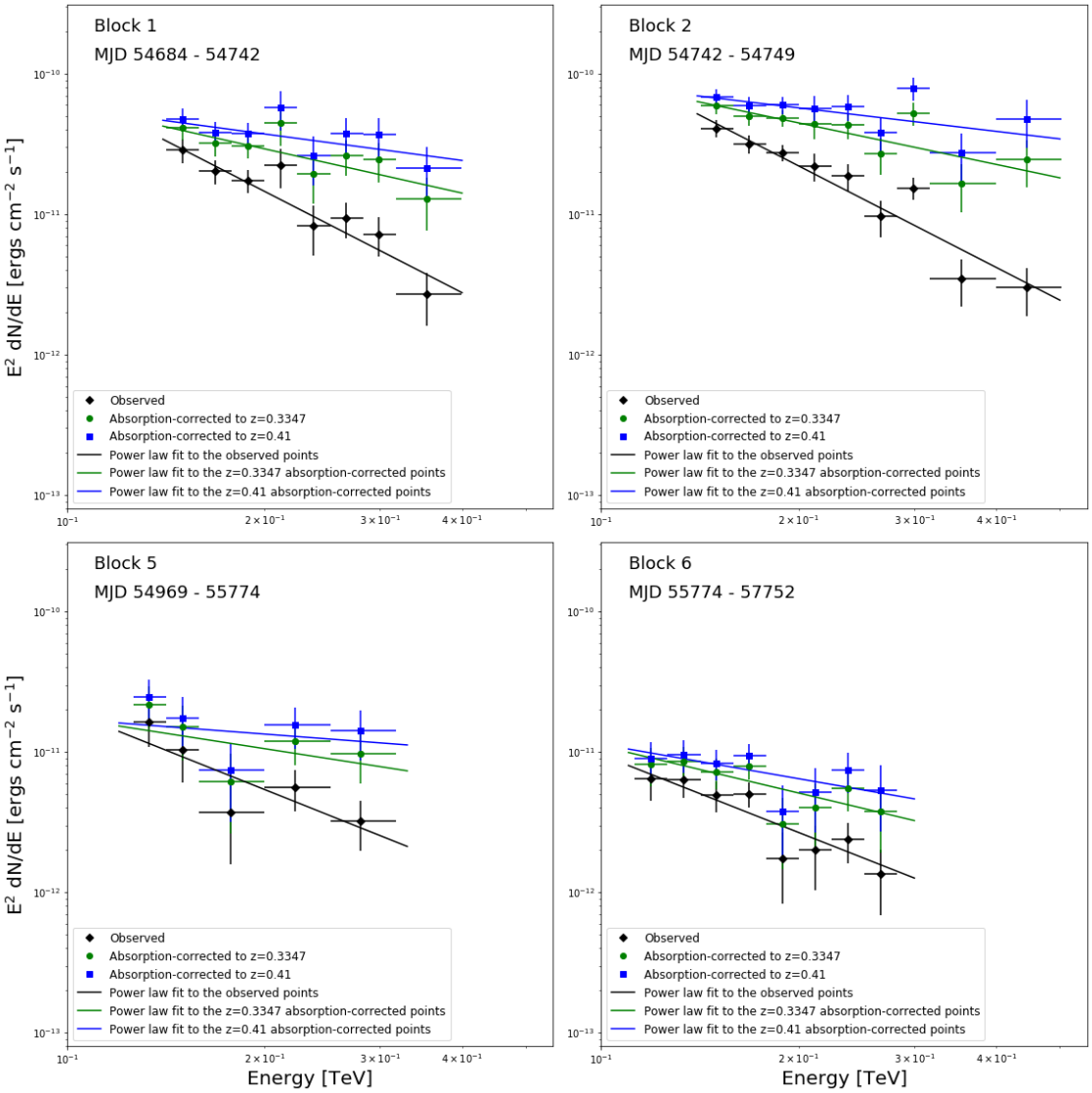

Figure 4.2: VHE spectral energy distribution of 3C 66A during the indicated blocks. The black points are the observed data. The green and blue colors are deabsorbed using the Gilmore 2012 EBL model to z=0.3347 and z=0.41, respectively. The lines indicate the best power-law fit to the data; fit parameters are listed in Table 4.2.

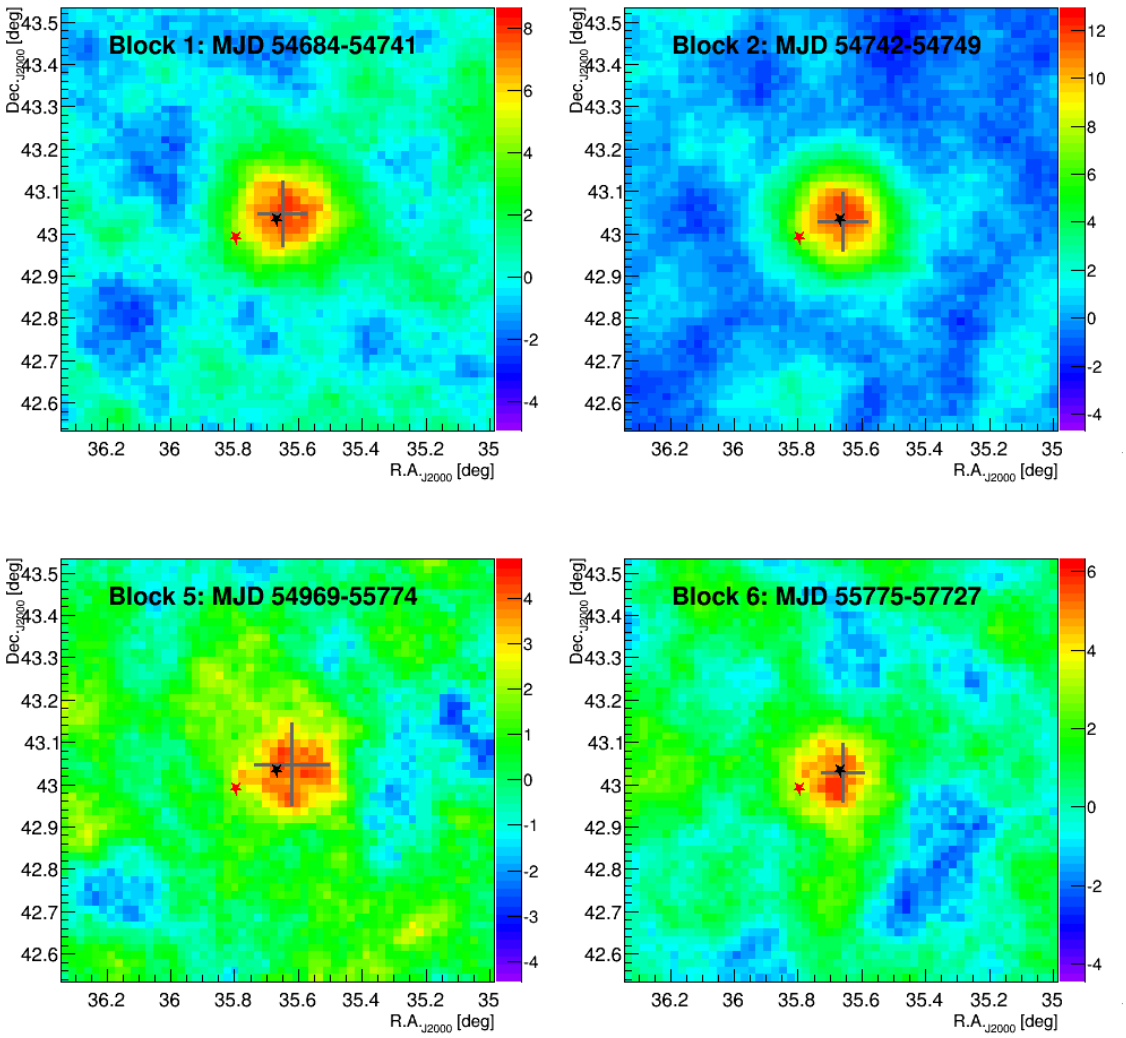

Figure 4.3: Significance maps generated using medium cuts. In each map, the position of the 2D Gaussian fit to the excess is shown by a gray cross. Exact values for the positions are listed in Table 4.1. The position of 3C 66A is shown by a black star, and the position of 3C 66B is shown with a red star. *Top left:* Block 1, MJD 54684 - 54742 *Top right:* Block 2, MJD 54741 - 54749 *Bottom left:* Block 5, MJD 54969 - 55774 *Bottom right:* Block 6, MJD 55775 - 57727

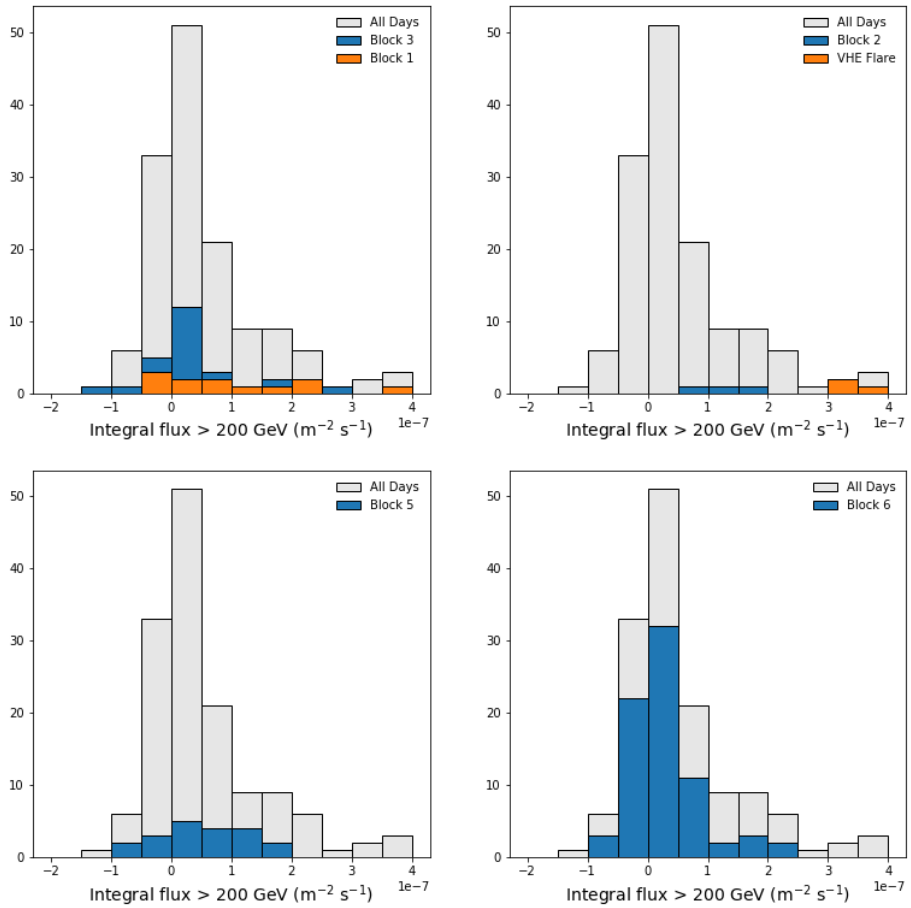

Figure 4.4: Distributions of daily integral flux (E > 200 GeV) as seen by VERITAS.

Table 4.2: Results of the power law fits to each VHE spectrum with E_0=190 GeV.

	N ($\times 10^{-10}$ TeV^{-1} cm^{-2} s^{-1})	Γ
Block 1, MJD 54684-54742		
Observed	2.85 ± 0.26	4.40 ±0.32
Deabsorbed, z=0.3347	5.34 ± 0.48	3.05 ± 0.34
Deabsorbed, z=0.41	6.67 ± 0.60	2.63 ± 0.35
High VHE Flux State, MJD 54747-54749		
Observed	6.38 ± 0.42	4.54 ± 0.20
Deabsorbed, z=0.3347	12.11 ± 0.79	3.09 ± 0.23
Deabsorbed, z=0.41	15.16 ± 0.99	2.67 ± 0.24
Block 2, MJD 54742-54749		
Observed	4.32 ± 0.28	4.40 ± 0.21
Deabsorbed, z=0.3347	8.14 ± 0.53	2.98 ± 0.23
Deabsorbed, z=0.41	10.18 ± 0.66	2.55 ± 0.23
Block 5, MJD 54969-55774		
Observed	1.03 ± 0.19	3.86 ± 0.83
Deabsorbed, z=0.3347	1.89 ± 3.45	2.73 ± 0.90
Deabsorbed, z=0.41	2.36 ± 4.31	2.36 ± 0.93
Block 6, MJD 55774-57727		
Observed	0.507 ± 0.066	4.01 ± 0.45
Deabsorbed, z=0.3347	0.93 ± 0.12	3.11 ± 0.48
Deabsorbed, z=0.41	1.16 ± 0.16	2.81 ± 0.49

4.3 *Fermi* Large Area Telescope Observations

The Large Area Telescope (LAT) is the primary instrument on board the *Fermi Gamma Ray Space Telescope*. The LAT is a pair conversion telescope which surveys the entire sky every three hours (Atwood et al., 2009). This continual, unbiased observing makes it an excellent instrument for long-term observations of blazars. We use Pass-8 data from August 2008 to December 2016 centered on 3C 66A.

Analysis of these observations is done using the binned maximum likelihood method implemented in version v10r0p5 of the public science tools, available from the Fermi Science Support Center. Only photons of event class 128 and event type

3 within a 10° radius of 3C 66A and detected with a zenith angle $< 90°$ are included in the analysis. The model input to the likelihood analysis is constructed using the user contributed tools[1] and the 3FGL catalog (Acero et al., 2015). Sources with $TS < 2.0$ were removed and remaining sources greater than 8° from 3C 66A were included with parameters frozen to their 3FGL values. Among the sourcers within the region of interest is a pulsar 0.95° away from 3C 66A, 3FGL J0218.1+4232. This pulsar does not exhibit variability on the time scales under investigation, so we froze its parameters to their 3FGL values. We fit both a PWL and a LGP to the 3C 66A spectral data for every *Fermi*-LAT analysis performed. To assess the significance of the LGP over the PWL, we use TS_{curve} which is first defined in Nolan et al. (2012) as $\mathrm{TS}_{curve} = 2(\log \mathcal{L}_{LGP} - \log \mathcal{L}_{PWL})$. We choose the LGP spectral shape if $\mathrm{TS}_{curve} > 9.0$, and the PWL shape otherwise. Results from the LAT analyses are provided in Table 4.3.

4.3.1 *Fermi* - LAT Light Curves and Treatment of Flux Variability

To create *Fermi*-LAT light curves, the model was altered such that the spectral shapes of all sources except 3C 66A were fixed to their 3FGL values. Normalizations were left to vary in the likelihood fit for all sources except the nearby pulsar, 3FGL J0218.1+4232, which had all its parameters frozen to their 3FGL values. We construct light curves of 3C 66A using 28-day, 7-day and one-day bins. The long-term light curve is shown in Fig. 4.5. Due to the variable nature of blazars, creating time-averaged spectra can result in the presence of unphysical or false features. It is thus pertinent to treat variability carefully and to construct spectra in separate flux states.

[1] http://fermi.gsfc.nasa.gov/ssc/data/analysis/user/make3FGLxml.py

To date, the Fermi collaboration has published three catalogs focusing on the highest energies detectable by the LAT, the 1FHL catalog (Ackermann et al., 2013), 2FHL catalog (Ackermann et al., 2016) and 3FHL catalog (The Fermi-LAT Collaboration, 2017). Each catalog does a Bayesian Blocks analysis to characterize the flux variability of each source. The result is a set of blocks, where one block defines a period of time during which the flux is consistent with being constant. See Ackermann et al. (2013) for further details of this analysis. Results from the 1FHL catalog (using photons with 10-500 GeV) show five distinct blocks between August, 2008 and August, 2011 for 3C 66A. Results from the 2FHL catalog (using photons with 50 GeV-2 TeV) show three distinct blocks between August, 2008 and August, 2015 for 3C 66A. Results from the 3FHL catalog (10 GeV-2 TeV) show four blocks between August, 2008 and August, 2015 for 3C 66A. All three analyses show a flare in May of 2009, but neither *Swift* nor VERITAS have observations during that time because 3C 66A was too close to the Sun. Only the 1FHL analysis results in a block with the flare in October of 2008; however, this remains a distinct feature of the long term light curve and consistent with the high energy flare presented in Abdo et al. (2011). A multiwavelength light curve during the 2008 October flare is shown in Fig. 4.6. 3C 66A has been in a quiescent state since May of 2009. The resulting blocks in the 3FHL have an edge near the end of the 1FHL time range (MJD $\sim$ 55600) indicating an even lower flux and a distinct quiescent state beginning at that time.

Note that though the Bayesian Blocks analysis works well for datasets with low statistics, it only works well when the photon coordinates are well localized (Ackermann et al., 2013). The localization is best at the highest energies detected by the LAT, so an analysis using the full energy range would not be possible or directly comparable to the FHL results. We therefore use the block edges from

the 1FHL analysis to guide our data selection for constructing the spectra in different flux states. The results from the spectral reconstruction in the five blocks produced in the 1FHL analysis and the specific dates used for each block are shown in Table 4.3. The available VERITAS observations go through 2016 December, however, none of the FHL catalog Bayesian Block analyses include data that recent. A sixth block is therefore created spanning from the end of the 1FHL dataset until December of 2016. The observed gamma-ray peaks in each of the six blocks are shown in Figure 4.7.

Table 4.3: LAT spectral analysis results broken down into each block time period with $E_0 = 914.5$ MeV. The spectral variables are defined in equations 4.1 and 4.2.

Block	MJD	Shape	TS_{curve}	N ($\times 10^{-11}$)	Γ	β ($\times 10^{-2}$)
				$cm^{-2}s^{-1}MeV^{-1}$		
1	54684 - 54741	PWL	2.33	2.62 ± 0.15	1.87 ± 0.04	n/a
2	54742 - 54749	PWL	<0	7.26 ± 0.57	1.89 ± 0.06	n/a
3	54749 - 54961	PWL	4.49	2.34 ± 0.08	1.89 ± 0.02	n/a
4	54961 - 54969	PWL	<0	13.62 ± 0.78	1.74 ± 0.04	n/a
5	54969 - 55774	LGP	17.8	2.51 ± 0.02	1.85 ± 0.01	6.60 ± 0.36
6	55774 - 57752	LGP	84.5	1.31 ± 0.03	1.86 ± 0.02	4.31 ± 0.74

4.4 *Swift* Observations

The X-Ray Telescope (XRT) is a focusing X-ray telescope on board the *Swift* satellite, and it is sensitive to photons in the energy range 0.2-10 keV (Gehrels et al., 2004). We utilize all observations in photon counting (PC) mode taken since the beginning of VERITAS observations in 2007. This amounts to 69 observations taken between 2 October 2008 and 5 December 2016. The data were analyzed with the tools provided in HEASoft v6.16, and the spectral analysis was done with v12.8.2 of XSPEC. The majority of the XRT observations have been taken

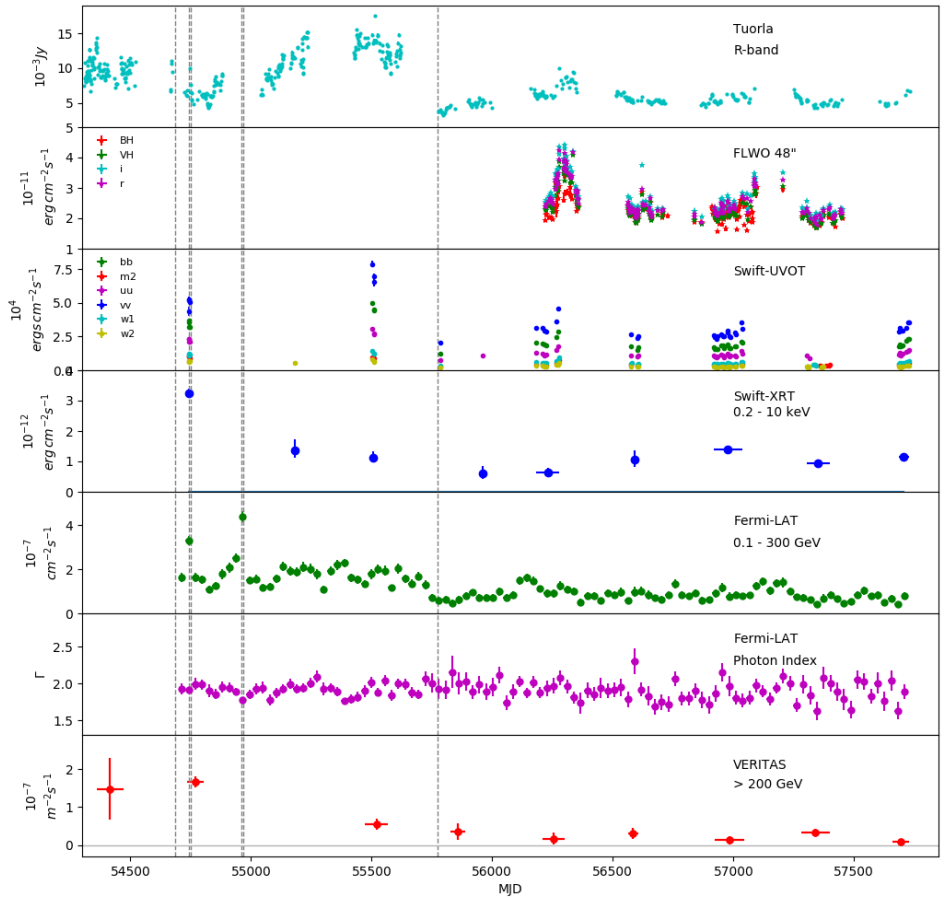

Figure 4.5: Long-term multiwavelength light curves of 3C 66A from September 2007 to December 2016. Dashed vertical lines indicate edges from the 1FHL Bayesian Block analysis. Seasonal flux is shown for both *Swift*-XRT and VERITAS, and the edges of the time bins indicate the first and last observations in each bin. Integral gamma-ray flux and the fitted photon indices seen by *Fermi*-LAT are shown in 28-day bins.

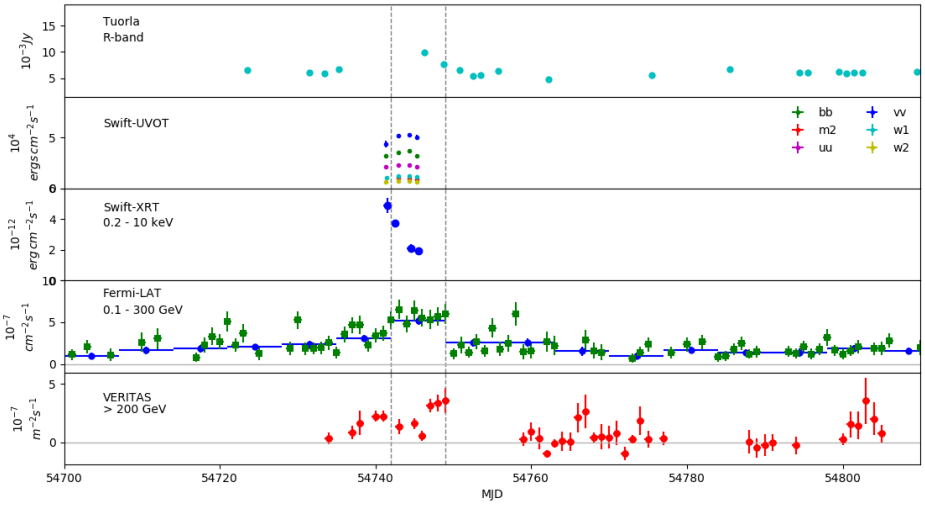

Figure 4.6: Multiwavelength light curves of 3C 66A covering the October 2008 high flux state (MJD 54700 - 54810 shown). Dashed vertical lines indicate the start and end of block 2 from the 1FHL Bayesian Block Analysis. All VERITAS and *Swift*-XRT data taken during blocks 1 and 3 are shown in this light curve.

contemporaneously with VERITAS, so the long term light curve shown in Fig. 4.5 is binned based on VERITAS observing seasons. The flux shows little variability in this band except for an elevated state in October, 2008 (MJD ∼54750). The daily light curve during this flare is shown in Fig.4.6. Figures 4.8, 4.9, 4.10 and 4.11 show the XRT spectra within the respective time blocks.

The Ultraviolet/Optical Telescope (UVOT) is a telescope on board the *Swift* satellite which utilizes broadband color filters and grisms to detect photons in the 170-600 nm band (Roming et al., 2005). Since the telescope is co-aligned with XRT, observations are simultaneously taken by both instruments. To analyze the data, the UVOT-specific tools included in the HEASoft 6.17 package were used. Aperture photometry with *uvotsource* was done using circular regions for the source and background with radii of 5" and 20", respectively. All images were inspected by eye and observations with issues or contamination were excluded.

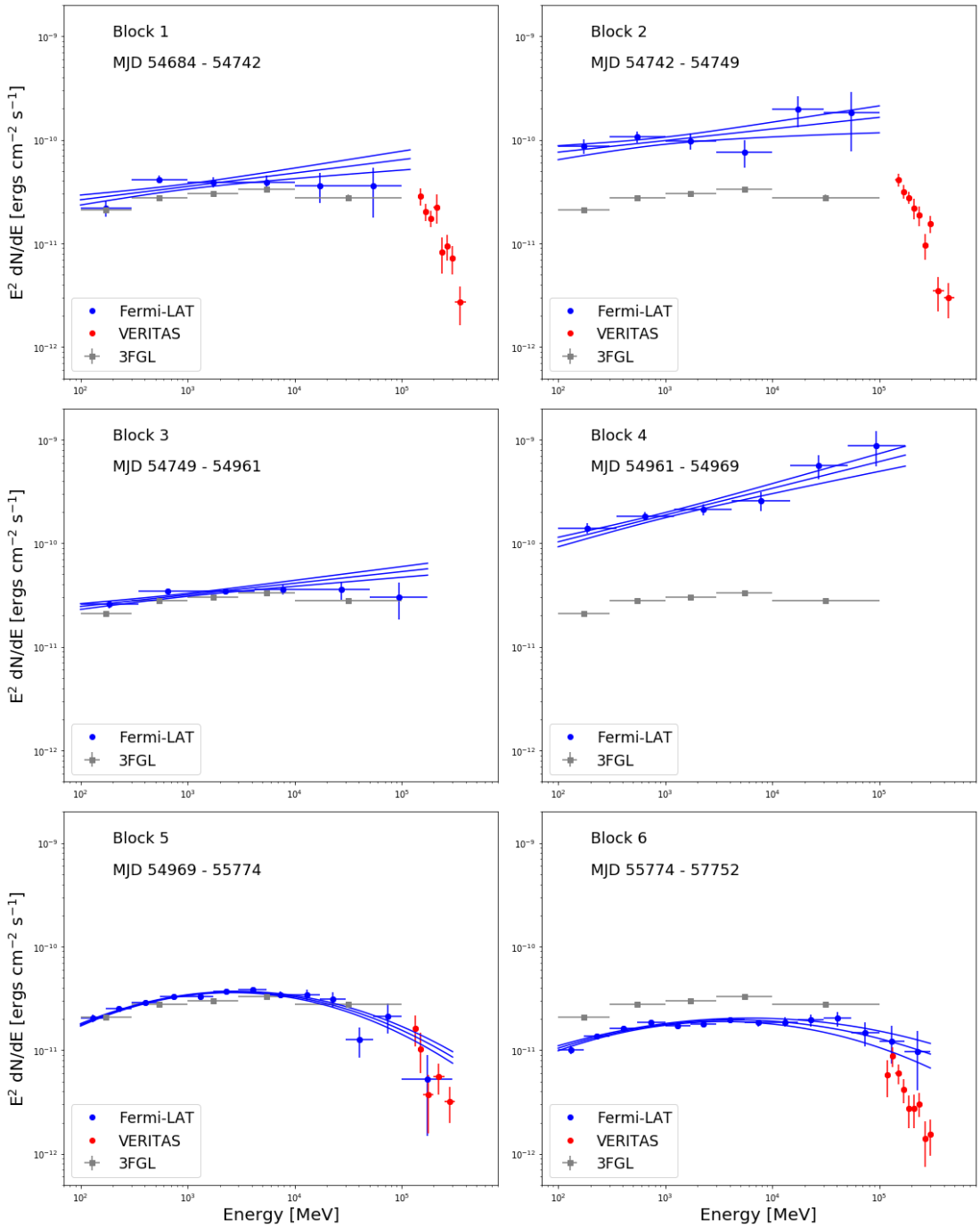

Figure 4.7: Observed gamma-ray peaks with spectral points from the 3FGL catalog for comparison (data from the 3FGL catalog is time averaged over four years). The butterflies shown outline the 1σ fit contours from Table 4.3

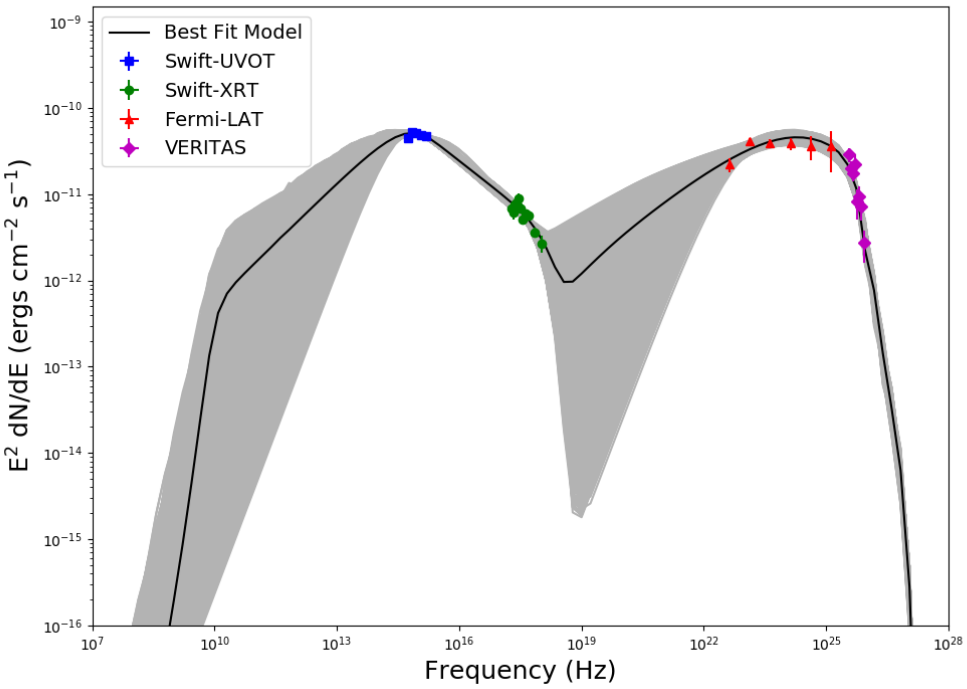

Figure 4.8: Block 1 MWL SED with the best fit SSC model shown as a black line. The grey region indicates the 1σ range of models using the parameter values detailed in Table 4.5.

Multiple images falling within the time ranges specified in each analysis were summed prior to extracting fluxes. An E(B-V) value of 0.085 is used in the extinction correction, obtained from Galactic dust maps from Schlafly and Finkbeiner (2011). The central wavelengths of the UVOT bands are taken from Poole et al. (2008). Extinction coefficients are derived for individual UVOT bands using the Fitzpatrick (1999) law with the York Extinction Solver.[2] The reconstructed spectra are shown in Figures 4.8, 4.9, 4.10 and 4.11.

[2]http://www.cadc-ccda.hia-iha.nrc-cnrc.gc.ca/community/YorkExtinctionSolver/coefficients.cgi

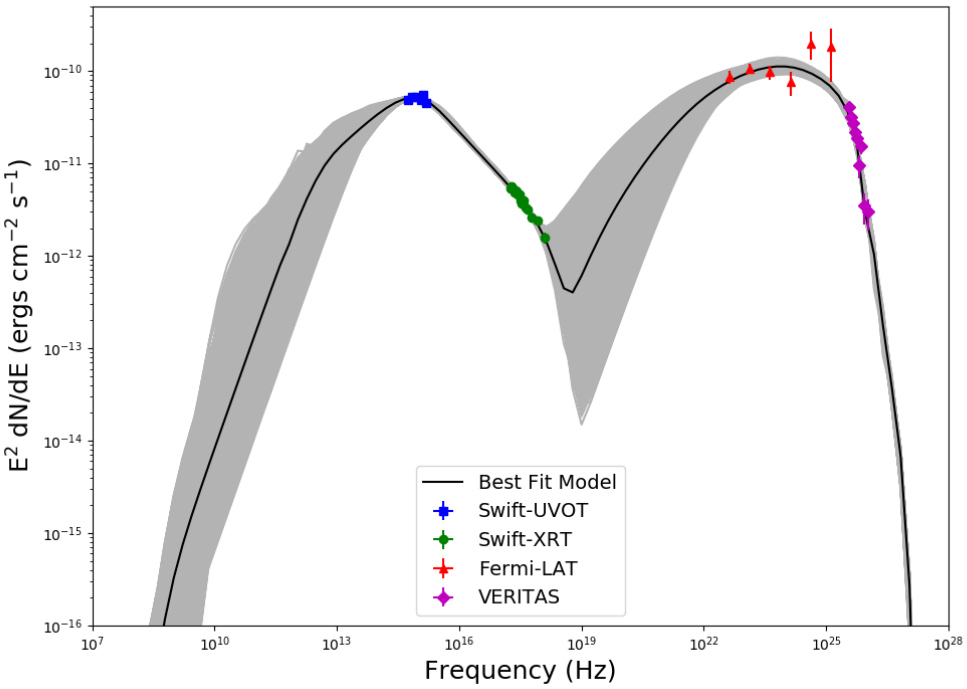

Figure 4.9: Block 2 MWL SED with the best fit SSC model shown as a black line. The grey region indicates the 1σ range of models using the parameter values detailed in Table 4.5.

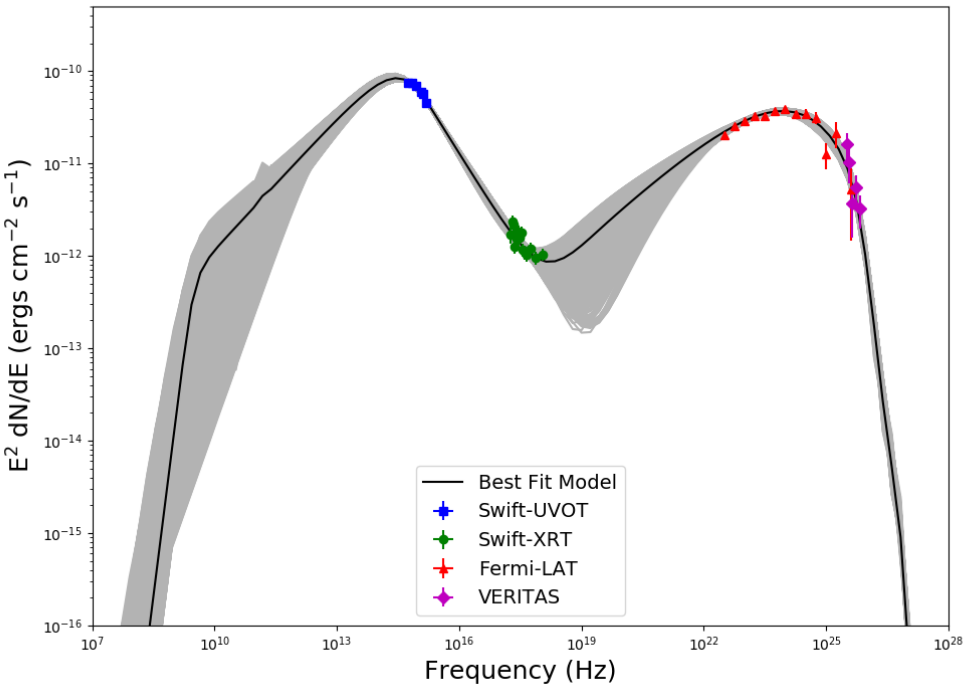

Figure 4.10: Block 5 MWL SED with the best fit SSC model shown as a black line. The grey region indicates the 1σ range of models using the parameter values detailed in Table 4.5.

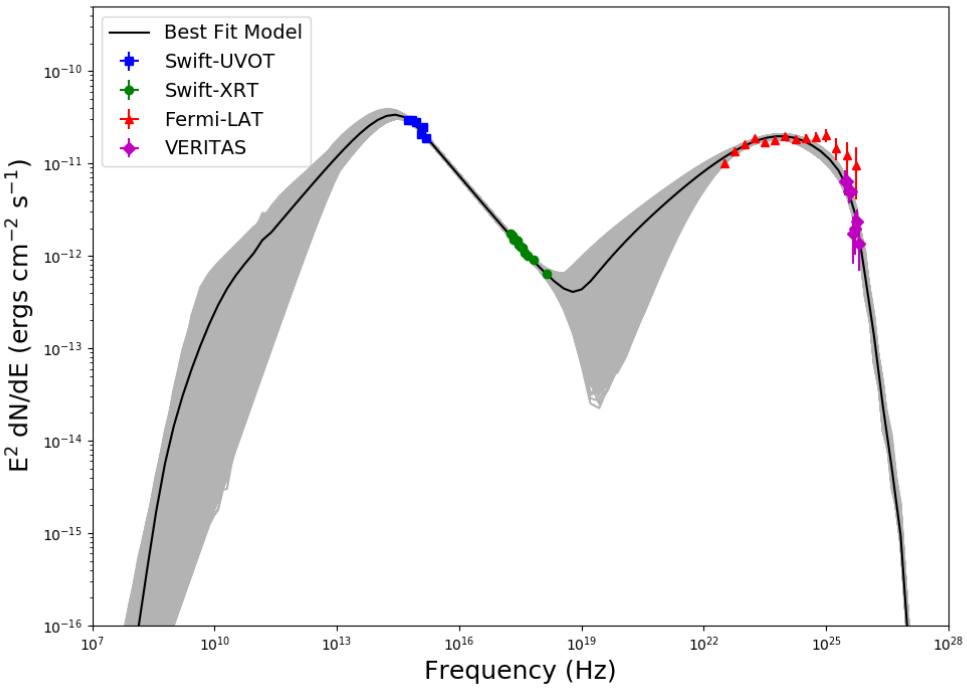

Figure 4.11: Block 6 MWL SED with the best fit SSC model shown as a black line. The grey region indicates the 1σ range of models using the parameter values detailed in Table 4.5.

4.5 Ground-Based Optical Observations

Observations of 3C 66A were taken using the 48" (1.2 m) telescope at FLWO on Mt. Hopkins beginning in October of 2012. The light curve is shown in Fig. 4.5. Four filters were used, r, i, Harris B (HB) and Harris V (HV), with central wavelengths of 0.623, 0.764, 0.440 and 0.550 μm, respectively. In an effort to remove abnormal observations (due to e.g. poor observing conditions), check stars are used at the FLWO in the blazar observation program. Data are removed solely based on check star magnitude and error. If a check star magnitude or its error is more than 3σ from the mean of the dataset, the data taken coincident with that observation are removed. This process is iterated twice to achieve the final, accepted dataset.

Data taken at the Tuorla Observatory in the Cousins R-band are shown in Figs. 4.5 and 4.6. The values are corrected for Galactic absorption and host galaxy flux. No data are available during the May 2009 outburst seen by *Fermi*-LAT.

4.6 SED Modeling

The previously modeled SED published in a VERITAS collaboration paper showed that both a pure SSC model and an SSC+EC model using an external near-infrared radiation for the source of Compton scattering fit the observations Abdo et al. (2011). These models assumed an injected electron spectrum described by a single power law with index, α. However, the pure SSC model required a large emitting region which was inconsistent with the variability timescale of $\sim$4 hours observed in the optical band on MJD 54747. The SSC+EC scenario was able to reproduce the SED and was consistent with observed variability. Table 4.4 summarizes the modeling results from Abdo et al. (2011) for comparison.

Table 4.4: Previous SED modeling results for 3C 66A from Abdo et al. (2011). Both models use a redshift of z=0.3 and are fit to a multiwavelength SED that uses data from 2008.

Parameter	SSC	SSC+EC
Low-energy cutoff, γ_{min}	2.2×10^4	6.5×10^3
High-energy cutoff, γ_{max}	4.0×10^5	1.5×10^5
Injection index, α	3.0	3.0
Injection luminosity, L_e (10^{45} erg s^{-1})	5.7	0.6
Comoving magnetic field, B (G)	0.02	0.21
Poynting flux, L_B (10^{43} erg s^{-1})	0.85	6.0
$\epsilon_B \equiv L_B/L_e$	1.5×10^{-3}	0.10
Doppler factor, δ	40	40
Plasmoid radius, R_B (10^{16} cm)	7.0	1.5
Variability time scale	21.1 hrs	4.5 hrs
Ext. radiation energy density (10^{-6} erg cm^{-3})	n/a	1.2

4.6.1 SSC Model Fit with an MCMC

To model each SED, we start with a single-zone, purely leptonic SSC emission model based on Katarzyński et al. (2001). The region is injected with a broken power law distribution of particle energies described by indices α_1, and α_2 with the break occurring at γ_{break}. The low- and high-energy cutoffs of the distribution are given by γ_{min} and γ_{max}, respectively. Normalization of the spectrum is given by K, and is evaluated at γ=1.0. The size of the emitting region is given by R, the strength of the magnetic field by B and the Doppler factor by δ. Additional details of the SSC model can be found in Chapter 3. We use a redshift of z=0.34, which is just higher than the lower bound for this source and consistent with Torres-Zafra et al. (2018). EBL absorption is accounted for using the model from Franceschini et al. (2008). We use a Markov Chain Monte Carlo (MCMC) technique implemented in Python by the `emcee` package (Foreman-Mackey et al., 2013b) to fit each SED as detailed in Chapter 3. A huge benefit to this technique is the ability to derive statistical uncertainties on each parameter that is fit. This

is useful in determining the significance of any change of parameters as well as determining uncertainties on derived quantities such as the variability timescale and distance from the base of the jet. Using this technique, we ran an MCMC using 300 walkers for 3000 steps on the SEDs generated in blocks 1, 2, 5 and 6 with an assumed redshift of z=0.34. The results for the best fit values of each parameter are shown in Table 4.5 and the evolution of the parameters from each block is shown in Figure 4.13. Figures 4.8, 4.9, 4.10 and 4.11 show the data along with the best fit SSC model in each block, and Figure 4.14 shows the best fit SSC models for all blocks overlaid. All SEDs are well explained using the purely leptonic, single-zone emission model except for block 6 which has a p-value of 5.6 $\times 10^{-16}$. For all blocks, we are not able to constrain the 1σ bounds of K, δ or γ_{min} well using this technique. The lack of constraint on K could partly be due to the fact that the normalization of the electron energy spectrum at $\gamma = 1$ is highly susceptible to small changes in α_1 and γ_{break}. Even though the normalization is not constrained well, the resulting electron spectrum appears to be well contained as shown in Figure 4.12.

There is no constraint on the allowed variability built into the MCMC, but we can compare the fitted parameter values to observations from the light curve. The smallest observed variability, Δt_{min}, is related to the diameter of the emitting region, D, by $D \leq \delta c \Delta t_{min}/(1+z)$. Given the values of R and δ for each model used in the fitting, we can therefore calculate a permissible value of Δt_{min} for every SED. Table 4.6 shows Δt_{min} for the best fit model in each block as well as the smallest Δt_{min} value for both the 1σ and 2σ sets of models. There is no observed VERITAS or *Fermi*-LAT flux change greater than 3σ within any of the blocks. The observation with fast variability on the timescale of $\sim$4 hours from Abdo et al. (2011) falls within the time period of block 2, and allows for a region size

Table 4.5: Fitted SSC Parameter Values with their 1σ uncertainties. The reduced χ^2 is given for each best fit model. Dates for each block are defined in Table 4.3. The SSC model used here is a single-zone, purely leptonic model.

Parameter	Block 1	Block 2	Block 5	Block 6
log R [cm]	$17.7^{+0.5}_{-1.3}$	$17.0^{+0.6}_{-0.6}$	$18.6^{+0.3}_{-0.6}$	$18.4^{+0.3}_{-0.7}$
log B [G]	$-2.6^{+0.7}_{-0.6}$	$-2.2^{+0.4}_{-0.3}$	$-2.9^{+0.3}_{-0.5}$	$-2.8^{+0.3}_{-0.4}$
δ	$48.1^{+50.6}_{-14.2}$	$57.5^{+41.2}_{-19.4}$	$32.1^{+41.3}_{-3.0}$	$27.9^{+27.8}_{-1.4}$
α_1	$2.1^{+0.9}_{-0.7}$	$2.2^{+0.6}_{-0.8}$	$2.1^{+0.2}_{-0.3}$	$1.9^{+0.6}_{-0.3}$
α_2	$3.7^{+0.2}_{-0.1}$	$3.9^{+0.1}_{-0.1}$	$4.4^{+0.2}_{-0.1}$	$4.04^{+0.04}_{-0.03}$
log K [cm^{-3}]	$2.0^{+4.7}_{-2.00}$	$3.6^{+2.7}_{-2.6}$	$0.6^{+0.9}_{-0.6}$	$0.5^{+3.1}_{-0.5}$
log γ_{min}	$1.6^{+2.4}_{-1.6}$	$3.2^{+0.6}_{-3.1}$	$1.1^{+2.5}_{-1.1}$	$2.5^{+1.5}_{-2.5}$
log γ_{break}	$4.6^{+0.3}_{-0.4}$	$4.5^{+0.3}_{-0.2}$	$4.8\ ^{+0.1}_{-0.2}$	$4.7^{+0.1}_{-0.2}$
log γ_{max}	$6.2^{+1.8}_{-0.5}$	$6.1^{+0.4}_{-0.4}$	$7.6^{+0.4}_{-1.4}$	$6.7^{+1.3}_{-0.4}$
Reduced χ^2	1.42	2.04	2.23	4.55
p-value	9.7×10^{-2}	4.1×10^{-3}	1.3×10^{-4}	5.6×10^{-16}

that falls within the $\sim 2\sigma$ bound of that determined by our SED fit, as detailed in Table 4.6.

Table 4.6: Variability timescales consistent with the SED fit results for each block. The 1σ and 2σ values are determined by taking the minimum Δt_{min} from the ensemble of models falling within the prescribed confidence range.

Block	Best Fit	1σ	2σ
1	11.1 days	6.9 hours	5.8 hours
2	1.9 days	7.1 hours	4.8 hours
5	140.3 days	15.6 days	12.8 days
6	95.6 days	10.1 days	9.5 days

There is also no constraint on the second slope of the injected electron spectrum, α_2, based on the X-ray analysis as detailed in Section 3.1. We can compare the slope resulting from the MCMC fit to that found in the XRT analysis. These are detailed in Table 4.7. The α_2 values determined from the MCMC are consistent with those given by the X-ray results within 2σ for blocks 1, 5 and 6. There is more tension with the slopes determined in block 2, though the best fit SED

begins to soften at the highest energies of the X-ray observations. This is consistent with the spectrum describing only the X-ray data (as found by the XRT analysis) having a steeper index than that determined by the full MCMC fit.

Table 4.7: Indices of the X-ray spectra fitted from the XRT analysis, Γ_{XRT}. For each block we also compute the implied constraints on the second slope in the injected electron spectrum, $\alpha_{2,XRT}$. The slope from the MCMC fit, $\alpha_{2,MCMC}$, is also listed for direct comparison. The uncertainties listed are the 1σ bounds.

Block	Γ_{XRT}	$\alpha_{2,XRT}$	$\alpha_{2,MCMC}$
1	2.66 $\pm$0.13	4.32 $\pm$ 0.26	$3.7^{+0.2}_{-0.1}$
2	2.78 $\pm$0.06	4.56 $\pm$ 0.13	$3.9^{+0.1}_{-0.1}$
5	2.53 $\pm$0.13	4.06 $\pm$ 0.27	$4.4^{+0.2}_{-0.1}$
6	2.62 $\pm$0.04	4.24 $\pm$ 0.08	$4.04^{+0.04}_{-0.03}$

There are both differences and similarities between the modeling results from the previous VERITAS collaboration paper (Abdo et al., 2011) and these results. For comparison, we use the results from the modeling of the SED in block 2 since it overlaps the most in time. The previous results used observations taken in a slightly different time period than block 2, and the SED fitting was not done separately for the full time period (called *darkrun*) and the observed VHE high state from MJD 54747-54749. Specifically, the darkrun time period of MJD 54734-54749 was used which encompasses the VHE flare and begins a few days before block 2 (block 2 is MJD 54742-54749). We find a larger radius, a smaller magnetic field and a larger Doppler factor, though all three are consistent within 1σ of the previous modeling results. The main difference in the modeling is the shape of the injected electron spectrum; Abdo et al. (2011) uses a single power law, while we use a broken power law. Though the index of 3.0 used by the previous results is in between the best-fit values of α_1 and α_2 determined here, it is not within the 1σ range for either index. The electron energies that we use extend both lower and higher than those used in the previous results. Finally, the variability timescale

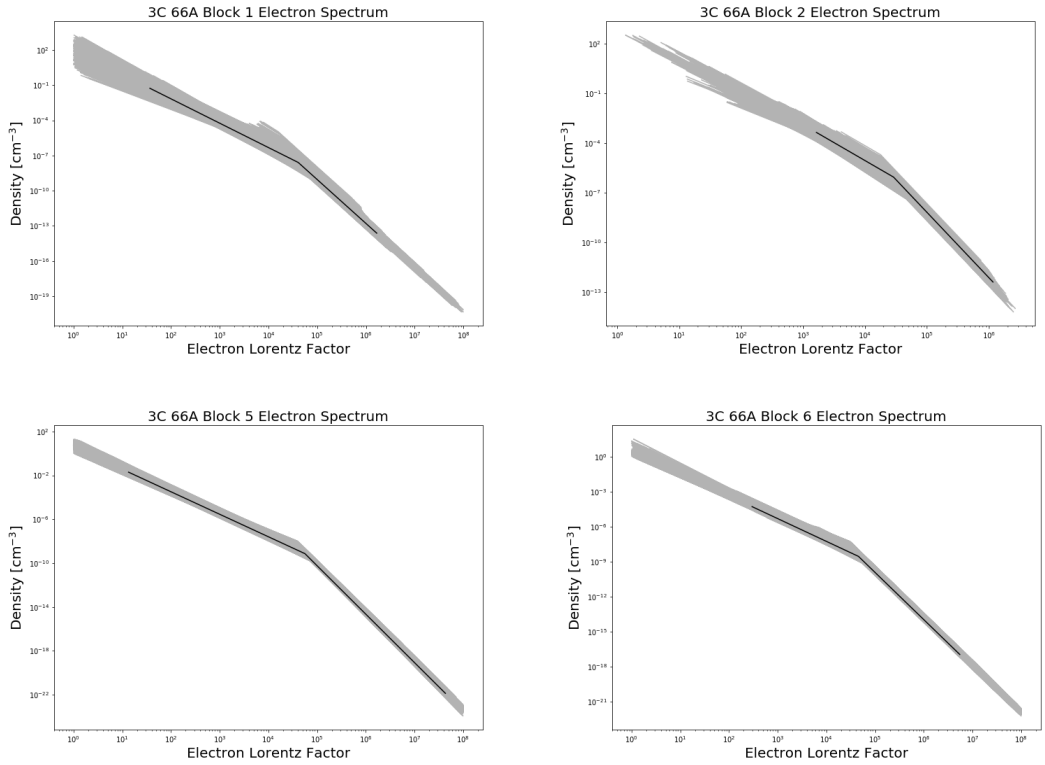

Figure 4.12: Electron spectra resulting from the MCMC fit to each blocks' multiwavelength SED. The best fit spectrum is shown as a black line, and the spectra associated with SED models falling within 1σ of the best fit are shown in grey.

determined by the MCMC fitting is comparable to that in the previous results; however, the uncertainty bounds allow us to calculate a 2σ limit on the variability timescale that is much lower than the best fit at 4.82 hours.

To understand the geometry of the jet, we can use the fitted region size combined with the apparent opening angle of 41.6° for 3C 66A (Hervet et al., 2016) to determine how far the emitting region is from the base of the jet. With our assumed line of sight angle (see Section 3.3), $\theta = 0.57°$, we obtain an intrinsic jet opening angle of $\eta = \eta_{apparent} \sin\theta = 0.41°$. Assuming a conical jet, this puts the region 47^{+102}_{-41} pc from the base of the jet for block 1, 10^{+25}_{-7} pc for block 2, 395^{+352}_{-302} pc for block 5 and 233^{+183}_{-185} pc for block 6. This is suggestive of two separate emitting regions: one closer to the base of the jet and dominant during the higher flux states (blocks 1 & 2) and one farther from the base of the jet that is dominant during the later, quiescent states (blocks 5 & 6). Using data from *Fermi*-LAT as well as photometric and polarization observations from the Kanata telescopes, Itoh et al. (2013) find evidence that might also be explained by the presence of two different emission components. One is dominant in 2008, and the other in 2009-2010; these correspond to blocks 1 &2 and block 5 in this work which would make the suggestive evidence consistent.

4.7 Signatures of UHECRs

Given the strong VHE signal from this moderate redshift blazar, it appears to be a good candidate to look for signatures of secondary gamma rays that are the result of UHECRs interacting with photon fields along the line of sight. Essey and Kusenko (2010) suggest that the MAGIC detection of 3C 66B could be the result of a burst of cosmic rays originating in 3C 66A, but with a trajectory bent by the magnetic fields of 3C 66B. The secondary photons at VHE produced by

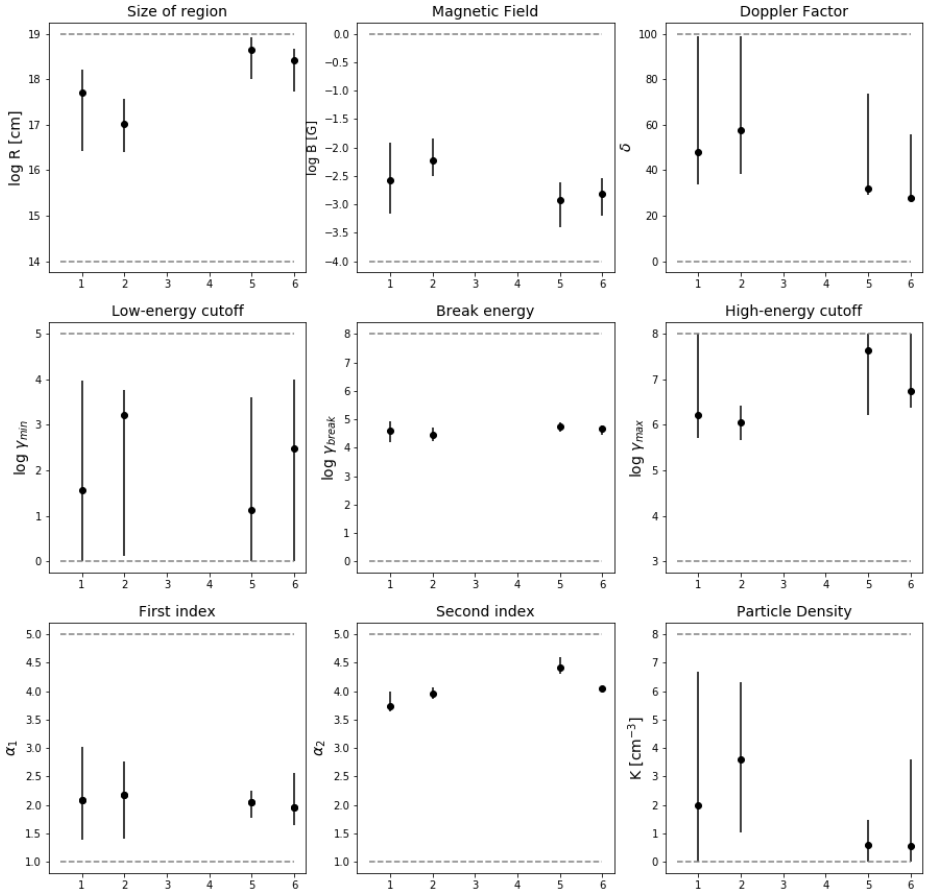

Figure 4.13: Evolution of the fitted MCMC parameter values and their 1σ ranges. The horizontal axis indicates the block of each SED. Dashed lines indicate the bounds built into the MCMC for each parameter.

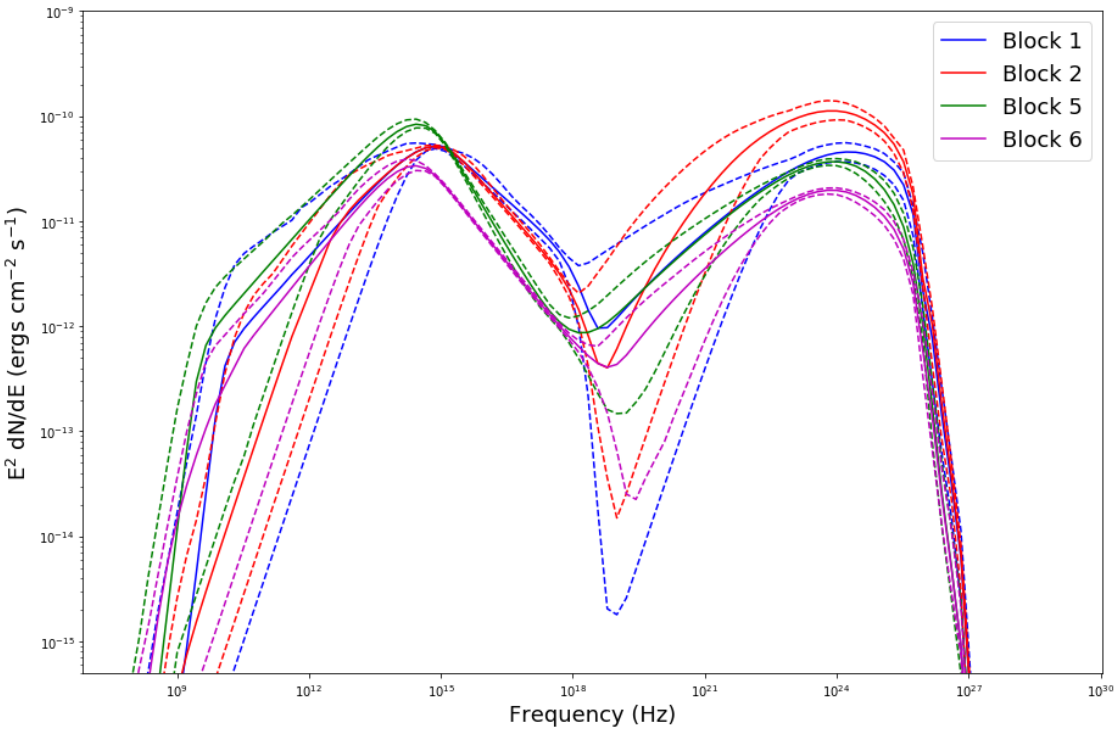

Figure 4.14: Best-fit SSC models for every 3C 66A SED modeled. The best fit model for each block is shown with a solid line, and the 1σ regions are shown in dashed lines.

these cosmic rays during a period of high flux would point back to 3C 66B. Thus, it is important for understanding line-of-sight processes to examine the location of the VHE emission during both high and quiescent flux states. As shown in Section 4.2.3, there is very little evidence for VHE emission from 3C 66B during any of the flux states observed by VERITAS or the full dataset. Based on the location of the gamma-ray excess, there is no evidence of secondary gamma rays from 3C 66B resulting from UHECRs in the jet of 3C 66A.

The VHE spectra can also hold signatures of evidence from secondary gamma rays. Anomalies in the deabsorbed VHE spectra can indicate a secondary gamma-ray component. Specifically, an uptick at the highest energies could indicate that too much EBL absorption has been removed; this results when VHE emission comes from a closer distance along the line of sight as it would in the case of UHECRs from the blazar producing gamma rays while propagating through the Universe. As seen in Figure 4.2, all deabsorbed spectra are consistent with a power-law fit and the highest energy data points are not higher than the fitted function by more than 1σ. The VHE high flux state spectrum is not shown, but there is also no evidence for an uptick at the highest energies.

Finally, the multiwavelength SEDs modeled in Section 4.6 are well-fit with a leptonic scenario. There is no need for any complex hadronic emission scenarios to explain these spectra, so there is therefore no good motivation to search for observable contribution from UHECRs. Though this moderate redshift blazar appeared to be a good candidate to look for a secondary component of gamma rays from UHECRs, upon investigation there is no need for such a component to explain the data. As in the investigation of gamma-ray production in the jet itself, it is pertinent to consider time averaging effects in the spectra when searching for spectral anomalies. Averaging VHE observations taken in different flux states and

different observing conditions can produce unphysical anomalies. The hunt for the source of UHECRs continues and is not solved by these observations from 3C 66A, though future observations with better sensitivity might prove this source still a viable candidate.

4.8 Acknowledgments

The *Swift*-UVOT analysis presented in this chapter was completed by Karlen Shahinyan, and the reduction of the FLWO optical data was completed by Piatra Pontrelli. The work presented in this chapter is largely based on a VERITAS collaboration journal article in preparation led by the author. Members of the VERITAS collaboration have contributed to the text.

Chapter 5

Spectral Line Monitoring in VHE blazars

5.1 Introduction

Understanding blazar physics requires a variety of observations taken in multiple wavebands. Photometric observations, spectroscopy and polarization data can be combined to explore the multiple facets of AGN. One of the most useful tools in understanding jet emission is the study of time variability and the search for correlations between observations in different bands. Logistically, these studies are difficult since they require the coordination of many ground- and space-based telescopes that have different observing constraints and demands for telescope time. To explore the role of the broad line region (BLR) and the location of the emission region in the jet, we can look for correlations in variability of the BLR spectral features with gamma-ray observations. Optical spectra of blazars are dominated by the non-thermal continuum emission from the jet, yet there can still be spectral features from the host galaxy or BLR present. By taking monthly

optical spectra of selected high-energy and VHE-detected blazars and comparing the emission line fluxes to gamma-ray observations taken by VERITAS and *Fermi*-LAT, we can attempt to search for such a connection.

The study of emission line variability in blazars has historically shown mixed results. Two examples are PKS 1221+216 and 3C 454.3. During observations taken in 2009-2011, PKS 1221+216 did not exhibit significant variability in its Mg II, Hβ, Hγ and Balmer emission line fluxes, even though the optical continuum and gamma-ray emission seen by the LAT vary dramatically. These results suggest that in PKS 1222+216, the variable, relativistic jet has little influence on the output of the broad line region. This could be because the non-thermal emission ionizes very little of the line-emitting gas in the BLR, or the non-thermal emitting region is located far enough out in the jet to not interact with the BLR (Smith et al., 2011). This also implies that the source of the ionizing flux in the BLR is relatively constant. On the other hand, 3C 454.3 has been shown to have emission line variation associated with changes in the gamma-ray emission seen by the LAT. During a December, 2009 gamma-ray flare of this blazar, there was an associated increase in the Mg II and Hγ line flux. However, in that same study, an April 2010 gamma-ray flare showed no associated line variability in any of the observed lines. This could indicate different mechanisms generating each flare, or different emitting regions located at different distances away from the BLR (Isler et al., 2013). Clearly, studying the variability of emission lines and their coinciding gamma-ray flux is a way to shed light on blazar flare mechanisms and the connection between the jet and its surrounding environment. Continual observations of these sources are necessary since variability patterns can exhibit differing behaviors even in the same source.

Very few blazars have been studied this way, and obtaining the necessary

contemporaneous multiwavelength data is logistically difficult. By increasing the sample size and waveband coverage in this study, we can further expand on the processes driving blazar flares and emission line variability. A study of this type has never been conducted using VHE data, so these results can help guide future efforts at observatories such as the Cherenkov Telescope Array.

5.2 Sources

We chose sources which are bright and variable in gamma rays, that were observed by VERITAS at least once per moon cycle during 2016 and have absorption or emission features previously observed at optical wavelengths. Since these sources are northern hemisphere sources observable by VERITAS, they are also observable at Lick Observatory. These selection criteria result in the five blazars studied here: Markarian 421, Markarian 501, 3C 279, PKS 1441+25 and PKS 1222+216. To characterize how variable a source's gamma-ray flux might be during this study, we can quantify each source's previously observed variability by its variability index published in the Third Fermi Large Area Telescope Catalog (3FGL) (Acero et al., 2015). The variability index quantifies variability on the timescale of months, and an index >72.44 indicates a >99% confidence probability that the source is variable. Each source has a variability index >200 except for PKS 1441+25 which has an index of ∼48. The 3FGL only includes LAT data taken through July, 2012, and PKS 1441+25 underwent two gamma-ray outbursts in 2015 (Abeysekara et al., 2015). Therefore, despite its small variability index in the 3FGL catalog, PKS 1441+25 has exhibited observed gamma-ray variability in the past.

Figure 5.1: Optical spectrum of PKS 1441+25 taken by the Sloan Digital Sky Survey (SDSS). The strong emission feature at 5500 Angstroms is Mg II emission (vacuum wavelength of 2799 Angstroms). Figure reproduced from `http://skyserver.sdss.org/dr10/en/get/SpecById.ashx?id=6780257851631206400`.

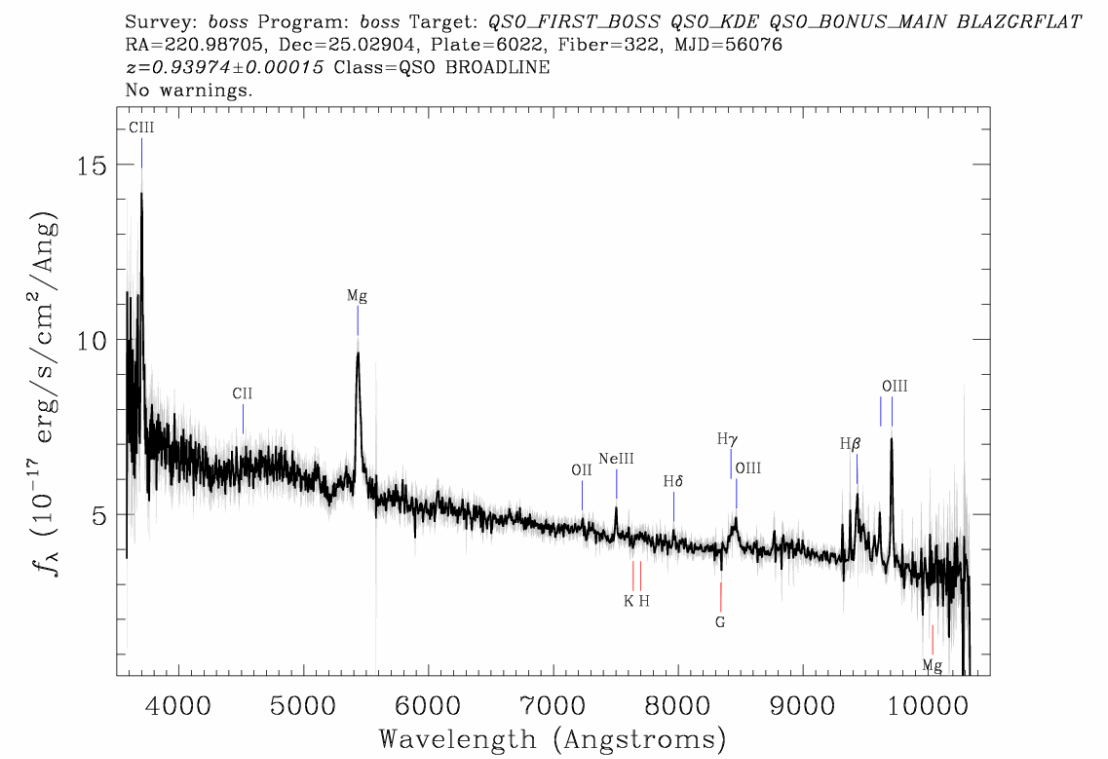

5.2.1 PKS 1441+25

PKS 1441+25 is an FSRQ at a redshift of z=0.940, and it was detected at VHE by VERITAS and MAGIC in April, 2015 (Ahnen et al., 2015; Abeysekara et al., 2015). An optical spectrum taken by the Sloan Digital Sky Survey (SDSS) in May, 2012 (MJD 56076) is shown in Fig. 5.1. This spectrum shows several prominent features at z=0.93974 ± 0.00015 including Mg II, C III, Hγ, Hβ, and O III.[1]

[1] `https://dr10.sdss.org/spectrumDetail?mjd=56076&fiber=322&plateid=6022`

5.2.2 PKS 1222+216

PKS 1222+216 (also known as 4C +21.35) is an FSRQ at a redshift of z=0.432. MAGIC discovered VHE emission from this source during an outburst in 2010, and VERITAS detected it in March, 2014 (M. Cerruti M. for the VERITAS Collaboration, 2015). Previously observed spectral features include Mg II, Hδ, Hγ and Hβ (Smith et al., 2011).

5.2.3 3C 279

3C 279 is an FSRQ at a redshift of z=0.5362 $\pm$ 0.0004 (Marziani et al., 1996). It has been widely studied for several decades, and it exhibits extreme variability across all observed wavebands. MAGIC originally discovered VHE emission from 3C 279 during a flare in 2006, but VERITAS has no published detection of this source (Errando et al., 2008). Between 2007 and 2012, VERITAS took an 8.3 hour exposure on this source triggered by flaring activity at lower wavelengths which resulted in a flux upper limit of 2.1% Crab Nebula flux above 260 GeV (Archambault et al., 2016).

5.2.4 Markarian 421

Markrian (Mrk) 421 is a BL Lac at z=0.031 and was the first extragalactic source detected at TeV energies (Punch et al., 1992). As a BL Lac, it has weak spectral features and does not immediately seem to be a good candidate for this study; however, any detection of strong emission lines regardless of its flux state would be an interesting result for this HSP blazar.

5.2.5 Markarian 501

Mrk 501 is an HSP blazar at a redshift of z=0.034. Similar to Mrk 421, it is one of the strongest extragalactic gamma-ray emitters. It has weak spectral features, so any detection of an increase in its spectral features would be scientifically interesting.

5.3 Observations

Each optical spectrum was taken at Lick Observatory with the Shane 3m telescope except for one spectrum taken at the W. M. Keck Observatory in April of 2015. Through the 2016A, 2016B and 2017A proposal cycles, this project was awarded 23 nights of telescope time with the Shane. These proposals resulted in observations taken on 19 nights after poor weather is taken into account. In the 2017B and 2018A semesters, we proposed target of opportunity (ToO) observations instead of monthly monitoring. Triggering this proposal resulted in 6 spectra. Not all spectra taken during this program are shown in this chapter; see Section 5.4 for details on data selection. Summaries of the observations included in this chapter for each blazar are available in Tables 5.1, 5.2, 5.3, 5.4 and 5.5.

The instrument on the Shane 3m used in this project is the Kast Spectrograph. Kast is a dual-armed spectrograph which splits the light into a "red" side and a "blue" side. A dichroic, which selectively passes or reflects light based on a crossover wavelength, is inserted into the path of the light to split the beam. The d55 dichroic splits the light at about 5500 Angstroms, and the d46 splits at about 4650 Angstorms. The dichroic affects ∼200 Angstroms near the crossover wavelength. A new dichroic with a splitting wavelength of roughly 5700 Angstroms was installed in October, 2016. Mrk 421, Mrk 501, PKS 1222+216 and 3C 279 were all

observed using the d57 or d55 dichroic. Strong Mg II emission from PKS 1441+25 occurs near the crossover of the d55 and d57 dichroics, so we can use the d46 to avoid splitting near this scientifically interesting portion of the spectrum. PKS 1441+25 was observed using the d46 dichroic as often as possible, though due to observing constraints, a few spectra were not taken with this dichroic. Table 5.3 lists which dichroic was used for each spectrum.

Table 5.1: Summary of Kast Observations for Mrk 421. All observations were taken with the d55 dichroic. The S/N is the average S/N per pixel. For the blue side this is between 3400 and 5400 Angstroms. For the red side this is between 5600 and 6800 Angstroms.

Obs. Date Local (YYYY-MM-DD)	Obs. Date UTC (MJD)	Obs. Type	Exposure (s)	S/N (blue/red)
2016-02-11	57430	Awarded	1800	179.9/219.7
2016-02-12	57431	Awarded	3600	254.0/318.4
2016-03-17	57465	Awarded	3600	235.3/309.7
2016-04-03	57482	Awarded	3600	259.3/331.9
2016-04-04	57483	Awarded	3600	231.9/321.0
2016-06-08	57548	Awarded	1800	224.4/593.7
2016-06-11	57551	ToO	1800	183.8/258.6
2016-06-12	57552	ToO	1800	169.2/239.9

Table 5.2: Summary of Kast Observations for Mrk 501. All observations were taken with the d55 dichroic. The S/N is the average S/N per pixel. For the blue side this is between 3400 and 5400 Angstroms. For the red side this is between 5600 and 6800 Angstroms. All observations were taken on awarded observing nights.

Local Obs. Date (YYYY-MM-DD)	Obs. Date UTC (MJD)	Exposure (s)	S/N (blue/red)
2016-02-11	57430	2100	57.5/126.4
2016-04-03	57482	4800	144.9/300.2
2016-06-08	57548	3600	167.0/546.9
2016-06-29	57569	3600	174.8/293.6
2016-08-04	57605	3600	179.0/310.9
2016-09-05	57637	1800	116.8/372.4

Table 5.3: Summary of Kast Observations for PKS 1441+25. The S/N is the average S/N per pixel. For observations with the d55 dichroic on the blue side this is between 3400 and 5400 Angstroms, and the red side is between 5600 and 6800 Angstroms. For observations with the d46 dichroic on the blue side this is between 3400 and 4500 Angstroms, and the red side is between 4700 and 6800 Angstroms. All observations were taken on awarded observing nights.

Local Obs. Date (YYYY-MM-DD)	Obs. Date UTC (MJD)	Dichroic	Exposure (s)	S/N (blue/red)
2015-06-20	57194	d55	5400	55.1/162.5
2015-07-20	57224	d55	3600	12.6/37.9
2015-07-21	57225	d46	3600	1.8/9.9
2016-02-11	57430	d46	3600	2.2/8.5
2016-02-12	57431	d46	1800	17.2/n/a
2016-03-17	57465	d46	5400	3.8/20.5
2016-04-03	57482	d55	2163	4.3/10.1
2016-04-04	57483	d46	5400	4.7/27.5
2016-06-08	57548	d46	5400	11.5/62.1
2016-06-29	57569	d46	3600	7.7/42.8

5.4 Data Reduction

Observations taken with Kast can be reduced using two packages: the Low-Redux Pipeline [2] and PypeIt [3]. Low-Redux is written in IDL, and PyPit is written in Python. In September of 2016, the CCD on the red side of Kast was replaced with a new Hamamatsu detector. The Low-Redux pipeline does not support reduction of the data taken with this new CCD, so PyPit must be used for spectra taken in September 2016 and later. PyPit is still currently under development, so observations taken after September 18th, 2016 (MJD 57650) are not included here. Researchers at UCSC will continue this work in the future by incorporating these later spectra.

Since exact flux measurements are important and necessary for this project, care must be taken when converting the observed CCD counts to flux (also called

[2]http://www.ucolick.org/ xavier/LowRedux/
[3]https://github.com/pypeit/PypeIt

Table 5.4: Summary of Kast Observations for PKS 1222+216. All observations were taken with the d55 dichroic. The S/N is the average S/N per pixel. For the blue side this is between 3400 and 5400 Angstroms. For the red side this is between 5600 and 7500 Angstroms. All observations were taken on awarded observing nights.

Local Obs. Date (YYYY-MM-DD)	Obs. Date UTC (MJD)	Exposure (s)	S/N (blue/red)
2016-02-11	57430	3600	85.4/164.2
2016-02-12	57431	3600	93.3/181.2
2016-03-17	57465	3600	60.2/121.8
2016-04-03	57482	3600	36.4/74.9
2016-04-04	57483	3600	101.1/180.7
2016-06-08	57548	3600	117.2/262.0

Table 5.5: Summary of Kast Observations for 3C 279. All observations were taken with the d55 dichroic. The S/N is the average S/N per pixel. For the blue side this is between 3400 and 5400 Angstroms. For the red side this is between 5600 and 6800 Angstroms. All observations were taken on awarded observing nights.

Local Obs. Date (YYYY-MM-DD)	Obs. Date UTC (MJD)	Exposure (s)	S/N (blue/red)
2016-02-12	57431	3600	84.2/198.5
2016-03-17	57465	3600	77.2/232.5
2016-04-03	57482	3600	86.6/207.4
2016-04-04	57483	3600	86.7/185.9

"fluxing"). A standard star is used to make this conversion. Standards are stars that have been observed with high accuracy in order to precisely calculate their flux in particular wave bands. They serve several purposes in the calibration of spectra. First, they remove any wavelength dependent change in sensitivity across the CCD in a way that flat fielding images cannot. The second correction is the extinction in the sky at the observatory's site. For Mount Hamilton, this is automatically applied in the Lox-Redux software.

Finally, an aperture correction is applied which accounts for the fact that the light from a point source may be spread out enough that it is truncated by the

width and length of the slit. This means that the observed CCD counts need to be adjusted before converting them to flux; this correction factor must be applied to both the standard star and the science exposures. Generally, this is done by fitting a Gaussian to the profile of the object trace across the CCD in the direction along the slit which allows for the computation of how wide the source is spread. Given the geometry of the slit, it is therefore straight forward to calculate the fraction of light contained within the slit. Correcting for this effect boils down to a multiplicative factor in the conversion from observed CCD counts to flux.

To perform the aperture correction, a cross-section of the object trace is taken from the sky-subtracted image. See Figure 5.2. The cross-section of the trace is fit with a Gaussian function,

$$f(x) = Ne^{\frac{-(x-x_0)^2}{2\sigma^2}} \ . \tag{5.1}$$

The total light is given by integrating over the spread in two dimensions, x and y:

$$\int_{-\infty}^{+\infty} N_x e^{\frac{-(x-x_0)^2}{2\sigma_x^2}} dx \int_{-\infty}^{+\infty} N_y e^{\frac{-(y-y_0)^2}{2\sigma_y^2}} dy = N_x \sigma_x \sqrt{2\pi} \times N_y \sigma_y \sqrt{2\pi} \ . \tag{5.2}$$

Assuming a symmetric spread of light in the x and y directions, the total amount of light from the source, T, is simply

$$T = 2\pi N^2 \sigma^2 \ . \tag{5.3}$$

Using a rectangle of length l and width w, we can calculate the amount of light that falls within the slit by doing another integration of the fitted Gaussian. The slit width is 2.0 arcsec for all spectra shown here. We can convert between CCD pixels and angular size using the plate scale of each detector. The blue side

detector and new red side CCD (installed in September 2016) have a plate scale of 0.43 arcsec per pixel. The red side CCD used prior to September, 2016, and for all spectra shown here has 0.774 arcsec per pixel.[4] We assume that the origin is in the center of the slit and replace the bounds of the integrals in Equation 5.2 with our slit dimensions. Since we again assume a symmetric spread, the values for N and σ in each dimension are equal. The amount of light contained in the slit, C, is given by

$$C = N^2 \int_{-l/2}^{+l/2} e^{\frac{-(x-x_0)^2}{2\sigma^2}} dx \int_{-w/2}^{+w/2} e^{\frac{-(y-y_0)^2}{2\sigma^2}} dy \ . \tag{5.4}$$

If we assume that the source is in the center of the slit so that $x_0 = y_0 = 0$, we can use the error function to complete the integration. The light contained in the slit becomes

$$C = N^2 \sigma^2 2\pi \, \mathrm{erf}\Big(\frac{l/2}{\sigma\sqrt{2}}\Big) \, \mathrm{erf}\Big(\frac{w/2}{\sigma\sqrt{2}}\Big) \ . \tag{5.5}$$

This results in the fraction of light contained in the slit, F, to be calculated as

$$F = \frac{C}{T} = \mathrm{erf}\Big(\frac{l/2}{\sigma\sqrt{2}}\Big) \, \mathrm{erf}\Big(\frac{w/2}{\sigma\sqrt{2}}\Big) \ . \tag{5.6}$$

The average signal-to-noise (S/N) per pixel for each spectrum is computed for both the red and the blue sides of the Kast spectrograph and shown in Tables 5.1, 5.2, 5.3, 5.4 and 5.5. There is a strong telluric feature at ∼6900 Angstroms and the CCD shows fringing behavior, so the spectra for all sources except PKS 1222+216 are truncated at 6800 Angstroms. PKS 1222+216 exhibits strong Hβ emission just redward of the telluric feature at 6900 Angstroms, so the spectra of this blazar are truncated at 7500 Angstroms instead.

[4]Holden, 2018, private communication

Figure 5.2: Sample plots from the aperture correction of a 120 second long exposure using the blue side of the standard star Feige 34. Left: Two-dimensional sky-subtracted image. The wavelength of the spectrum increases from top to bottom. Top: Cross-section of the object trace taken across the CCD at pixel 1000 along with the fit to a Gaussian. Middle: The width of the Gaussian fit, σ, of the fitted Gaussian at every cross-section of the CCD. The wavelength calibration has been applied in order to demonstrate the relationship with wavelength. Bottom: Fraction of light contained at every cross-section of the CCD, shown as a function of the wavelength of the spectrum at that pixel.

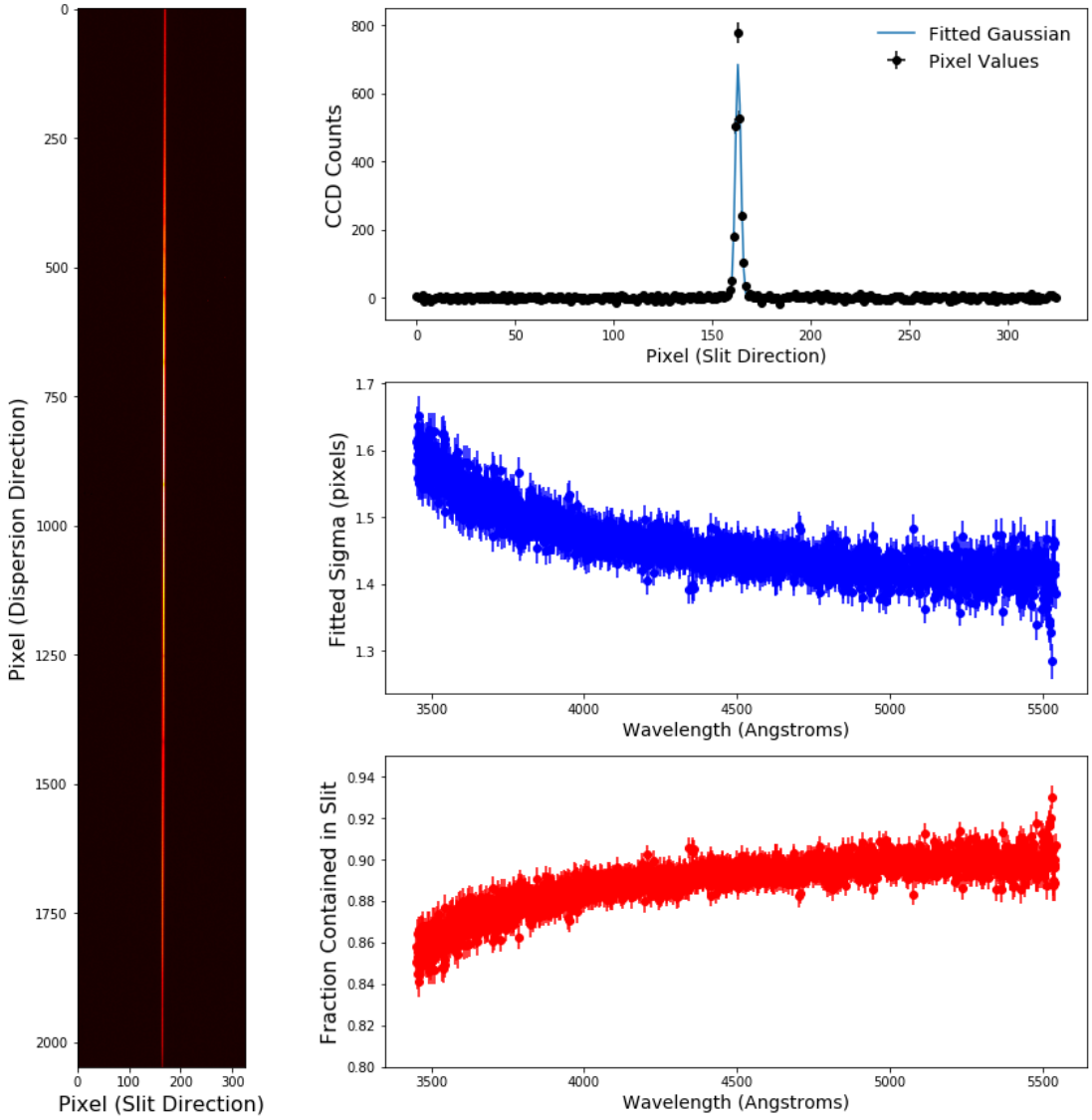

For each blazar, the VERITAS data were analyzed using VEGAS as described in Chapter 2. For 3C 279, PKS 1441+25 and PKS 1222+216 soft cuts are used, while medium cuts are used for Mrk 421 and Mrk 501. Before creating the light curve for each blazar, an analysis of the full dataset is completed; results from each source are summarized in Section 5.6. To create light curves, the datasets are broken into bins spanning the lunar month. Each dataset undergoes quality checks to ensure that no observations during poor weather or hardware malfunctions are included.

The *Fermi*-LAT data for each blazar are analyzed using v10r0p5 of the publicly available Fermi Science tools. Only events of event class "P8 SOURCE" (evclass=128) and event type "FRONT+BACK" (evtype=3) and with energies from 100 MeV to 300 GeV are used. A region with radius of 10° centered on each source location is used to spatially select events. The recommended analysis configurations for a point source as listed in the *Fermi*-LAT analysis Cicerone are used for all analyses.[5] Due to the near-constant observing cadence with the LAT, data selection is not restricted to the seasons or lunar cycles in the same way that ground-based observations are when constructing light curves. Each source has its own time selection as detailed in Section 5.6. First, an analysis in the entire frame is produced, then the dataset is broken into 28-day bins to construct the light curve. A more finely binned light curve can be created, though there must be enough statistics to produce a test statistic (TS) > 9.0 in the bins. When constructing the source model used for the likelihood analysis, sources with TS < 2 are removed and those more than 10° from the source are frozen (in the latter case these are therefore outside the region of used to select data). This is an iterative process of removing sources and checking for appropriate residual maps to generate the best source model for each region of the sky under investigation.

[5]https://fermi.gsfc.nasa.gov/ssc/data/analysis/documentation/Cicerone/

5.5 Analysis Techniques

After producing a fluxed spectrum and gamma-ray light curves, there are a few calculations useful for analyzing the data. These are defined below.

Equivalent Width: The strength of a spectral line can be measured in terms of its equivalent width (EW). If F_c is the continuum flux and F_λ is the total flux, the EW is calculated as

$$\mathrm{EW} = \int \frac{F_c - F_\lambda}{F_c} d\lambda \,, \tag{5.7}$$

where the integral is taken across the line. Before this calculation can be done, proper determination of the continuum must be made. Often this can be done by extrapolating across a spectral feature or by fitting a function to the spectrum. The EW of a line is defined as the width of a rectangle reaching up to the continuum which has the same area has the spectral line; therefore, the EW is dependent on the strength of the continuum flux. Due to the subtraction of the line's flux from from the continuum flux, emission lines have EW < 0 and absorption lines have EW > 0 (B. W. Carroll and D. A. Ostlie, 2007).

Line Flux:

The flux of an emission line is calculated by

$$F_{line} = \int F_\lambda - F_c \, d\lambda \,. \tag{5.8}$$

In the discrete case where we have a binned spectrum, this calculation becomes

$$F_{line} = \sum (F_{\lambda_i} - F_{C_i}) \Delta\lambda_i \,. \tag{5.9}$$

The uncertainty on the line flux is therefore

$$\sigma^2_{line} = \sum(\sigma^2_{\lambda_i} + \sigma^2_{C_i})\Delta\lambda^2 \,. \tag{5.10}$$

The flux of a line is not dependent on the flux of the continuum in the same way that the EW is.

Test of Variability: A basic way to test for variability of a measured value is to fit the value as a function of time with a constant, straight line. The χ^2 value of that fit can be used to rule out a non-variable behavior of that measured value. For example, we can fit a light curve (flux vs. time) to a constant to rule out constant flux.

Correlation: We will be quantifying the correlations between fluxes in different bands and the line flux of a variety of optical spectral features. For any two random variables X and Y, the correlation coefficient of these variables is defined as

$$\rho(X,Y) = \frac{\mathrm{cov}(X,Y)}{\sigma_X \sigma_Y} \tag{5.11}$$

where σ indicates the variance of the individual variable, and the covariance between X and Y is defined as

$$\mathrm{cov}(X,Y) = E[(X-\mu_x)(Y-\mu_y)] = E[XY] - E[X]E[Y] \tag{5.12}$$

where E[A] represents the expectation value of any quantity, A.

Correlation coefficients have values between -1 and +1, and random variables for which $\rho = 0$ are considered to be uncorrelated. This coefficient, often referred to as Pearson's correlation coefficient, measures the strength of a linear relationship between the variables and cannot explicitly be used to test non-linear dependencies.

5.6 Analysis & Results

5.6.1 Mrk 421

The VERITAS data for Mrk 421 were analyzed from MJD 57371 to 58237 (15 December 2015 - 29 April 2018) resulting in a live time of 48.49 hours and a total significance of 297σ. To calculate the integral flux in each bin, we use a spectral index of 2.52 and an energy threshold of 0.224 TeV. There are observations during 16 lunar months during this time period. The *Fermi*-LAT data used here span MJD 57388 - 57946 (1 January 2016 - 12 July 2017). Both gamma-ray light curves are shown in Figure 5.3. Fitting both the VERITAS and *Fermi*-LAT light curves to a constant flux results in a p-value of the fit $< 1 \times 10^{-75}$. The gamma-ray flux therefore is highly variable during the observations presented here.

There are eight spectra taken of Mrk 421 with Kast, and they are shown in Figures 5.4 and 5.5. There are weak features associated with the host galaxy (at z=0.031), but no features associated with a thermal component of the nucleus itself. This is expected given previous observations and its nature as an HSP blazar, but it unfortunately means there are no spectral features with which to conduct a correlation study.

5.6.2 Mrk 501

The VERITAS data for Mrk 501 were analyzed from MJD 57440 to 58296 (22 February 2016 - 27 June 2018) resulting in a live time of 23.88 hours and a total significance of 59σ. To calculate the integral flux in each bin, we use a power law with spectral index of 2.41 and an energy threshold of 0.158 TeV. There are observations during 12 lunar months during this time period. The *Fermi*-LAT data used here span MJD 57388 - 57958 (1 January 2016 - 24 July 2017). Both

Figure 5.3: Gamma ray light curves of Mrk 421 taken starting in 2016 as seen by VERITAS (top) and *Fermi*-LAT (bottom). The VERITAS light curve is binned in lunar months with the edges of the time bins marking the beginning and end of observations during that lunar month. The *Fermi*-LAT light curve is binned in 28-day bins represented with the bin edges. The dates with Kast observations presented here are marked with vertical dashed lines.

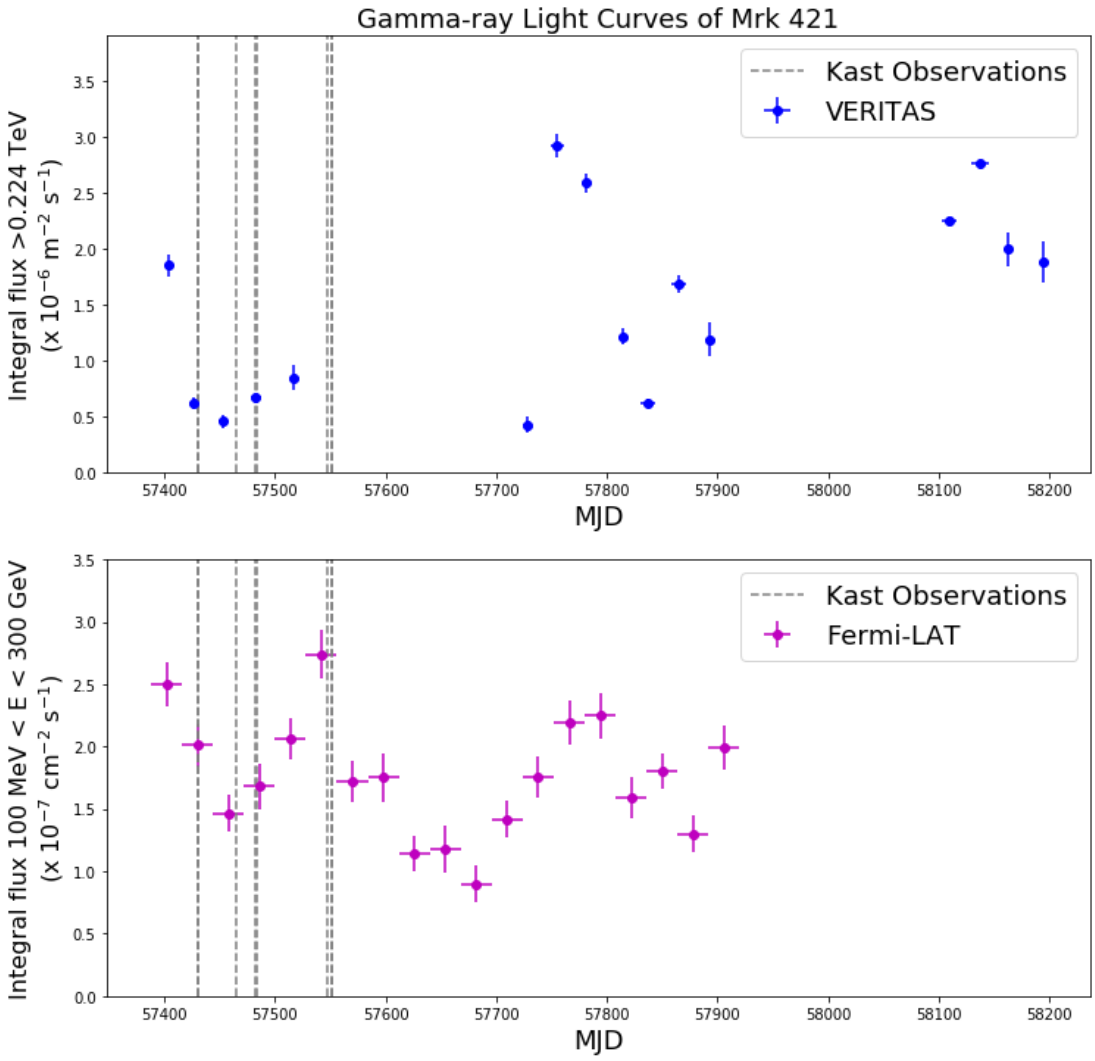

Figure 5.4: Kast spectra taken of Mrk 421 from 11 February to 3 April 2016. The black line indicates the measured flux with a smoothing function applied. The uncertainties on the flux are shown as grey lines, and and instrumental gap caused by the dichroic crossover is indicated as a rectangle from 5400 to 5600 Angstroms. Vertical lines indicate the locations of spectral features: blue indicates features at z=0.031 and light gray indicates features at z=0.0.

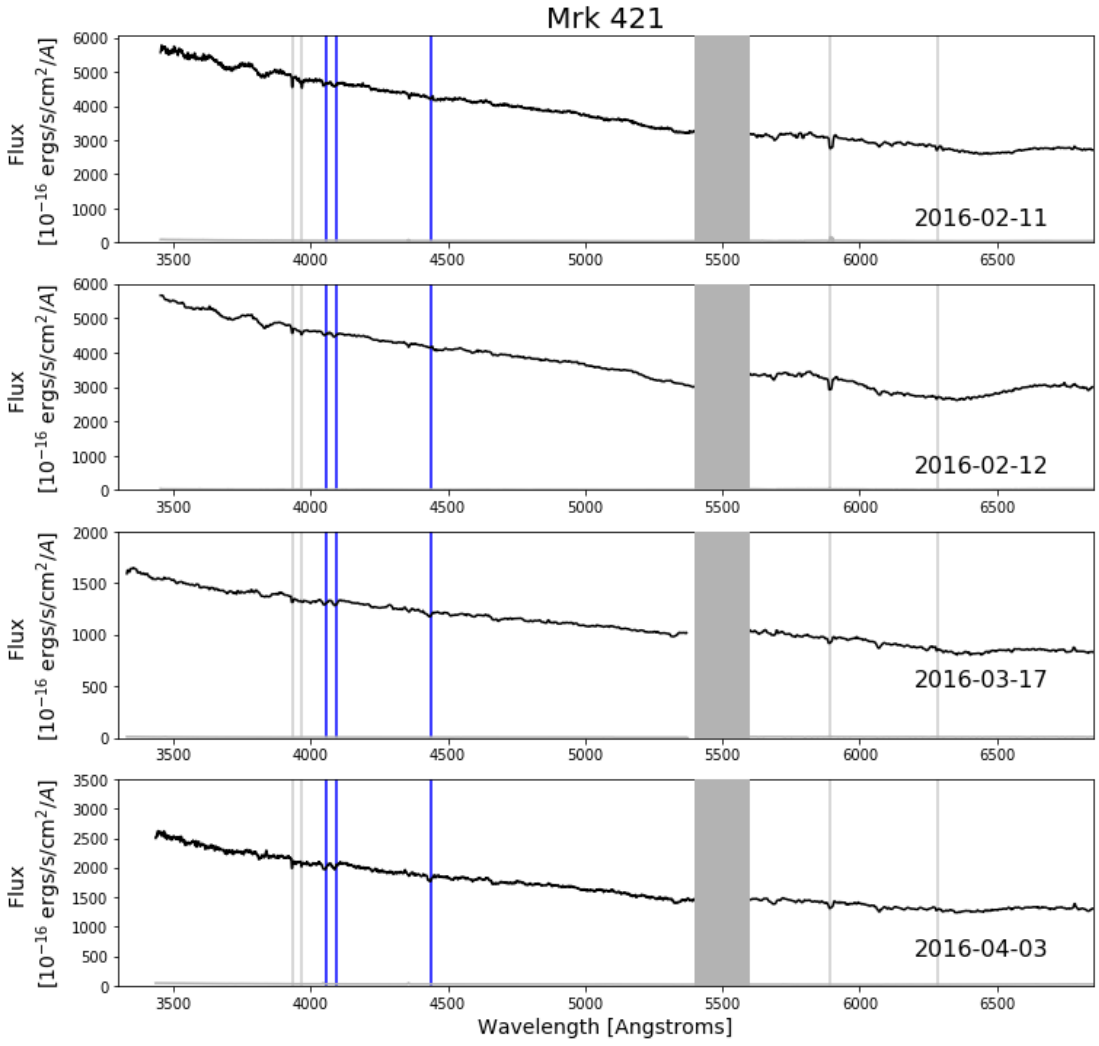

Figure 5.5: Kast spectra taken of Mrk 421 from 4 April to 12 June 2016. The black line indicates the measured flux with a smoothing function applied. The uncertainties on the flux are shown as grey lines, and and instrumental gap caused by the dichroic crossover is indicated as a rectangle from 5400 to 5600 Angstroms. The red side spectra from 11 and 12 June 2016 do not extend cover the exact same wavelength as the other spectra since they were taken as part of a target of opportunity effort and the wavelength coverage for the primary observers' setup was different than ours. Vertical lines indicate the locations of spectral features: blue indicates features at z=0.031 and light gray indicates features at z=0.0.

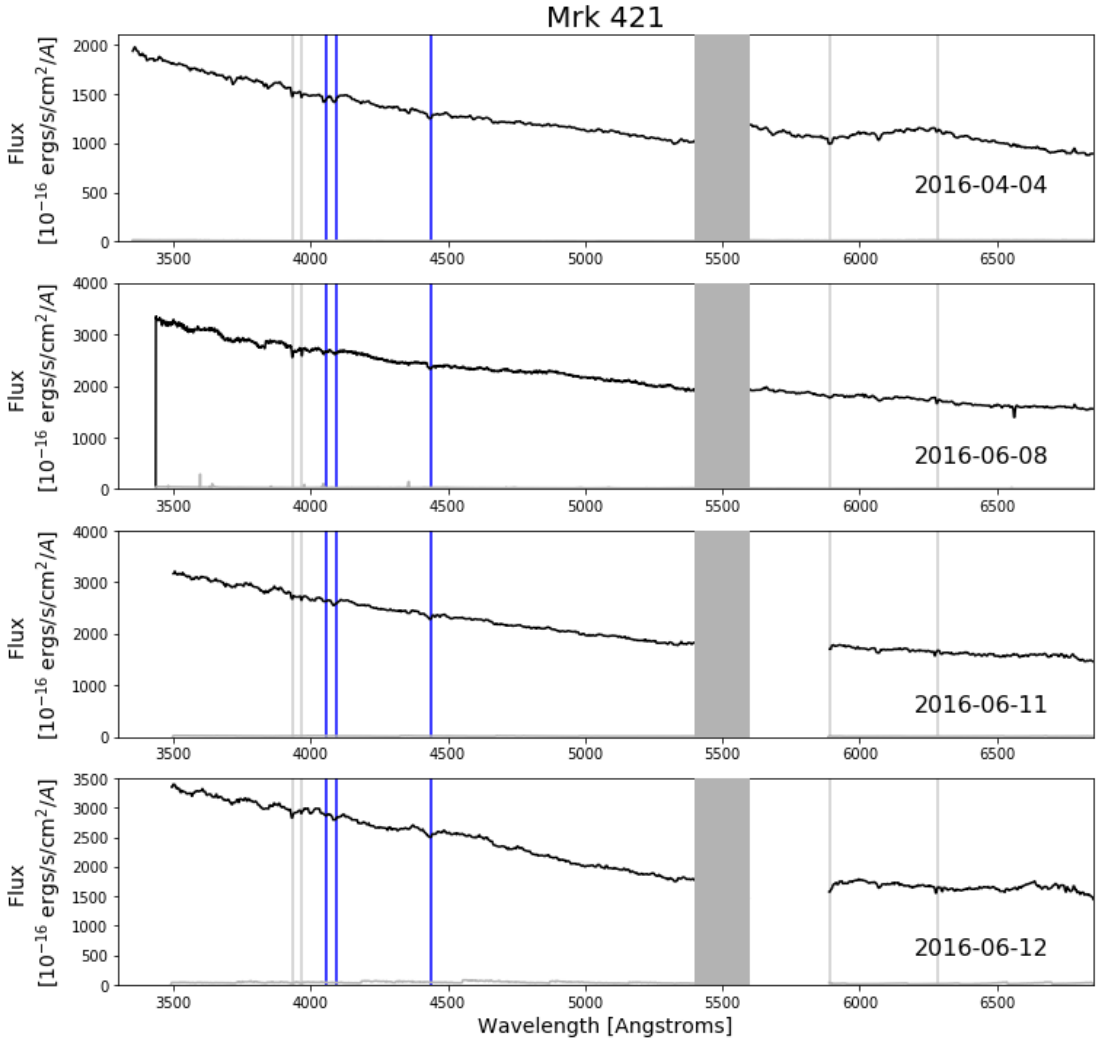

gamma-ray light curves are shown in Figure 5.6. Fitting the VERITAS light curve to a constant results in a p-value $< 1 \times 10^{-75}$, and fitting the Fermi-LAT light curve to a constant results in a p-value of 2.9×10^{-4}. Based on these tests, it is clear that the gamma-ray flux observed over these time periods from Mrk 501 is variable.

The Kast spectra taken of Mrk 501 are shown in Figure 5.7. There are several absorption features associated with the host galaxy (z=0.034), but no strong emission or absorption features definitively associated with the BLR or other thermal components of the AGN. Like Mrk 421, this is expected, and means that it is not possible to conduct any correlation studies with the variable gamma-ray light curves.

5.6.3 PKS 1441+25

The VERITAS data for PKS 1441+25 were analyzed from MJD 57116 to 58296 (4 April 2015 - 27 June 2018) resulting in a live time of 25.56 hours and a total significance of 5.9σ. To calculate the integral flux in each bin, we use an energy threshold of 0.100 TeV. There are observations during 16 lunar months during this time period. The *Fermi*-LAT data used here span MJD 57023 - 57939 (1 January 2015 - 5 July 2017). The 28-day binned Fermi-LAT light curve and the VERITAS lunar-month binned light curve are shown in Figure 5.8. A fit to a constant of the VERITAS light curve results in an average flux value of (-0.29 $\pm$ 1.54) $\times 10^{-8}$ m^{-2} s^{-1} with a reduced χ^2 of 3.29 (p-value of 1.5×10^{-5}). Due to the lack of statistics during the latter portion of the VERITAS observations, it is difficult to conclude much about the variability of this source in VHE gamma rays after the outburst in spring of 2015. A fit to a constant of the *Fermi*-LAT light curve results in a flux value of (1.14 $\pm$ 0.20) $\times 10^{-7}$ cm^{-2} s^{-1} with a reduced

Figure 5.6: Gamma ray light curves of Mrk 501 taken starting in 2016 as seen by VERITAS (top) and *Fermi*-LAT (bottom). The VERITAS light curves are binned in lunar months with the edges of the time bins marking the beginning and end of observations during that lunar month. The *Fermi*-LAT light curve is binned in 28-day bins represented with the bin edges. The dates with Kast observations presented here are marked with vertical dashed lines.

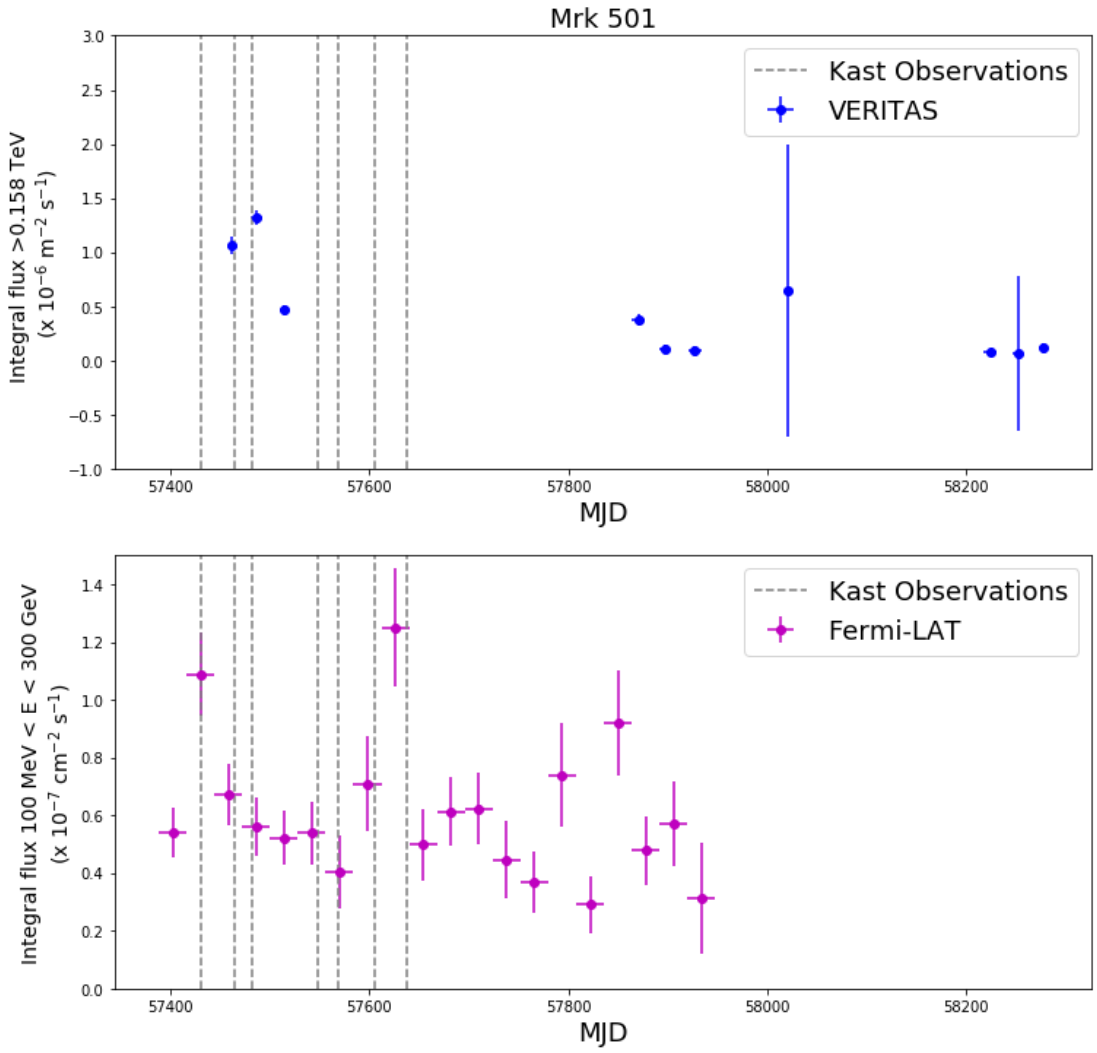

Figure 5.7: Kast spectra taken of Mrk 501 from 11 February to 5 September 2016. The black line indicates the measured flux with a smoothing function applied. The uncertainties on the flux are shown as grey lines, and and instrumental gap caused by the dichroic crossover is indicated as a rectangle from 5400 to 5600 Angstroms. Absorption features are associated with the host galaxy; they are redshifted to z=0.034.

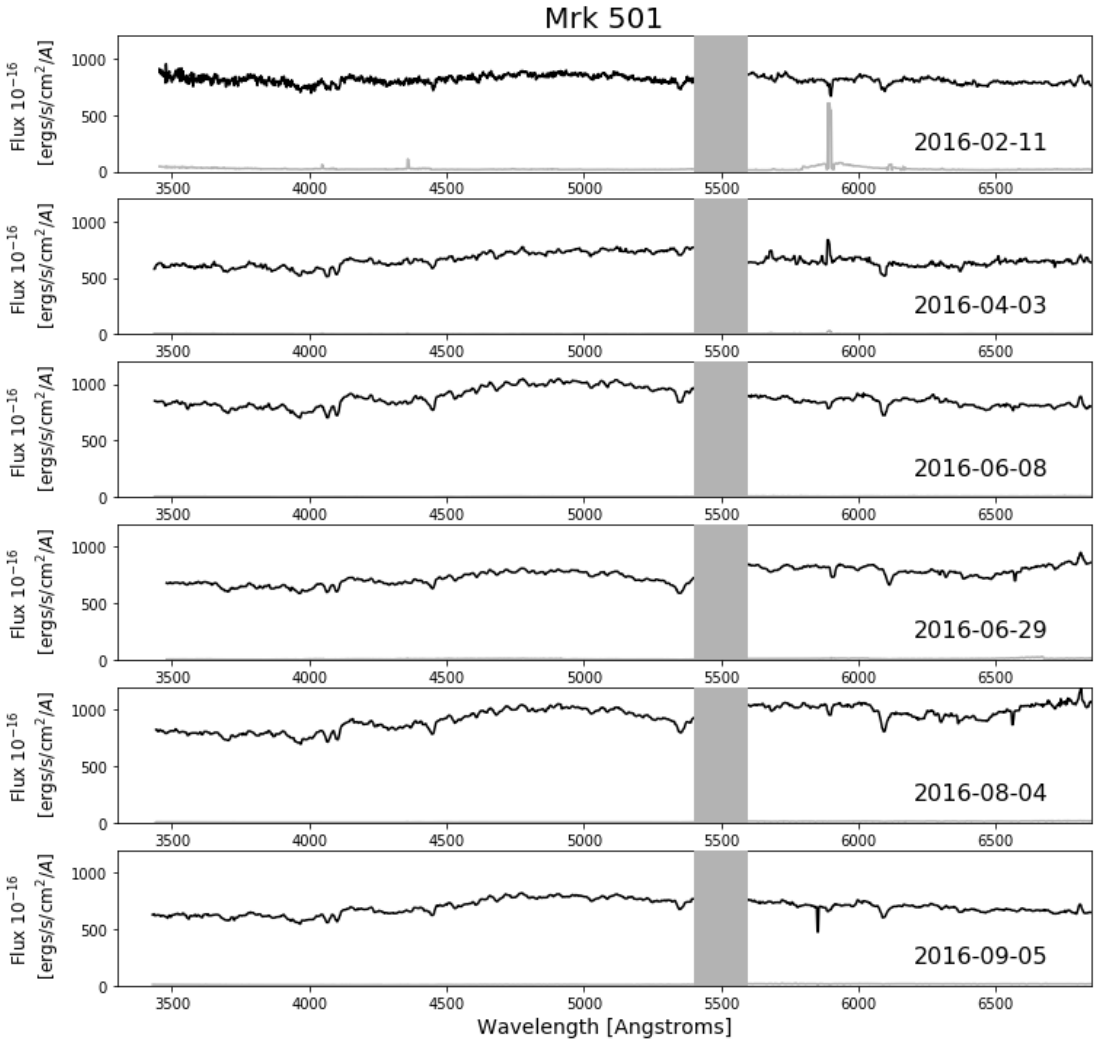

χ^2 of 44.0 (p-value $< 1.0 \times 10^{-75}$).

The Kast spectra of PKS 1441+25 suffer from many poor observing conditions making it difficult to reliably trust any flux calibrations. This is unfortunate since, similar to PKS 1222+216, there are several strong emission features associated with the BLR that are observable within our wavelength coverage. Accurate line flux measurements can be done by calculating the continuum flux through independent, simultaneous photometric observations. The continuum flux can then be used to convert the EW of a line to a line flux (Isler et al., 2013).

5.6.4 3C 279

The VERITAS data for 3C 279 were analyzed from MJD 57411 to 58296 (24 January 2016 - 27 June 2018) resulting in a live time of 11.83 hours and a total significance of 0.6σ. Since there is no detection of VHE emission during this time period, we are not able to use the VHE data to conduct correlation studies with this waveband or to construct a light curve. The *Fermi*-LAT data used here span MJD 57388 - 57939 (1 January 2016 - 5 July 2017), and the 7-day binned light curve is shown in Figure 5.11. A fit to a constant line for this 7-day binned light curve results in a reduced χ^2 value of 73.4 and a p-value $< 1.0\times10^{-75}$. This conclusively rules out a constant flux as observed by the *Fermi*-LAT. The average flux is $(4.49 \pm 0.45)\times10^{-7}$ cm^{-2} s^{-1}.

In the Kast spectra of 3C 279, shown in Figure 5.9, we do not observe any strong emission or absorption features associated with the blazar. Mg II and O II emission from the blazar could be observed given our wavelength coverage. O III features could potentially be detected in the red side of Kast, but fringing in the observations presented here prevent accurate flux calibration in that wavelength range. We do see a Mg II absorption doublet at z=0.395; this is indicative of an

Figure 5.8: Gamma ray light curves of PKS 1441+25 taken starting in 2015 as seen by VERITAS (top) and *Fermi*-LAT (bottom). The VERITAS light curve is binned in lunar months with the edges of the time bins marking the beginning and end of observations during that lunar month. The *Fermi*-LAT light curve is binned in 28-day bins represented with the bin edges. The dates with Kast observations presented here are marked with vertical dashed lines.

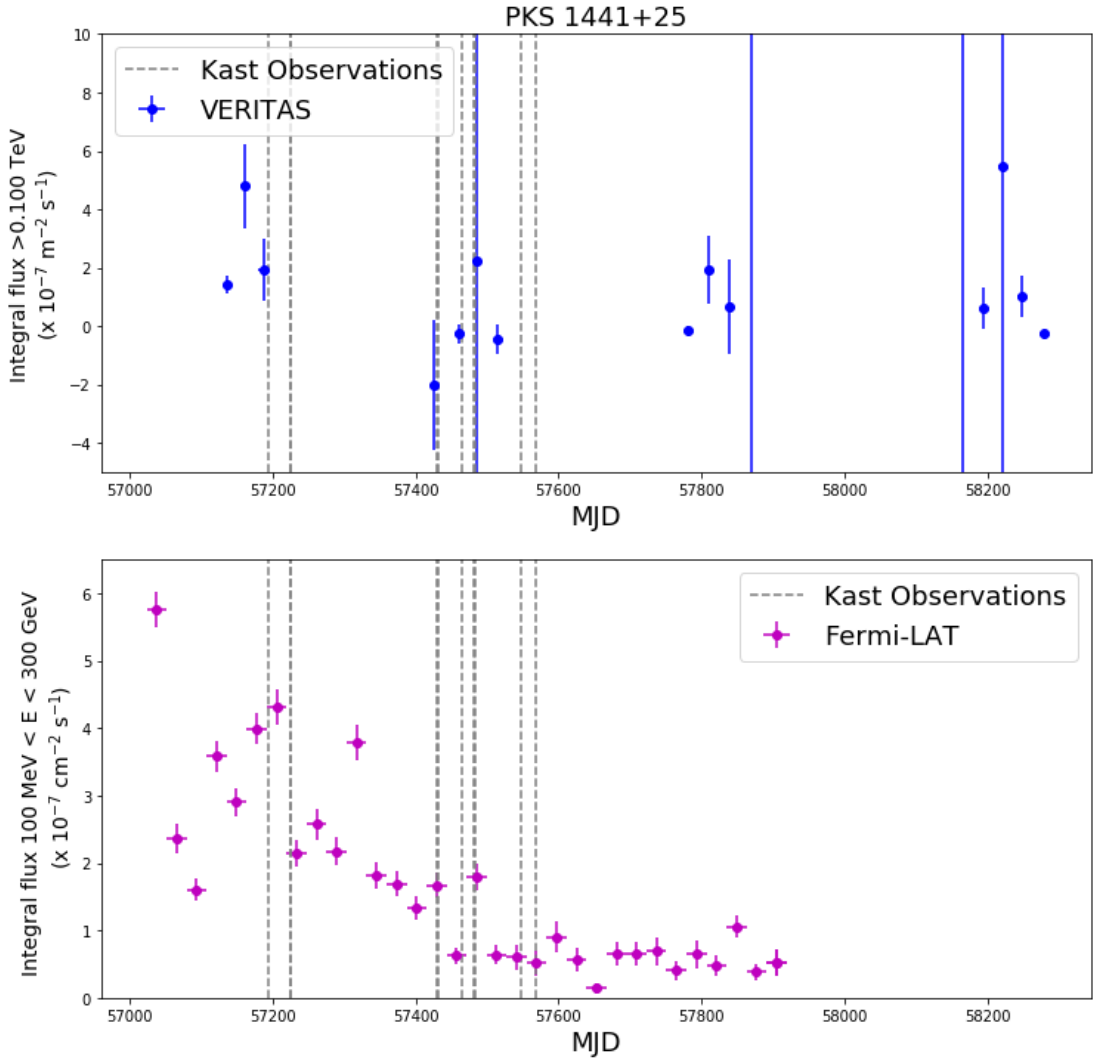

absorbing system located along the light of sight.

5.6.5 PKS 1222+216

The VERITAS data for PKS 1222+216 were analyzed from MJD 57381 to 58277 (25 December 2015 - 8 June 2017) resulting in a live time of 3.40 hours and a total significance of -0.3σ. Since there is no detection of VHE emission during this time period, we are not able to use the VHE data to conduct correlation studies with this waveband. The *Fermi*-LAT data used here span MJD 57388 - 57939 (1 January 2016 - 5 July 2017). The 28-day binned light curve is shown in Figure 5.11. A fit to a constant results in a flux value of (3.22 $\pm$ 0.84) cm^{-2} s^{-1} with a reduced χ^2 of 8.78 (p-value $< 1 \times 10^{-75}$).

The Kast spectra taken of PKS 1222+216 are shown in Figure 5.12. There is strong Mg II, H-γ and H-β emission seen in several of the spectra, and these features are shown in Figures 5.13, 5.14 and 5.15. In order to describe the continuum emission, we fit a power law function to the entire spectrum, combining the measurements from the red and blue sides of the detector for each observation. To describe only the non-thermal continuum emission, we block the dichroic crossover, Telluric features and the spectral features of interest from this fit by removing those portions of the spectrum. Local to the Mg II and H-γ features, this does not provide a good fit to the continuum, so measurement of the line flux cannot be done this way. Future work is needed to understand and model the intricacies of the observed continuum emission.

Figure 5.9: Kast spectra taken of 3C 279. The black line indicates the measured flux with a smoothing function applied. The uncertainties on the flux are shown as grey lines, and and instrumental gap caused by the dichroic crossover is indicated as a rectangle from 5400 to 5600 Angstroms. The Mg II doublet absorption feature at z=0.395 is shown as blue vertical lines in each spectra.

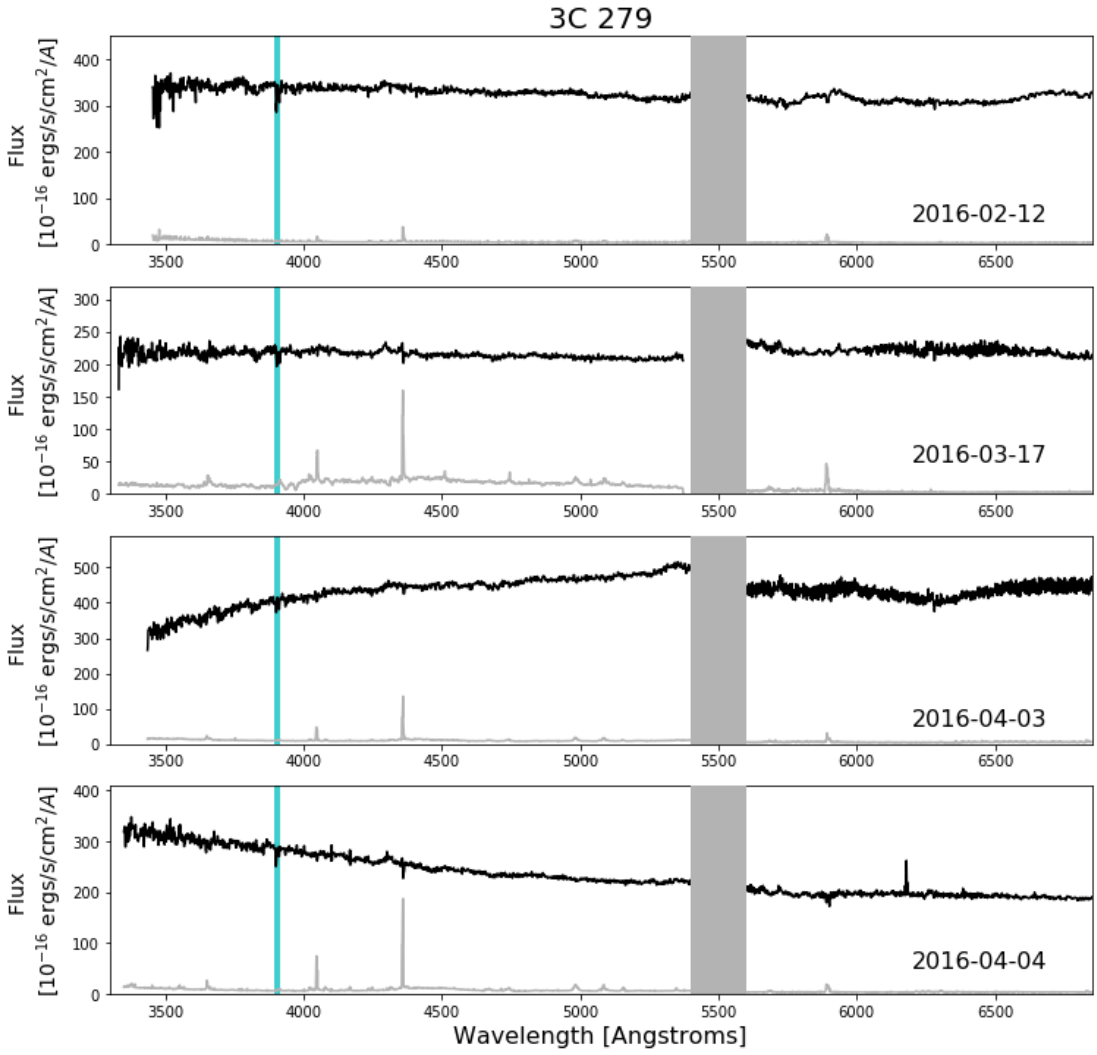

Figure 5.10: Mg II absorption doublet seen in the Kast spectra taken of 3C 279. The absorption feature is at z=0.395, a lower redshift than the blazar, indicating the presence of an absorbing system between the Earth and the source. The observed flux is shown as a black line, and the uncertainty on flux as a grey line. The Mg II feature is denoted in blue.

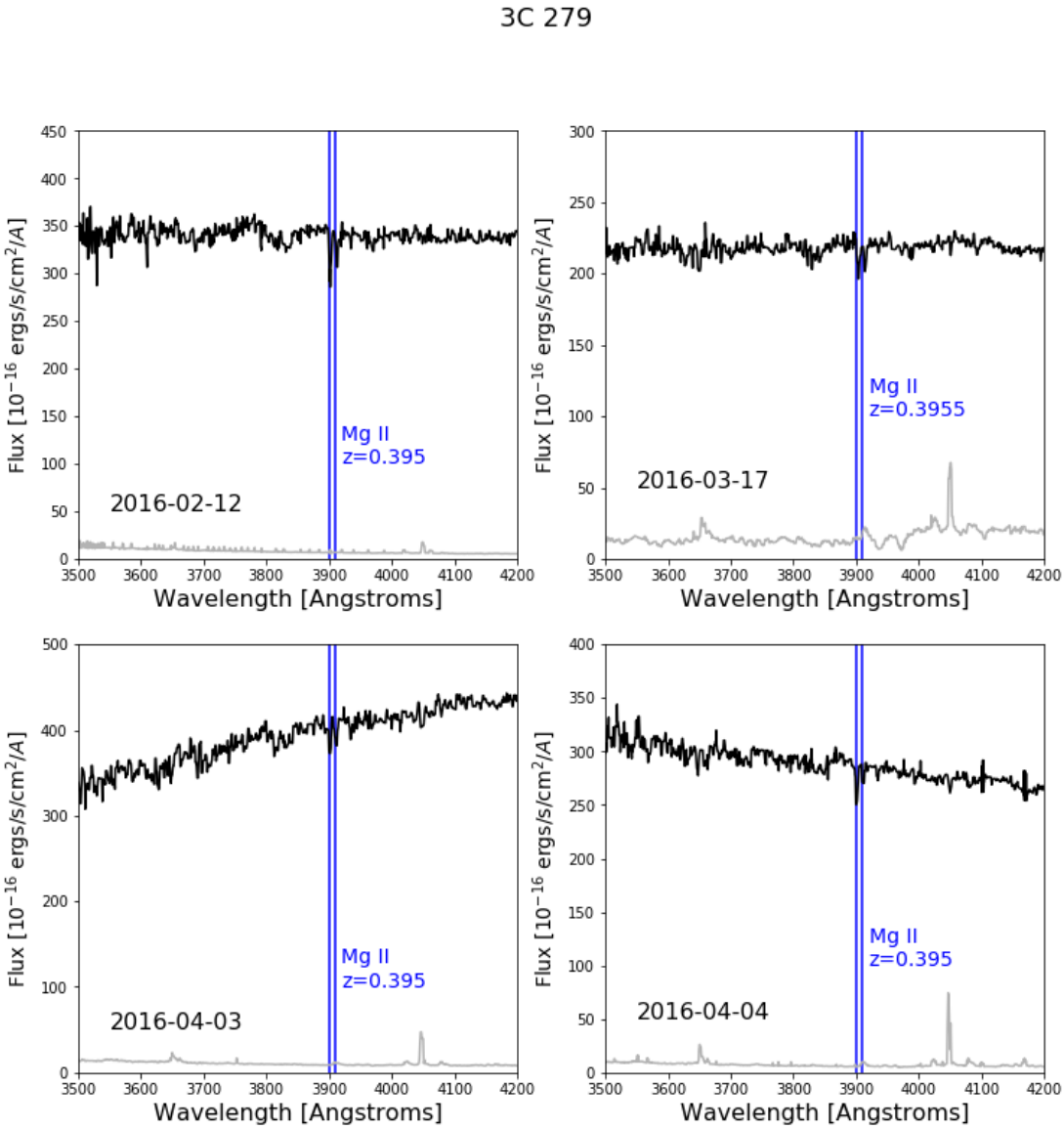

Figure 5.11: *Fermi*-LAT light curves for the two blazars without a VHE detection during the time frame presented here. Top: Light curve of PKS 1222+216. Each bin is 28 days, and the flux is integrated from 100 MeV to 300 GeV. Bottom: Light curve of 3C 279 shown with 7 day bins. The integral flux is shown from 100 MeV to 300 GeV. In each light curve, dates during which we have Kast spectra analyzed here are indicated with vertical dashed lines.

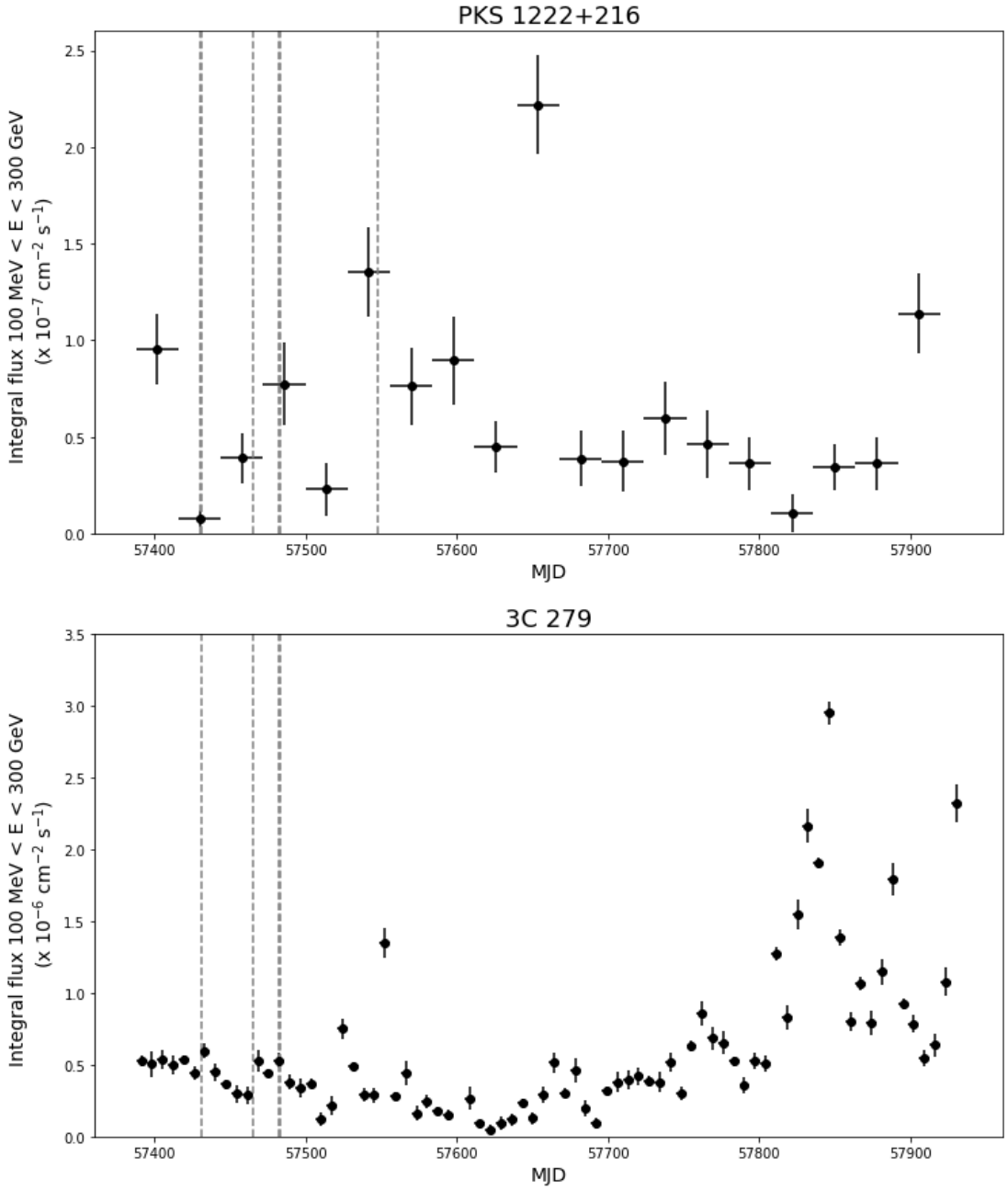

Figure 5.12: Kast spectra taken of PKS 1222+216. The black line indicates the measured flux with a smoothing function applied. The uncertainties on the flux are shown as grey lines, and and instrumental gap caused by the dichroic crossover is indicated as a rectangle from 5400 to 5600 Angstroms. Telluric lines are shown as vertical, dashed lines. Features associated with PKS 1222+216 at a redshift of z=0.432 are shown by vertical blue lines.

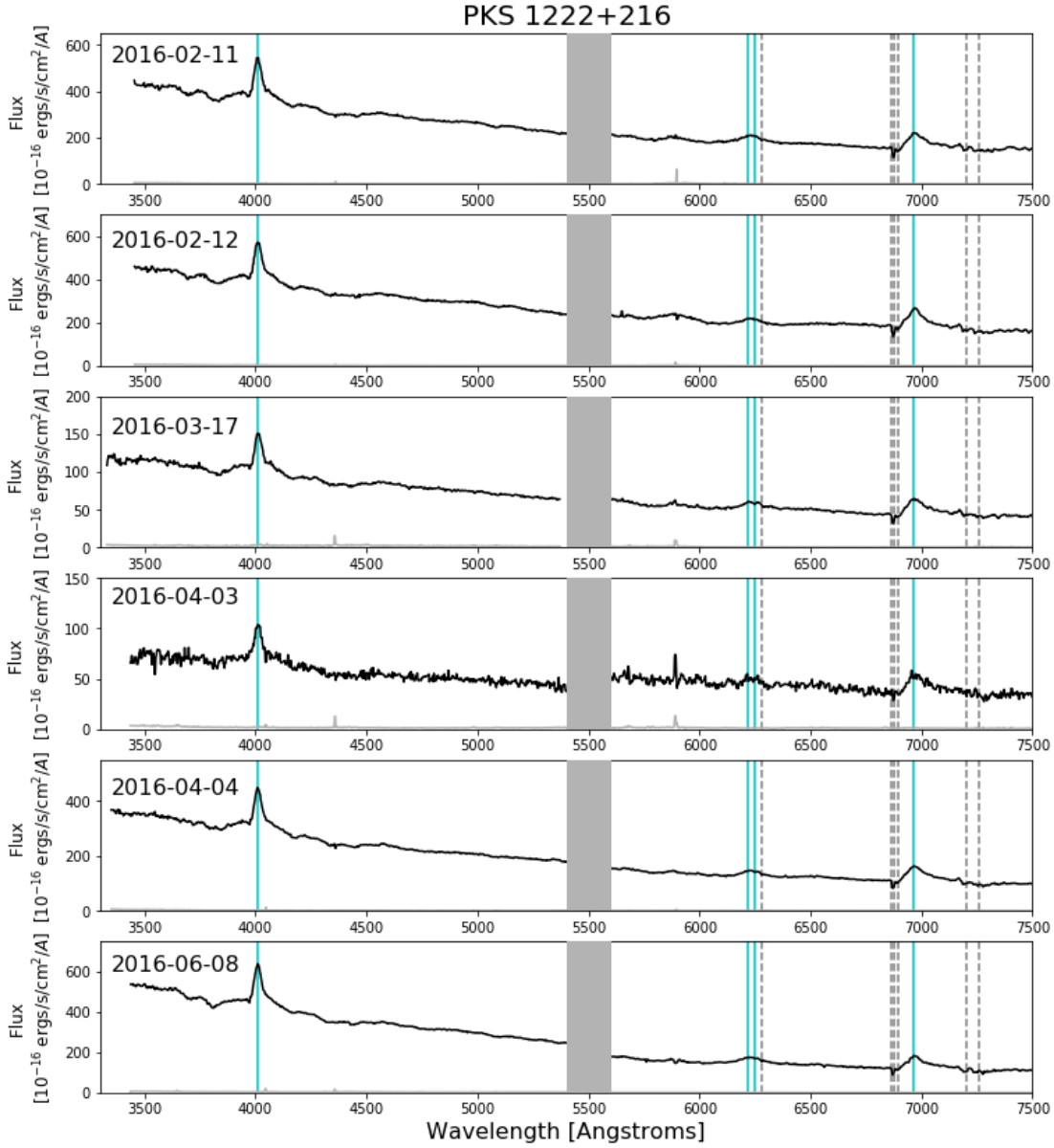

Figure 5.13: Optical spectra taken of PKS 1222+216 showing the broad Mg II emission feature. The colored lines indicate the measured flux with a smoothing function applied for each night of observation. The vertical black line shows Mg II at a redshift of z=0.432. Dashed lines indicate the fit to the continuum represented by a power law; the colors correspond to the same color of spectrum that is being fit.

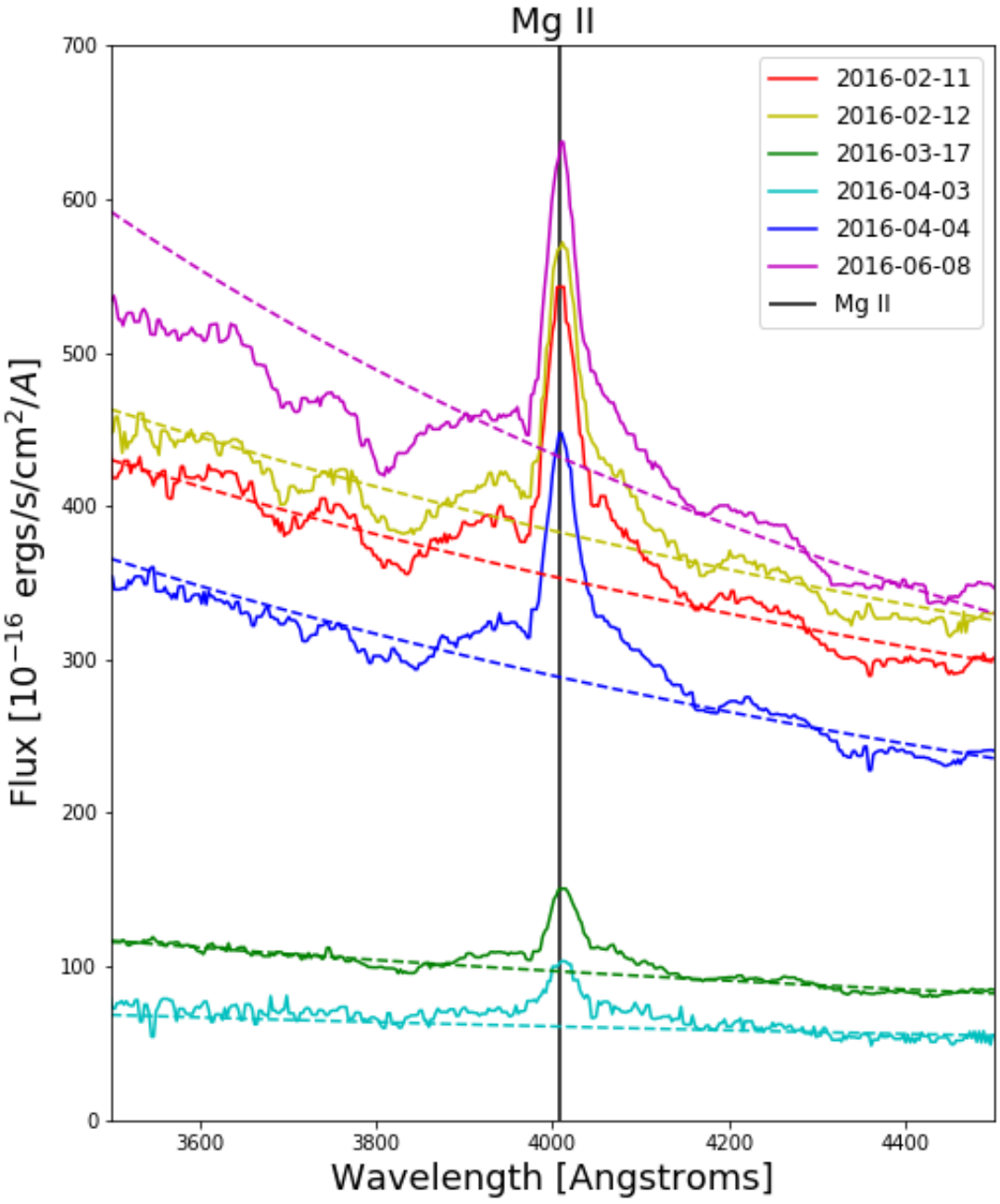

Figure 5.14: Optical spectra taken of PKS 1222+216 showing the H-γ emission feature. The colored lines indicate the measured flux with a smoothing function applied for each night of observation. The vertical black line shows H-γ at a redshift of z=0.432. The presence of Telluric absorption is seen near this emission feature and is indicated with a vertical dashed line. Dashed, colored lines indicate the fit to the continuum represented by a power law; the colors correspond to the same color of spectrum that is being fit.

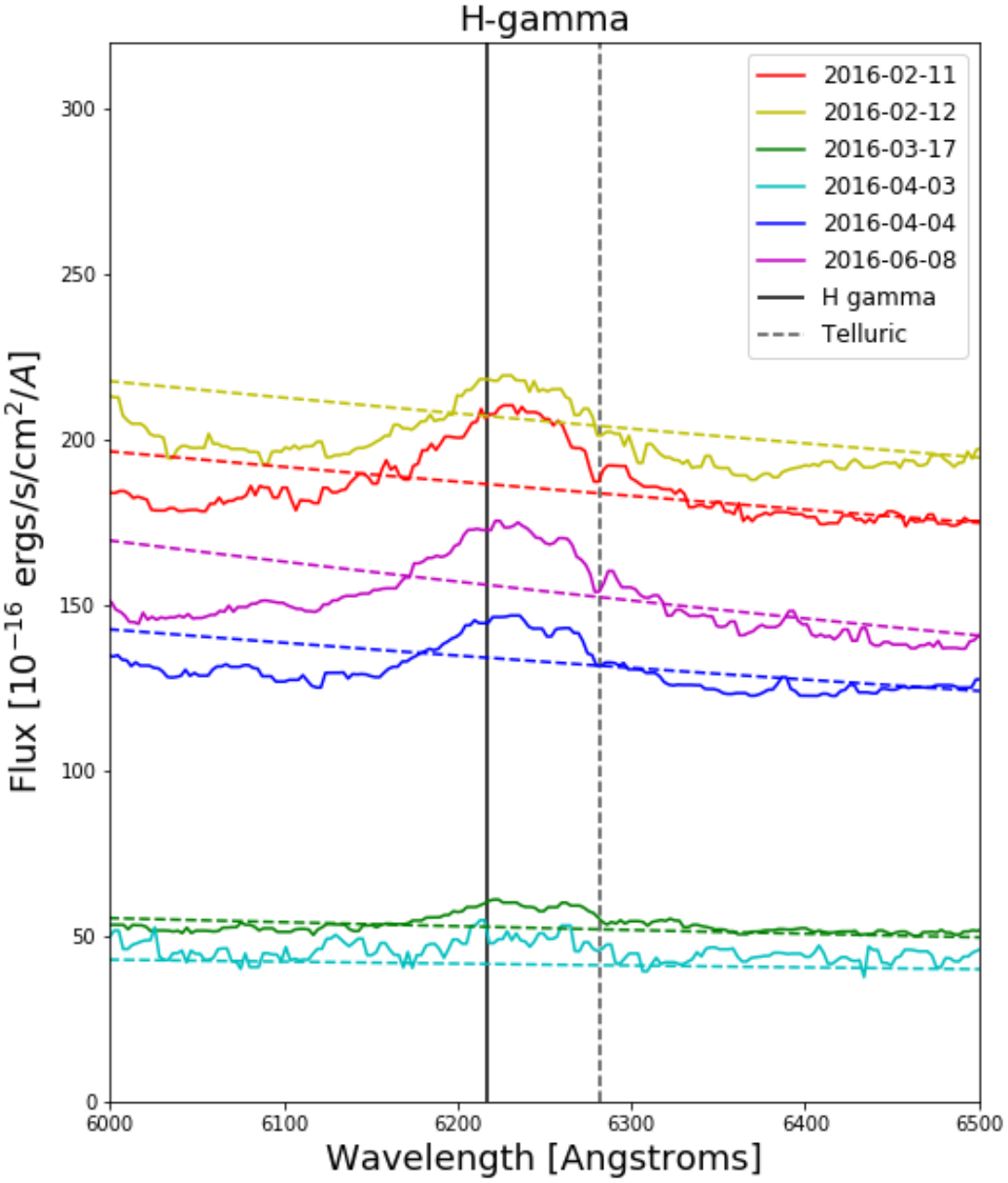

Figure 5.15: Optical spectra taken of PKS 1222+216 showing the H-β emission feature. The colored lines indicate the measured flux with a smoothing function applied for each night of observation. The vertical black line shows H-β at a redshift of z=0.432. The presence of Telluric absorption features are seen near this emission feature and are indicated with vertical dashed lines. Dashed, colored lines indicate the fit to the continuum represented by a power law; the colors correspond to the same color of spectrum that is being fit.

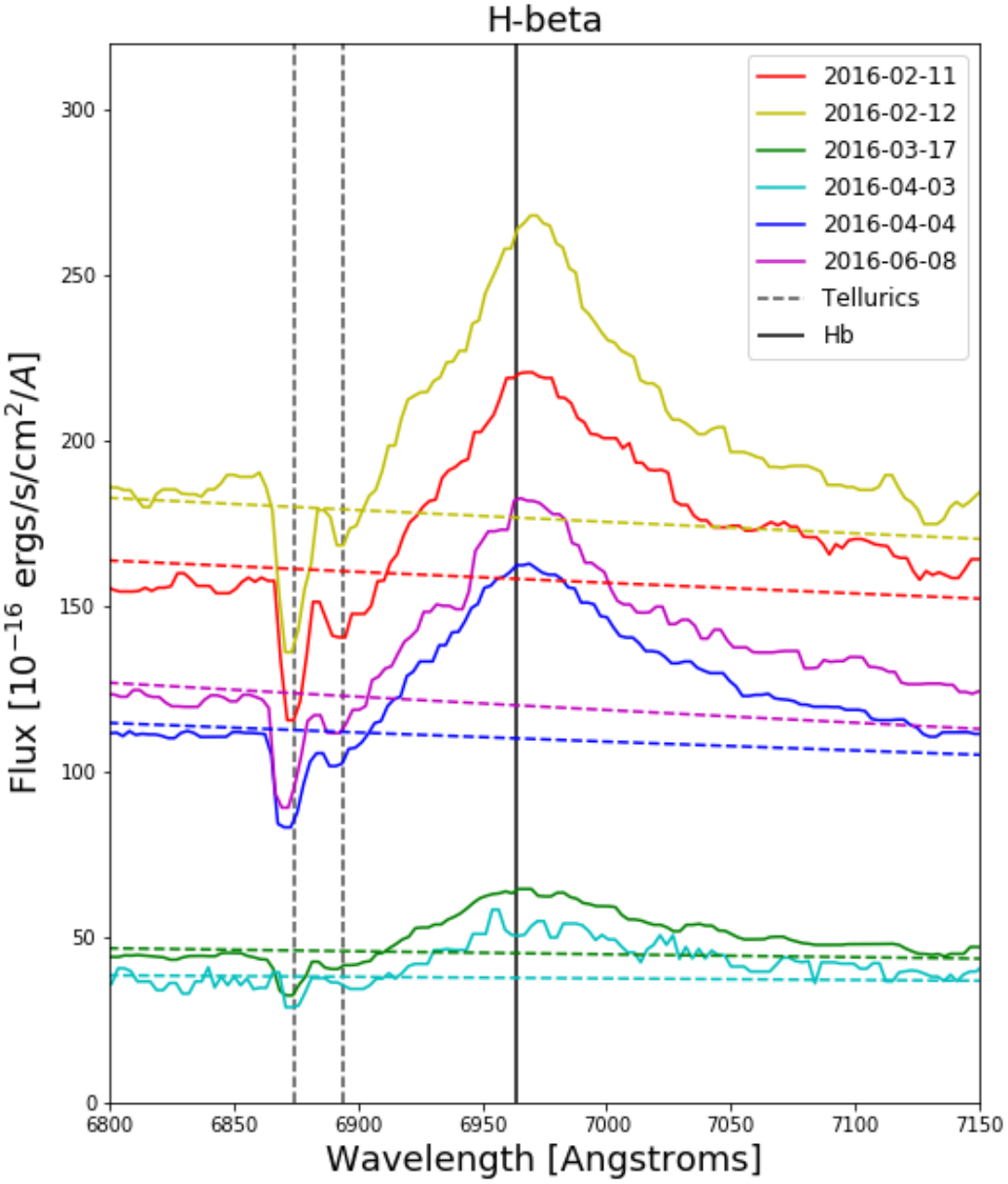

5.7 Conclusions

Multiwavelength observations are important for understanding the nature of blazars and relativistic jets, and this work has expanded by looking for correlations between thermal signatures in optical spectroscopy and observed gamma-ray emission resulting from non-thermal processes. A difficulty with these studies is obtaining the necessary contemporaneous observations, which we were able to successfully do with the combination of access to VERITAS, public *Fermi*-LAT data and monthly observations with the Kast spectrograph on the Shane 3m telescope at Lick Observatory. Producing accurately flux-calibrated spectra was another difficulty, and it is necessary because we are looking to measure the line flux of any relevant features. Over the full range of the optical spectra, we use a power law to fit the continuum. However, for PKS 1222+216 that does not provide a good fit local to the spectral features of interest, and so an accurate measure of the line flux would require further investigation into additional continuum fitting techniques. This study is the first of its kind for two HSPs, Mrk 421 and Mrk 501. Though we do not observe any strong optical features associated with the AGN for these sources, any future indication would be a new, interesting result.

5.8 Acknowledgments

I would like to thank Brad Holden and Camille Leibler for their helpful conversations about the proper processes of flux calibrating these spectra. Two spectra of Mrk 421 were taken as ToOs by Tiffany Hsyu who kindly gave up her observing time for our science. Two UCSC undergraduates, Nicolas Vazquez and Brandon Cavins, assisted in this project by providing the reduction of gamma-ray observations.

Chapter 6

Conclusions & Looking Forward

> No observational problem will not be solved by more data.
>
> Vera Rubin

This thesis presented multiwavelength observations of VHE emitting blazars and investigated the connection between thermal and non-thermal emission in the blazar environment and the jet. 3C 66A showed no spectral anomalies when correcting for EBL absorption, and modeling of multiwavelength SEDs showed a good fit in three out of the four time periods by a single-zone, purely leptonic SSC emission scenario. These SEDs were created by carefully constructing the spectra in different flux states, and show that EC production from photons originating outside the jet probably does not play a large role in explaining the observed emission. We implemented a new SED modeling approach which utilizes an MCMC technique. This technique is promising and allows for the determination of uncertainties on the input parameters into the model as well as uncertainties on derived quantities such as the allowed variability timescale.

We also presented the first search for variability in spectral lines from the VHE

blazars Mrk 501, Mrk 421, 3C 279 and PKS 1441+25. Further, we presented the first search for variability in spectral features combined with VHE observations for the first time for these four blazars as well as a fifth blazar, PKS 1222+216. We do not observe any strong spectral features associated with the nucleus of the AGN in Mrk 421, Mrk 501 and 3C 279. Accurately flux-calibrating spectra and modeling the continuum emission were challenging parts of this project and prevented the detection of line flux variability in PKS 1222+216 and PKS 1441+25. Future studies such as these have the potential to provide insight into the interaction between the jet and its surrounding environment, though target collection and flux calibration of spectra must be done with care.

The future of VHE astrophysics will be led by the Cherenkov Telescope Array (CTA), an array of NN telescopes currently under development and construction (Cherenkov Telescope Array Consortium et al., 2017). Two arrays will make up CTA: one located in the northern hemisphere and one in the southern hemisphere. There will be ∼100 telescopes at the southern site, and ∼20 at the northern site. CTA is projected to have angular resolution down to one arcminute, energy sensitivity ranging from 20 GeV to 300 TeV and flux sensitivity substantially better than the current generation of IACTs and the *Fermi*-LAT. Blazars are one of the key science targets for CTA due to their potential for understanding the nature of relativistic jets and the EBL. With recent advances in multi-messenger astronomy, CTA observations of blazars will also be highly complementary to gravitational wave and neutrino experiments (e.g. IceCube Collaboration et al. (2018)).

Appendix A

MCMC Blazar SED Fitting Plots

This appendix contains useful diagnostic plots resulting from the Markov Chain Monte Carlo runs.

A.1 1RXS J101015.9-311909

Figures A.1 - A.9 show the results from the MCMC modeling of 1RXS J101015.9-311909.

A.2 3C 66A: Block 1

Figures A.10 - A.18 show the results from the MCMC modeling of the SED of 3C 66A during block 1.

A.3 3C 66A: Block 2

Figures A.19 - A.27 show the results from the MCMC modeling of the SED of 3C 66A during block 2.

1RXS J101015.9-311909: R

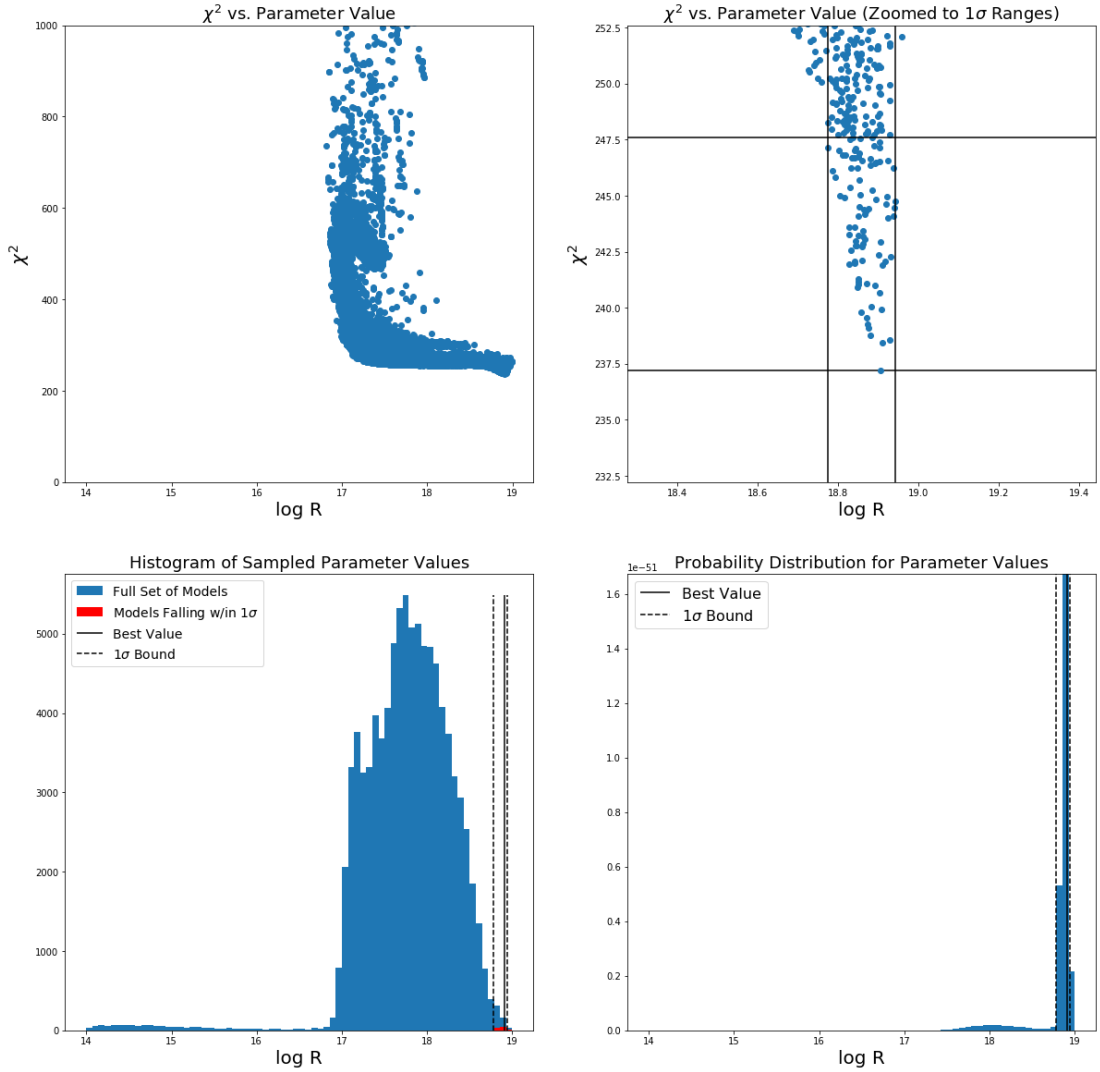

Figure A.1: Diagnostic plots from running the MCMC SED fitting on 1RXS J101015.9-311909. *Top left*: χ^2 value plotted as a function of the R value. *Top right*: χ^2 vs. R value with the smallest χ^2 value and largest χ^2 1σ bounds shown as horizontal lines. The smallest and largest 1σ values of R are marked with vertical lines. *Bottom left*: Distribution of R values in the accepted steps. *Bottom right*: Non-normalized probability distribution for R.

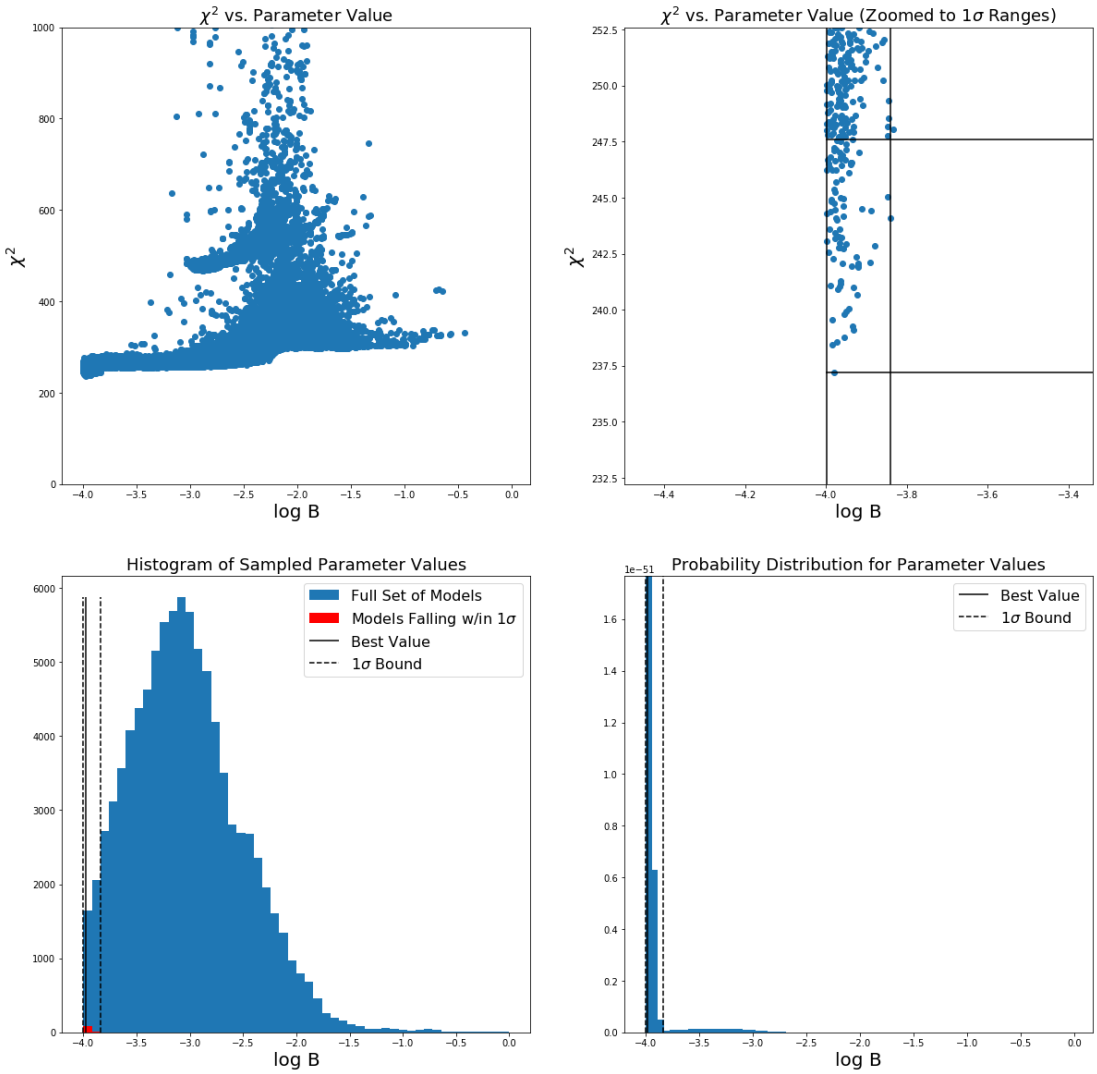

Figure A.2: Diagnostic plots from running the MCMC SED fitting on 1RXS J101015.9-311909. *Top left*: χ^2 value plotted as a function of the B value. *Top right*: χ^2 vs. B value with the smallest χ^2 value and largest χ^2 1σ bounds shown as horizontal lines. The smallest and largest 1σ values of B are marked with vertical lines. *Bottom left*: Distribution of B values in the accepted steps. *Bottom right*: Non-normalized probability distribution for B.

1RXS J101015.9-311909: δ

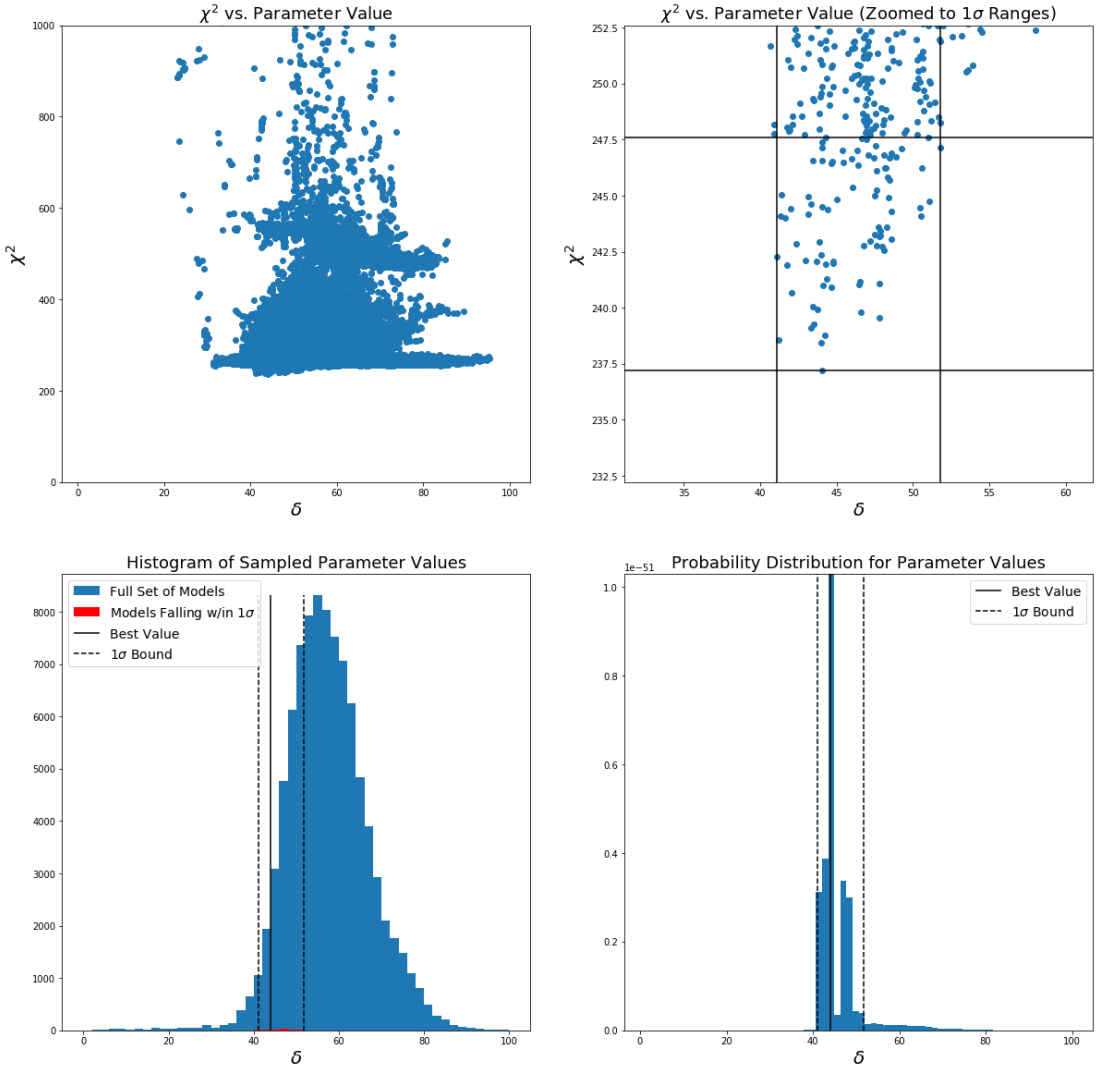

Figure A.3: Diagnostic plots from running the MCMC SED fitting on 1RXS J101015.9-311909. *Top left*: χ^2 value plotted as a function of the δ value. *Top right*: χ^2 vs. δ value with the smallest χ^2 value and largest χ^2 1σ bounds shown as horizontal lines. The smallest and largest 1σ values of δ are marked with vertical lines. *Bottom left*: Distribution of δ values in the accepted steps. *Bottom right*: Non-normalized probability distribution for δ.

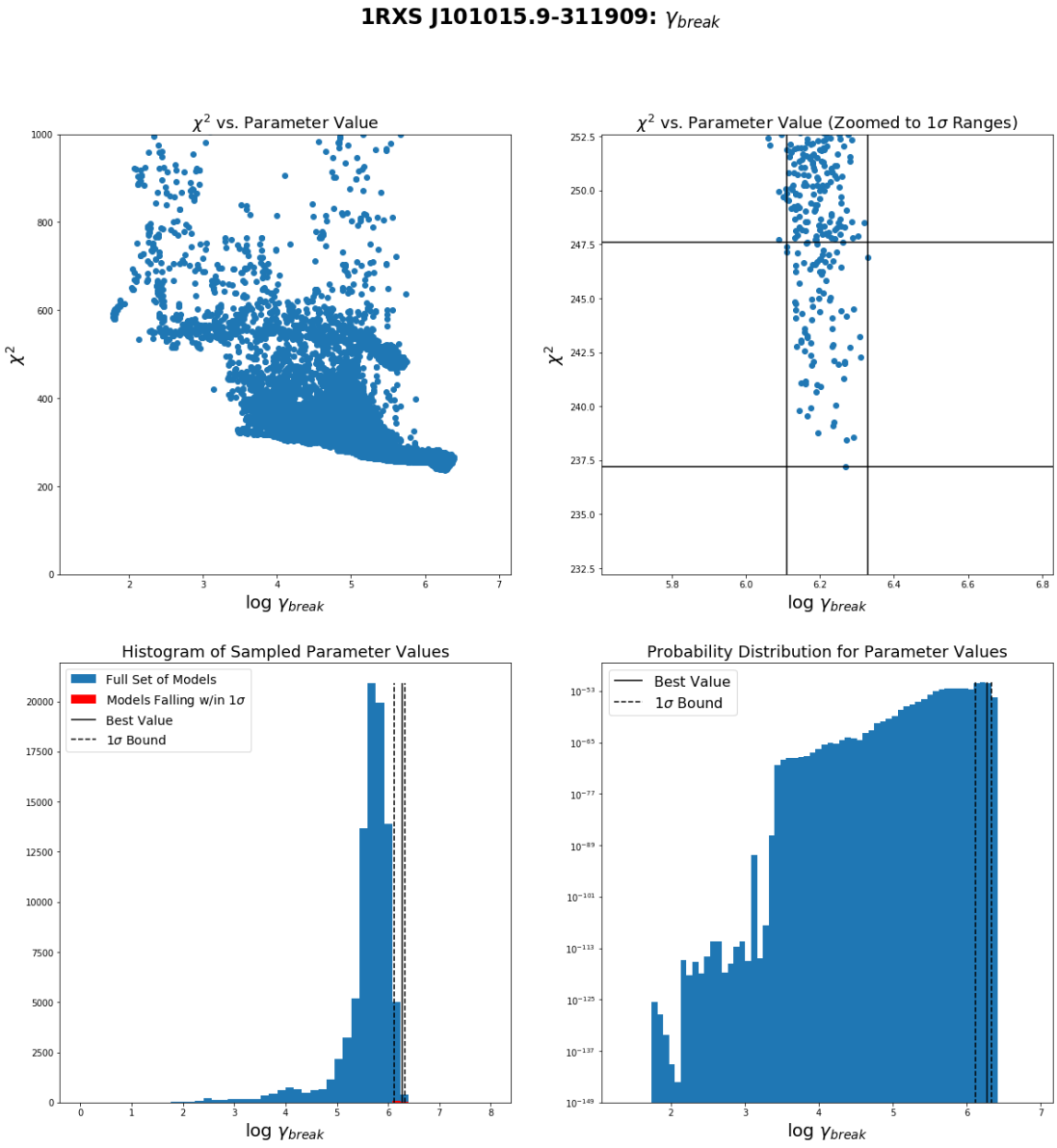

Figure A.4: Diagnostic plots from running the MCMC SED fitting on 1RXS J101015.9-311909. *Top left*: χ^2 value plotted as a function of the γ_{break} value. *Top right*: χ^2 vs. γ_{break} value with the smallest χ^2 value and largest χ^2 1σ bounds shown as horizontal lines. The smallest and largest 1σ values of γ_{break} are marked with vertical lines. *Bottom left*: Distribution of γ_{break} values in the accepted steps. *Bottom right*: Non-normalized probability distribution for γ_{break}.

1RXS J101015.9-311909: α_1

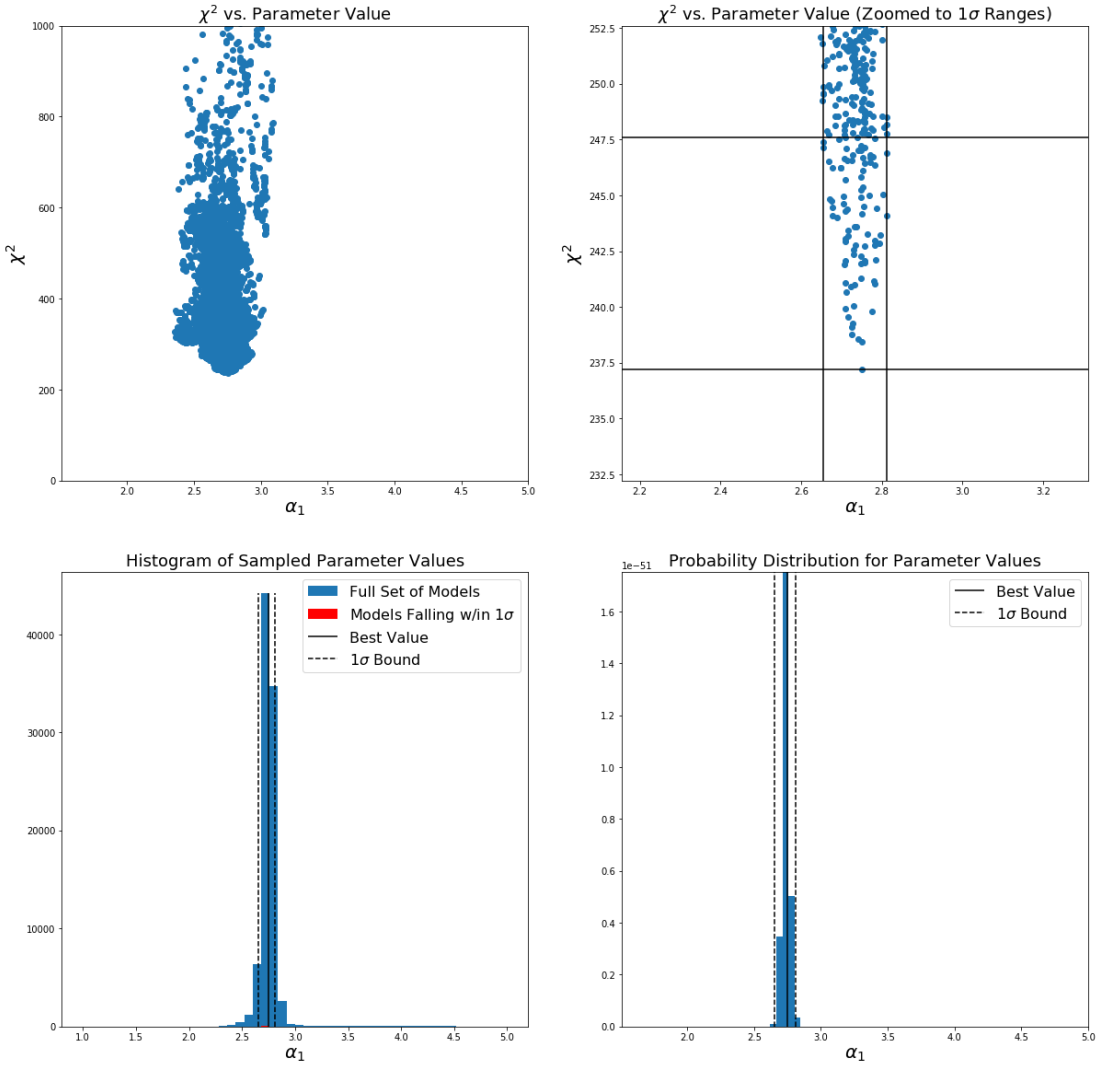

Figure A.5: Diagnostic plots from running the MCMC SED fitting on 1RXS J101015.9-311909. *Top left*: χ^2 value plotted as a function of the α_1 value. *Top right*: χ^2 vs. α_1 value with the smallest χ^2 value and largest χ^2 1σ bounds shown as horizontal lines. The smallest and largest 1σ values of α_1 are marked with vertical lines. *Bottom left*: Distribution of α_1 values in the accepted steps. *Bottom right*: Non-normalized probability distribution for α_1.

1RXS J101015.9-311909: K

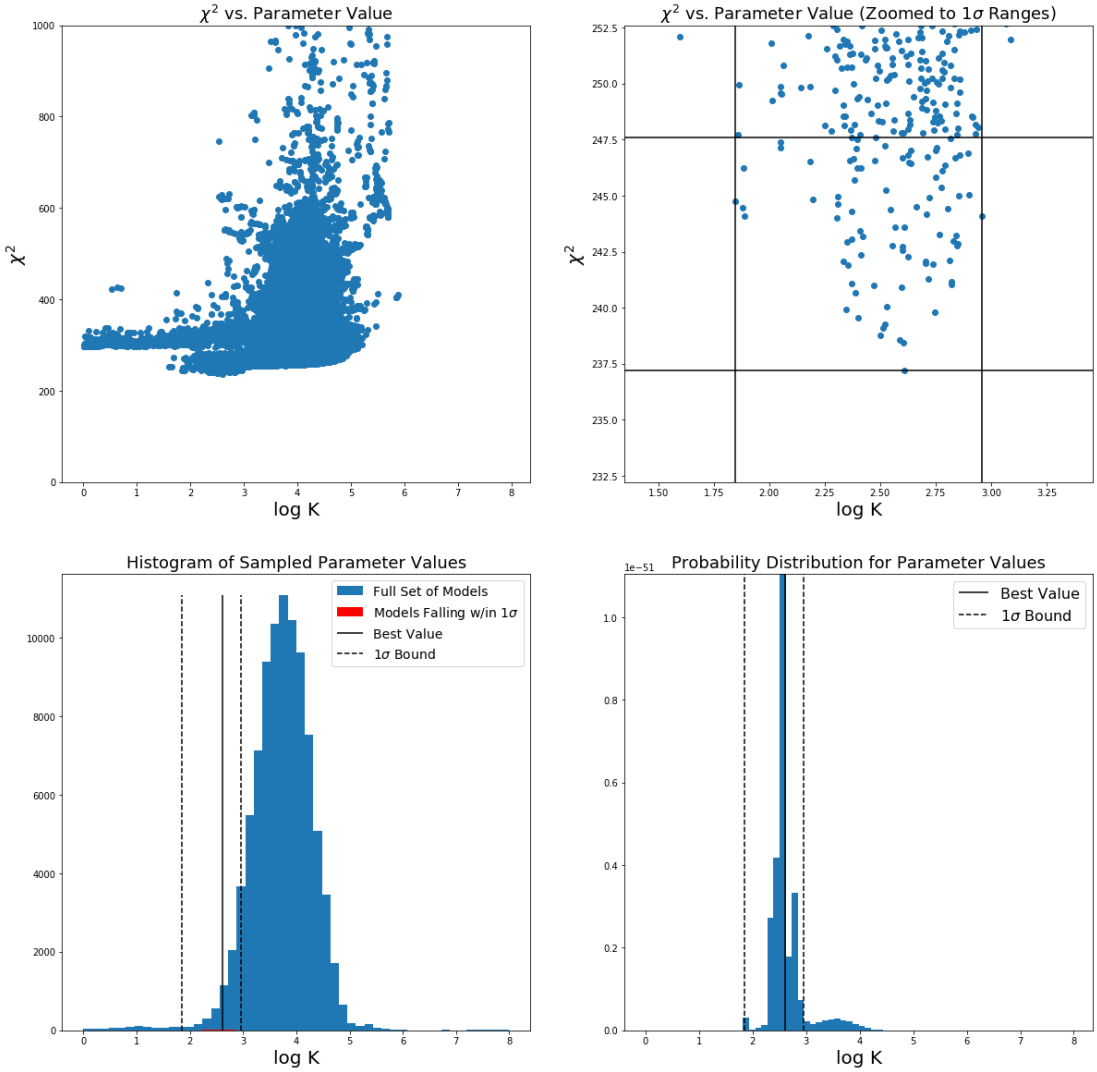

Figure A.6: Diagnostic plots from running the MCMC SED fitting on 1RXS J101015.9-311909. *Top left*: χ^2 value plotted as a function of the K value. *Top right*: χ^2 vs. K value with the smallest χ^2 value and largest χ^2 1σ bounds shown as horizontal lines. The smallest and largest 1σ values of K are marked with vertical lines. *Bottom left*: Distribution of K values in the accepted steps. *Bottom right*: Non-normalized probability distribution for K.

1RXS J101015.9-311909: γ_{min}

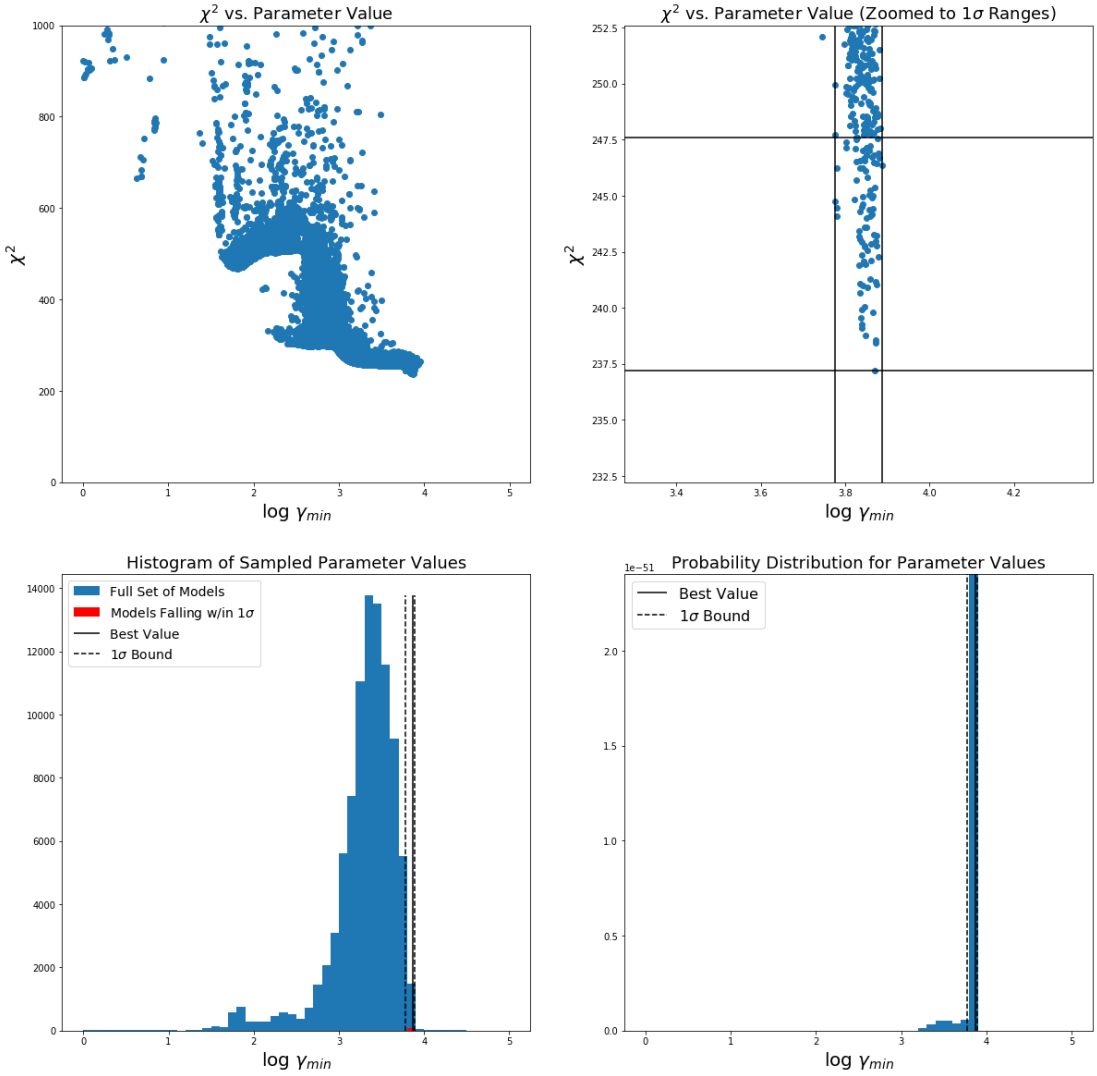

Figure A.7: Diagnostic plots from running the MCMC SED fitting on 1RXS J101015.9-311909. *Top left*: χ^2 value plotted as a function of the γ_{min} value. *Top right*: χ^2 vs. γ_{min} value with the smallest χ^2 value and largest χ^2 1σ bounds shown as horizontal lines. The smallest and largest 1σ values of γ_{min} are marked with vertical lines. *Bottom left*: Distribution of γ_{min} values in the accepted steps. *Bottom right*: Non-normalized probability distribution for γ_{min}.

1RXS J101015.9-311909: γ_{max}

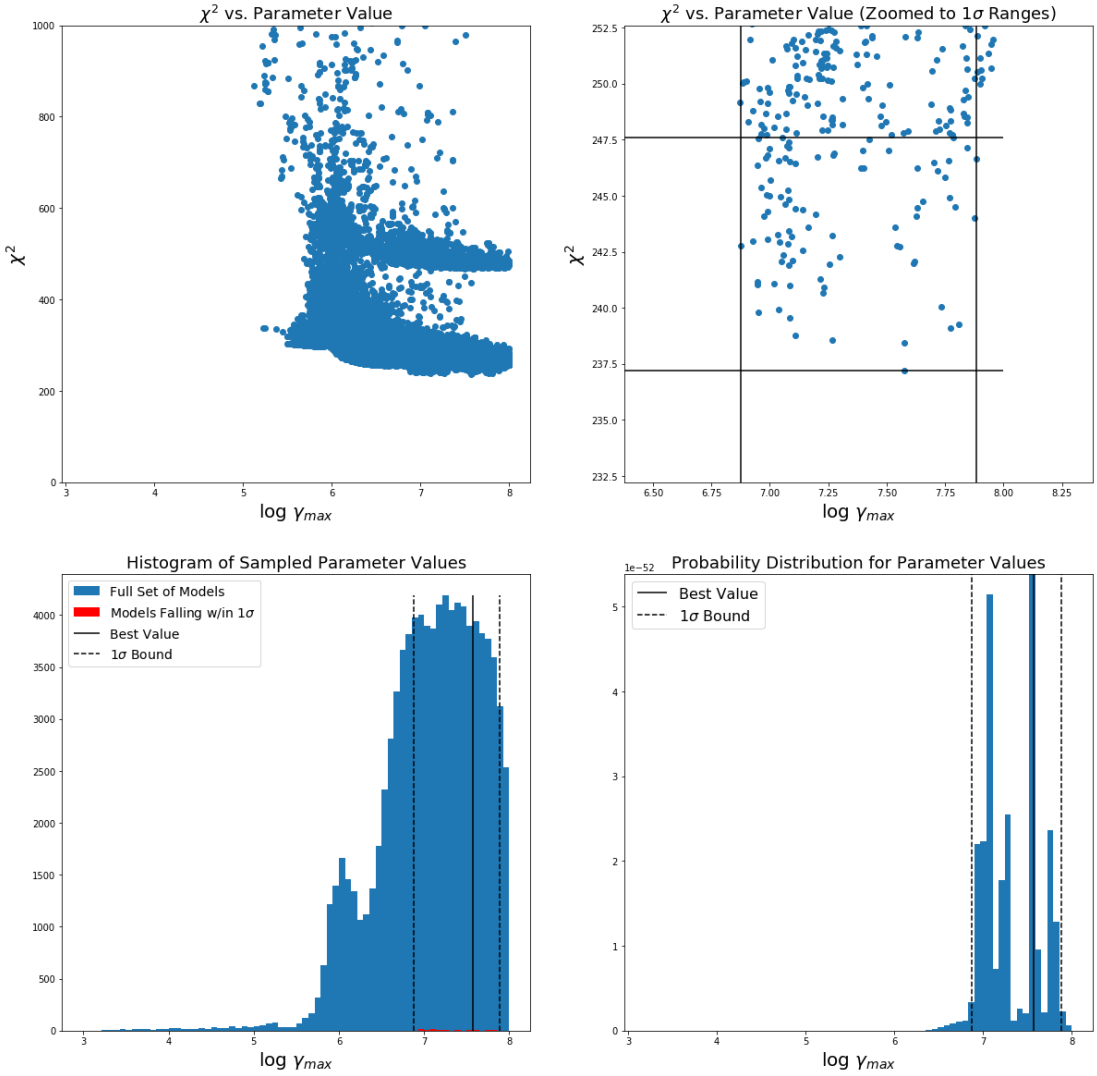

Figure A.8: Diagnostic plots from running the MCMC SED fitting on 1RXS J101015.9-311909. *Top left*: χ^2 value plotted as a function of the γ_{max} value. *Top right*: χ^2 vs. γ_{max} value with the smallest χ^2 value and largest χ^2 1σ bounds shown as horizontal lines. The smallest and largest 1σ values of γ_{max} are marked with vertical lines. *Bottom left*: Distribution of γ_{max} values in the accepted steps. *Bottom right*: Non-normalized probability distribution for γ_{max}.

1RXS J101015.9-311909: α_2

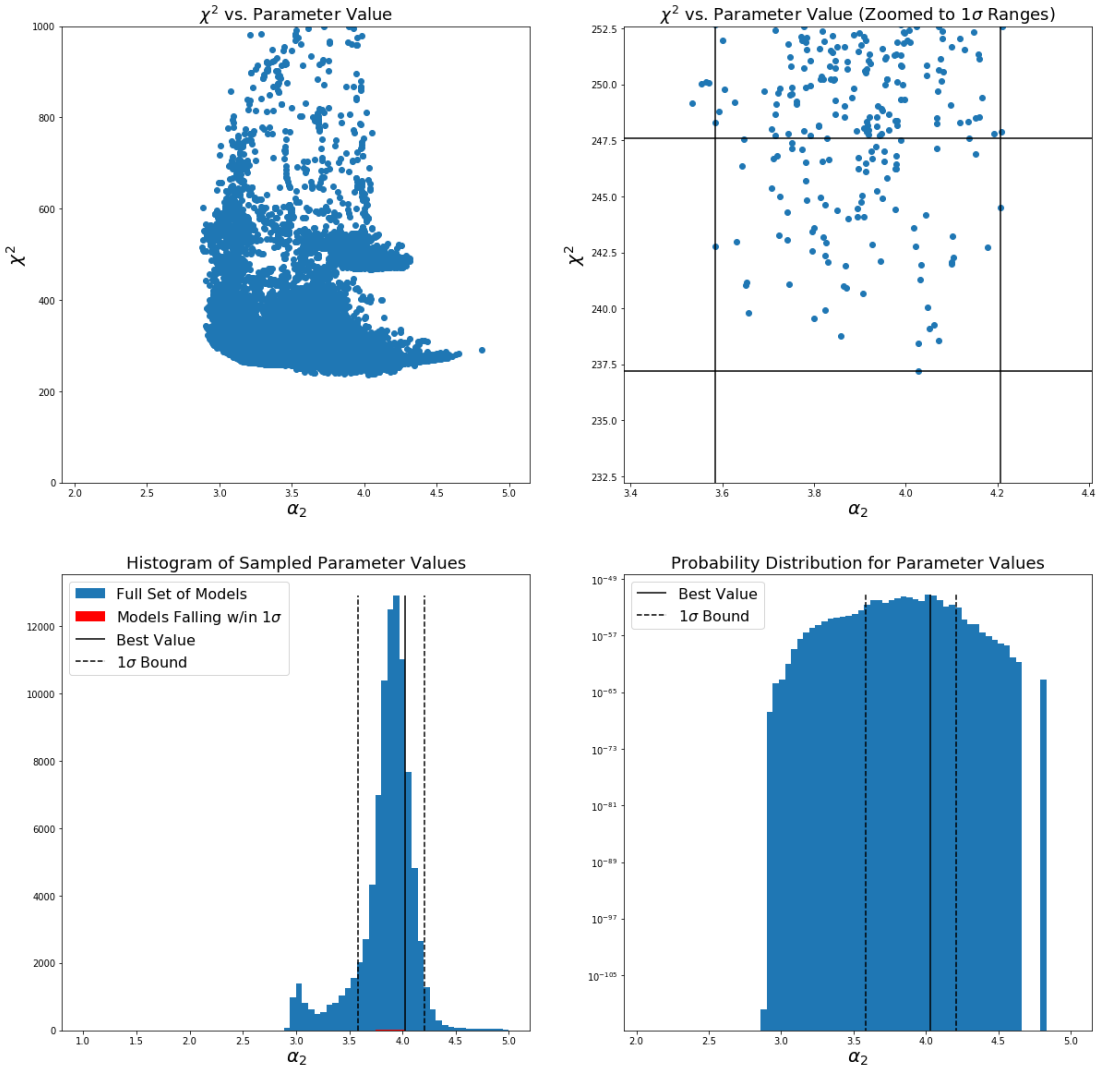

Figure A.9: Diagnostic plots from running the MCMC SED fitting on 1RXS J101015.9-311909. *Top left*: χ^2 value plotted as a function of the α_2 value. *Top right*: χ^2 vs. α_2 value with the smallest χ^2 value and largest χ^2 1σ bounds shown as horizontal lines. The smallest and largest 1σ values of α_2 are marked with vertical lines. *Bottom left*: Distribution of α_2 values in the accepted steps. *Bottom right*: Non-normalized probability distribution for α_2.

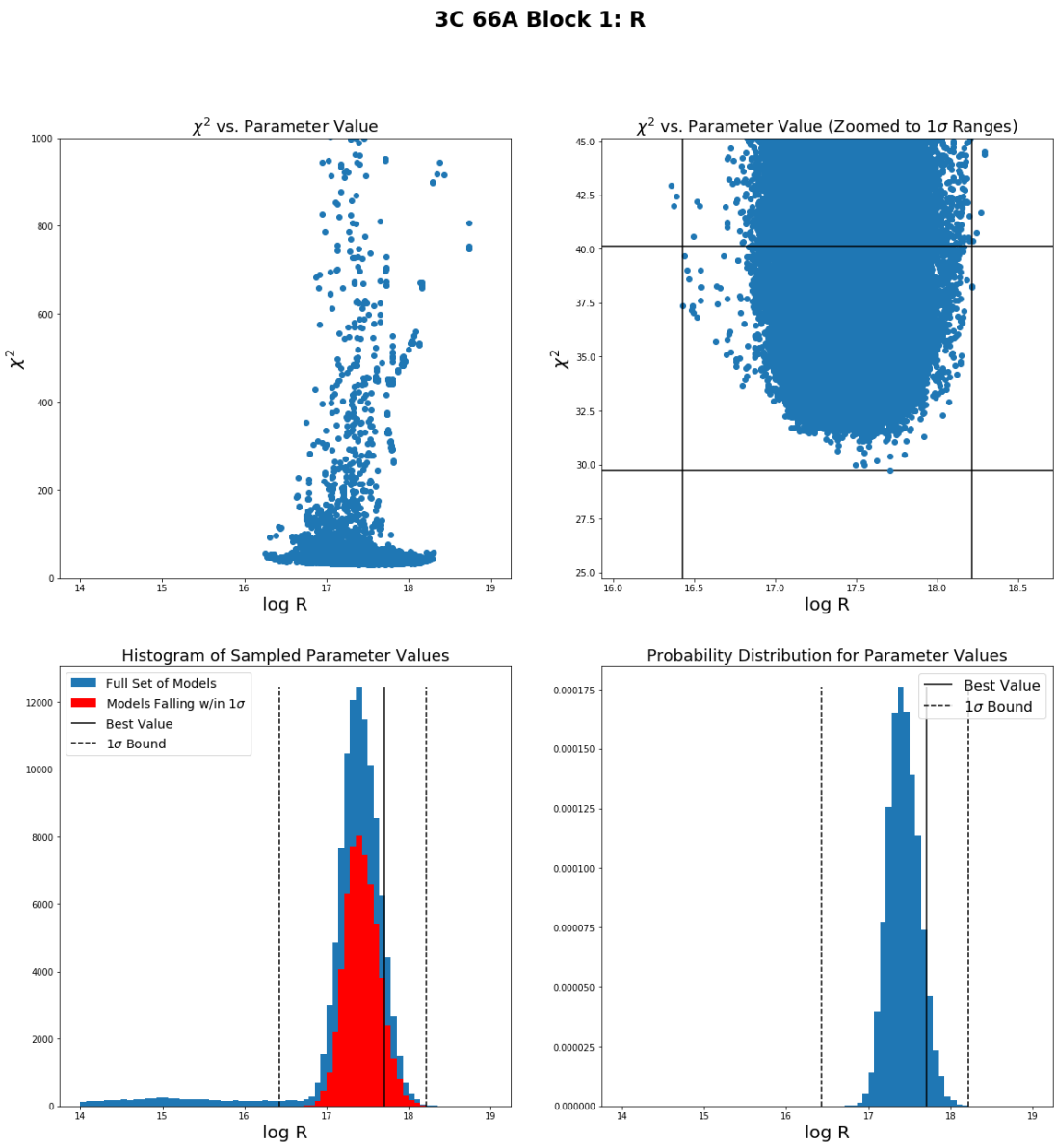

Figure A.10: *Top left*: χ^2 value plotted as a function of the R value. *Top right*: χ^2 vs. R value with the smallest χ^2 value and largest χ^2 1σ bounds shown as horizontal lines. The smallest and largest 1σ values of R are marked with vertical lines. *Bottom left*: Distribution of R values in the accepted steps. *Bottom right*: Non-normalized probability distribution for R.

3C 66A Block 1: B

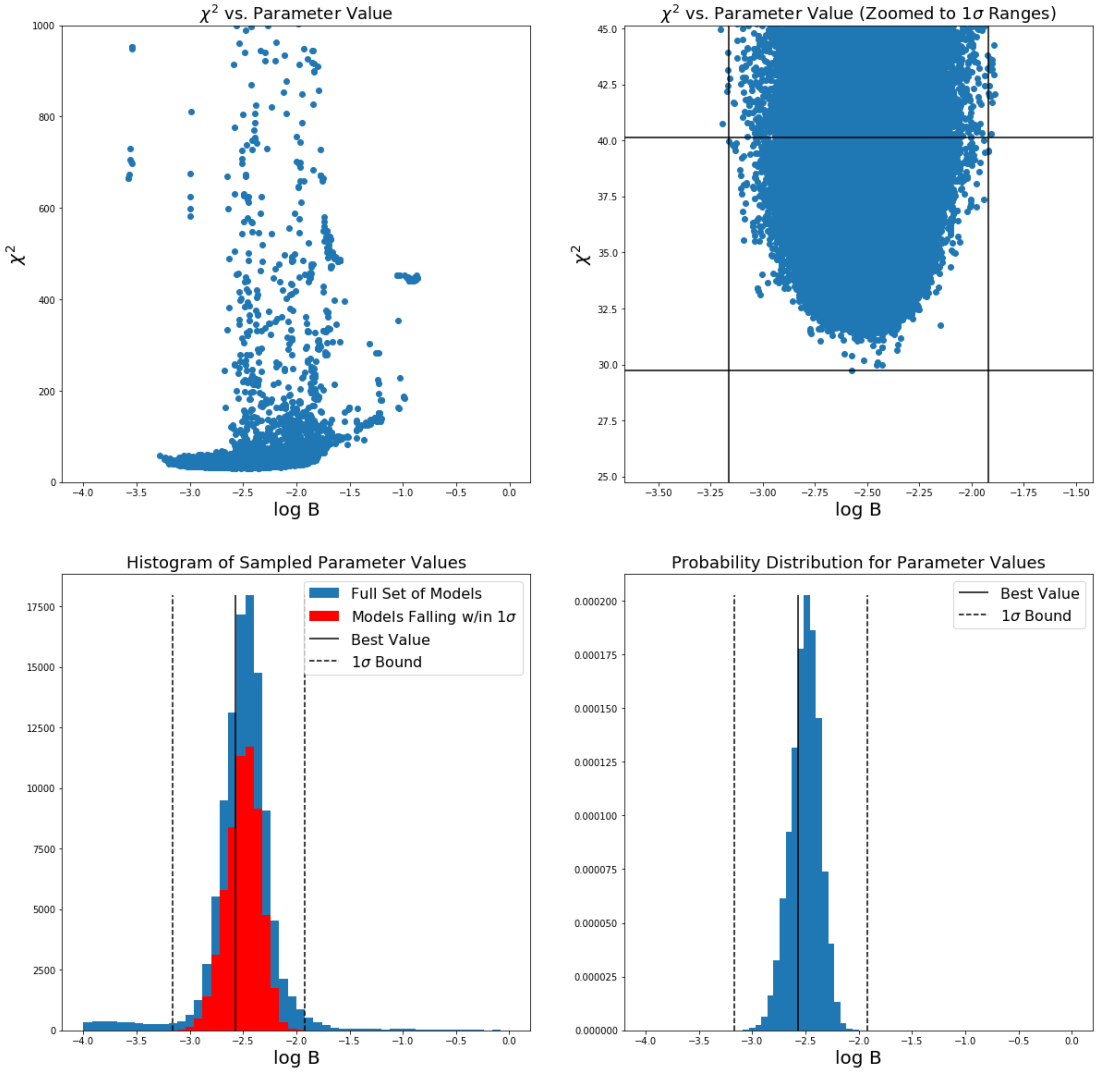

Figure A.11: *Top left*: χ^2 value plotted as a function of the B value. *Top right*: χ^2 vs. B value with the smallest χ^2 value and largest χ^2 1σ bounds shown as horizontal lines. The smallest and largest 1σ values of B are marked with vertical lines. *Bottom left*: Distribution of B values in the accepted steps. *Bottom right*: Non-normalized probability distribution for B.

3C 66A Block 1: δ

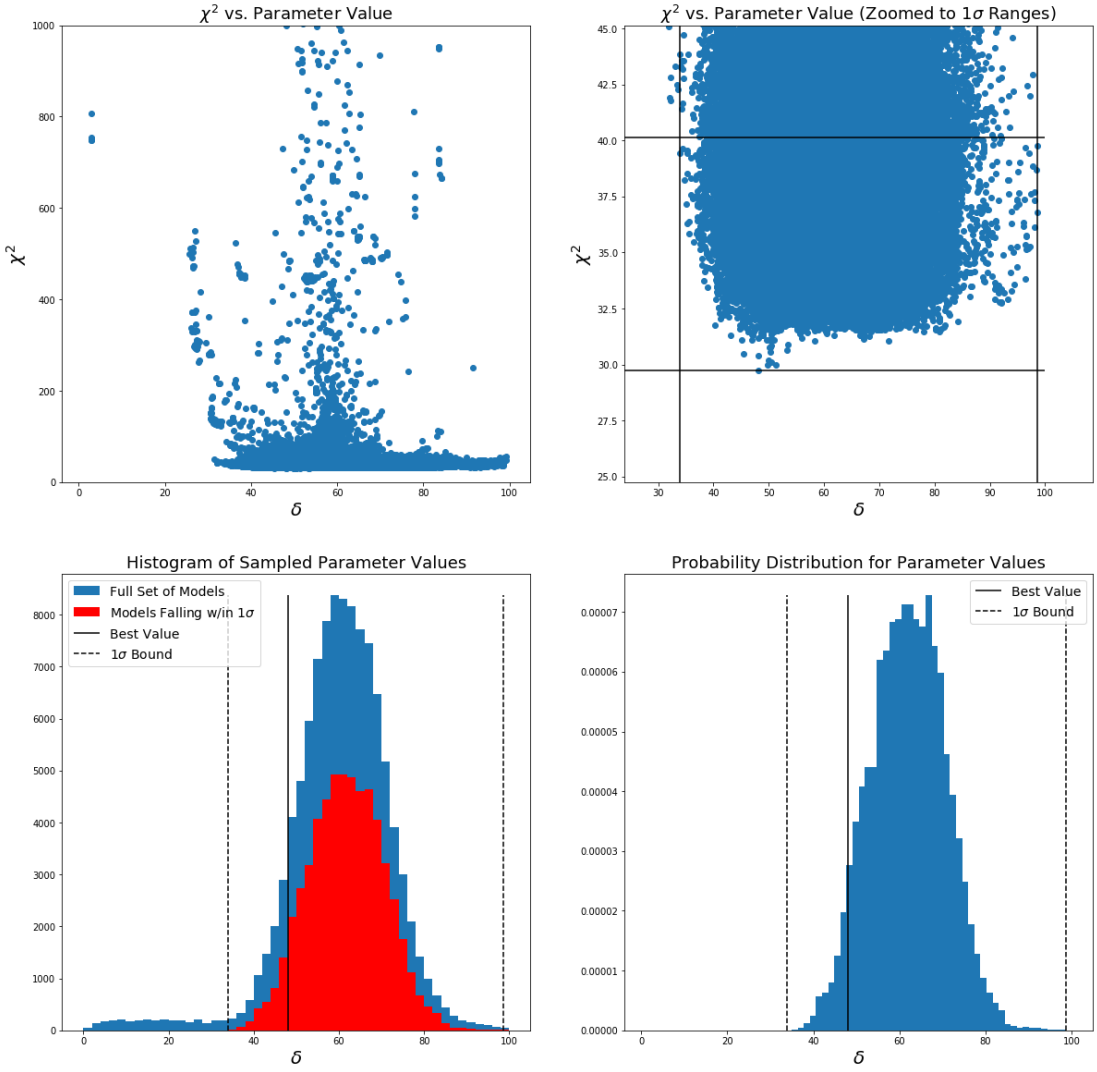

Figure A.12: *Top left*: χ^2 value plotted as a function of the δ value. *Top right*: χ^2 vs. δ value with the smallest χ^2 value and largest χ^2 1σ bounds shown as horizontal lines. The smallest and largest 1σ values of δ are marked with vertical lines. *Bottom left*: Distribution of δ values in the accepted steps. *Bottom right*: Non-normalized probability distribution for δ.

3C 66A Block 1: γ_{break}

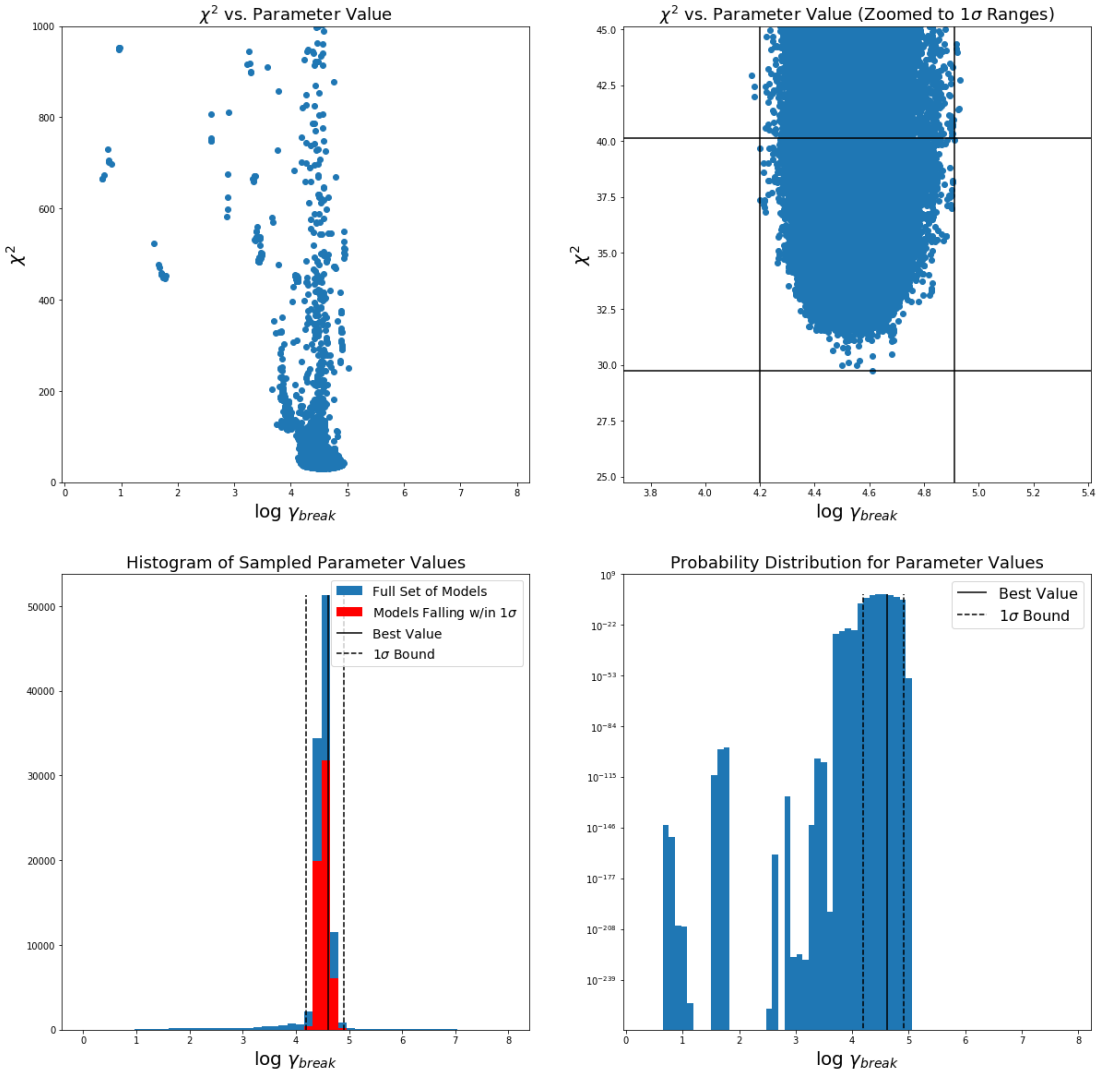

Figure A.13: *Top left*: χ^2 value plotted as a function of the γ_{break} value. *Top right*: χ^2 vs. γ_{break} value with the smallest χ^2 value and largest χ^2 1σ bounds shown as horizontal lines. The smallest and largest 1σ values of γ_{break} are marked with vertical lines. *Bottom left*: Distribution of γ_{break} values in the accepted steps. *Bottom right*: Non-normalized probability distribution for γ_{break}.

3C 66A Block 1: α_1

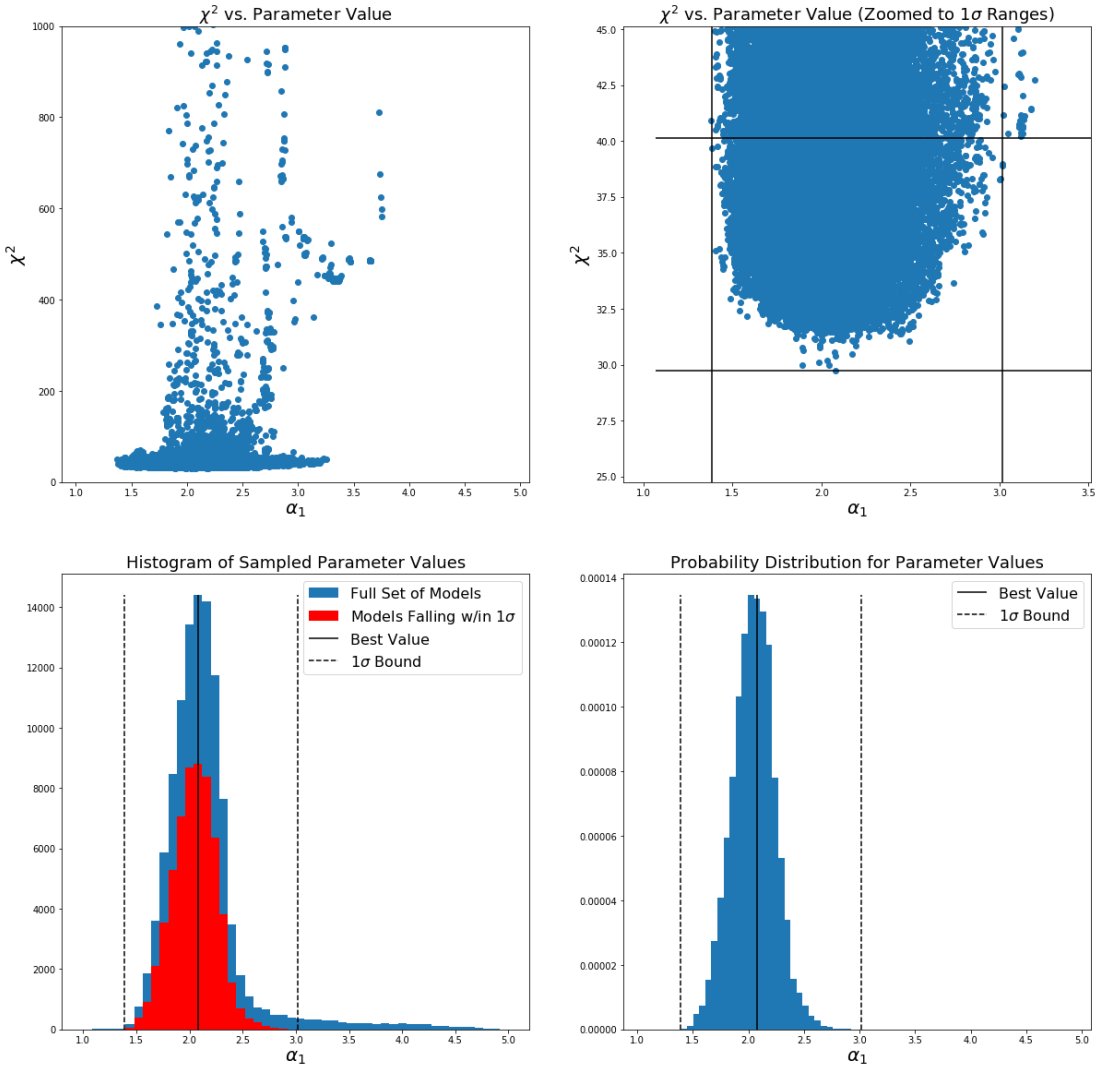

Figure A.14: *Top left*: χ^2 value plotted as a function of the α_1 value. *Top right*: χ^2 vs. α_1 value with the smallest χ^2 value and largest χ^2 1σ bounds shown as horizontal lines. The smallest and largest 1σ values of α_1 are marked with vertical lines. *Bottom left*: Distribution of α_1 values in the accepted steps. *Bottom right*: Non-normalized probability distribution for α_1.

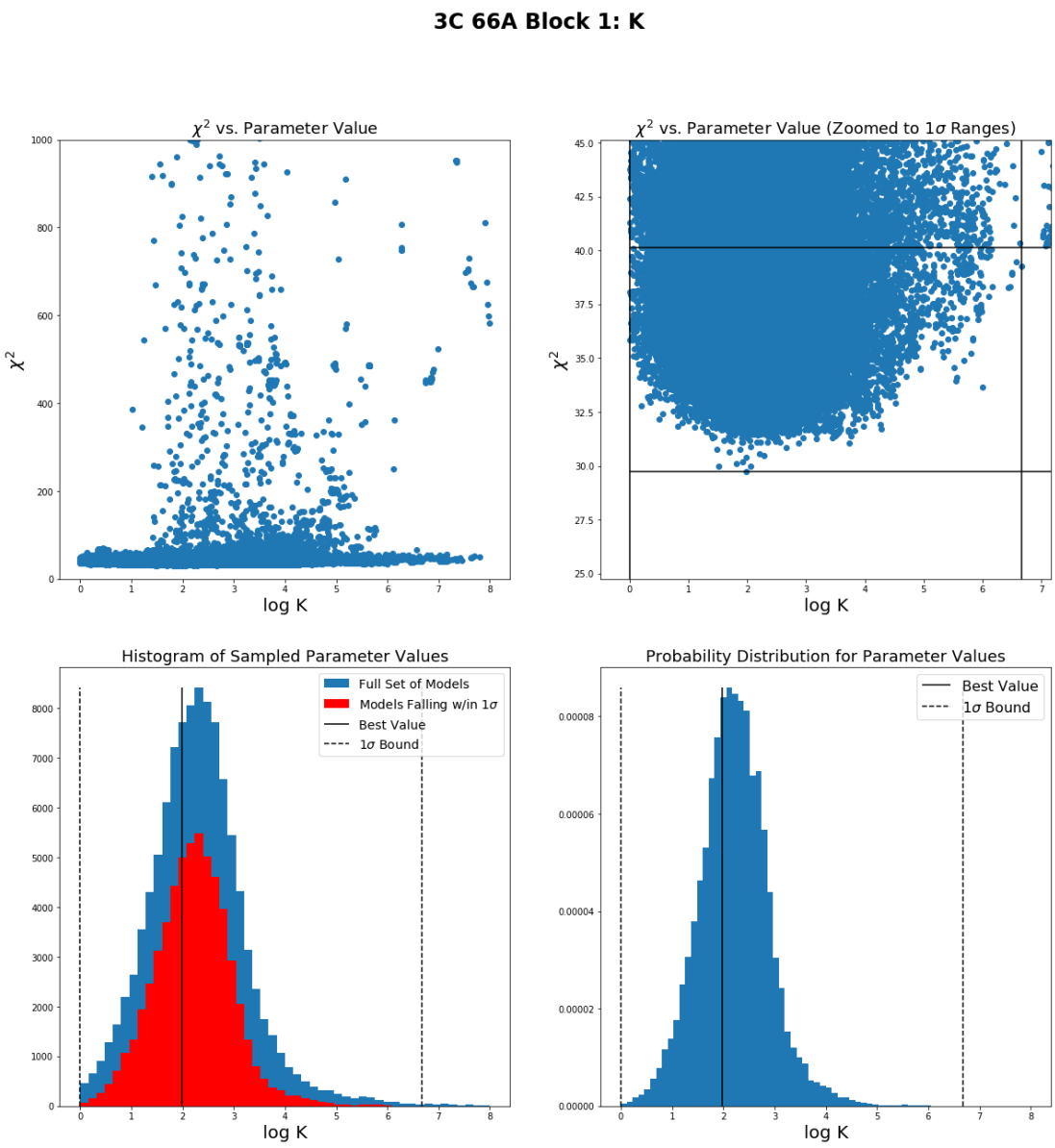

Figure A.15: *Top left*: χ^2 value plotted as a function of the K value. *Top right*: χ^2 vs. K value with the smallest χ^2 value and largest χ^2 1σ bounds shown as horizontal lines. The smallest and largest 1σ values of K are marked with vertical lines. *Bottom left*: Distribution of K values in the accepted steps. *Bottom right*: Non-normalized probability distribution for K.

3C 66A Block 1: γ_{min}

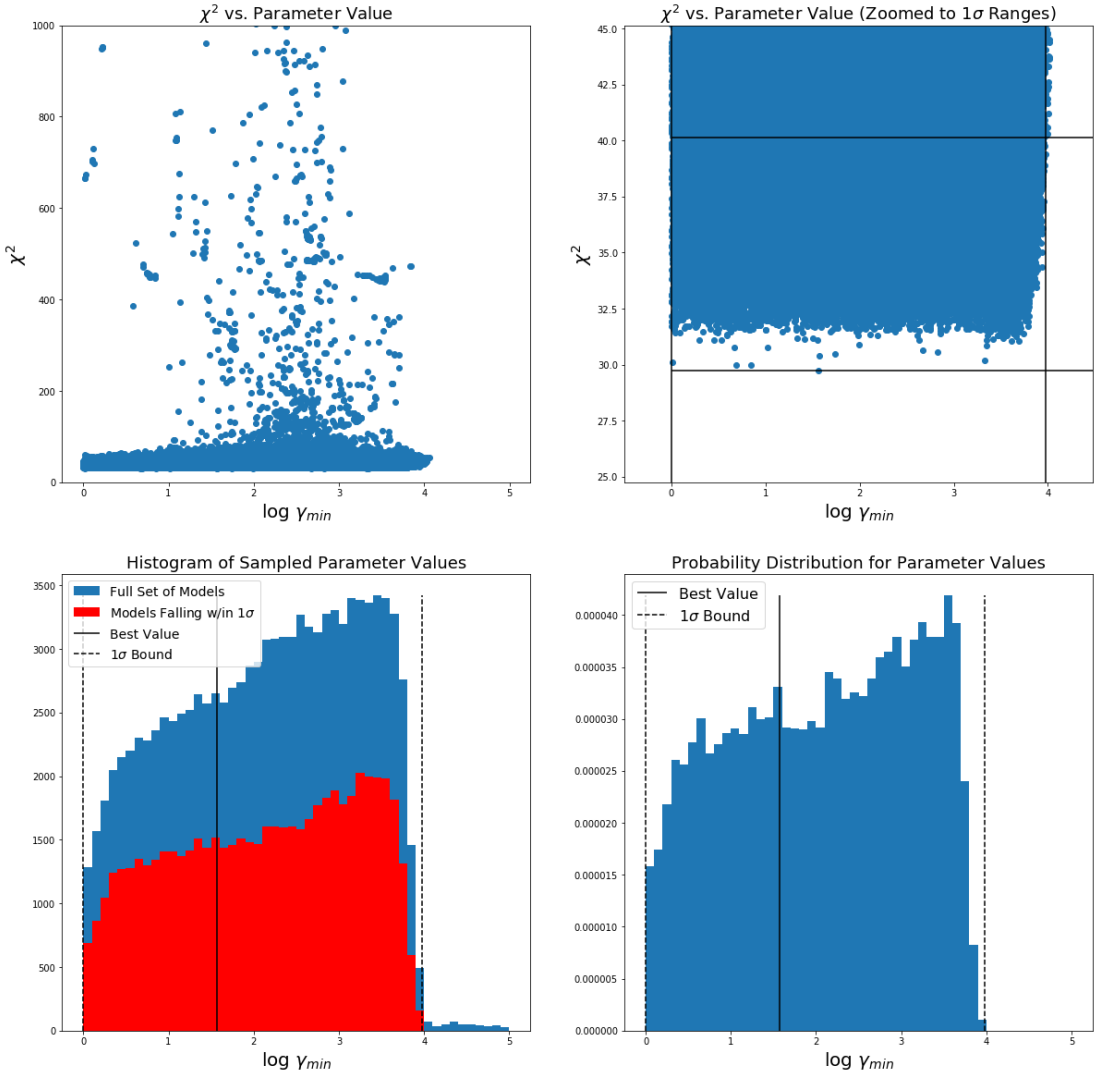

Figure A.16: *Top left*: χ^2 value plotted as a function of the γ_{min} value. *Top right*: χ^2 vs. γ_{min} value with the smallest χ^2 value and largest χ^2 1σ bounds shown as horizontal lines. The smallest and largest 1σ values of γ_{min} are marked with vertical lines. *Bottom left*: Distribution of γ_{min} values in the accepted steps. *Bottom right*: Non-normalized probability distribution for γ_{min}.

3C 66A Block 1: γ_{max}

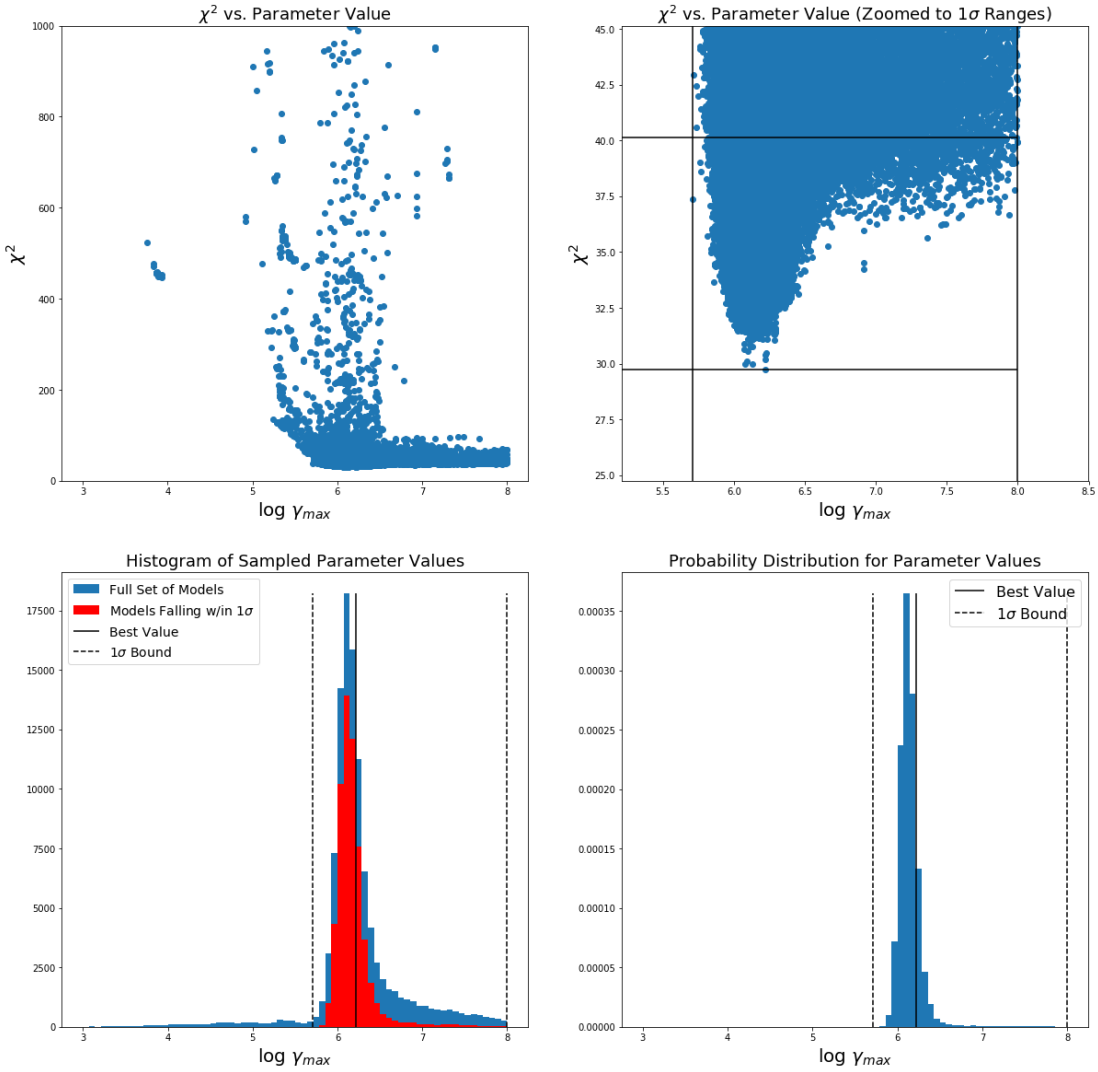

Figure A.17: *Top left*: χ^2 value plotted as a function of the γ_{max} value. *Top right*: χ^2 vs. γ_{max} value with the smallest χ^2 value and largest χ^2 1σ bounds shown as horizontal lines. The smallest and largest 1σ values of γ_{max} are marked with vertical lines. *Bottom left*: Distribution of γ_{max} values in the accepted steps. *Bottom right*: Non-normalized probability distribution for γ_{max}.

3C 66A Block 1: α_2

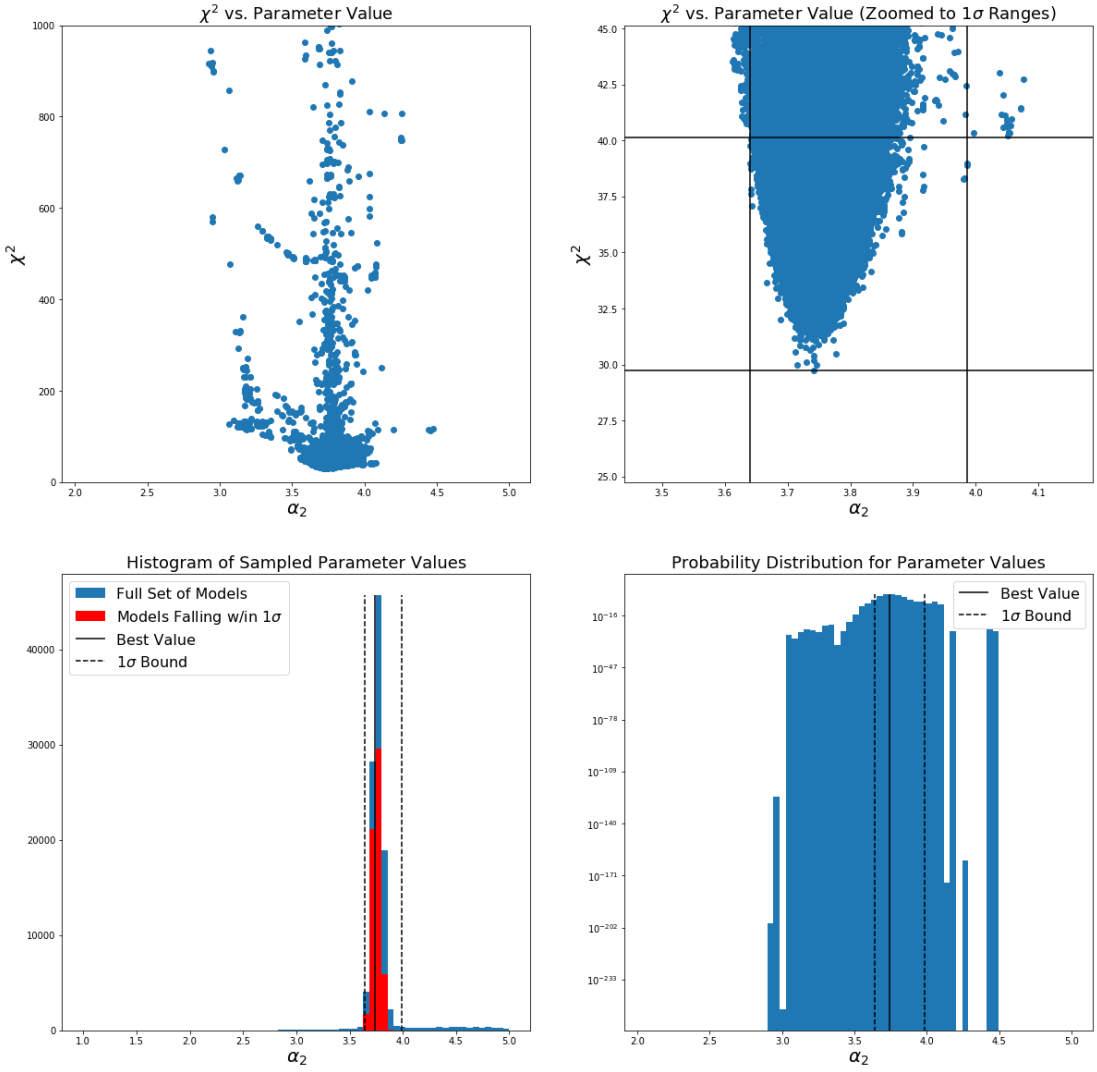

Figure A.18: *Top left*: χ^2 value plotted as a function of the α_2 value. *Top right*: χ^2 vs. α_2 value with the smallest χ^2 value and largest χ^2 1σ bounds shown as horizontal lines. The smallest and largest 1σ values of α_2 are marked with vertical lines. *Bottom left*: Distribution of α_2 values in the accepted steps. *Bottom right*: Non-normalized probability distribution for α_2.

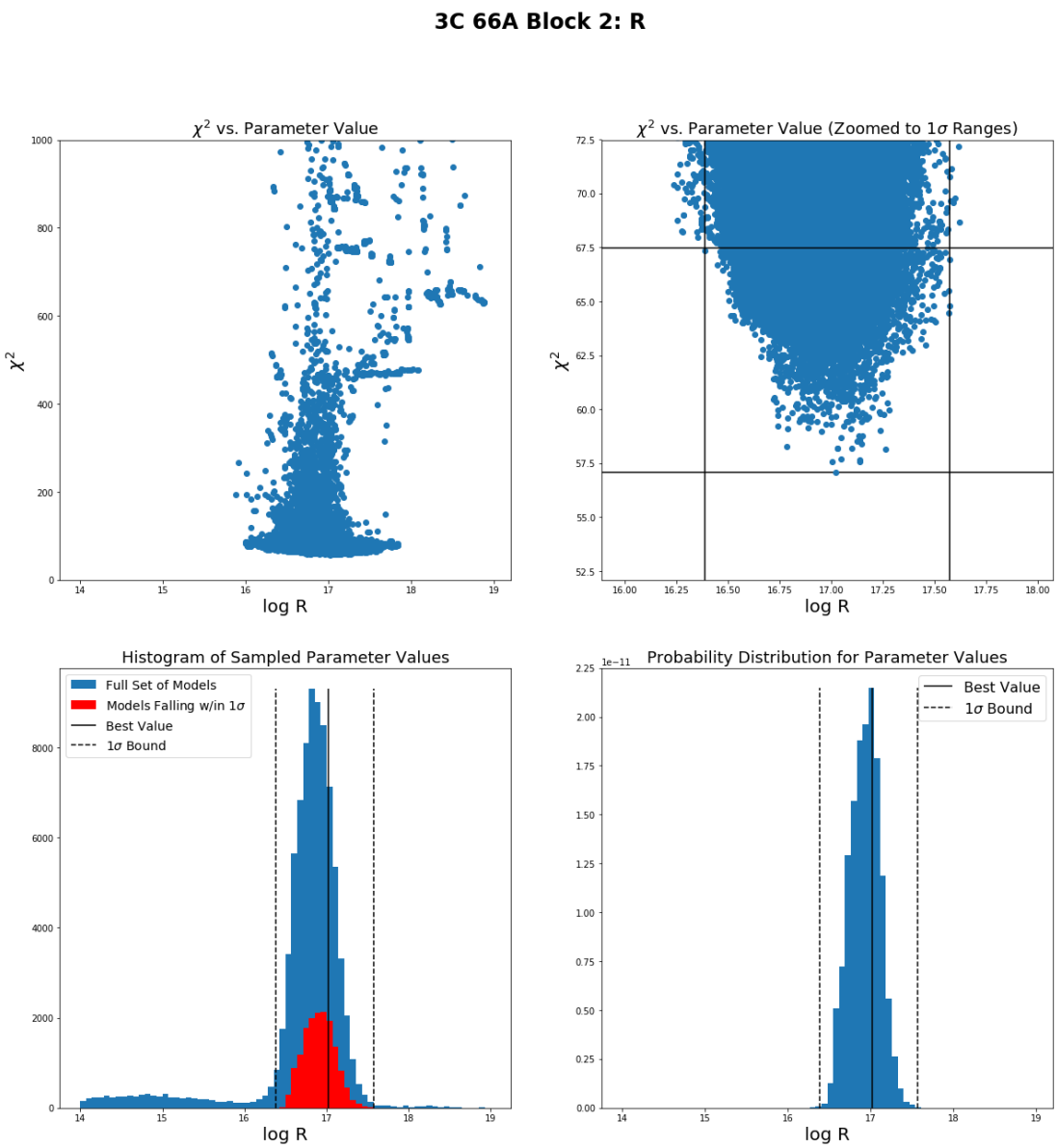

Figure A.19: *Top left*: χ^2 value plotted as a function of the R value. *Top right*: χ^2 vs. R value with the smallest χ^2 value and largest χ^2 1σ bounds shown as horizontal lines. The smallest and largest 1σ values of R are marked with vertical lines. *Bottom left*: Distribution of R values in the accepted steps. *Bottom right*: Non-normalized probability distribution for R.

3C 66A Block 2: B

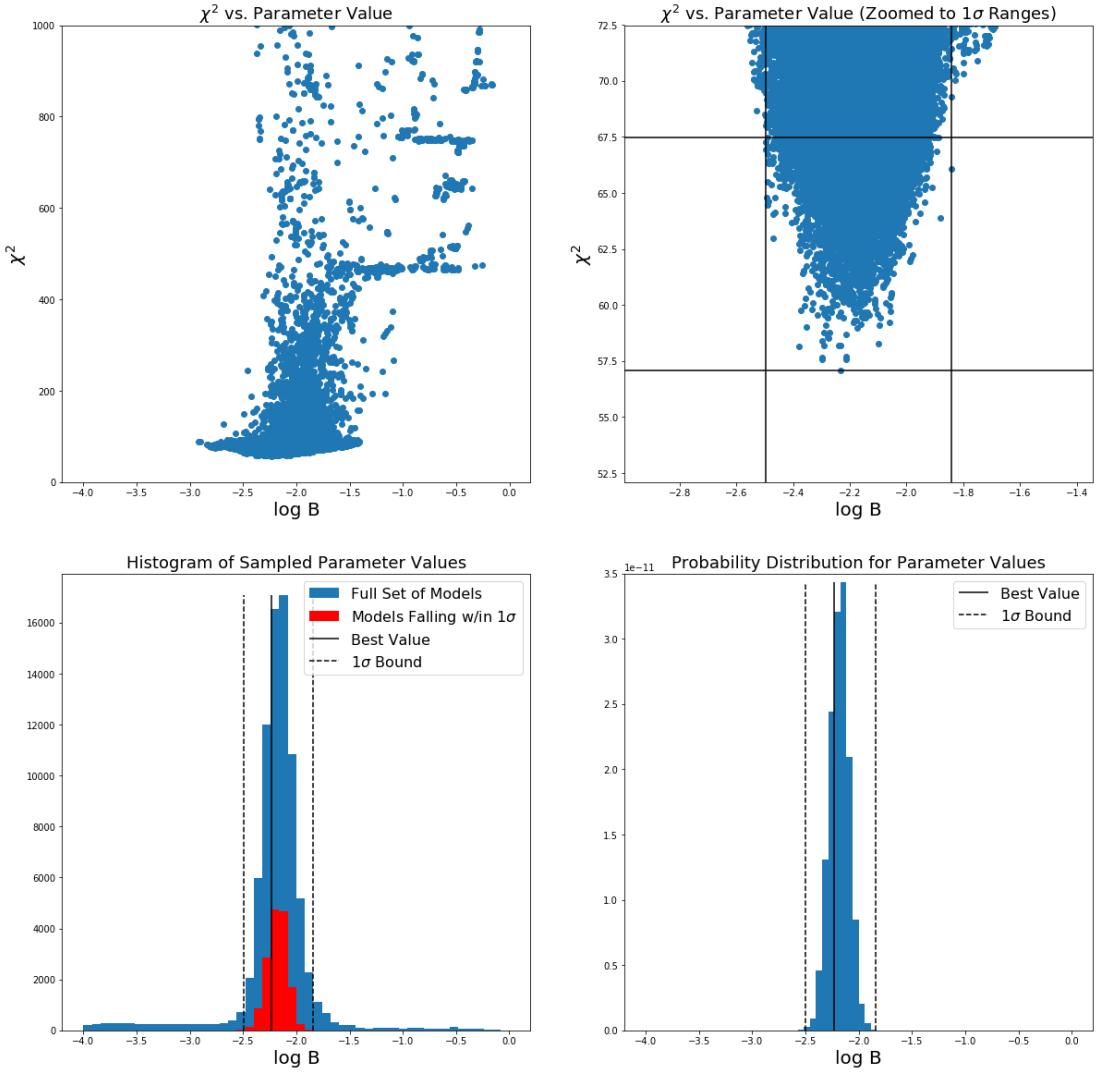

Figure A.20: *Top left*: χ^2 value plotted as a function of the B value. *Top right*: χ^2 vs. B value with the smallest χ^2 value and largest χ^2 1σ bounds shown as horizontal lines. The smallest and largest 1σ values of B are marked with vertical lines. *Bottom left*: Distribution of B values in the accepted steps. *Bottom right*: Non-normalized probability distribution for B.

3C 66A Block 2: δ

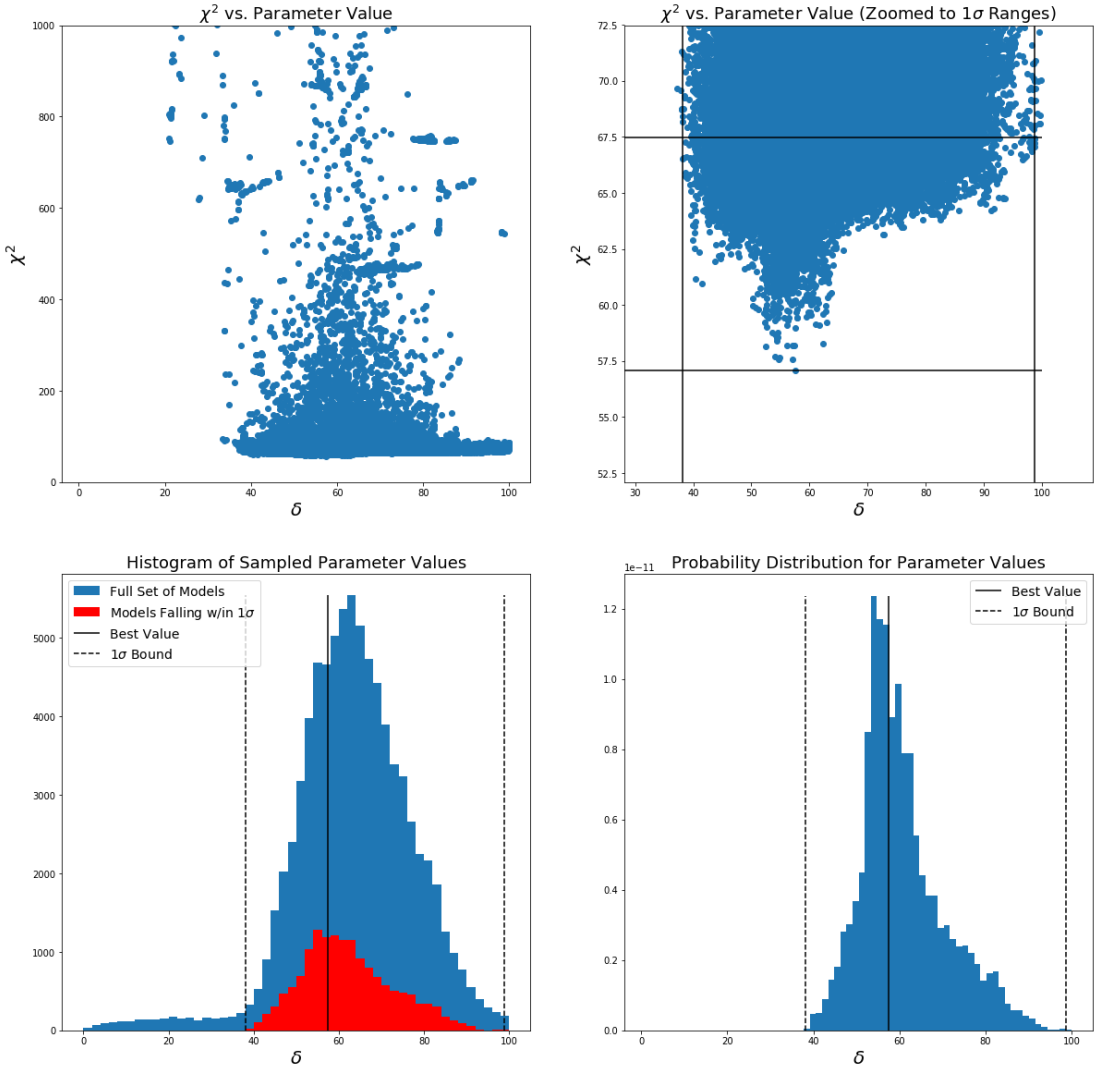

Figure A.21: *Top left*: χ^2 value plotted as a function of the δ value. *Top right*: χ^2 vs. δ value with the smallest χ^2 value and largest χ^2 1σ bounds shown as horizontal lines. The smallest and largest 1σ values of δ are marked with vertical lines. *Bottom left*: Distribution of δ values in the accepted steps. *Bottom right*: Non-normalized probability distribution for δ.

3C 66A Block 2: γ_{break}

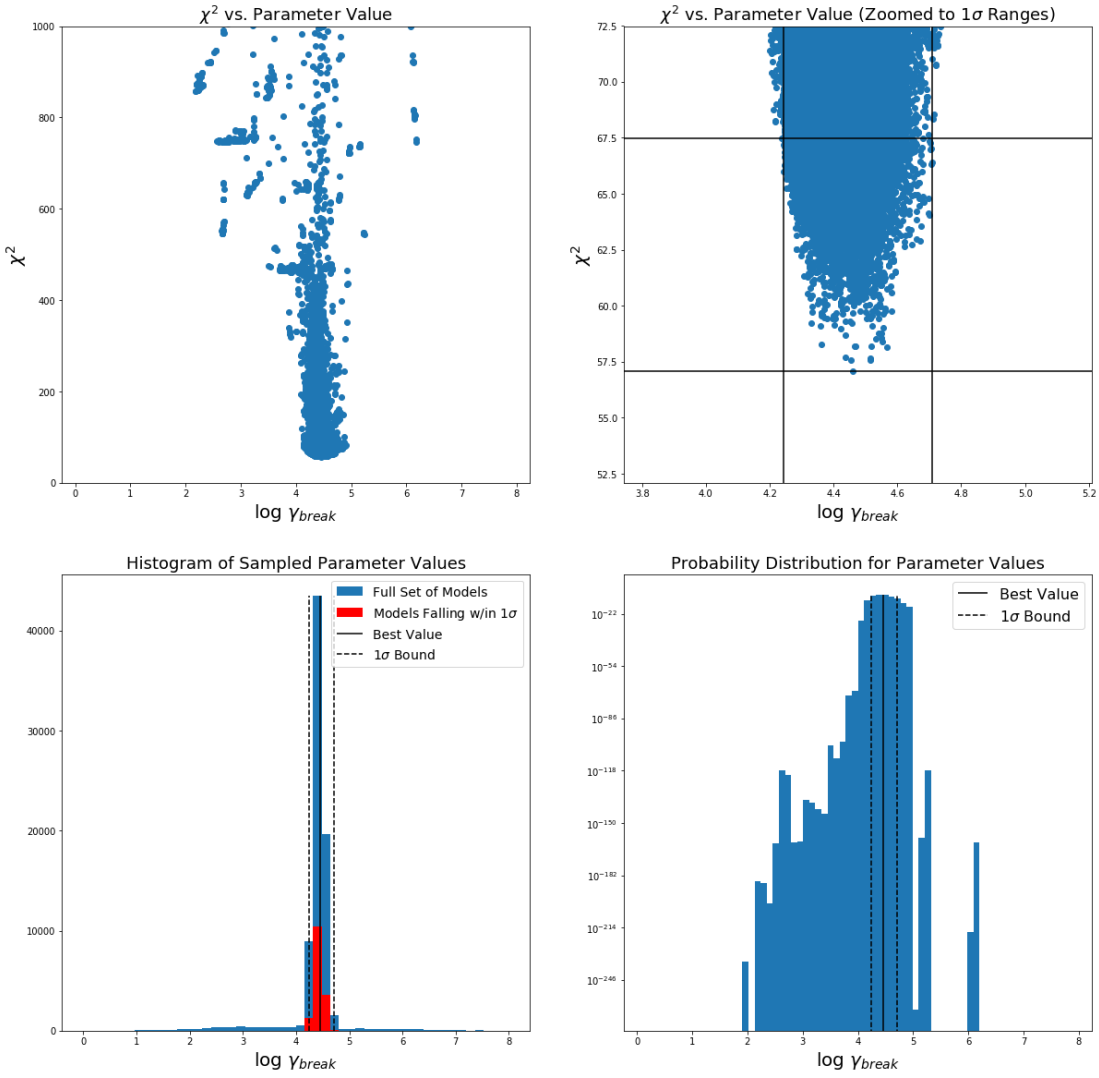

Figure A.22: *Top left*: χ^2 value plotted as a function of the γ_{break} value. *Top right*: χ^2 vs. γ_{break} value with the smallest χ^2 value and largest χ^2 1σ bounds shown as horizontal lines. The smallest and largest 1σ values of γ_{break} are marked with vertical lines. *Bottom left*: Distribution of γ_{break} values in the accepted steps. *Bottom right*: Non-normalized probability distribution for γ_{break}.

3C 66A Block 2: α_1

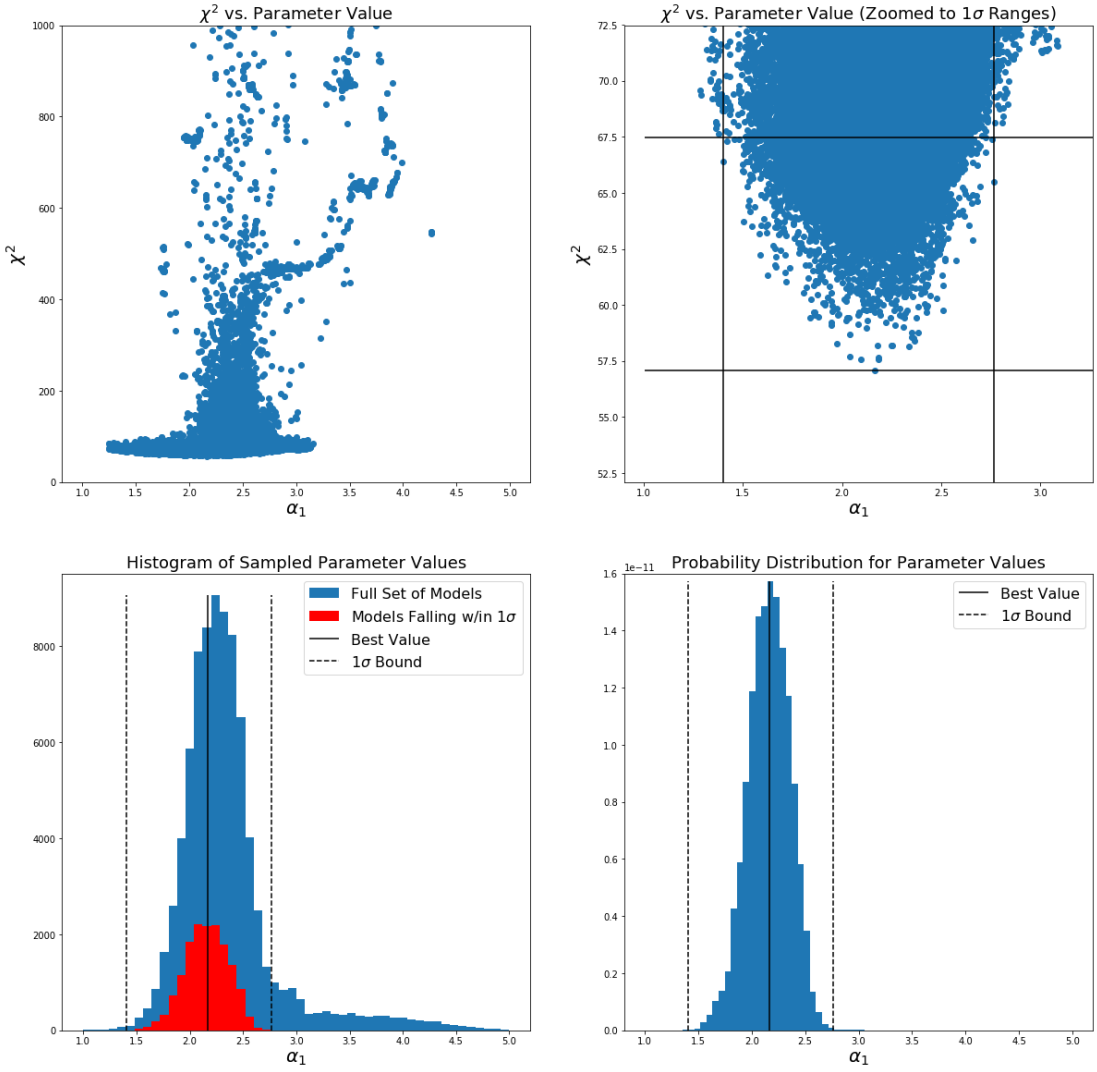

Figure A.23: *Top left*: χ^2 value plotted as a function of the α_1 value. *Top right*: χ^2 vs. α_1 value with the smallest χ^2 value and largest χ^2 1σ bounds shown as horizontal lines. The smallest and largest 1σ values of α_1 are marked with vertical lines. *Bottom left*: Distribution of α_1 values in the accepted steps. *Bottom right*: Non-normalized probability distribution for α_1.

3C 66A Block 2: K

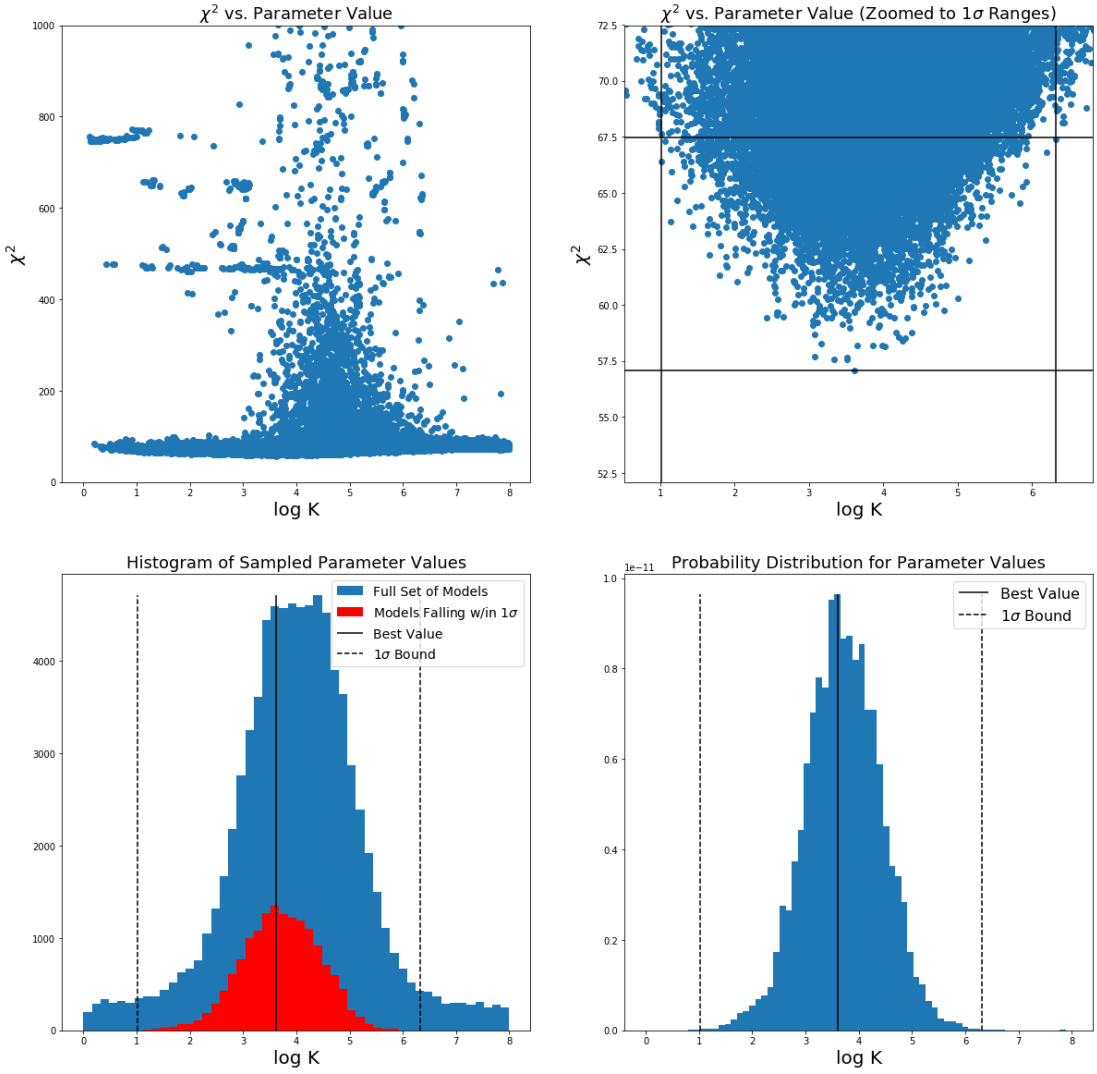

Figure A.24: *Top left*: χ^2 value plotted as a function of the K value. *Top right*: χ^2 vs. K value with the smallest χ^2 value and largest χ^2 1σ bounds shown as horizontal lines. The smallest and largest 1σ values of K are marked with vertical lines. *Bottom left*: Distribution of K values in the accepted steps. *Bottom right*: Non-normalized probability distribution for K.

3C 66A Block 2: γ_{min}

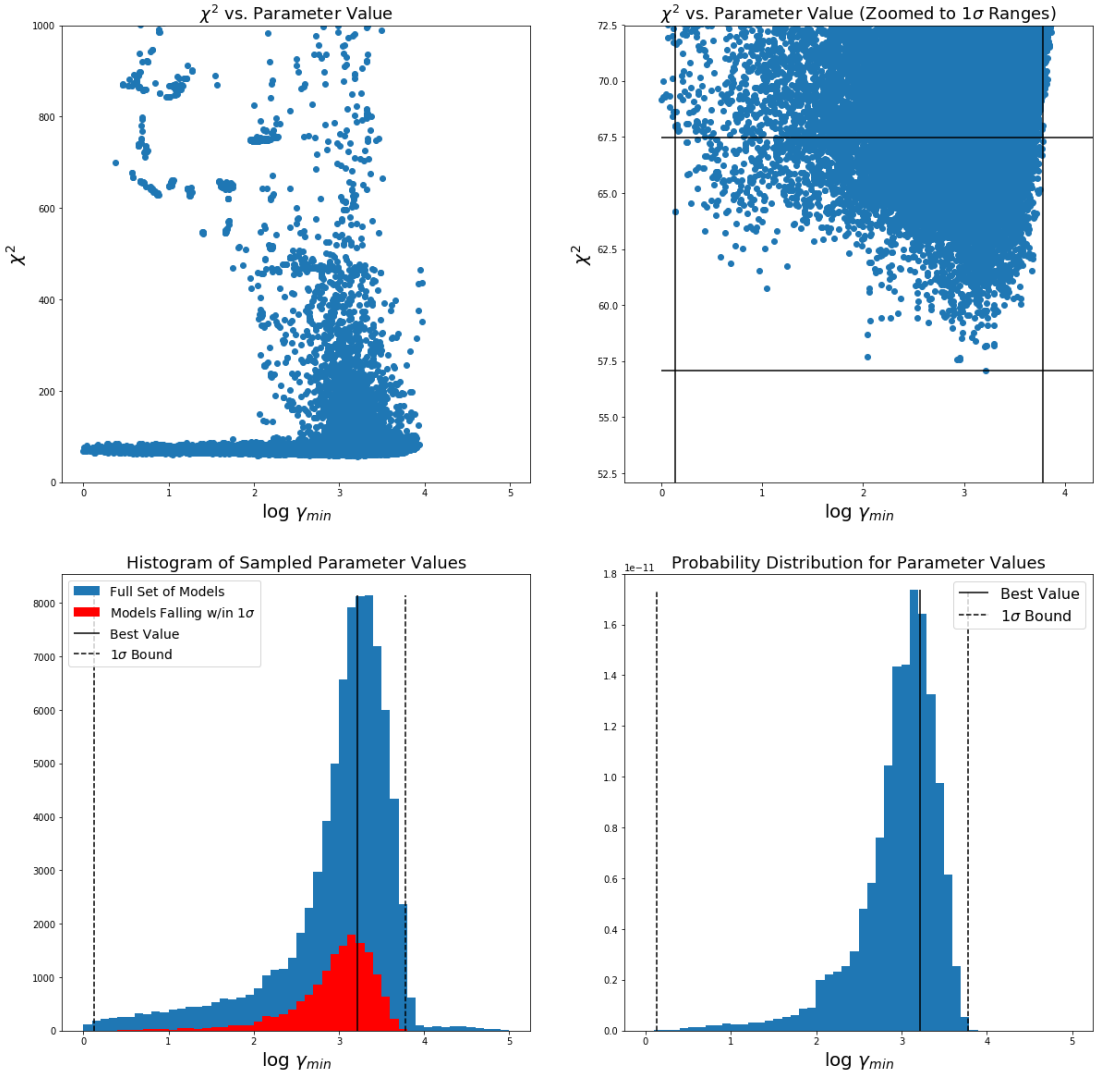

Figure A.25: *Top left*: χ^2 value plotted as a function of the γ_{min} value. *Top right*: χ^2 vs. γ_{min} value with the smallest χ^2 value and largest χ^2 1σ bounds shown as horizontal lines. The smallest and largest 1σ values of γ_{min} are marked with vertical lines. *Bottom left*: Distribution of γ_{min} values in the accepted steps. *Bottom right*: Non-normalized probability distribution for γ_{min}.

3C 66A Block 2: γ_{max}

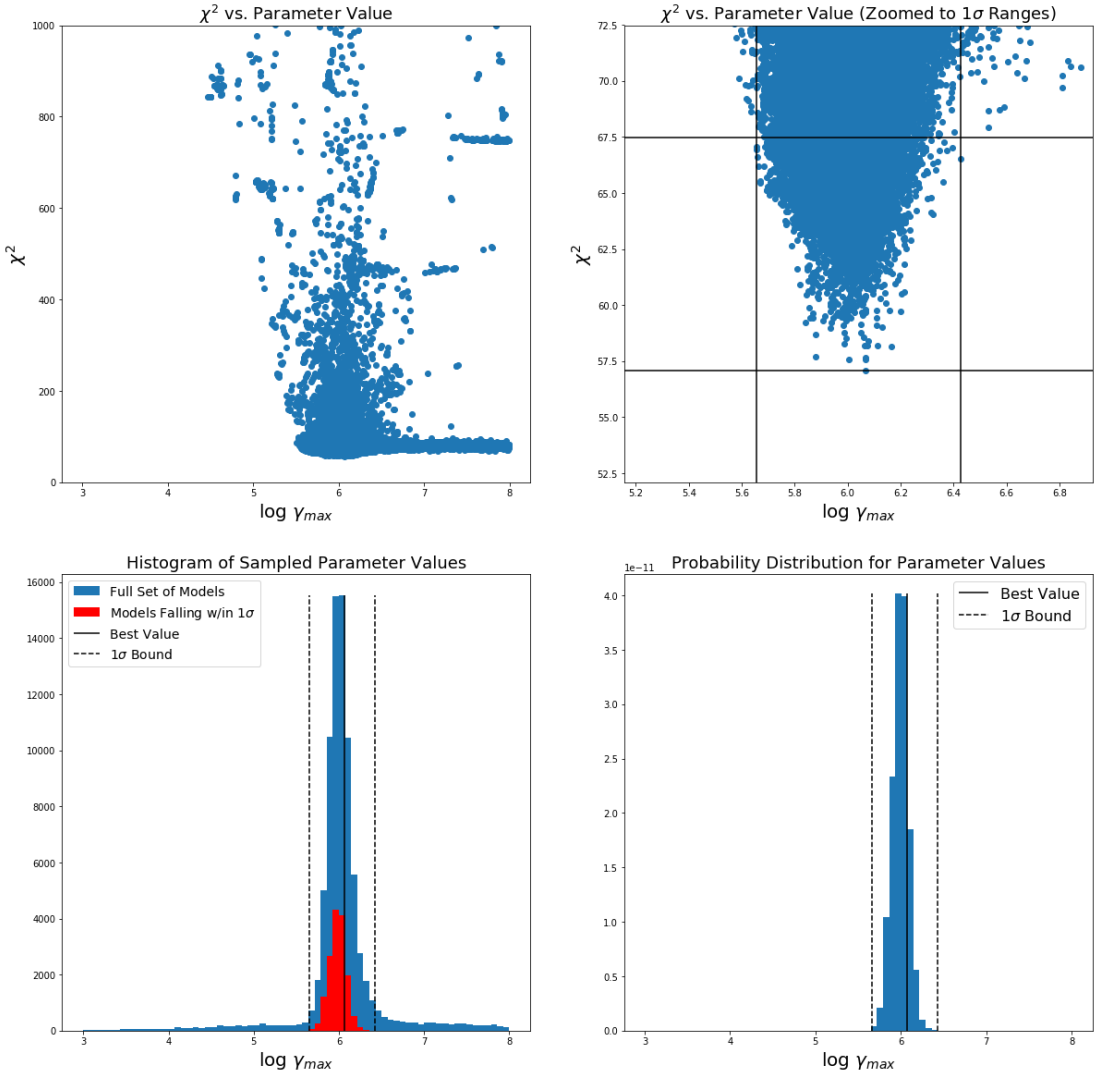

Figure A.26: *Top left*: χ^2 value plotted as a function of the γ_{max} value. *Top right*: χ^2 vs. γ_{max} value with the smallest χ^2 value and largest χ^2 1σ bounds shown as horizontal lines. The smallest and largest 1σ values of γ_{max} are marked with vertical lines. *Bottom left*: Distribution of γ_{max} values in the accepted steps. *Bottom right*: Non-normalized probability distribution for γ_{max}.

3C 66A Block 2: α_2

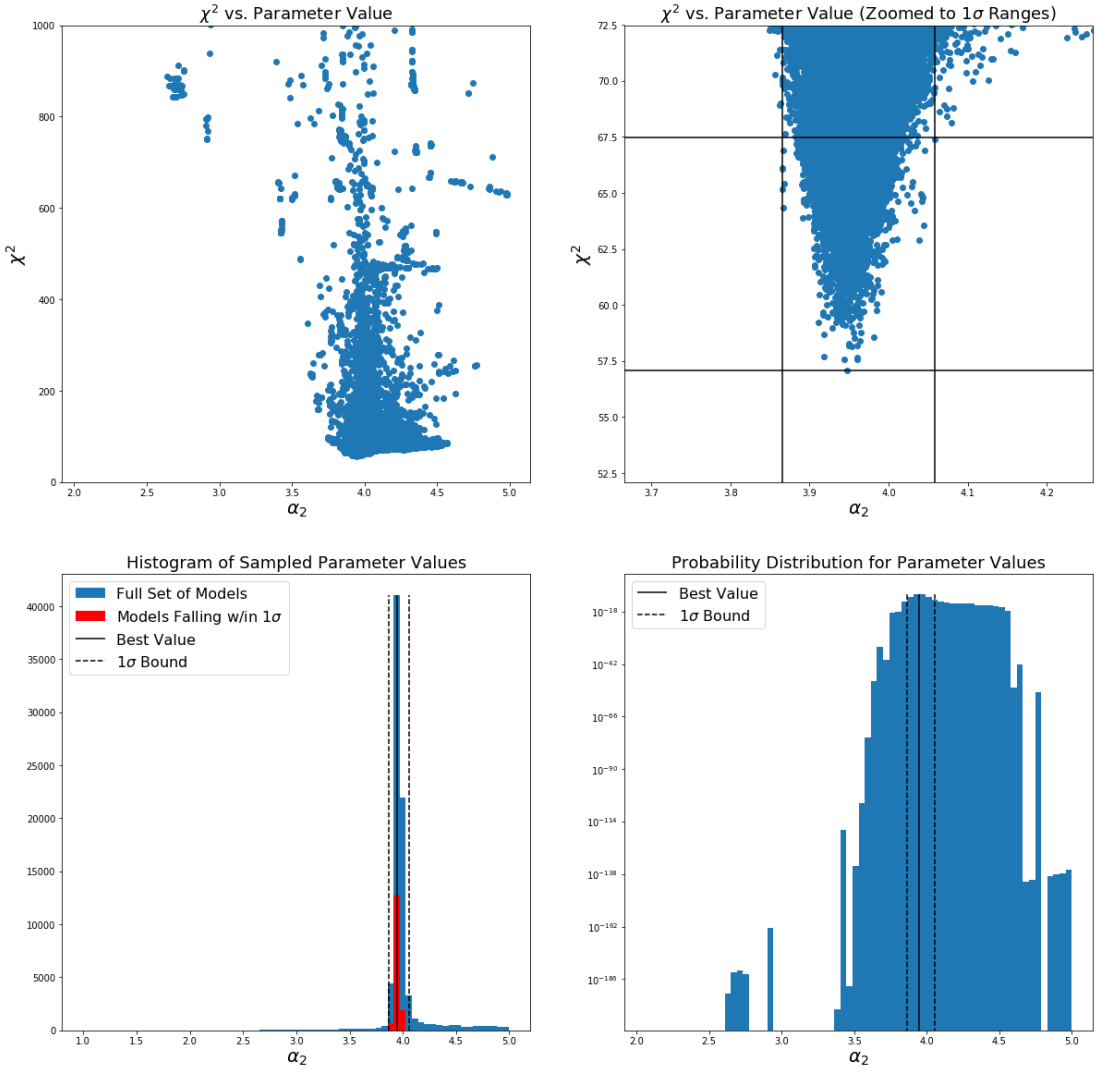

Figure A.27: *Top left*: χ^2 value plotted as a function of the α_2 value. *Top right*: χ^2 vs. α_2 value with the smallest χ^2 value and largest χ^2 1σ bounds shown as horizontal lines. The smallest and largest 1σ values of α_2 are marked with vertical lines. *Bottom left*: Distribution of α_2 values in the accepted steps. *Bottom right*: Non-normalized probability distribution for α_2.

A.4 3C 66A: Block 5

Figures A.28 - A.36 show the results from the MCMC modeling of the SED of 3C 66A during block 5.

A.5 3C 66A: Block 6

Figures A.37 - A.45 show the results from the MCMC modeling of the SED of 3C 66A during block 6.

3C 66A Block 5: R

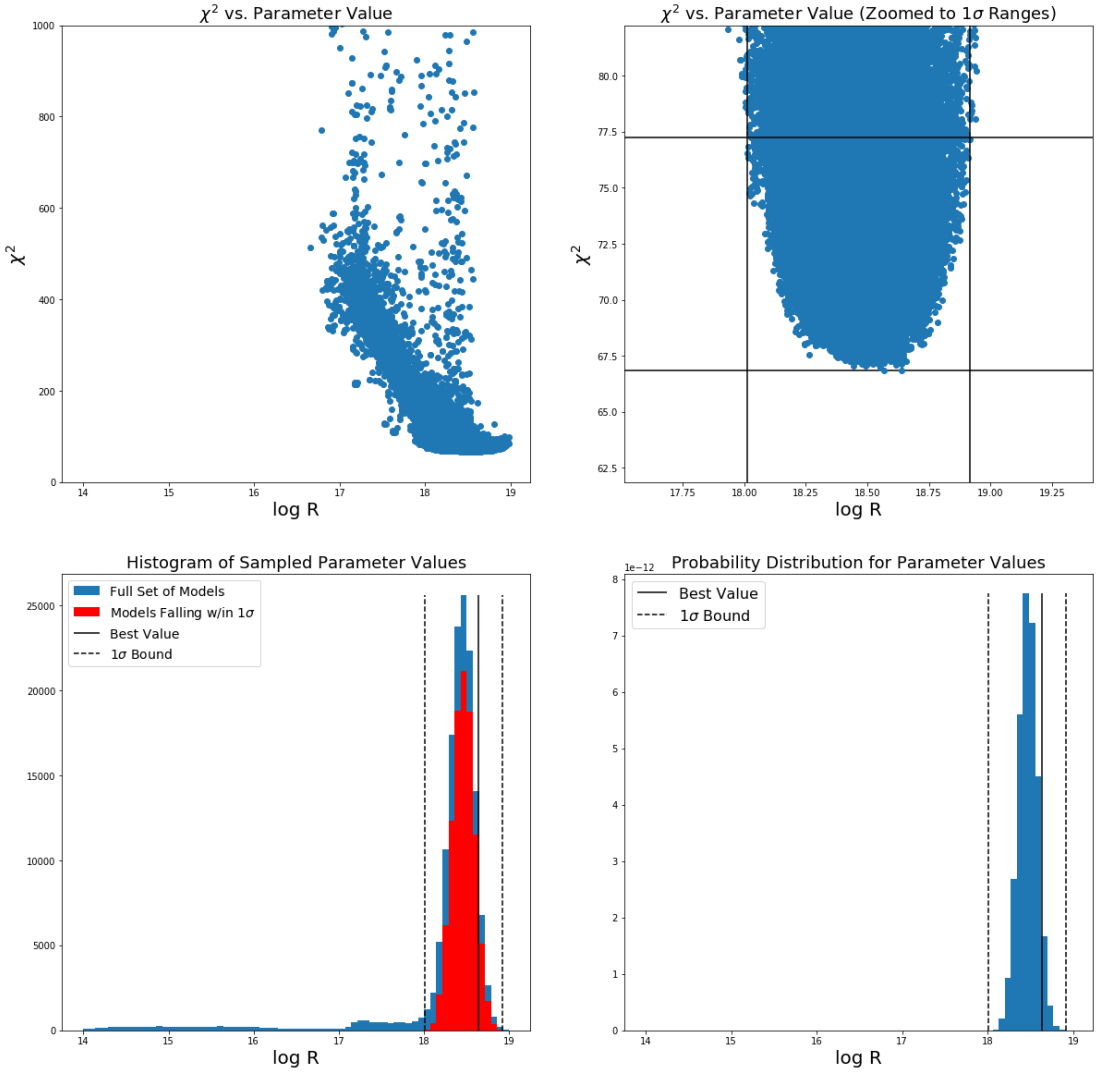

Figure A.28: *Top left*: χ^2 value plotted as a function of the R value. *Top right*: χ^2 vs. R value with the smallest χ^2 value and largest χ^2 1σ bounds shown as horizontal lines. The smallest and largest 1σ values of R are marked with vertical lines. *Bottom left*: Distribution of R values in the accepted steps. *Bottom right*: Non-normalized probability distribution for R.

3C 66A Block 5: B

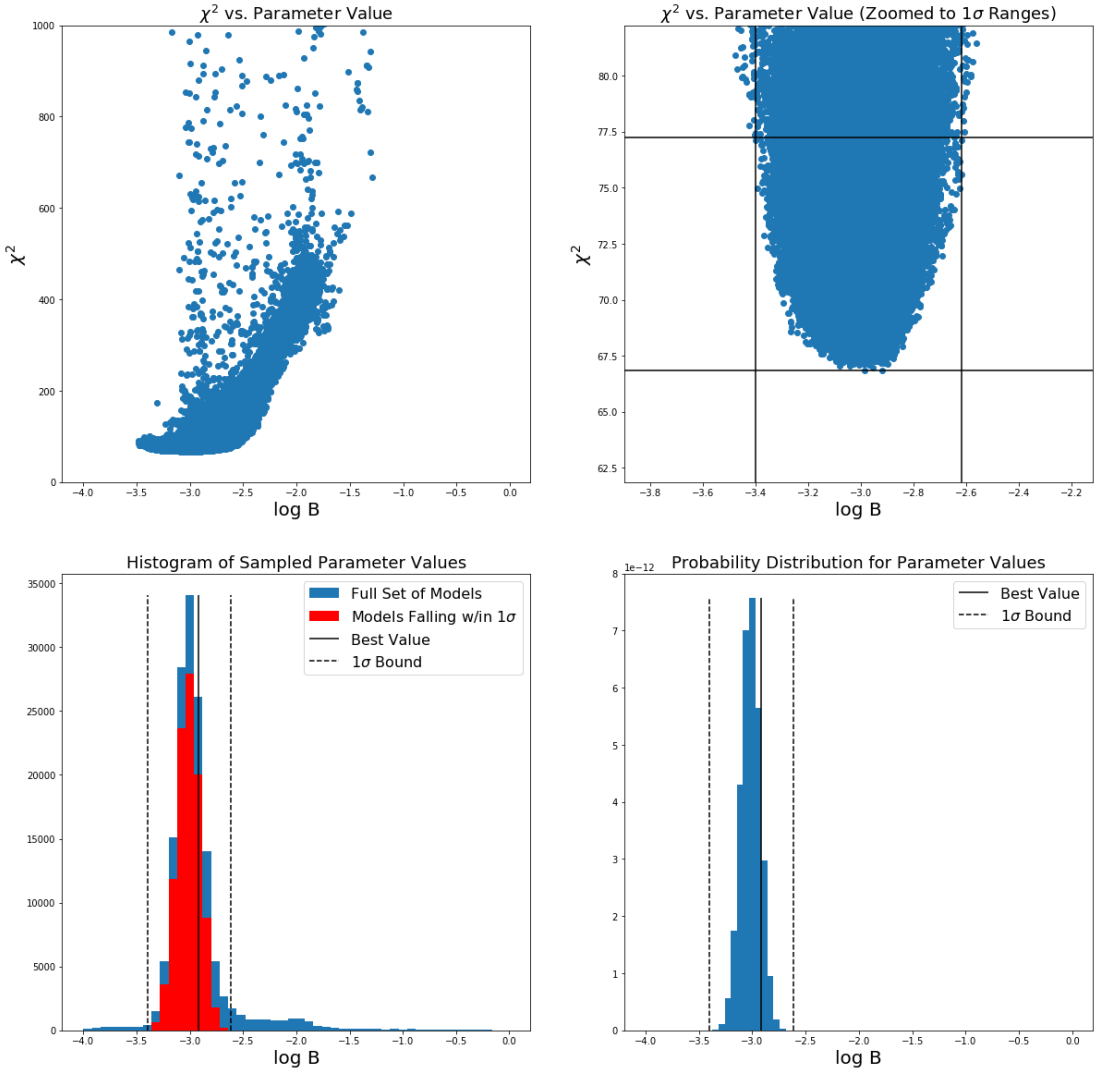

Figure A.29: *Top left*: χ^2 value plotted as a function of the B value. *Top right*: χ^2 vs. B value with the smallest χ^2 value and largest χ^2 1σ bounds shown as horizontal lines. The smallest and largest 1σ values of B are marked with vertical lines. *Bottom left*: Distribution of B values in the accepted steps. *Bottom right*: Non-normalized probability distribution for B.

3C 66A Block 5: δ

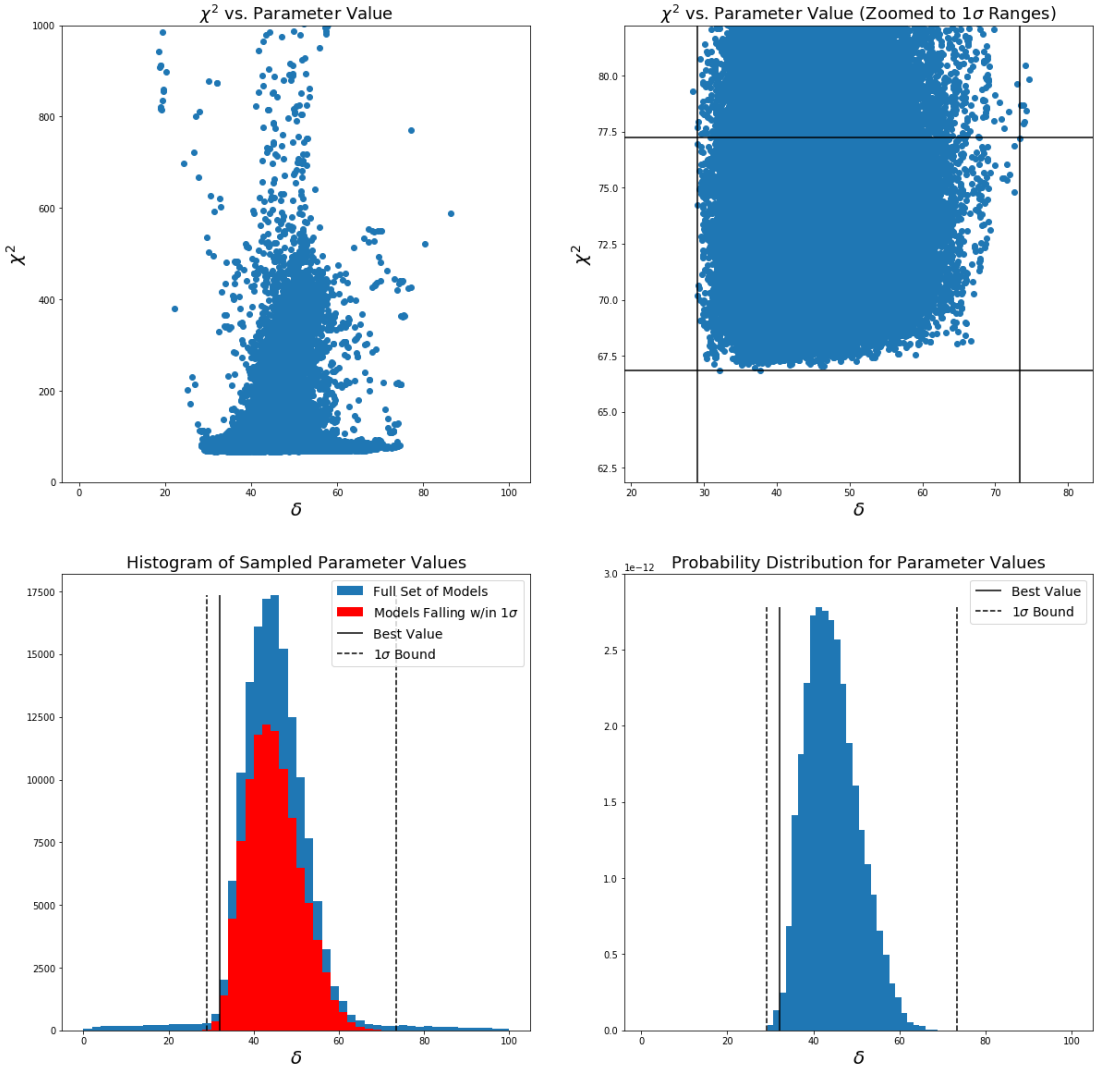

Figure A.30: *Top left*: χ^2 value plotted as a function of the δ value. *Top right*: χ^2 vs. δ value with the smallest χ^2 value and largest χ^2 1σ bounds shown as horizontal lines. The smallest and largest 1σ values of δ are marked with vertical lines. *Bottom left*: Distribution of δ values in the accepted steps. *Bottom right*: Non-normalized probability distribution for δ.

3C 66A Block 5: γ_{break}

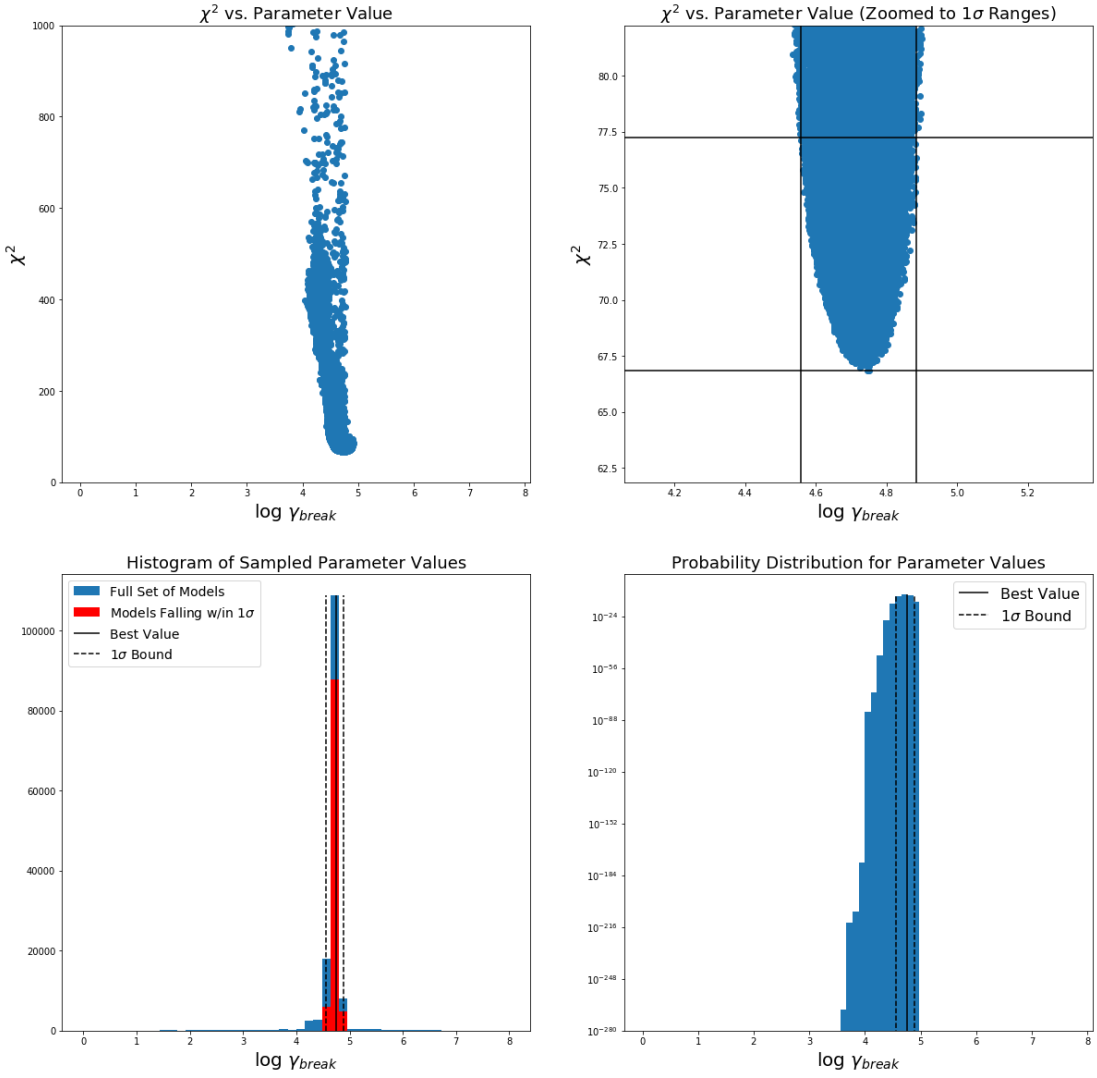

Figure A.31: *Top left*: χ^2 value plotted as a function of the γ_{break} value. *Top right*: χ^2 vs. γ_{break} value with the smallest χ^2 value and largest χ^2 1σ bounds shown as horizontal lines. The smallest and largest 1σ values of γ_{break} are marked with vertical lines. *Bottom left*: Distribution of γ_{break} values in the accepted steps. *Bottom right*: Non-normalized probability distribution for γ_{break}.

3C 66A Block 5: α_1

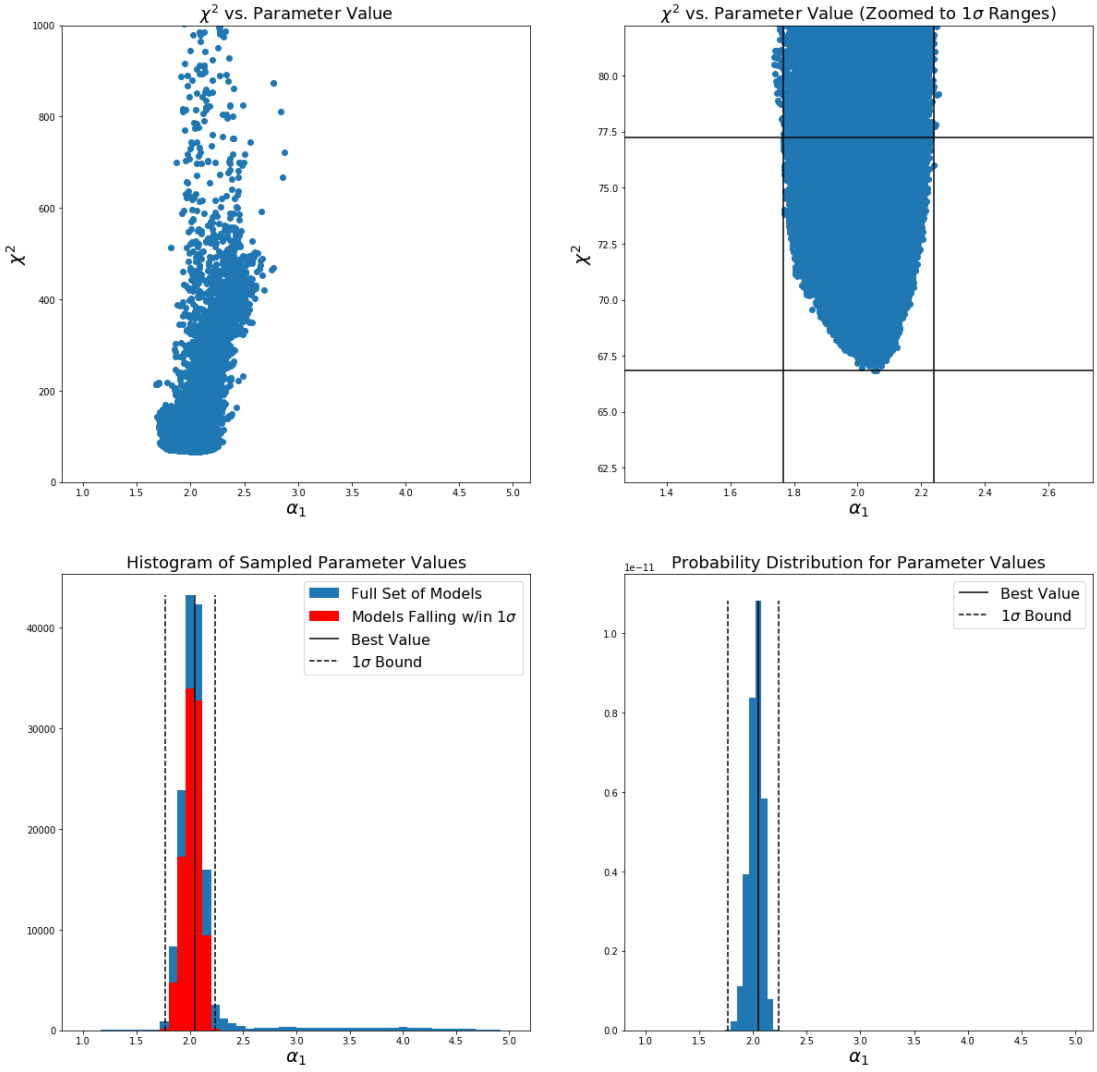

Figure A.32: *Top left*: χ^2 value plotted as a function of the α_1 value. *Top right*: χ^2 vs. α_1 value with the smallest χ^2 value and largest χ^2 1σ bounds shown as horizontal lines. The smallest and largest 1σ values of α_1 are marked with vertical lines. *Bottom left*: Distribution of α_1 values in the accepted steps. *Bottom right*: Non-normalized probability distribution for α_1.

3C 66A Block 5: K

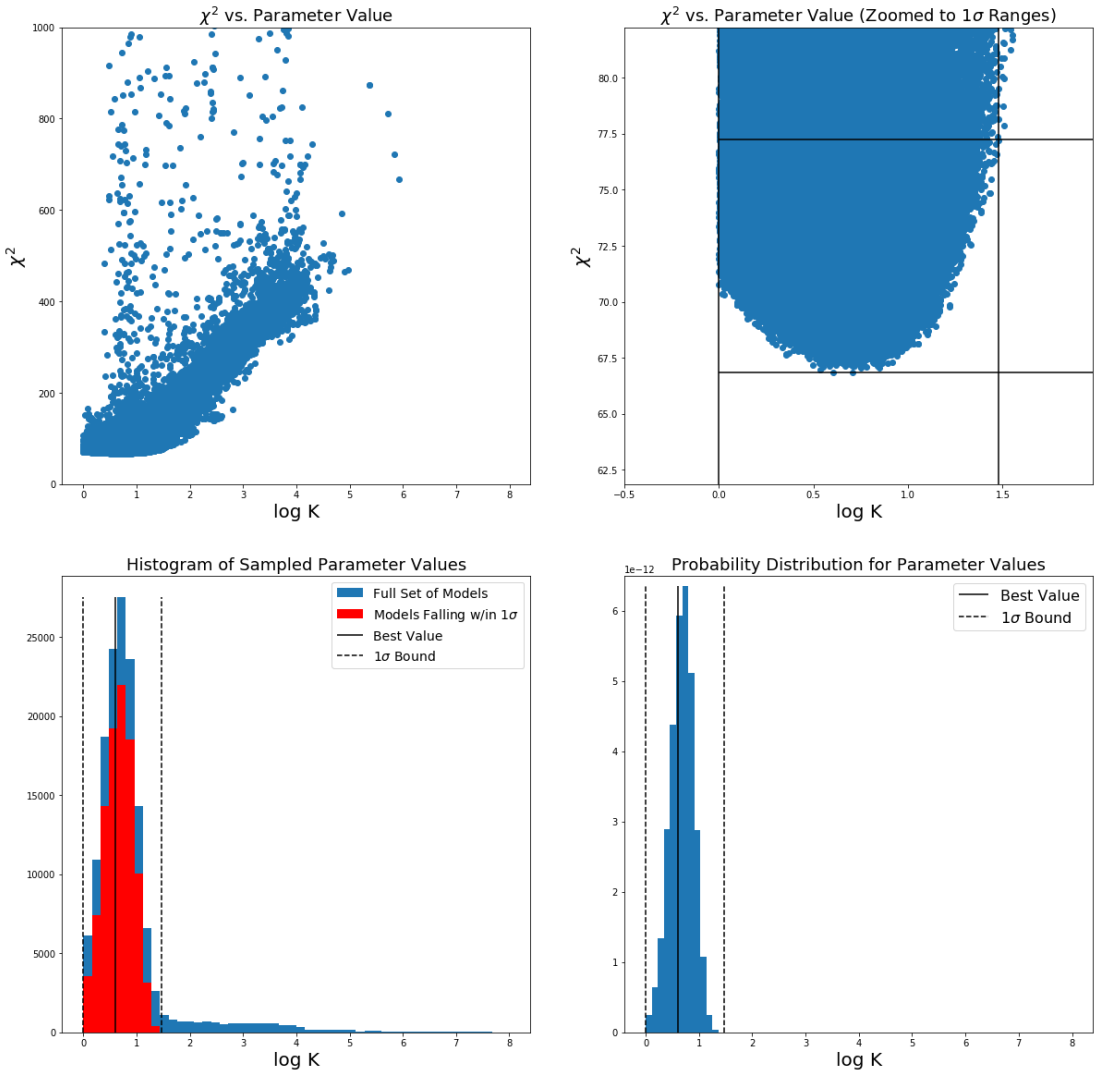

Figure A.33: *Top left*: χ^2 value plotted as a function of the K value. *Top right*: χ^2 vs. K value with the smallest χ^2 value and largest χ^2 1σ bounds shown as horizontal lines. The smallest and largest 1σ values of K are marked with vertical lines. *Bottom left*: Distribution of K values in the accepted steps. *Bottom right*: Non-normalized probability distribution for K.

3C 66A Block 5: γ_{min}

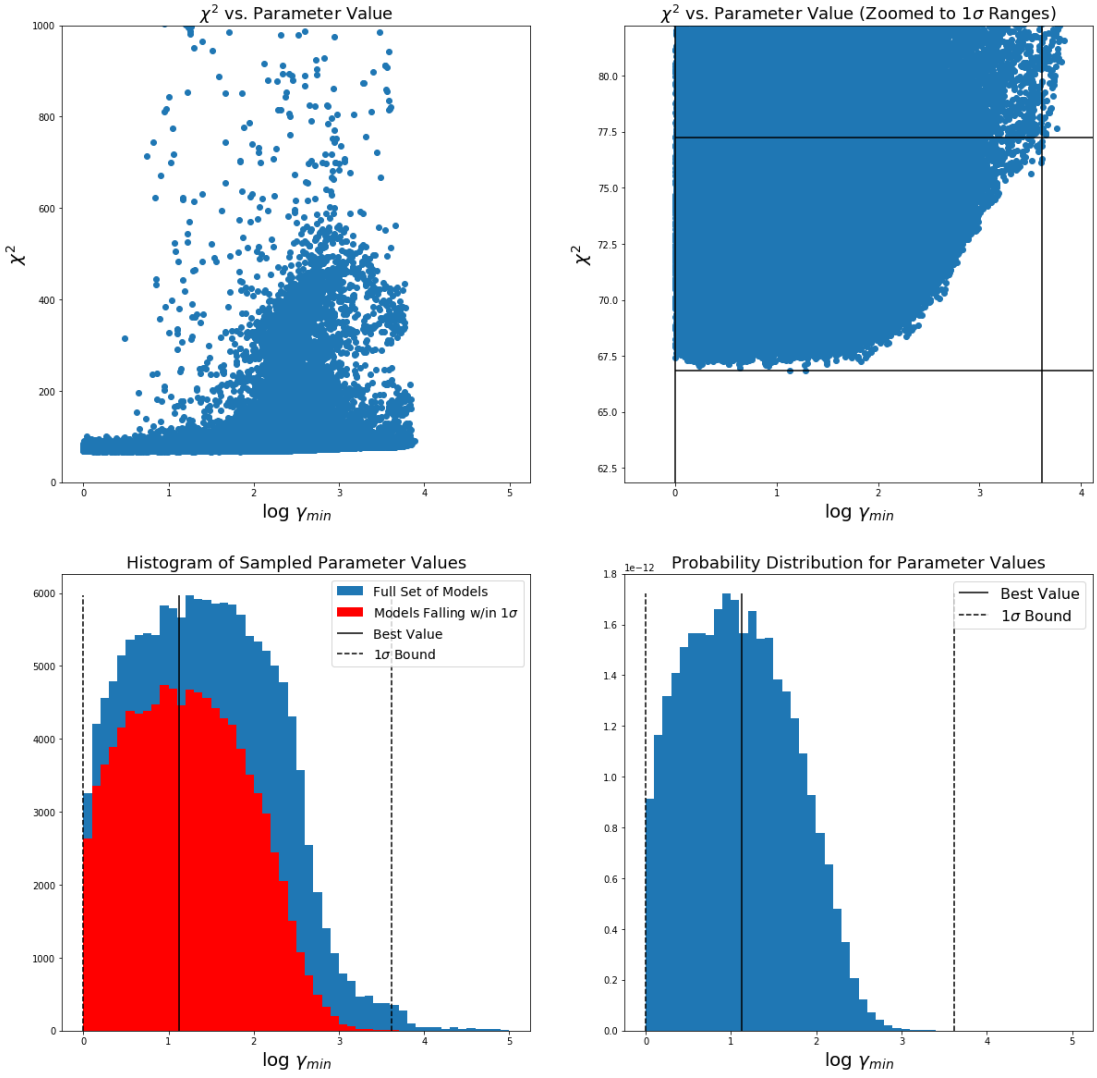

Figure A.34: *Top left*: χ^2 value plotted as a function of the γ_{min} value. *Top right*: χ^2 vs. γ_{min} value with the smallest χ^2 value and largest χ^2 1σ bounds shown as horizontal lines. The smallest and largest 1σ values of γ_{min} are marked with vertical lines. *Bottom left*: Distribution of γ_{min} values in the accepted steps. *Bottom right*: Non-normalized probability distribution for γ_{min}.

3C 66A Block 5: γ_{max}

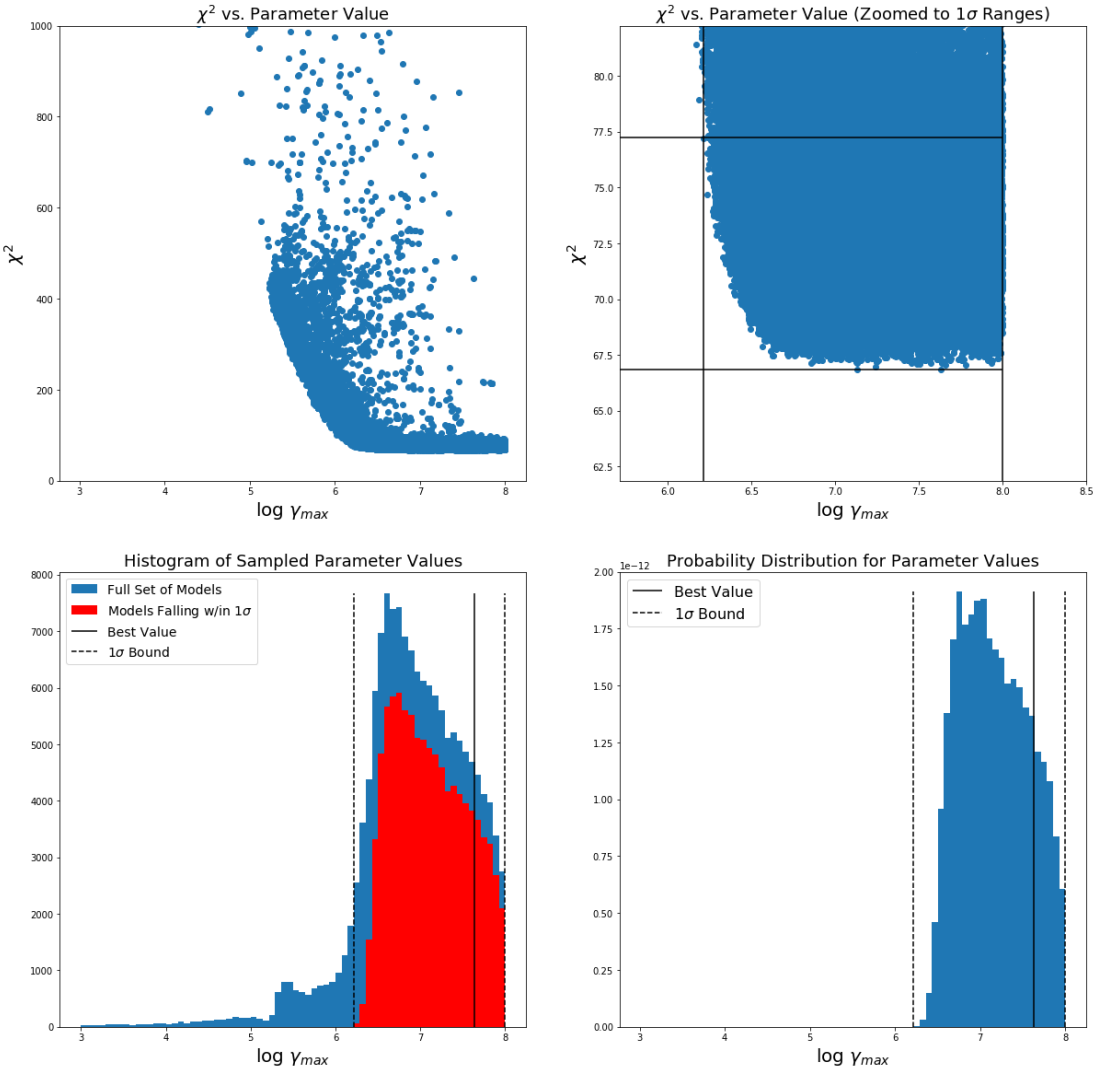

Figure A.35: *Top left*: χ^2 value plotted as a function of the γ_{max} value. *Top right*: χ^2 vs. γ_{max} value with the smallest χ^2 value and largest χ^2 1σ bounds shown as horizontal lines. The smallest and largest 1σ values of γ_{max} are marked with vertical lines. *Bottom left*: Distribution of γ_{max} values in the accepted steps. *Bottom right*: Non-normalized probability distribution for γ_{max}.

3C 66A Block 5: α_2

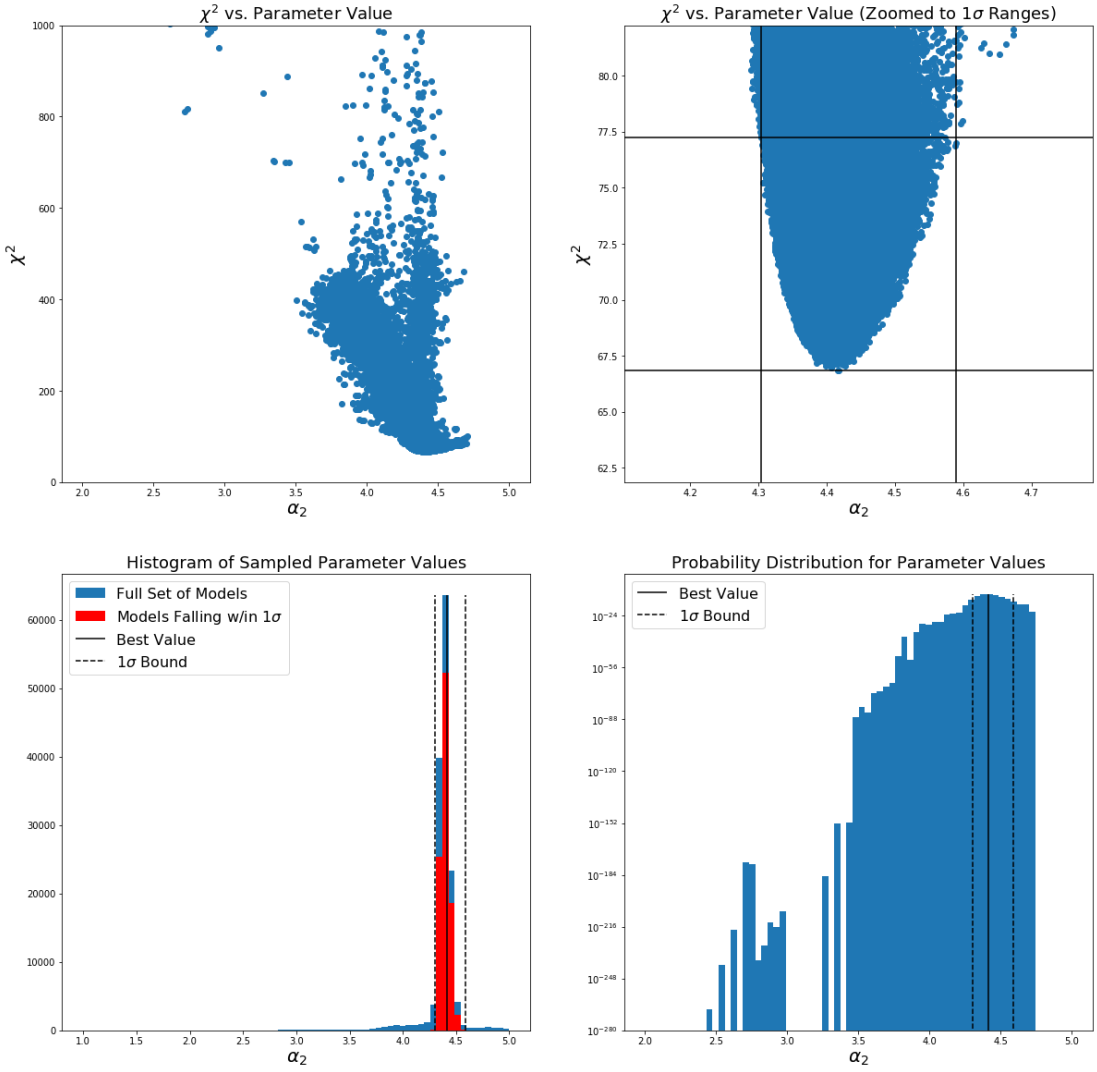

Figure A.36: *Top left*: χ^2 value plotted as a function of the α_2 value. *Top right*: χ^2 vs. α_2 value with the smallest χ^2 value and largest χ^2 1σ bounds shown as horizontal lines. The smallest and largest 1σ values of α_2 are marked with vertical lines. *Bottom left*: Distribution of α_2 values in the accepted steps. *Bottom right*: Non-normalized probability distribution for α_2.

3C 66A Block 6: R

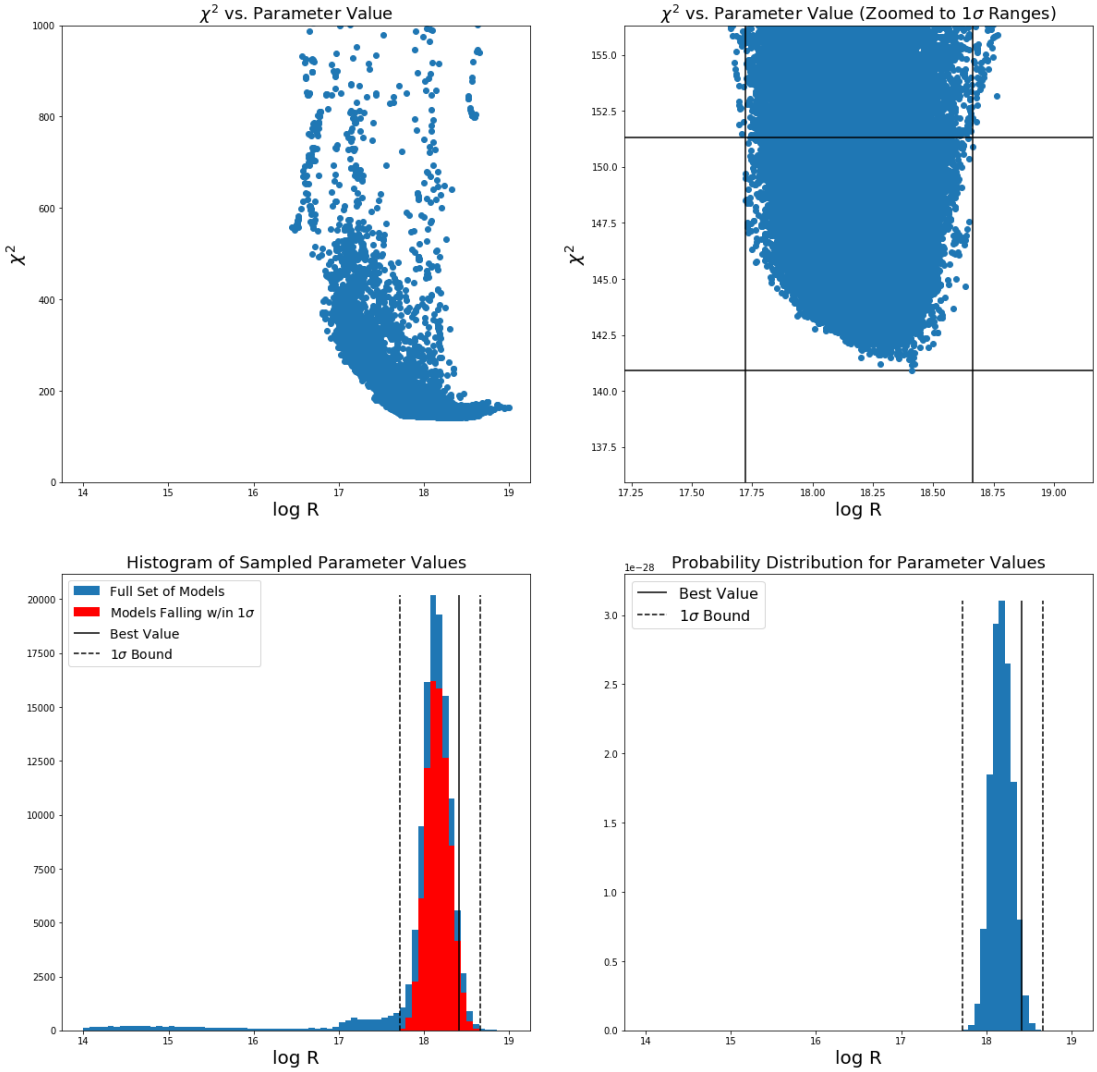

Figure A.37: *Top left*: χ^2 value plotted as a function of the R value. *Top right*: χ^2 vs. R value with the smallest χ^2 value and largest χ^2 1σ bounds shown as horizontal lines. The smallest and largest 1σ values of R are marked with vertical lines. *Bottom left*: Distribution of R values in the accepted steps. *Bottom right*: Non-normalized probability distribution for R.

3C 66A Block 6: B

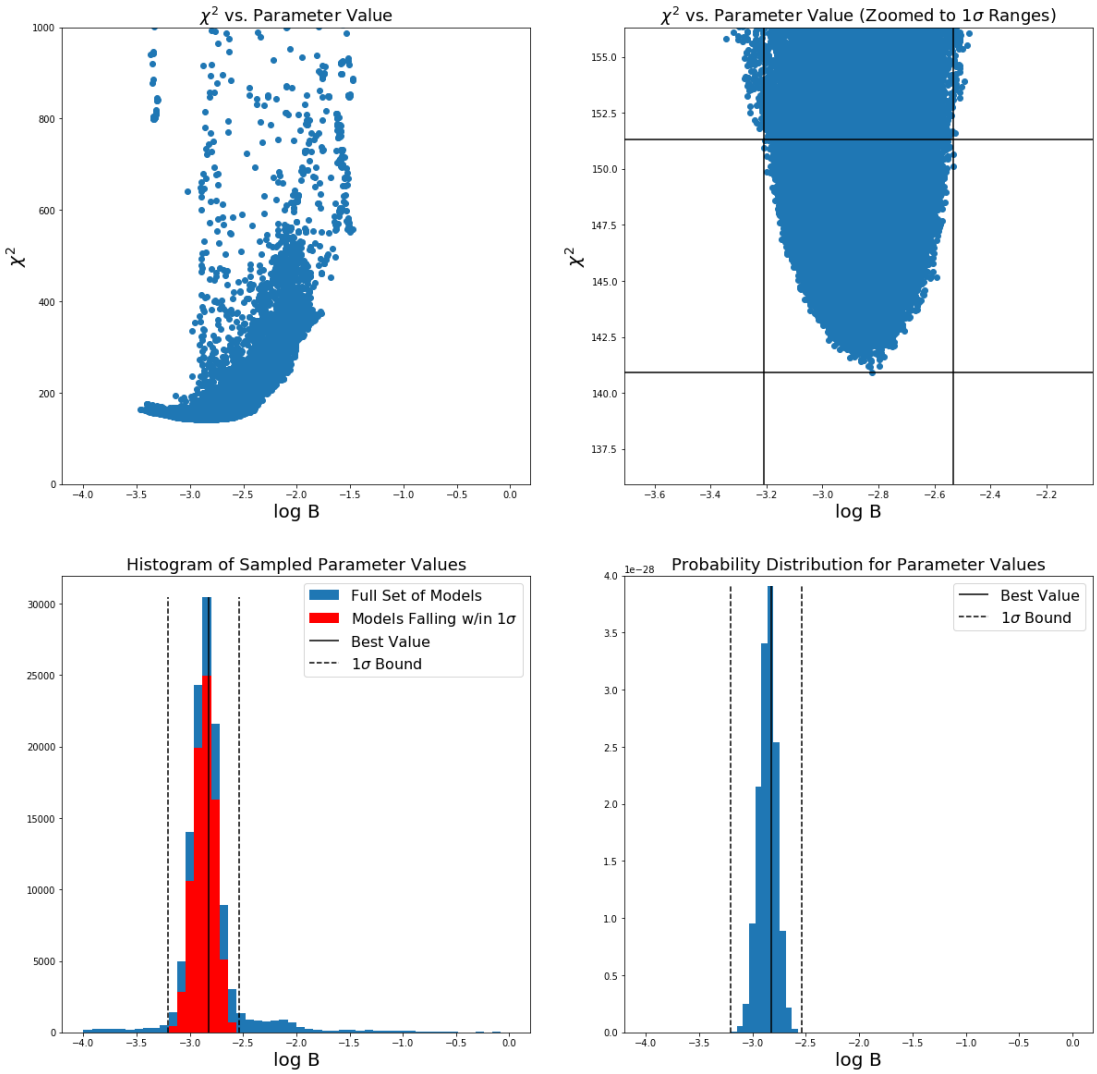

Figure A.38: *Top left*: χ^2 value plotted as a function of the B value. *Top right*: χ^2 vs. B value with the smallest χ^2 value and largest χ^2 1σ bounds shown as horizontal lines. The smallest and largest 1σ values of B are marked with vertical lines. *Bottom left*: Distribution of B values in the accepted steps. *Bottom right*: Non-normalized probability distribution for B.

3C 66A Block 6: δ

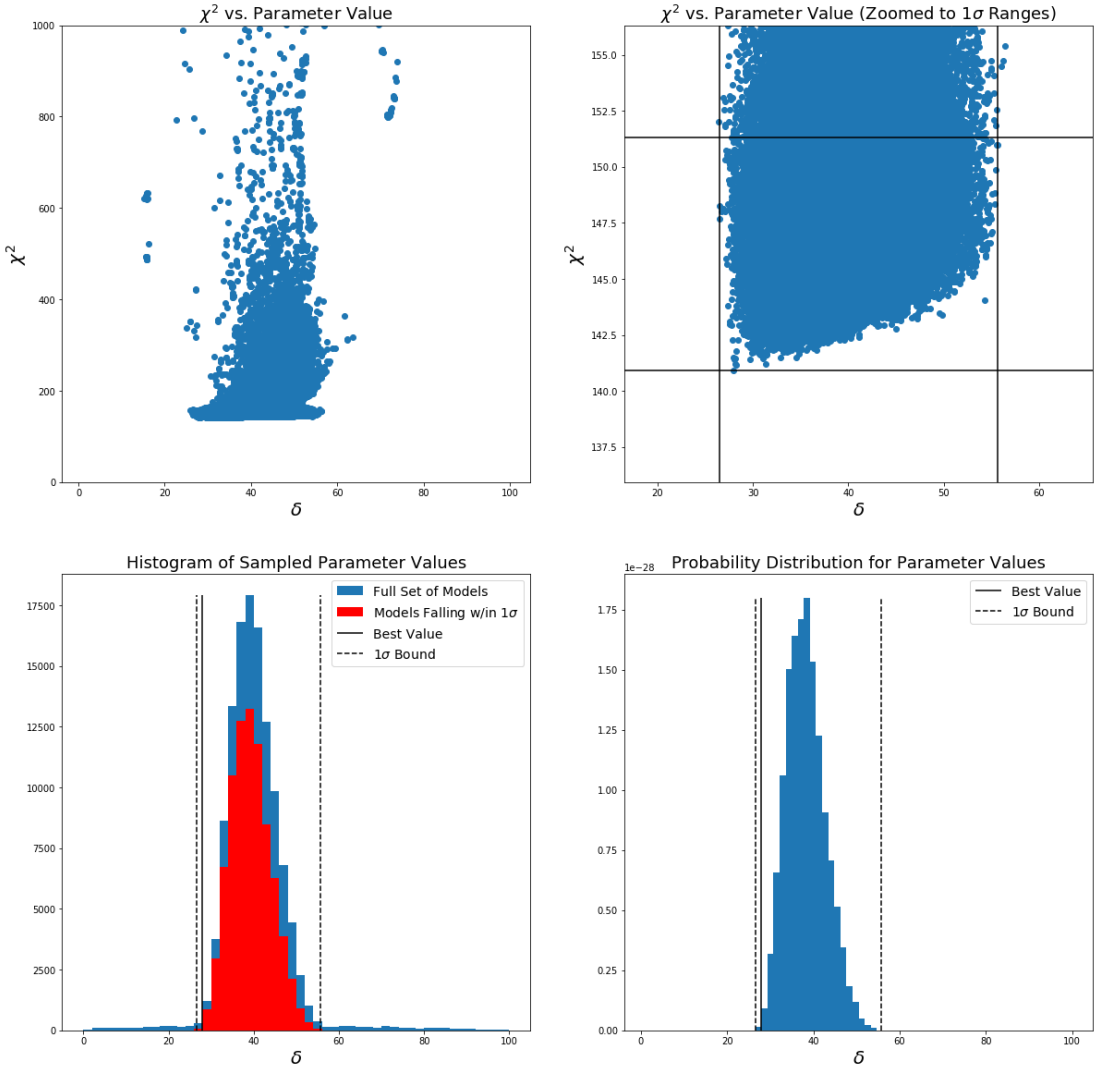

Figure A.39: *Top left*: χ^2 value plotted as a function of the δ value. *Top right*: χ^2 vs. δ value with the smallest χ^2 value and largest χ^2 1σ bounds shown as horizontal lines. The smallest and largest 1σ values of δ are marked with vertical lines. *Bottom left*: Distribution of δ values in the accepted steps. *Bottom right*: Non-normalized probability distribution for δ.

3C 66A Block 6: γ_{break}

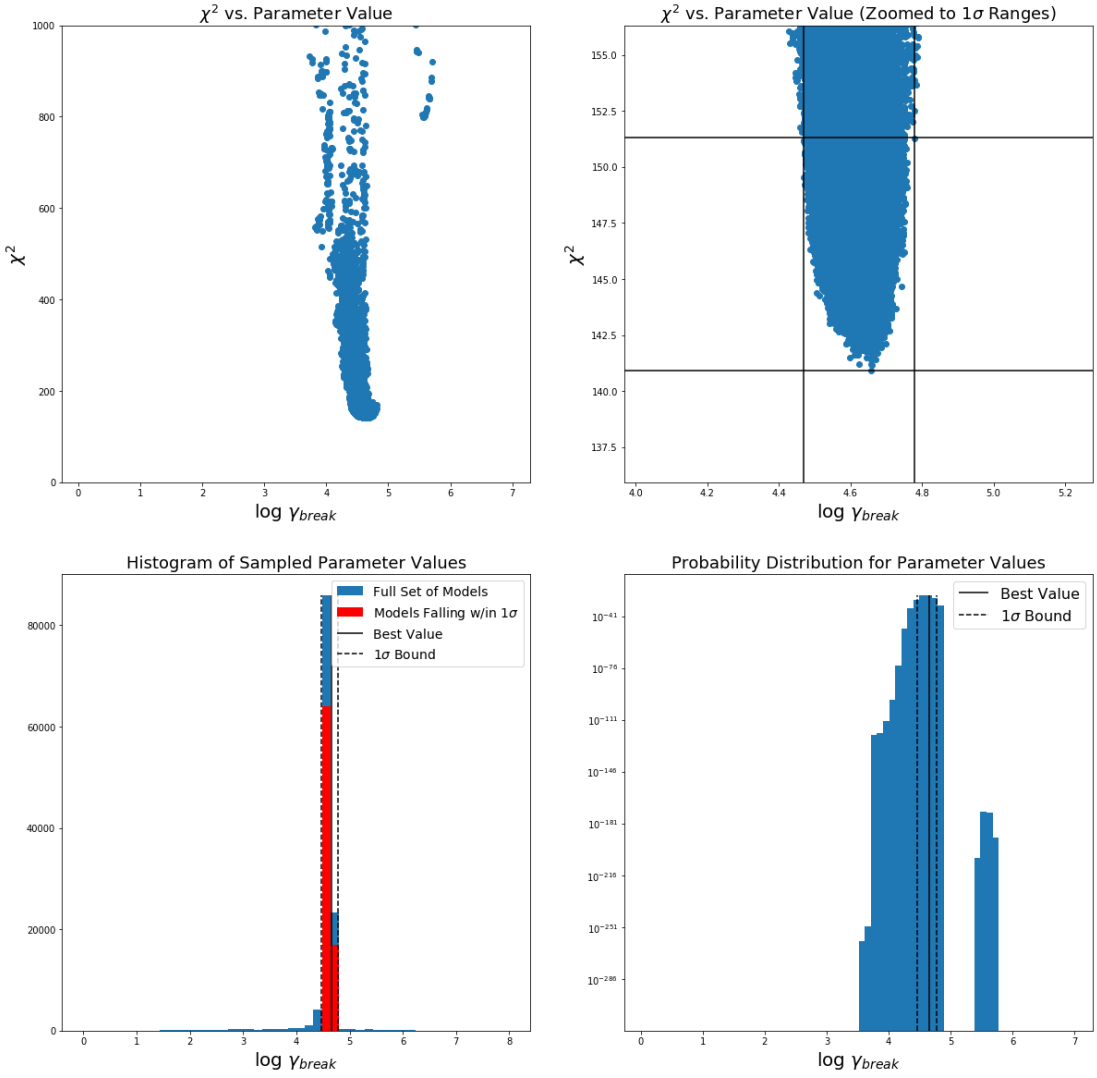

Figure A.40: *Top left*: χ^2 value plotted as a function of the γ_{break} value. *Top right*: χ^2 vs. γ_{break} value with the smallest χ^2 value and largest χ^2 1σ bounds shown as horizontal lines. The smallest and largest 1σ values of γ_{break} are marked with vertical lines. *Bottom left*: Distribution of γ_{break} values in the accepted steps. *Bottom right*: Non-normalized probability distribution for γ_{break}.

3C 66A Block 6: α_1

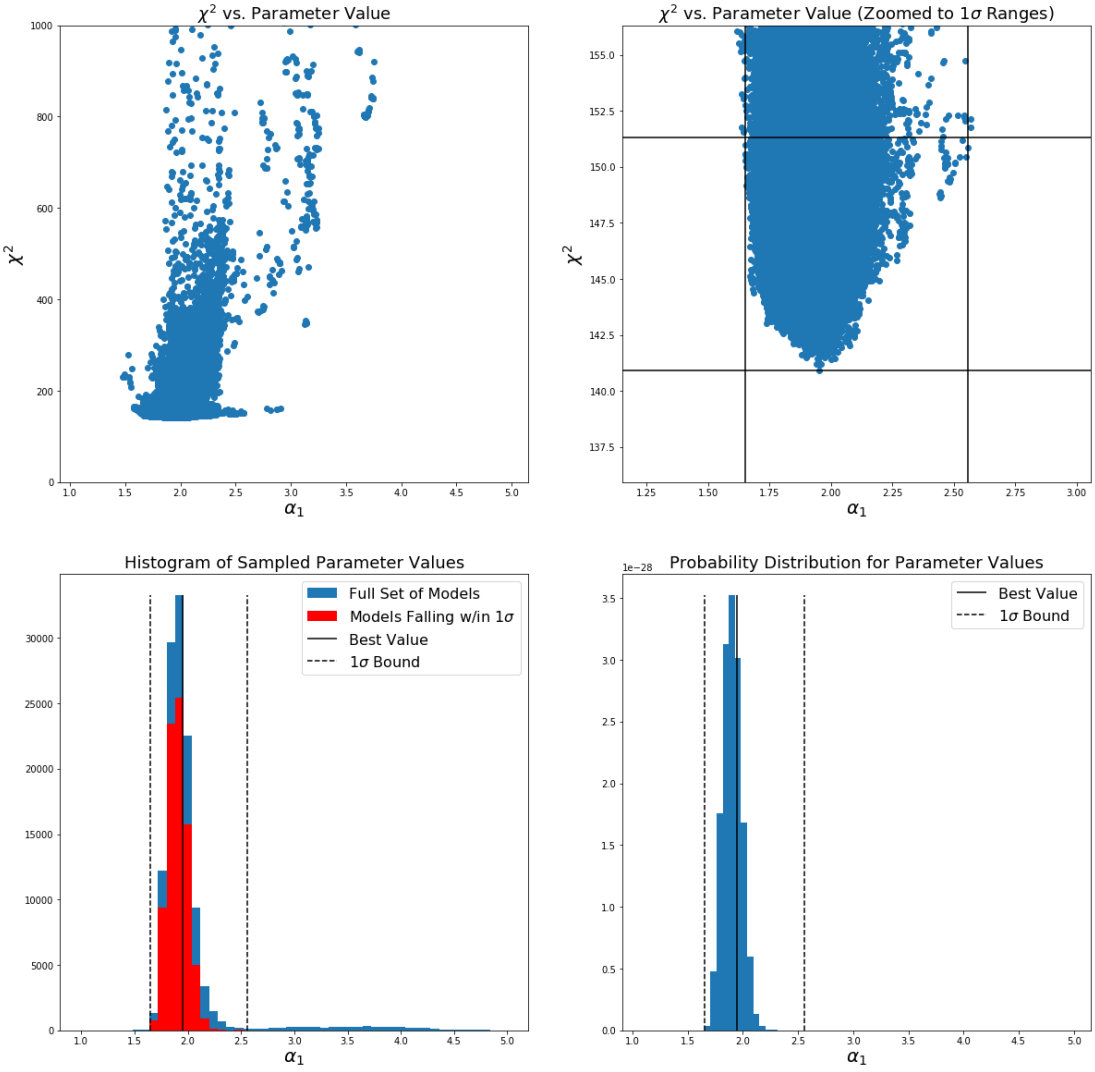

Figure A.41: *Top left*: χ^2 value plotted as a function of the α_1 value. *Top right*: χ^2 vs. α_1 value with the smallest χ^2 value and largest χ^2 1σ bounds shown as horizontal lines. The smallest and largest 1σ values of α_1 are marked with vertical lines. *Bottom left*: Distribution of α_1 values in the accepted steps. *Bottom right*: Non-normalized probability distribution for α_1.

3C 66A Block 6: K

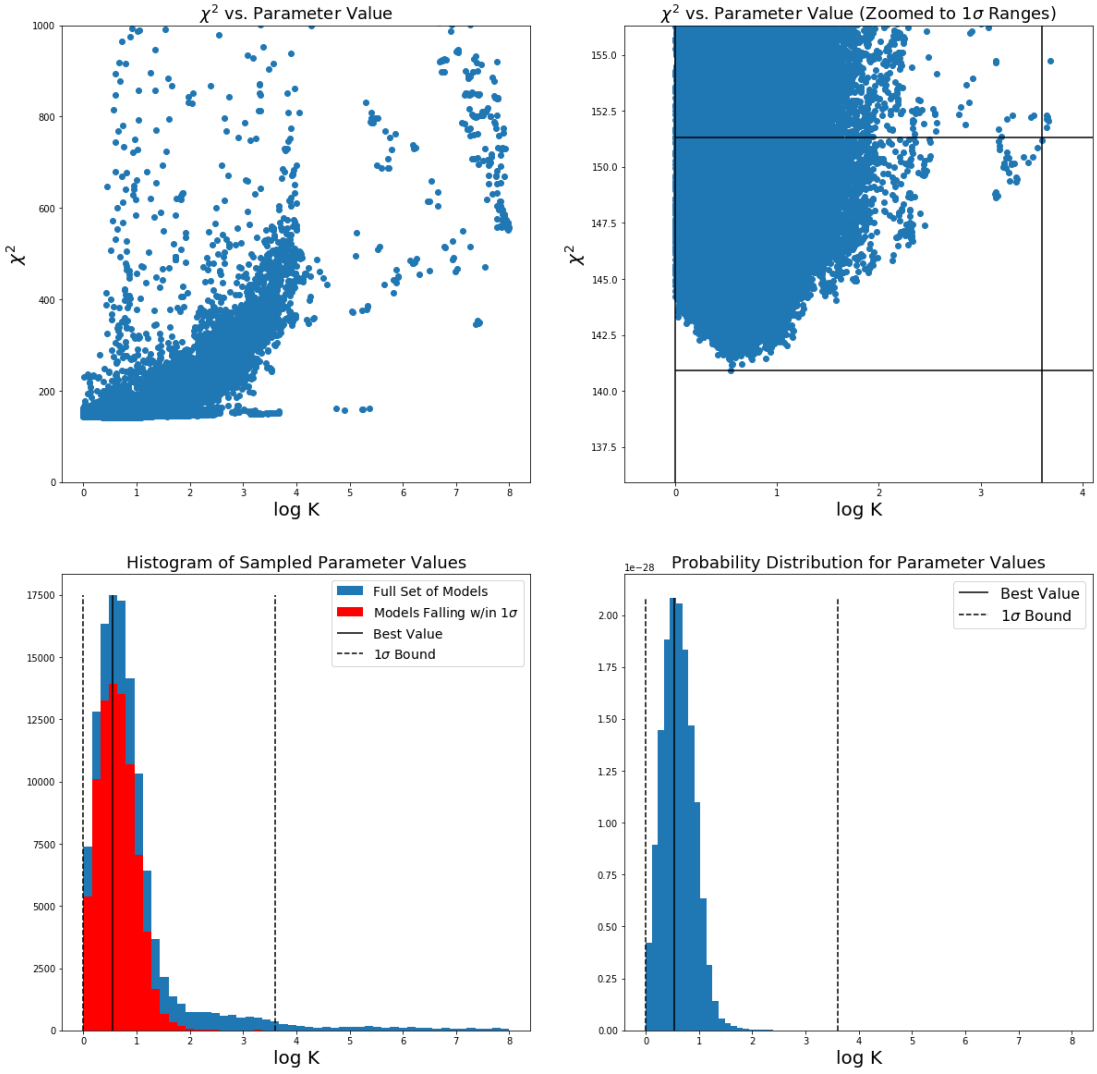

Figure A.42: *Top left*: χ^2 value plotted as a function of the K value. *Top right*: χ^2 vs. K value with the smallest χ^2 value and largest χ^2 1σ bounds shown as horizontal lines. The smallest and largest 1σ values of K are marked with vertical lines. *Bottom left*: Distribution of K values in the accepted steps. *Bottom right*: Non-normalized probability distribution for K.

3C 66A Block 6: γ_{min}

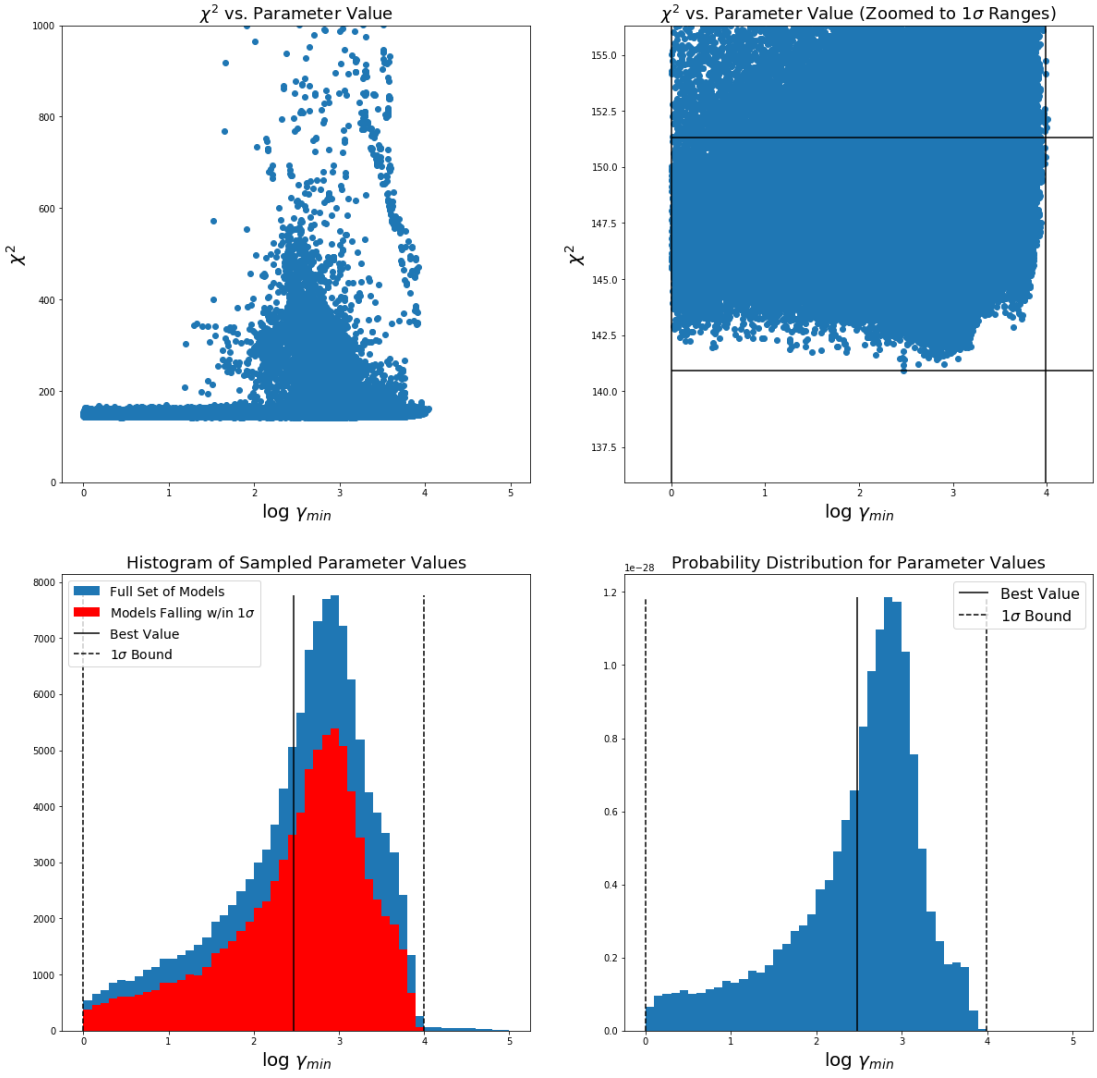

Figure A.43: *Top left*: χ^2 value plotted as a function of the γ_{min} value. *Top right*: χ^2 vs. γ_{min} value with the smallest χ^2 value and largest χ^2 1σ bounds shown as horizontal lines. The smallest and largest 1σ values of γ_{min} are marked with vertical lines. *Bottom left*: Distribution of γ_{min} values in the accepted steps. *Bottom right*: Non-normalized probability distribution for γ_{min}.

3C 66A Block 6: γ_{max}

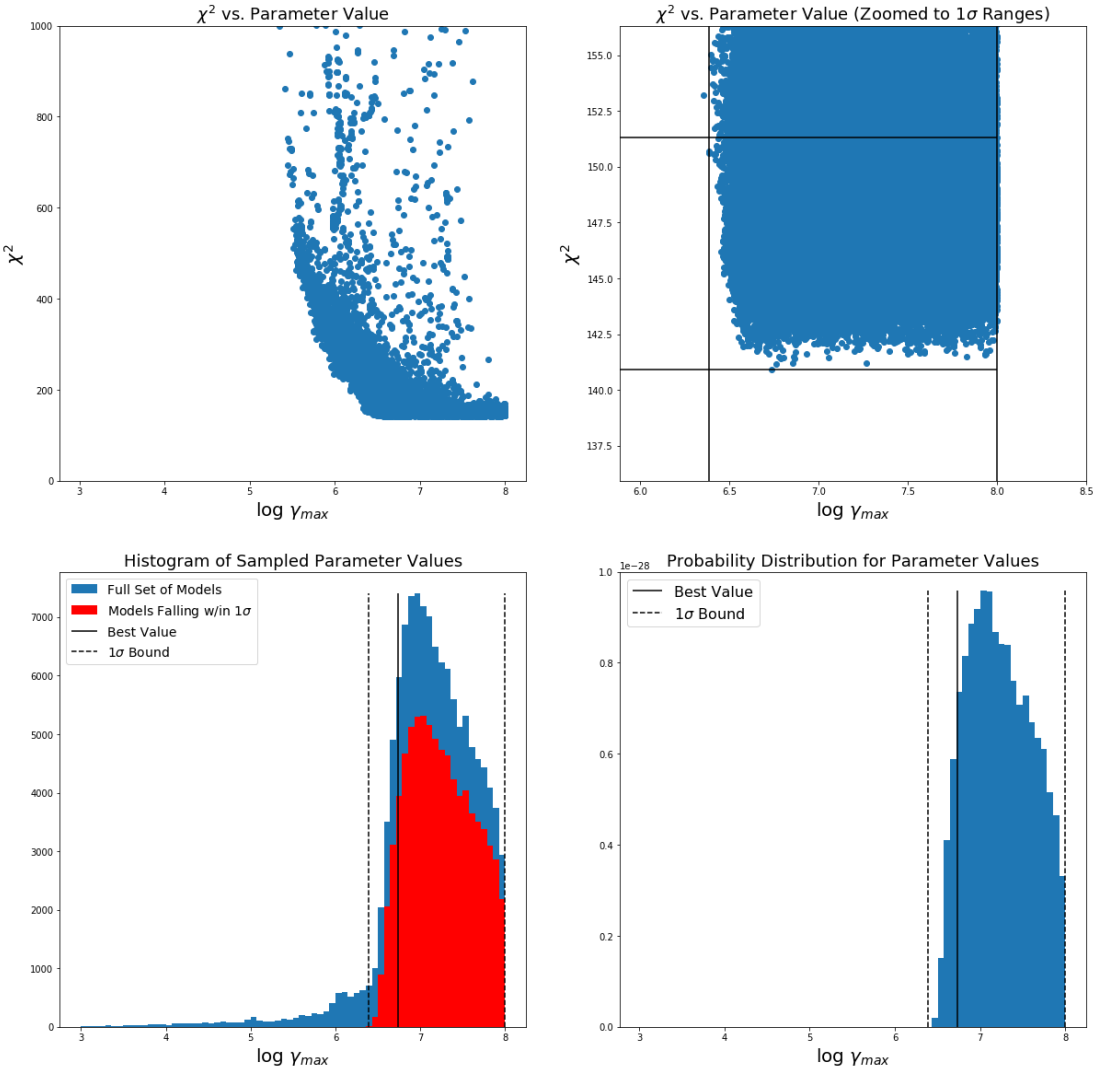

Figure A.44: *Top left*: χ^2 value plotted as a function of the γ_{max} value. *Top right*: χ^2 vs. γ_{max} value with the smallest χ^2 value and largest χ^2 1σ bounds shown as horizontal lines. The smallest and largest 1σ values of γ_{max} are marked with vertical lines. *Bottom left*: Distribution of γ_{max} values in the accepted steps. *Bottom right*: Non-normalized probability distribution for γ_{max}.

3C 66A Block 6: α_2

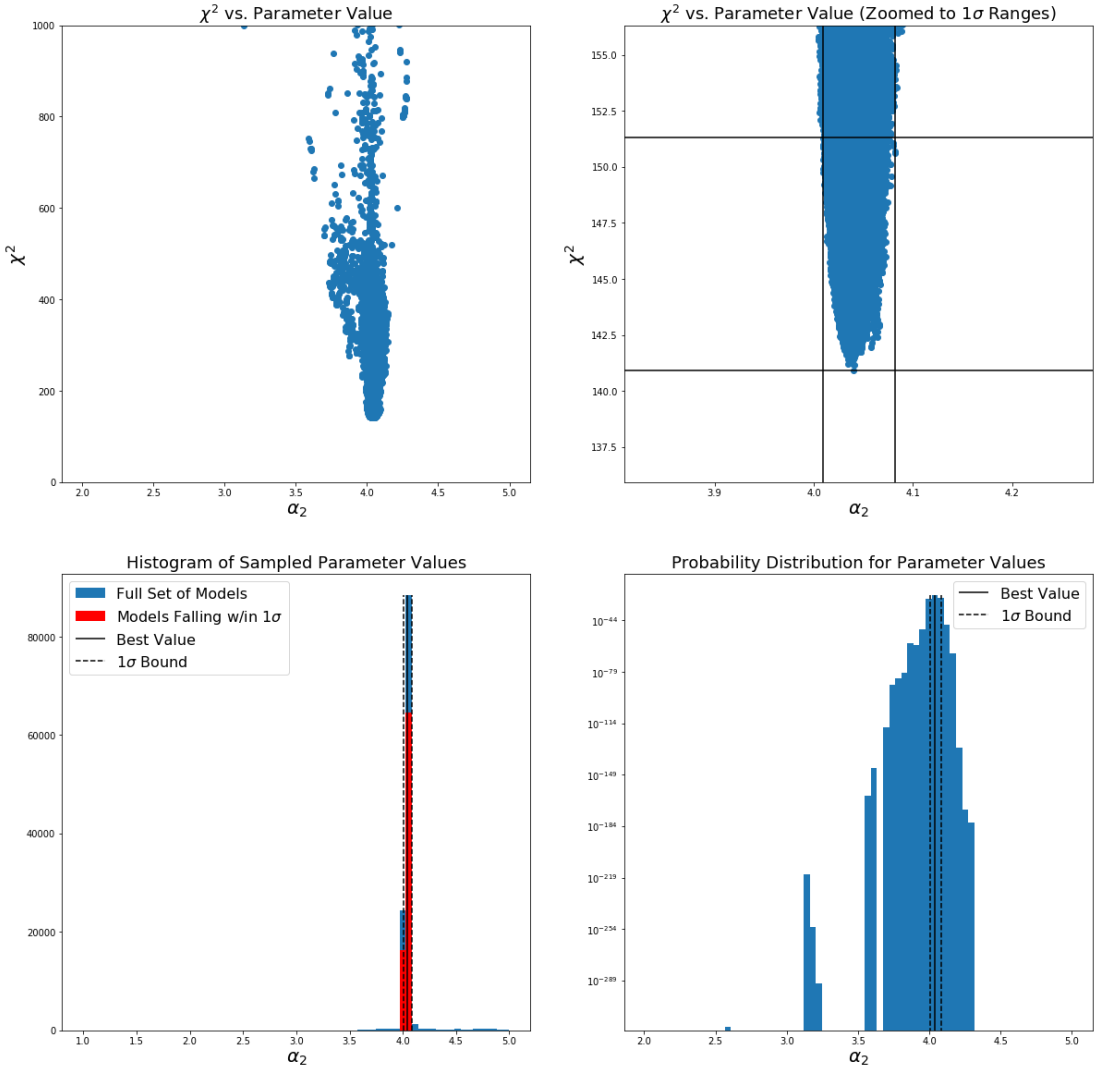

Figure A.45: *Top left*: χ^2 value plotted as a function of the α_2 value. *Top right*: χ^2 vs. α_2 value with the smallest χ^2 value and largest χ^2 1σ bounds shown as horizontal lines. The smallest and largest 1σ values of α_2 are marked with vertical lines. *Bottom left*: Distribution of α_2 values in the accepted steps. *Bottom right*: Non-normalized probability distribution for α_2.

Bibliography

A. A. Abdo, M. Ackermann, I. Agudo, M. Ajello, H. D. Aller, M. F. Aller, E. Angelakis, A. A. Arkharov, M. Axelsson, U. Bach, and others. The Spectral Energy Distribution of Fermi Bright Blazars. *ApJ*, 716:30–70, June 2010. doi: 10.1088/0004-637X/716/1/30.

A. A. Abdo, M. Ackermann, M. Ajello, L. Baldini, J. Ballet, G. Barbiellini, D. Bastieri, K. Bechtol, R. Bellazzini, B. Berenji, and others. Multi-wavelength Observations of the Flaring Gamma-ray Blazar 3C 66A in 2008 October. *ApJ*, 726:43, January 2011. doi: 10.1088/0004-637X/726/1/43.

A. U. Abeysekara, S. Archambault, A. Archer, T. Aune, A. Barnacka, W. Benbow, R. Bird, J. Biteau, J. H. Buckley, V. Bugaev, J. V. Cardenzana, M. Cerruti, X. Chen, J. L. Christiansen, L. Ciupik, M. P. Connolly, P. Coppi, W. Cui, H. J. Dickinson, J. Dumm, J. D. Eisch, M. Errando, A. Falcone, Q. Feng, J. P. Finley, H. Fleischhack, A. Flinders, P. Fortin, L. Fortson, A. Furniss, G. H. Gillanders, S. Griffin, J. Grube, G. Gyuk, M. Hütten, N. Håkansson, D. Hanna, J. Holder, T. B. Humensky, C. A. Johnson, P. Kaaret, P. Kar, N. Kelley-Hoskins, Y. Khassen, D. Kieda, M. Krause, F. Krennrich, S. Kumar, M. J. Lang, G. Maier, S. McArthur, A. McCann, K. Meagher, P. Moriarty, R. Mukherjee, D. Nieto, A. O'Faoláin de Bhróithe, R. A. Ong, A. N. Otte, N. Park, J. S. Perkins, A. Petrashyk, M. Pohl, A. Popkow, E. Pueschel, J. Quinn, K. Ragan, G. Ratliff, P. T. Reynolds, G. T. Richards, E. Roache, J. Rousselle, M. Santander, G. H. Sembroski, K. Shahinyan, A. W. Smith, D. Staszak, I. Telezhinsky, N. W. Todd, J. V. Tucci, J. Tyler, V. V. Vassiliev, S. Vincent, S. P. Wakely, O. M. Weiner, A. Weinstein, A. Wilhelm, D. A. Williams, B. Zitzer, VERITAS, P. S. Smith, SPOL, T. W.-S. Holoien, J. L. Prieto, C. S. Kochanek, K. Z. Stanek, B. Shappee, ASAS-SN, T. Hovatta, W. Max-Moerbeck, T. J. Pearson, R. A. Reeves, J. L. Richards, A. C. S. Readhead, OVRO, G. M. Madejski, NuSTAR, S. G. Djorgovski, A. J. Drake, M. J. Graham, A. Mahabal, and CRTS. Gamma-Rays from the Quasar PKS 1441+25: Story of an Escape. *Astrophysical Journal Letters*, 815:L22, December 2015. doi: 10.1088/2041-8205/815/2/L22.

A. U. Abeysekara, W. Benbow, R. Bird, T. Brantseg, R. Brose, M. Buchovecky, J. H. Buckley, V. Bugaev, M. P. Connolly, W. Cui, M. K. Daniel, A. Falcone,

Q. Feng, J. P. Finley, L. Fortson, A. Furniss, G. H. Gillanders, I. Gunawardhana, M. Hütten, D. Hanna, O. Hervet, J. Holder, G. Hughes, T. B. Humensky, C. A. Johnson, P. Kaaret, P. Kar, M. Kertzman, F. Krennrich, M. J. Lang, T. T. Y. Lin, S. McArthur, P. Moriarty, R. Mukherjee, S. O'Brien, R. A. Ong, A. N. Otte, N. Park, A. Petrashyk, M. Pohl, E. Pueschel, J. Quinn, K. Ragan, P. T. Reynolds, G. T. Richards, E. Roache, C. Rulten, I. Sadeh, M. Santander, G. H. Sembroski, K. Shahinyan, S. P. Wakely, A. Weinstein, R. M. Wells, P. Wilcox, D. A. Williams, B. Zitzer, The VERITAS Collaboration, S. G. Jorstad, A. P. Marscher, M. L. Lister, Y. Y. Kovalev, A. B. Pushkarev, T. Savolainen, I. Agudo, S. N. Molina, J. L. Gómez, V. M. Larionov, G. A. Borman, A. A. Mokrushina, M. Tornikoski, A. Lähteenmäki, W. Chamani, S. Enestam, S. Kiehlmann, T. Hovatta, P. S. Smith, and P. Pontrelli. Multiwavelength Observations of the Blazar BL Lacertae: A New Fast TeV Gamma-Ray Flare. *ApJ*, 856:95, April 2018. doi: 10.3847/1538-4357/aab35c.

F. Acero, M. Ackermann, M. Ajello, A. Albert, W. B. Atwood, M. Axelsson, L. Baldini, J. Ballet, G. Barbiellini, D. Bastieri, A. Belfiore, R. Bellazzini, E. Bissaldi, R. D. Blandford, E. D. Bloom, J. R. Bogart, R. Bonino, E. Bottacini, J. Bregeon, R. J. Britto, P. Bruel, R. Buehler, T. H. Burnett, S. Buson, G. A. Caliandro, R. A. Cameron, R. Caputo, M. Caragiulo, P. A. Caraveo, J. M. Casandjian, E. Cavazzuti, E. Charles, R. C. G. Chaves, A. Chekhtman, C. C. Cheung, J. Chiang, G. Chiaro, S. Ciprini, R. Claus, J. Cohen-Tanugi, L. R. Cominsky, J. Conrad, S. Cutini, F. D'Ammando, A. de Angelis, M. DeKlotz, F. de Palma, R. Desiante, S. W. Digel, L. Di Venere, P. S. Drell, R. Dubois, D. Dumora, C. Favuzzi, S. J. Fegan, E. C. Ferrara, J. Finke, A. Franckowiak, Y. Fukazawa, S. Funk, P. Fusco, F. Gargano, D. Gasparrini, B. Giebels, N. Giglietto, P. Giommi, F. Giordano, M. Giroletti, T. Glanzman, G. Godfrey, I. A. Grenier, M.-H. Grondin, J. E. Grove, L. Guillemot, S. Guiriec, D. Hadasch, A. K. Harding, E. Hays, J. W. Hewitt, A. B. Hill, D. Horan, G. Iafrate, T. Jogler, G. Jóhannesson, R. P. Johnson, A. S. Johnson, T. J. Johnson, W. N. Johnson, T. Kamae, J. Kataoka, J. Katsuta, M. Kuss, G. La Mura, D. Landriu, S. Larsson, L. Latronico, M. Lemoine-Goumard, J. Li, L. Li, F. Longo, F. Loparco, B. Lott, M. N. Lovellette, P. Lubrano, G. M. Madejski, F. Massaro, M. Mayer, M. N. Mazziotta, J. E. McEnery, P. F. Michelson, N. Mirabal, T. Mizuno, A. A. Moiseev, M. Mongelli, M. E. Monzani, A. Morselli, I. V. Moskalenko, S. Murgia, E. Nuss, M. Ohno, T. Ohsugi, N. Omodei, M. Orienti, E. Orlando, J. F. Ormes, D. Paneque, J. H. Panetta, J. S. Perkins, M. Pesce-Rollins, F. Piron, G. Pivato, T. A. Porter, J. L. Racusin, R. Rando, M. Razzano, S. Razzaque, A. Reimer, O. Reimer, T. Reposeur, L. S. Rochester, R. W. Romani, D. Salvetti, M. Sánchez-Conde, P. M. Saz Parkinson, A. Schulz, E. J. Siskind, D. A. Smith, F. Spada, G. Spandre, P. Spinelli, T. E. Stephens, A. W. Strong, D. J. Suson, H. Takahashi, T. Takahashi, Y. Tanaka, J. G. Thayer, J. B. Thayer,

D. J. Thompson, L. Tibaldo, O. Tibolla, D. F. Torres, E. Torresi, G. Tosti, E. Troja, B. Van Klaveren, G. Vianello, B. L. Winer, K. S. Wood, M. Wood, S. Zimmer, and Fermi-LAT Collaboration. Fermi Large Area Telescope Third Source Catalog. *ApJS*, 218:23, June 2015. doi: 10.1088/0067-0049/218/2/23.

M. Ackermann, M. Ajello, A. Allafort, W. B. Atwood, L. Baldini, J. Ballet, G. Barbiellini, D. Bastieri, K. Bechtol, A. Belfiore, R. Bellazzini, E. Bernieri, E. Bissaldi, E. D. Bloom, E. Bonamente, T. J. Brandt, J. Bregeon, M. Brigida, P. Bruel, R. Buehler, T. H. Burnett, S. Buson, G. A. Caliandro, R. A. Cameron, R. Campana, P. A. Caraveo, J. M. Casandjian, E. Cavazzuti, C. Cecchi, E. Charles, R. C. G. Chaves, A. Chekhtman, C. C. Cheung, J. Chiang, G. Chiaro, S. Ciprini, R. Claus, J. Cohen-Tanugi, L. R. Cominsky, J. Conrad, S. Cutini, F. D'Ammando, A. de Angelis, F. de Palma, C. D. Dermer, R. Desiante, S. W. Digel, L. Di Venere, P. S. Drell, A. Drlica-Wagner, C. Favuzzi, S. J. Fegan, E. C. Ferrara, W. B. Focke, P. Fortin, A. Franckowiak, S. Funk, P. Fusco, F. Gargano, D. Gasparrini, N. Gehrels, S. Germani, N. Giglietto, P. Giommi, F. Giordano, M. Giroletti, G. Godfrey, G. A. Gomez-Vargas, I. A. Grenier, S. Guiriec, D. Hadasch, Y. Hanabata, A. K. Harding, M. Hayashida, E. Hays, J. Hewitt, A. B. Hill, D. Horan, R. E. Hughes, T. Jogler, G. Jóhannesson, A. S. Johnson, T. J. Johnson, W. N. Johnson, T. Kamae, J. Kataoka, T. Kawano, J. Knödlseder, M. Kuss, J. Lande, S. Larsson, L. Latronico, M. Lemoine-Goumard, F. Longo, F. Loparco, B. Lott, M. N. Lovellette, P. Lubrano, E. Massaro, M. Mayer, M. N. Mazziotta, J. E. McEnery, J. Mehault, P. F. Michelson, T. Mizuno, A. A. Moiseev, M. E. Monzani, A. Morselli, I. V. Moskalenko, S. Murgia, R. Nemmen, E. Nuss, T. Ohsugi, A. Okumura, M. Orienti, J. F. Ormes, D. Paneque, J. S. Perkins, M. Pesce-Rollins, F. Piron, G. Pivato, T. A. Porter, S. Rainò, M. Razzano, A. Reimer, O. Reimer, T. Reposeur, S. Ritz, R. W. Romani, M. Roth, P. M. Saz Parkinson, A. Schulz, C. Sgrò, E. J. Siskind, D. A. Smith, G. Spandre, P. Spinelli, Ł. Stawarz, A. W. Strong, D. J. Suson, H. Takahashi, J. G. Thayer, J. B. Thayer, D. J. Thompson, L. Tibaldo, M. Tinivella, D. F. Torres, G. Tosti, E. Troja, Y. Uchiyama, T. L. Usher, J. Vandenbroucke, V. Vasileiou, G. Vianello, V. Vitale, M. Werner, B. L. Winer, K. S. Wood, and M. Wood. The First Fermi-LAT Catalog of Sources above 10 GeV. *ApJS*, 209:34, December 2013. doi: 10.1088/0067-0049/209/2/34.

M. Ackermann, M. Ajello, A. Albert, W. B. Atwood, L. Baldini, J. Ballet, G. Barbiellini, D. Bastieri, J. Becerra Gonzalez, R. Bellazzini, E. Bissaldi, R. D. Blandford, E. D. Bloom, R. Bonino, E. Bottacini, J. Bregeon, P. Bruel, R. Buehler, S. Buson, G. A. Caliandro, R. A. Cameron, R. Caputo, M. Caragiulo, P. A. Caraveo, E. Cavazzuti, C. Cecchi, A. Chekhtman, J. Chiang, G. Chiaro, S. Ciprini, J. Cohen-Tanugi, J. Conrad, S. Cutini, F. D'Ammando, A. de Angelis, F. de Palma, R. Desiante, L. Di Venere, A. Domínguez, P. S. Drell, C. Favuzzi, S. J. Fegan, E. C. Ferrara, W. B. Focke, L. Fuhrmann, Y. Fukazawa, P. Fusco,

F. Gargano, D. Gasparrini, N. Giglietto, P. Giommi, F. Giordano, M. Giroletti, G. Godfrey, D. Green, I. A. Grenier, J. E. Grove, S. Guiriec, A. K. Harding, E. Hays, J. W. Hewitt, A. B. Hill, D. Horan, T. Jogler, G. Jóhannesson, A. S. Johnson, T. Kamae, M. Kuss, S. Larsson, L. Latronico, J. Li, L. Li, F. Longo, F. Loparco, B. Lott, M. N. Lovellette, P. Lubrano, J. Magill, S. Maldera, A. Manfreda, W. Max-Moerbeck, M. Mayer, M. N. Mazziotta, J. E. McEnery, P. F. Michelson, T. Mizuno, M. E. Monzani, A. Morselli, I. V. Moskalenko, S. Murgia, E. Nuss, M. Ohno, T. Ohsugi, R. Ojha, N. Omodei, E. Orlando, J. F. Ormes, D. Paneque, T. J. Pearson, J. S. Perkins, M. Perri, M. Pesce-Rollins, V. Petrosian, F. Piron, G. Pivato, T. A. Porter, S. Rainò, R. Rando, M. Razzano, A. Readhead, A. Reimer, O. Reimer, A. Schulz, C. Sgrò, E. J. Siskind, F. Spada, G. Spandre, P. Spinelli, D. J. Suson, H. Takahashi, J. B. Thayer, D. J. Thompson, L. Tibaldo, D. F. Torres, G. Tosti, E. Troja, Y. Uchiyama, G. Vianello, K. S. Wood, M. Wood, S. Zimmer, A. Berdyugin, R. H. D. Corbet, T. Hovatta, E. Lindfors, K. Nilsson, R. Reinthal, A. Sillanpää, A. Stamerra, L. O. Takalo, and M. J. Valtonen. Multiwavelength Evidence for Quasi-periodic Modulation in the Gamma-Ray Blazar PG 1553+113. *ApJL*, 813:L41, November 2015. doi: 10.1088/2041-8205/813/2/L41.

M. Ackermann, M. Ajello, W. B. Atwood, L. Baldini, J. Ballet, G. Barbiellini, D. Bastieri, J. Becerra Gonzalez, R. Bellazzini, E. Bissaldi, R. D. Blandford, E. D. Bloom, R. Bonino, E. Bottacini, T. J. Brandt, J. Bregeon, P. Bruel, R. Buehler, S. Buson, G. A. Caliandro, R. A. Cameron, R. Caputo, M. Caragiulo, P. A. Caraveo, E. Cavazzuti, C. Cecchi, E. Charles, A. Chekhtman, C. C. Cheung, J. Chiang, G. Chiaro, S. Ciprini, J. M. Cohen, J. Cohen-Tanugi, L. R. Cominsky, J. Conrad, A. Cuoco, S. Cutini, F. D'Ammando, A. de Angelis, F. de Palma, R. Desiante, M. Di Mauro, L. Di Venere, A. Domínguez, P. S. Drell, C. Favuzzi, S. J. Fegan, E. C. Ferrara, W. B. Focke, P. Fortin, A. Franckowiak, Y. Fukazawa, S. Funk, A. K. Furniss, P. Fusco, F. Gargano, D. Gasparrini, N. Giglietto, P. Giommi, F. Giordano, M. Giroletti, T. Glanzman, G. Godfrey, I. A. Grenier, M.-H. Grondin, L. Guillemot, S. Guiriec, A. K. Harding, E. Hays, J. W. Hewitt, A. B. Hill, D. Horan, G. Iafrate, D. Hartmann, T. Jogler, G. Jóhannesson, A. S. Johnson, T. Kamae, J. Kataoka, J. Knödlseder, M. Kuss, G. La Mura, S. Larsson, L. Latronico, M. Lemoine-Goumard, J. Li, L. Li, F. Longo, F. Loparco, B. Lott, M. N. Lovellette, P. Lubrano, G. M. Madejski, S. Maldera, A. Manfreda, M. Mayer, M. N. Mazziotta, P. F. Michelson, N. Mirabal, W. Mitthumsiri, T. Mizuno, A. A. Moiseev, M. E. Monzani, A. Morselli, I. V. Moskalenko, S. Murgia, E. Nuss, T. Ohsugi, N. Omodei, M. Orienti, E. Orlando, J. F. Ormes, D. Paneque, J. S. Perkins, M. Pesce-Rollins, V. Petrosian, F. Piron, G. Pivato, T. A. Porter, S. Rainò, R. Rando, M. Razzano, S. Razzaque, A. Reimer, O. Reimer, T. Reposeur, R. W. Romani, M. Sánchez-Conde, P. M. Saz Parkinson, J. Schmid, A. Schulz, C. Sgrò, E. J. Siskind, F. Spada,

G. Spandre, P. Spinelli, D. J. Suson, H. Tajima, H. Takahashi, M. Takahashi, T. Takahashi, J. B. Thayer, D. J. Thompson, L. Tibaldo, D. F. Torres, G. Tosti, E. Troja, G. Vianello, K. S. Wood, M. Wood, M. Yassine, G. Zaharijas, and S. Zimmer. 2FHL: The Second Catalog of Hard Fermi-LAT Sources. *ApJS*, 222: 5, January 2016. doi: 10.3847/0067-0049/222/1/5.

F. Aharonian, A. Akhperjanian, M. Beilicke, K. Bernlöhr, H.-G. Börst, H. Bojahr, O. Bolz, T. Coarasa, J. L. Contreras, J. Cortina, S. Denninghoff, M. V. Fonseca, M. Girma, N. Götting, G. Heinzelmann, G. Hermann, A. Heusler, W. Hofmann, D. Horns, I. Jung, R. Kankanyan, M. Kestel, A. Kohnle, A. Konopelko, H. Kornmeyer, D. Kranich, H. Lampeitl, M. Lopez, E. Lorenz, F. Lucarelli, O. Mang, H. Meyer, R. Mirzoyan, A. Moralejo, E. Ona-Wilhelmi, M. Panter, A. Plyasheshnikov, G. Pühlhofer, R. de los Reyes, W. Rhode, J. Ripken, G. Rowell, V. Sahakian, M. Samorski, M. Schilling, M. Siems, D. Sobzynska, W. Stamm, M. Tluczykont, V. Vitale, H. J. Völk, C. A. Wiedner, and W. Wittek. Is the giant radio galaxy M 87 a TeV gamma-ray emitter? *A&A*, 403: L1–L5, May 2003. doi: 10.1051/0004-6361:20030372.

M. L. Ahnen, S. Ansoldi, L. A. Antonelli, P. Antoranz, A. Babic, B. Banerjee, P. Bangale, U. Barres de Almeida, J. A. Barrio, W. Bednarek, and others. Very High Energy γ-Rays from the Universe's Middle Age: Detection of the z = 0.940 Blazar PKS 1441+25 with MAGIC. *ApJL*, 815:L23, December 2015. doi: 10.1088/2041-8205/815/2/L23.

J. Aleksić, L. A. Antonelli, P. Antoranz, M. Backes, J. A. Barrio, D. Bastieri, J. Becerra González, W. Bednarek, A. Berdyugin, K. Berger, E. Bernardini, A. Biland, O. Blanch, R. K. Bock, A. Boller, G. Bonnoli, P. Bordas, D. Borla Tridon, V. Bosch-Ramon, D. Bose, I. Braun, T. Bretz, M. Camara, A. Cañellas, E. Carmona, A. Carosi, P. Colin, E. Colombo, J. L. Contreras, J. Cortina, L. Cossio, S. Covino, F. Dazzi, A. De Angelis, E. De Cea del Pozo, B. De Lotto, M. De Maria, F. De Sabata, C. Delgado Mendez, A. Diago Ortega, M. Doert, A. Domínguez, D. Dominis Prester, D. Dorner, M. Doro, D. Elsaesser, M. Errando, D. Ferenc, M. V. Fonseca, L. Font, R. J. García López, M. Garczarczyk, G. Giavitto, N. Godinović, D. Hadasch, A. Herrero, D. Hildebrand, D. Höhne-Mönch, J. Hose, D. Hrupec, T. Jogler, S. Klepser, T. Krähenbühl, D. Kranich, J. Krause, A. La Barbera, E. Leonardo, E. Lindfors, S. Lombardi, F. Longo, M. López, E. Lorenz, P. Majumdar, M. Makariev, G. Maneva, N. Mankuzhiyil, K. Mannheim, L. Maraschi, M. Mariotti, M. Martínez, D. Mazin, M. Meucci, J. M. Miranda, R. Mirzoyan, H. Miyamoto, J. Moldón, A. Moralejo, D. Nieto, K. Nilsson, R. Orito, I. Oya, R. Paoletti, J. M. Paredes, S. Partini, M. Pasanen, F. Pauss, R. G. Pegna, M. A. Perez-Torres, M. Persic, L. Peruzzo, J. Pochon, F. Prada, P. G. Prada Moroni, E. Prandini, N. Puchades, I. Puljak, I. Reichardt, R. Reinthal, W. Rhode, M. Ribó, J. Rico, S. Rügamer,

A. Saggion, K. Saito, T. Y. Saito, M. Salvati, M. Sánchez-Conde, K. Satalecka, V. Scalzotto, V. Scapin, C. Schultz, T. Schweizer, M. Shayduk, S. N. Shore, A. Sierpowska-Bartosik, A. Sillanpää, J. Sitarek, D. Sobczynska, F. Spanier, S. Spiro, A. Stamerra, B. Steinke, J. Storz, N. Strah, J. C. Struebig, T. Suric, L. Takalo, F. Tavecchio, P. Temnikov, T. Terzić, D. Tescaro, M. Teshima, M. Thom, D. F. Torres, H. Vankov, R. M. Wagner, Q. Weitzel, V. Zabalza, F. Zandanel, and R. Zanin. Observations of the Blazar 3C 66A with the Magic Telescopes in Stereoscopic Mode. *ApJ*, 726:58, January 2011. doi: 10.1088/0004-637X/726/2/58.

E. Aliu, H. Anderhub, L. A. Antonelli, P. Antoranz, M. Backes, C. Baixeras, S. Balestra, J. A. Barrio, H. Bartko, D. Bastieri, J. Becerra González, J. K. Becker, W. Bednarek, K. Berger, E. Bernardini, A. Biland, R. K. Bock, G. Bonnoli, P. Bordas, D. Borla Tridon, V. Bosch-Ramon, T. Bretz, I. Britvitch, M. Camara, E. Carmona, A. Chilingarian, S. Commichau, J. L. Contreras, J. Cortina, M. T. Costado, S. Covino, V. Curtef, F. Dazzi, A. DeAngelis, E. DeCea del Pozo, R. de los Reyes, B. DeLotto, M. DeMaria, F. DeSabata, C. Delgado Mendez, A. Dominguez, D. Dorner, M. Doro, D. Elsaesser, M. Errando, D. Ferenc, E. Fernández, R. Firpo, M. V. Fonseca, L. Font, N. Galante, R. J. García López, M. Garczarczyk, M. Gaug, F. Goebel, D. Hadasch, M. Hayashida, A. Herrero, D. Höhne-Mönch, J. Hose, C. C. Hsu, S. Huber, T. Jogler, D. Kranich, A. La Barbera, A. Laille, E. Leonardo, E. Lindfors, S. Lombardi, F. Longo, M. López, E. Lorenz, P. Majumdar, G. Maneva, N. Mankuzhiyil, K. Mannheim, L. Maraschi, M. Mariotti, M. Martínez, D. Mazin, M. Meucci, M. Meyer, J. M. Miranda, R. Mirzoyan, J. Moldón, M. Moles, A. Moralejo, D. Nieto, K. Nilsson, J. Ninkovic, N. Otte, I. Oya, R. Paoletti, J. M. Paredes, M. Pasanen, D. Pascoli, F. Pauss, R. G. Pegna, M. A. Perez-Torres, M. Persic, L. Peruzzo, F. Prada, E. Prandini, N. Puchades, A. Raymers, W. Rhode, M. Ribó, J. Rico, M. Rissi, A. Robert, S. Rügamer, A. Saggion, T. Y. Saito, M. Salvati, M. Sanchez-Conde, P. Sartori, K. Satalecka, V. Scalzotto, V. Scapin, T. Schweizer, M. Shayduk, K. Shinozaki, S. N. Shore, N. Sidro, A. Sierpowska-Bartosik, A. Sillanpää, J. Sitarek, D. Sobczynska, F. Spanier, A. Stamerra, L. S. Stark, L. Takalo, F. Tavecchio, P. Temnikov, D. Tescaro, M. Teshima, M. Tluczykont, D. F. Torres, N. Turini, H. Vankov, A. Venturini, V. Vitale, R. M. Wagner, W. Wittek, V. Zabalza, F. Zandanel, R. Zanin, and J. Zapatero. Discovery of a Very High Energy Gamma-Ray Signal from the 3C 66A/B Region. *ApJL*, 692:L29–L33, February 2009. doi: 10.1088/0004-637X/692/1/L29.

S. Archambault, T. Aune, B. Behera, M. Beilicke, W. Benbow, K. Berger, R. Bird, J. Biteau, V. Bugaev, K. Byrum, J. V. Cardenzana, M. Cerruti, X. Chen, L. Ciupik, M. P. Connolly, W. Cui, J. Dumm, M. Errando, A. Falcone, S. Federici, Q. Feng, J. P. Finley, H. Fleischhack, L. Fortson, A. Furniss, N. Galante, G. H. Gillanders, S. Griffin, S. T. Griffiths, J. Grube, G. Gyuk, D. Hanna,

J. Holder, G. Hughes, T. B. Humensky, C. A. Johnson, P. Kaaret, M. Kertzman, Y. Khassen, D. Kieda, H. Krawczynski, F. Krennrich, S. Kumar, M. J. Lang, A. S. Madhavan, G. Maier, A. McCann, K. Meagher, P. Moriarty, R. Mukherjee, D. Nieto, A. O'Faoláin de Bhróithe, R. A. Ong, A. N. Otte, N. Park, M. Pohl, A. Popkow, H. Prokoph, J. Quinn, K. Ragan, J. Rajotte, L. C. Reyes, P. T. Reynolds, G. T. Richards, E. Roache, G. H. Sembroski, K. Shahinyan, D. Staszak, I. Telezhinsky, J. V. Tucci, J. Tyler, A. Varlotta, V. V. Vassiliev, S. Vincent, S. P. Wakely, A. Weinstein, R. Welsing, A. Wilhelm, D. A. Williams, VERITAS Collaboration, M. Ackermann, M. Ajello, A. Albert, L. Baldini, D. Bastieri, R. Bellazzini, E. Bissaldi, J. Bregeon, R. Buehler, S. Buson, G. A. Caliandro, R. A. Cameron, P. A. Caraveo, E. Cavazzuti, E. Charles, J. Chiang, S. Ciprini, R. Claus, S. Cutini, F. D'Ammando, A. de Angelis, F. de Palma, C. D. Dermer, S. W. Digel, L. Di Venere, P. S. Drell, C. Favuzzi, A. Franckowiak, P. Fusco, F. Gargano, D. Gasparrini, N. Giglietto, F. Giordano, M. Giroletti, I. A. Grenier, S. Guiriec, T. Jogler, M. Kuss, S. Larsson, L. Latronico, F. Longo, F. Loparco, P. Lubrano, G. M. Madejski, M. Mayer, M. N. Mazziotta, P. F. Michelson, T. Mizuno, M. E. Monzani, A. Morselli, S. Murgia, E. Nuss, T. Ohsugi, J. F. Ormes, D. Paneque, J. S. Perkins, F. Piron, G. Pivato, S. Rainò, M. Razzano, A. Reimer, O. Reimer, S. Ritz, M. Schaal, C. Sgrò, E. J. Siskind, P. Spinelli, H. Takahashi, L. Tibaldo, M. Tinivella, E. Troja, G. Vianello, M. Werner, M. Wood, and Fermi LAT Collaboration. Deep Broadband Observations of the Distant Gamma-Ray Blazar PKS 1424+240. *ApJL*, 785:L16, April 2014. doi: 10.1088/2041-8205/785/1/L16.

S. Archambault, A. Archer, W. Benbow, R. Bird, J. Biteau, M. Buchovecky, J. H. Buckley, V. Bugaev, K. Byrum, M. Cerruti, X. Chen, L. Ciupik, M. P. Connolly, W. Cui, J. D. Eisch, M. Errando, A. Falcone, Q. Feng, J. P. Finley, H. Fleischhack, P. Fortin, L. Fortson, A. Furniss, G. H. Gillanders, S. Griffin, J. Grube, G. Gyuk, M. Hütten, N. Håkansson, D. Hanna, J. Holder, T. B. Humensky, C. A. Johnson, P. Kaaret, P. Kar, N. Kelley-Hoskins, M. Kertzman, D. Kieda, M. Krause, F. Krennrich, S. Kumar, M. J. Lang, G. Maier, S. McArthur, A. McCann, K. Meagher, P. Moriarty, R. Mukherjee, T. Nguyen, D. Nieto, A. O'Faoláin de Bhróithe, R. A. Ong, A. N. Otte, N. Park, J. S. Perkins, A. Pichel, M. Pohl, A. Popkow, E. Pueschel, J. Quinn, K. Ragan, P. T. Reynolds, G. T. Richards, E. Roache, A. C. Rovero, M. Santander, G. H. Sembroski, K. Shahinyan, A. W. Smith, D. Staszak, I. Telezhinsky, J. V. Tucci, J. Tyler, S. Vincent, S. P. Wakely, O. M. Weiner, A. Weinstein, D. A. Williams, B. Zitzer, VERITAS Collaboration, M. Fumagalli, and J. X. Prochaska. Upper Limits from Five Years of Blazar Observations with the VERITAS Cherenkov Telescopes. *AJ*, 151:142, June 2016. doi: 10.3847/0004-6256/151/6/142.

S. Archambault, A. Archer, W. Benbow, R. Bird, E. Bourbeau, A. Bouvier, M. Buchovecky, V. Bugaev, J. V. Cardenzana, M. Cerruti, L. Ciupik, M. P.

Connolly, W. Cui, M. K. Daniel, M. Errando, A. Falcone, Q. Feng, J. P. Finley, H. Fleischhack, L. Fortson, A. Furniss, G. H. Gillanders, S. Griffin, D. Hanna, O. Hervet, J. Holder, G. Hughes, T. B. Humensky, M. Hütten, C. A. Johnson, P. Kaaret, P. Kar, M. Kertzman, D. Kieda, M. Krause, M. J. Lang, T. T. Y. Lin, G. Maier, S. McArthur, P. Moriarty, R. Mukherjee, D. Nieto, S. O'Brien, R. A. Ong, A. N. Otte, N. Park, M. Pohl, A. Popkow, E. Pueschel, J. Quinn, K. Ragan, P. T. Reynolds, G. T. Richards, E. Roache, C. Rulten, I. Sadeh, G. H. Sembroski, K. Shahinyan, D. Staszak, I. Telezhinsky, S. Trepanier, S. P. Wakely, A. Weinstein, P. Wilcox, D. A. Williams, and B. Zitzer. Gamma-ray observations under bright moonlight with VERITAS. *Astroparticle Physics*, 91: 34–43, May 2017. doi: 10.1016/j.astropartphys.2017.03.001.

W. B. Atwood, A. A. Abdo, M. Ackermann, W. Althouse, B. Anderson, M. Axelsson, L. Baldini, J. Ballet, D. L. Band, G. Barbiellini, and others. The Large Area Telescope on the Fermi Gamma-Ray Space Telescope Mission. *ApJ*, 697: 1071–1102, June 2009. doi: 10.1088/0004-637X/697/2/1071.

B. W. Carroll and D. A. Ostlie. *An Introduction to Modern Astrophysics*. Pearson Education, Inc., 2 edition, 2007. ISBN 0805304029.

B. Zitzer for the VERITAS Collaboration. The VERITAS Upgraded Telescope-Level Trigger Systems: Technical Details and Performance Characterization. *ArXiv e-prints*, July 2013.

B. Zitzer for the VERITAS Collaboration. Background Systematic Studies in VERITAS Data. *ArXiv e-prints*, August 2017.

M. Boettcher, D. E. Harris, and H. Krawczynski. *Relativistic Jets from Active Galactic Nuclei*. January 2012.

A. Bouvier, L. Gebremedhin, C. A. Johnson, A. Kuznetsov, D. A. Williams, N. Otte, R. Strausbaugh, N. Hidaka, H. Tajima, J. Hinton, R. White, M. Errando, and R. Mukherjee. Photosensor characterization for the Cherenkov Telescope Array: silicon photomultiplier versus multi-anode photomultiplier tube. In *Hard X-Ray, Gamma-Ray, and Neutron Detector Physics XV*, volume 8852, page 88520K, September 2013. doi: 10.1117/12.2023778.

M. Cerruti, C. Boisson, and A. Zech. Constraining the parameter space of the one-zone synchrotron-self-Compton model for GeV-TeV detected BL Lacertae objects. *A&A*, 558:A47, October 2013. doi: 10.1051/0004-6361/201220963.

Cherenkov Telescope Array Consortium, :, B. S. Acharya, I. Agudo, I. A. Samarai, R. Alfaro, J. Alfaro, C. Alispach, R. Alves Batista, J.-P. Amans, and others. Science with the Cherenkov Telescope Array. *ArXiv e-prints*, September 2017.

P. Cogan. VEGAS, the VERITAS Gamma-ray Analysis Suite. *International Cosmic Ray Conference*, 3:1385–1388, 2008.

Peter Cogan. *Nanosecond Sampling of Atmospheric Cherenkov Radiation Applied to TeV Gamma-Ray Observations*. PhD thesis, University College Dublin, 2006.

D. B. Kieda for the VERITAS Collaboration. The Gamma Ray Detection sensitivity of the upgraded VERITAS Observatory. *ArXiv e-prints*, August 2013.

M. K. Daniel. The VERITAS standard data analysis. *International Cosmic Ray Conference*, 3:1325–1328, 2008.

R. A. Edelson and J. H. Krolik. The discrete correlation function - A new method for analyzing unevenly sampled variability data. *ApJ*, 333:646–659, October 1988. doi: 10.1086/166773.

M. Errando, R. Bock, D. Kranich, E. Lorenz, P. Majumdar, M. Mariotti, D. Mazin, E. Prandini, F. Tavecchio, M. Teshima, and R. Wagner. Discovery of very high energy gamma-rays from the flat spectrum radio quasar 3C 279 with the MAGIC telescope. In F. A. Aharonian, W. Hofmann, and F. Rieger, editors, *American Institute of Physics Conference Series*, volume 1085 of *American Institute of Physics Conference Series*, pages 423–426, December 2008. doi: 10.1063/1.3076698.

W. Essey and A. Kusenko. A new interpretation of the gamma-ray observations of distant active galactic nuclei. *Astroparticle Physics*, 33:81–85, March 2010. doi: 10.1016/j.astropartphys.2009.11.007.

D. J. Fegan. TOPICAL REVIEW: γ/hadron separation at TeV energies. *Journal of Physics G Nuclear Physics*, 23:1013–1060, September 1997. doi: 10.1088/0954-3899/23/9/004.

E. L. Fitzpatrick. Correcting for the Effects of Interstellar Extinction. *PASP*, 111: 63–75, January 1999. doi: 10.1086/316293.

V. P. Fomin, A. A. Stepanian, R. C. Lamb, D. A. Lewis, M. Punch, and T. C. Weekes. New methods of atmospheric Cherenkov imaging for gamma-ray astronomy. I. The false source method. *Astroparticle Physics*, 2:137–150, May 1994. doi: 10.1016/0927-6505(94)90036-1.

D. Foreman-Mackey, D. W. Hogg, D. Lang, and J. Goodman. emcee: The MCMC Hammer. *PASP*, 125:306, March 2013a. doi: 10.1086/670067.

D. Foreman-Mackey, D. W. Hogg, D. Lang, and J. Goodman. emcee: The MCMC Hammer. *PASP*, 125:306, March 2013b. doi: 10.1086/670067.

G. Fossati, L. Maraschi, A. Celotti, A. Comastri, and G. Ghisellini. A unifying view of the spectral energy distributions of blazars. *MNRAS*, 299:433–448, September 1998. doi: 10.1046/j.1365-8711.1998.01828.x.

A. Franceschini, G. Rodighiero, and M. Vaccari. Extragalactic optical-infrared background radiation, its time evolution and the cosmic photon-photon opacity. *A&A*, 487:837–852, September 2008. doi: 10.1051/0004-6361:200809691.

A. Furniss, M. Fumagalli, C. Danforth, D. A. Williams, and J. X. Prochaska. On the Redshift of the Very High Energy Blazar 3C 66A. *ApJ*, 766:35, March 2013. doi: 10.1088/0004-637X/766/1/35.

N. Gehrels, G. Chincarini, P. Giommi, K. O. Mason, J. A. Nousek, A. A. Wells, N. E. White, S. D. Barthelmy, D. N. Burrows, L. R. Cominsky, K. C. Hurley, F. E. Marshall, P. Mészáros, P. W. A. Roming, L. Angelini, L. M. Barbier, T. Belloni, S. Campana, P. A. Caraveo, M. M. Chester, O. Citterio, T. L. Cline, M. S. Cropper, J. R. Cummings, A. J. Dean, E. D. Feigelson, E. E. Fenimore, D. A. Frail, A. S. Fruchter, G. P. Garmire, K. Gendreau, G. Ghisellini, J. Greiner, J. E. Hill, S. D. Hunsberger, H. A. Krimm, S. R. Kulkarni, P. Kumar, F. Lebrun, N. M. Lloyd-Ronning, C. B. Markwardt, B. J. Mattson, R. F. Mushotzky, J. P. Norris, J. Osborne, B. Paczynski, D. M. Palmer, H.-S. Park, A. M. Parsons, J. Paul, M. J. Rees, C. S. Reynolds, J. E. Rhoads, T. P. Sasseen, B. E. Schaefer, A. T. Short, A. P. Smale, I. A. Smith, L. Stella, G. Tagliaferri, T. Takahashi, M. Tashiro, L. K. Townsley, J. Tueller, M. J. L. Turner, M. Vietri, W. Voges, M. J. Ward, R. Willingale, F. M. Zerbi, and W. W. Zhang. The Swift Gamma-Ray Burst Mission. *ApJ*, 611:1005–1020, August 2004. doi: 10.1086/422091.

G. Ghisellini. The Blazar Sequence 2.0. *Galaxies*, 4:36, September 2016. doi: 10.3390/galaxies4040036.

R. C. Gilmore, R. S. Somerville, J. R. Primack, and A. Domínguez. Semi-analytic modelling of the extragalactic background light and consequences for extragalactic gamma-ray spectra. *MNRAS*, 422:3189–3207, June 2012. doi: 10.1111/j.1365-2966.2012.20841.x.

J. Goodman and J. Weare. Ensemble samplers with affine invariance. *Communications in Applied Mathematics and Computational Science, Vol. 5, No. 1, p. 65-80, 2010*, 5:65–80, 2010. doi: 10.2140/camcos.2010.5.65.

D. Hanna, A. McCann, M. McCutcheon, and L. Nikkinen. An LED-based flasher system for VERITAS. *Nuclear Instruments and Methods in Physics Research A*, 612:278–287, January 2010. doi: 10.1016/j.nima.2009.10.107.

D. Heck, J. Knapp, J. N. Capdevielle, G. Schatz, and T. Thouw. *CORSIKA: a Monte Carlo code to simulate extensive air showers.* February 1998.

O. Hervet, C. Boisson, and H. Sol. An innovative blazar classification based on radio jet kinematics. *A&A*, 592:A22, July 2016. doi: 10.1051/0004-6361/201628117.

H.E.S.S. Collaboration, A. Abramowski, F. Acero, F. Aharonian, A. G. Akhperjanian, G. Anton, A. Balzer, A. Barnacka, Y. Becherini, J. Becker, K. Bernlöhr, E. Birsin, J. Biteau, A. Bochow, C. Boisson, J. Bolmont, P. Bordas, J. Brucker, F. Brun, P. Brun, T. Bulik, I. Büsching, S. Carrigan, S. Casanova, M. Cerruti, P. M. Chadwick, A. Charbonnier, R. C. G. Chaves, A. Cheesebrough, G. Cologna, J. Conrad, M. Dalton, M. K. Daniel, I. D. Davids, B. Degrange, C. Deil, H. J. Dickinson, A. Djannati-Ataï, W. Domainko, L. O. Drury, G. Dubus, K. Dutson, J. Dyks, M. Dyrda, K. Egberts, P. Eger, P. Espigat, L. Fallon, S. Fegan, F. Feinstein, M. V. Fernandes, A. Fiasson, G. Fontaine, A. Förster, M. Füßling, Y. A. Gallant, H. Gast, L. Gérard, D. Gerbig, B. Giebels, J. F. Glicenstein, B. Glück, D. Göring, S. Häffner, J. D. Hague, J. Hahn, D. Hampf, J. Harris, M. Hauser, S. Heinz, G. Heinzelmann, G. Henri, G. Hermann, A. Hillert, J. A. Hinton, W. Hofmann, P. Hofverberg, M. Holler, D. Horns, A. Jacholkowska, O. C. de Jager, C. Jahn, M. Jamrozy, I. Jung, M. A. Kastendieck, K. Katarzyński, U. Katz, S. Kaufmann, D. Keogh, B. Khélifi, D. Klochkov, W. Kluźniak, T. Kneiske, N. Komin, K. Kosack, R. Kossakowski, F. Krayzel, H. Laffon, G. Lamanna, J.-P. Lenain, D. Lennarz, T. Lohse, A. Lopatin, C.-C. Lu, V. Marandon, A. Marcowith, J. Masbou, N. Maxted, M. Mayer, T. J. L. McComb, M. C. Medina, J. Méhault, R. Moderski, M. Mohamed, E. Moulin, C. L. Naumann, M. Naumann-Godo, M. de Naurois, D. Nedbal, D. Nekrassov, N. Nguyen, B. Nicholas, J. Niemiec, S. J. Nolan, S. Ohm, E. de Oña Wilhelmi, B. Opitz, M. Ostrowski, I. Oya, M. Panter, M. Paz Arribas, N. W. Pekeur, G. Pelletier, J. Perez, P.-O. Petrucci, B. Peyaud, S. Pita, G. Pühlhofer, M. Punch, A. Quirrenbach, M. Raue, S. M. Rayner, A. Reimer, O. Reimer, M. Renaud, R. de los Reyes, F. Rieger, J. Ripken, L. Rob, S. Rosier-Lees, G. Rowell, B. Rudak, C. B. Rulten, V. Sahakian, D. A. Sanchez, A. Santangelo, R. Schlickeiser, A. Schulz, U. Schwanke, S. Schwarzburg, S. Schwemmer, F. Sheidaei, J. L. Skilton, H. Sol, G. Spengler, Ł. Stawarz, R. Steenkamp, C. Stegmann, F. Stinzing, K. Stycz, I. Sushch, A. Szostek, J.-P. Tavernet, R. Terrier, M. Tluczykont, K. Valerius, C. van Eldik, G. Vasileiadis, C. Venter, A. Viana, P. Vincent, H. J. Völk, F. Volpe, S. Vorobiov, M. Vorster, S. J. Wagner, M. Ward, R. White, A. Wierzcholska, M. Zacharias, A. Zajczyk, A. A. Zdziarski, A. Zech, and H.-S. Zechlin. Discovery of VHE γ-ray emission and multi-wavelength observations of the BL Lacertae object 1RXS J101015.9-311909. *A&A*, 542:A94, June 2012. doi: 10.1051/0004-6361/201218910.

A. M. Hillas. Cerenkov light images of EAS produced by primary gamma. *International Cosmic Ray Conference*, 3, August 1985.

IceCube Collaboration, M. G. Aartsen, M. Ackermann, J. Adams, J. A. Aguilar, M. Ahlers, M. Ahrens, I. Al Samarai, D. Altmann, K. Andeen, and others. Multimessenger observations of a flaring blazar coincident with high-energy neutrino IceCube-170922A. *Science*, 361:eaat1378, July 2018. doi: 10.1126/science.aat1378.

S. Inoue and F. Takahara. Electron Acceleration and Gamma-Ray Emission from Blazars. *ApJ*, 463:555, June 1996. doi: 10.1086/177270.

J. C. Isler, C. M. Urry, P. Coppi, C. Bailyn, R. Chatterjee, G. Fossati, E. W. Bonning, L. Maraschi, and M. Buxton. A Time-resolved Study of the Broad-line Region in Blazar 3C 454.3. *ApJ*, 779:100, December 2013. doi: 10.1088/0004-637X/779/2/100.

R. Itoh, Y. Fukazawa, J. Chiang, Y. Hanabata, M. Hayashida, K. Hayashi, T. Mizuno, M. Ohno, T. Ohsugi, J. S. Perkins, S. Rainò, L. C. Reyes, H. Takahashi, Y. Tanaka, G. Tosti, H. Akitaya, A. Arai, M. Kino, Y. Ikejiri, K. S. Kawabata, T. Komatsu, K. Sakimoto, M. Sasada, S. Sato, M. Uemura, T. Ui, M. Yamanaka, and M. Yoshida. A Study of the Long-Term Spectral Variations of 3C 66A Observed with the Fermi and Kanata Telescopes. *PASJ*, 65:18, February 2013. doi: 10.1093/pasj/65.1.18.

J. Cardenzana for the VERITAS Collaboration. A Novel Method for Detecting Extended Sources with VERITAS. In *34th International Cosmic Ray Conference (ICRC2015)*, volume 34 of *International Cosmic Ray Conference*, page 1031, July 2015.

J. Christiansen for the VERITAS Collaboration. Characterization of a Maximum Likelihood Gamma-Ray Reconstruction Algorithm for VERITAS. *International Cosmic Ray Conference*, 35:789, January 2017.

J. Vievering for the VERITAS Collaboration. VHE Analyses of Long-Term Low-Flux-State Observations by VERITAS of Intermediate-Frequency-Peaked BL Lacertae Sources: 3C 66A and W Comae. *ArXiv e-prints*, August 2015.

J. D. Jackson. *Classical electrodynamics*. 1975.

K. Katarzyński, H. Sol, and A. Kus. The multifrequency emission of Mrk 501. From radio to TeV gamma-rays. *A&A*, 367:809–825, March 2001. doi: 10.1051/0004-6361:20000538.

M. Lampton, B. Margon, and S. Bowyer. Parameter estimation in X-ray astronomy. *ApJ*, 208:177–190, August 1976. doi: 10.1086/154592.

T.-P. Li and Y.-Q. Ma. Analysis methods for results in gamma-ray astronomy. *Astrophysical Journal*, 272:317–324, September 1983. doi: 10.1086/161295.

M. Cerruti M. for the VERITAS Collaboration. Very-high-energy blazars: updates from VERITAS observations and multi-wavelength campaigns. *ArXiv e-prints*, January 2015.

P. Marziani, J. W. Sulentic, D. Dultzin-Hacyan, M. Calvani, and M. Moles. Comparative Analysis of the High- and Low-Ionization Lines in the Broad-Line Region of Active Galactic Nuclei. *ApJS*, 104:37, May 1996. doi: 10.1086/192291.

R. Mirzoyan. Discovery of Very High Energy Gamma-Ray Emission From Gravitationally Lensed Blazar S3 0218+357 With the MAGIC Telescopes. *The Astronomer's Telegram*, 6349, July 2014.

R. Mukherjee. Very-high-energy gamma-ray emission from PKS 1441+25 detected with VERITAS. *The Astronomer's Telegram*, 7433, April 2015.

R. Mukherjee. VERITAS discovery of VHE emission from the FRI radio galaxy 3C 264. *The Astronomer's Telegram*, 11436, March 2018.

Y. I. Neshpor, A. A. Stepanyan, O. P. Kalekin, V. P. Fomin, N. N. Chalenko, and V. G. Shitov. Blazar 3C 66A: Another extragalactic source of ultra-high-energy gamma-ray photons. *Astronomy Letters*, 24:134–138, March 1998.

H. Netzer. Revisiting the Unified Model of Active Galactic Nuclei. *ARAA*, 53: 365–408, August 2015. doi: 10.1146/annurev-astro-082214-122302.

A. I. Nikishov. Absorption of High-Energy Photons in the Universe . *Soviet Journal of Experimental and Theoretical Physics*, 41:549, 1962.

P. L. Nolan, A. A. Abdo, M. Ackermann, M. Ajello, A. Allafort, E. Antolini, W. B. Atwood, M. Axelsson, L. Baldini, J. Ballet, and others. Fermi Large Area Telescope Second Source Catalog. *ApJS*, 199:31, April 2012. doi: 10.1088/0067-0049/199/2/31.

T. S. Poole, A. A. Breeveld, M. J. Page, W. Landsman, S. T. Holland, P. Roming, N. P. M. Kuin, P. J. Brown, C. Gronwall, S. Hunsberger, S. Koch, K. O. Mason, P. Schady, D. vanden Berk, A. J. Blustin, P. Boyd, P. Broos, M. Carter, M. M. Chester, A. Cucchiara, B. Hancock, H. Huckle, S. Immler, M. Ivanushkina, T. Kennedy, F. Marshall, A. Morgan, S. B. Pandey, M. de Pasquale, P. J. Smith, and M. Still. Photometric calibration of the Swift ultraviolet/optical telescope. *MNRAS*, 383:627–645, January 2008. doi: 10.1111/j.1365-2966.2007.12563.x.

M. Punch, C. W. Akerlof, M. F. Cawley, M. Chantell, D. J. Fegan, S. Fennell, J. A. Gaidos, J. Hagan, A. M. Hillas, Y. Jiang, A. D. Kerrick, R. C. Lamb, M. A. Lawrence, D. A. Lewis, D. I. Meyer, G. Mohanty, K. S. O'Flaherty, P. T. Reynolds, A. C. Rovero, M. S. Schubnell, G. Sembroski, T. C. Weekes, T. Whitaker, and C. Wilson. Detection of TeV photons from the active galaxy Markarian 421. *Nature*, 358:477, August 1992. doi: 10.1038/358477a0.

J. Quinn, C. W. Akerlof, S. Biller, J. Buckley, D. A. Carter-Lewis, M. F. Cawley, M. Catanese, V. Connaughton, D. J. Fegan, J. P. Finley, J. Gaidos, A. M. Hillas, R. C. Lamb, F. Krennrich, R. Lessard, J. E. McEnery, D. I. Meyer, G. Mohanty, A. J. Rodgers, H. J. Rose, G. Sembroski, M. S. Schubnell, T. C. Weekes, C. Wilson, and J. Zweerink. Detection of Gamma Rays with E $>$ 300 GeV from Markarian 501. *ApJL*, 456:L83, January 1996. doi: 10.1086/309878.

R. Wells for the VERITAS Collaboration. Multi-TeV Energy Resolution Studies with VERITAS. *ArXiv e-prints*, August 2017.

P. F. Rebillot, J. H. Buckley, P. Dowkontt, and K. Kosack. The VERITAS Flash ADC Electronics System. *International Cosmic Ray Conference*, 5:2827, July 2003.

E. Roache, R. Irvin, J. S. Perkins, K. Harris, A. Falcone, J. Finley, and T. Weeks. Mirror Facets for the VERITAS Telescopes. *International Cosmic Ray Conference*, 3:1397–1400, 2008.

P. W. A. Roming, T. E. Kennedy, K. O. Mason, J. A. Nousek, L. Ahr, R. E. Bingham, P. S. Broos, M. J. Carter, B. K. Hancock, H. E. Huckle, S. D. Hunsberger, H. Kawakami, R. Killough, T. S. Koch, M. K. McLelland, K. Smith, P. J. Smith, J. C. Soto, P. T. Boyd, A. A. Breeveld, S. T. Holland, M. Ivanushkina, M. S. Pryzby, M. D. Still, and J. Stock. The Swift Ultra-Violet/Optical Telescope. *SSRv*, 120:95–142, October 2005. doi: 10.1007/s11214-005-5095-4.

G. B. Rybicki and A. P. Lightman. *Radiative processes in astrophysics*. 1979.

S. Vincent for the VERITAS Collaboration. A Monte Carlo template-based analysis for very high definition imaging atmospheric Cherenkov telescopes as applied to the VERITAS telescope array. *ArXiv e-prints*, September 2015.

E. F. Schlafly and D. P. Finkbeiner. Measuring Reddening with Sloan Digital Sky Survey Stellar Spectra and Recalibrating SFD. *ApJ*, 737:103, August 2011. doi: 10.1088/0004-637X/737/2/103.

P. S. Smith, G. D. Schmidt, and B. T. Jannuzi. The Optical Properties of PKS 1222+216 During the Fermi Mission. *ArXiv e-prints*, October 2011.

G. Spengler. Significance in gamma ray astronomy with systematic errors. *Astroparticle Physics*, 67:70–74, July 2015. doi: 10.1016/j.astropartphys.2015.02.002.

S. Swordy. Discovery of >100 GeV Gamma-ray Emission from the Blazar 3C66A by VERITAS. *The Astronomer's Telegram*, 1753, October 2008.

The Fermi-LAT Collaboration. 3FHL: The Third Catalog of Hard Fermi-LAT Sources. *ArXiv e-prints*, February 2017.

J. Torres-Zafra, S. A. Cellone, A. Buzzoni, I. Andruchow, and J. G. Portilla. Redshift determination of the BL Lac object 3C 66A by the detection of its host galaxy cluster at z = 0.340. *MNRAS*, 474:3162–3172, March 2018. doi: 10.1093/mnras/stx2561.

C. M. Urry and P. Padovani. Unified Schemes for Radio-Loud Active Galactic Nuclei. *PASP*, 107:803, September 1995. doi: 10.1086/133630.

T. C. Weekes, M. F. Cawley, D. J. Fegan, K. G. Gibbs, A. M. Hillas, P. W. Kowk, R. C. Lamb, D. A. Lewis, D. Macomb, N. A. Porter, P. T. Reynolds, and G. Vacanti. Observation of TeV gamma rays from the Crab nebula using the atmospheric Cerenkov imaging technique. *ApJ*, 342:379–395, July 1989. doi: 10.1086/167599.

A. Weinstein. The VERITAS Trigger System. *International Cosmic Ray Conference*, 3:1539–1542, 2008.

B. Zitzer. The VERITAS Dark Matter Program. *ArXiv e-prints*, March 2015.